Towards terahertz microscopy

Proefschift

ter verkrijging van de graad van doctor
aan de Technische Universiteit Delft,
op gezag van de Rector Magnificus prof. dr. ir. J.T. Fokkema,
voorzitter van het College voor Promoties,
in het openbaar te verdedigen op
maandag 28 november 2005 om 15:30 uur

door

Nicolaas Cornelis Johannes VAN DER VALK

natuurkundig ingenieur
geboren te Delft.

Dit proefschrift is goedgekeurd door de promotoren:
Prof. dr. ir. J. J. M. Braat
Prof. dr. H. J. Bakker

Toegevoegd promotor:
Dr. P. C. M. Planken

Samenstelling promotiecommissie:

Rector Magnificus,	voorzitter
Prof. dr. ir. J. J. M. Braat,	Technische Universiteit Delft, promotor
Prof. dr. H. J. Bakker,	Universiteit van Amsterdam, promotor
Dr. P. C. M. Planken,	Technische Universiteit Delft, toegevoegd promotor
Prof. dr. D. M. Mittleman,	Rice University, Verenigde Staten
Prof. dr. P. Haring Bolívar,	University of Siegen, Duitsland
Prof. dr. ir. P. Kruit,	Technische Universiteit Delft
Prof. dr. ir. P. M. van den Berg,	Technische Universiteit Delft

This work was performed as part of the EU TERAVISION Program (IST-199-10154), and as part of the research program of the "Stichting voor Fundamenteel Onderzoek der Materie (FOM)," which is financially supported by the "Nederlandse Organisatie voor Wetenschappelijk Onderzoek (NWO)."

Aan mijn ouders

Contents

Chapter 1

Introduction

This chapter starts with a quick introduction into the physics of electromagnetic radiation with a frequency in the terahertz range. In section 1.2, we will introduce terahertz spectroscopy, and we will compare the technique used throughout this thesis, time-domain spectroscopy, with an alternative method based on homodyne detection. Section 1.3 discusses the possible applications of terahertz spectroscopy, ending with the main focus of this thesis: terahertz microscopy.

1.1 Terahertz radiation, background

Terahertz radiation is electromagnetic radiation with a frequency in the range between 0.1 THz and 30 THz (1 THz = 10^{12} Hz). As can be seen in figure 1.1, this range is situated at the transition between the microwave part and the infrared part of the electromagnetic spectrum. The terahertz region can therefore be seen as the transition region from electronics to optics. In electronics, electromagnetic radiation is mostly seen as electrical waves, of which the phase can be directly measured. In optics, however, electromagnetic radiation is seen as rays of light, which can easily be manipulated by mirrors and lenses, but of which only the intensity can be directly measured. In the terahertz field, we try to combine electronics and optics, using the best of both fields. On the one hand, the terahertz field shares the advantage with electronics, that the phase of the electric field can be directly measured. On the other hand, components from the field of optics, such as mirrors and lenses, can be used to manipulate terahertz beams.

The boundaries of the terahertz region are, more or less arbitrarily, determined by the techniques available to generate and to detect the radiation. Historically, terahertz spectroscopy was characterized by a lack of good sources and detectors. The available detectors could only measure the power in a terahertz beam, and were thus not sensitive to the phase of the light. Therefore, interferometric techniques had to be used to measure the phase of a terahertz beam.

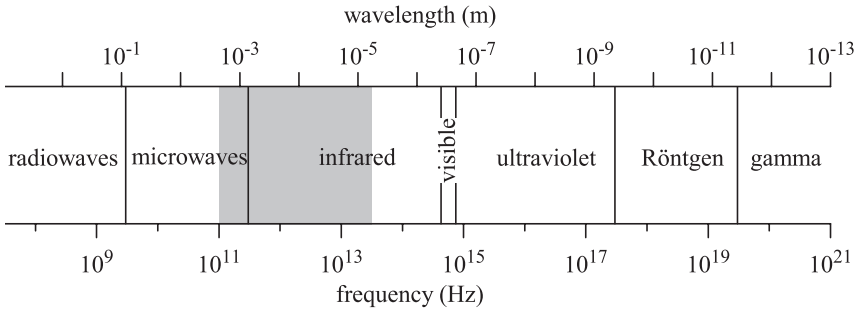

Figure 1.1: Schematic picture of the electromagnetic spectrum with the position of the terahertz region indicated in gray. The top and bottom axes represent respectively the wavelength and the frequency of the radiation on a logarithmic scale.

The first terahertz sources were based on thermal radiation from heated objects. However, these sources are very inefficient, and cannot produce coherent light. Later, coherent sources were developed. Coherent sources can be divided into two groups: Electronic techniques extended to higher frequencies, and optical sources extended to lower frequencies. Most intense terahertz sources based on electronic techniques rely on the acceleration and deceleration of an electron beam in a microwave cavity. Of this class of instruments, the so-called backward-wave oscillator is able to produce coherent radiation with a slightly tunable frequency. However, the power levels that can be reached with such a device rapidly decrease with frequency to values on the order of milliwatts at 1 THz. A good overview of electronic terahertz sources is given by Martin and Mizuno.[1]

New terahertz sources based on optics involved lasers. The first terahertz lasers were based on transitions between rotational states in molecular gasses or on transitions between impurity states in semiconductors. The molecular gas laser can provide high power levels, on the order of kilowatts, but the frequency of these lasers is not continuously tunable.[2] Semiconductor lasers are slightly tunable, but, as phonon scattering can easily destroy the population inversion in such a laser, these devises need to be cooled to very low temperatures.[1] Recently, a new type of laser was introduced to the terahertz field: the quantum cascade laser.[3,4] As this type of laser may have a large impact on the terahertz field, it will be discussed in more detail in section 1.2.1.

An important milestone for the terahertz field was reached, when ultrafast laser pulses were used for the generation (fig. 1.2) and detection of terahertz radiation. These ultrafast lasers allow the use of time-gating techniques, which make it possible to directly measure the electric field of a terahertz pulse as a function of time. Such a measurement provides not only the amplitude of the electric field at each terahertz frequency, but also the phase, and can do this for a large range of frequencies simultaneously. The time-gated detection methods that became available by the use of ultrafast lasers are described in more detail in section 1.2.2.

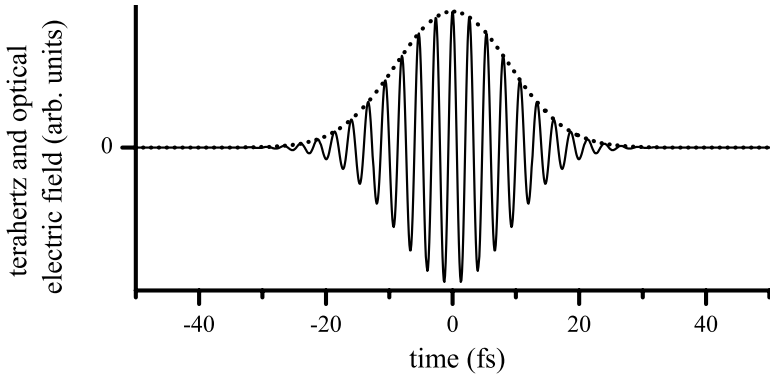

Figure 1.2: The electric field of an ultrafast laser pulse with a duration of 15 fs and a central wavelength of 800 nm (solid line). In a process called optical rectification, the laser pulse generates a terahertz pulse (dotted line), which is proportional to the intensity envelope of the laser pulse.

The generation and time-gated detection of terahertz radiation was soon used for many applications. For instance, it has been applied to spectroscopic analysis of the complex dielectric function of gases,[5] dielectrics and semiconductors.[6] It also has been used to study a variety of physical processes, such as intervalley scattering,[7] Cooper pair breaking[8] and ionization of Rydberg atoms.[9]

In 1995 Hu and Nuss demonstrated the first terahertz imaging setup.[10] In this imaging method, the object is scanned through the focus of a terahertz beam, while for each pixel a terahertz pulse as a function of time is measured. Since each pixel does not represent a value but a complex waveform, a large amount of data is collected in a single scan of the object. The introduction of imaging to the terahertz field has led to a series of new developments. The need to scan the object was removed by the use of CCD camera's in two-dimensional imaging.[11] In 1997 three-dimensional images were made in the first demonstration of terahertz computed tomography.[12] One year later, Jiang and Zhang showed single-shot imaging, where a full trace of the terahertz electric field versus time could be measured along a one-dimensional line using a single terahertz pulse.[13] In 1998, the first terahertz near-field images were also reported.[14]

Although there is an ever increasing interest in the use of terahertz radiation, especially since the development of terahertz imaging, the progress in commercialization of the new developments is limited. This is largely due to a lack of a "terahertz killer application". A terahertz killer application is an application for which only terahertz radiation can be used or for which the alternatives are much more expensive. We feel that such an application might soon arise, as an increasing number of materials shows distinct features in the terahertz region. Also, new techniques are developed that reduce the cost of a terahertz system. Section 1.3 presents an overview of possible future applications.

1.2 Terahertz phase-sensitive spectroscopy

In the terahertz region, there are generally two ways to do spectroscopy in which both the amplitude and the phase of the light is obtained. The first uses continuous, monochromatic sources and homodyne detection methods, and the second, which is the method that we employ, uses ultrafast pulsed sources and directly measures the electric field of the pulses. We compare the two methods and discuss their advantages and disadvantages. In this way, we hope to give the reader an idea of the applicability of the methods discussed in this thesis.

We will not discuss spectroscopy methods that provide only amplitude information and no phase information. With only amplitude information, it is much more difficult to obtain physical quantities related to retardation times, such as the refractive index of a material. There are, of course, situations in which an amplitude-only detection scheme suffices, but this thesis focusses on the many situations where phase information *is* essential.

When the terahertz refractive index and absorption coefficient is to be determined, it is also possible to use incoherent sources.[15,16] However, techniques using such sources are sensitive to thermal radiation from the surroundings, which severely limits their sensitivity. Low-frequency noise due to fluctuations of thermal radiation, for instance due to air turbulence, can be removed with lock-in detection techniques. However, the shot noise from thermal radiation cannot be removed from the measurement and places an upper limit on the detection sensitivity.

1.2.1 Homodyne spectroscopy

Continuous-wave spectroscopy uses beams with discrete, narrow band frequencies to obtain spectroscopic information. The continuous-wave spectroscopy techniques can be divided into two groups: homodyne and heterodyne spectroscopy. For both groups, the phase of the terahertz beam under study, called the object beam, is obtained by interference between the object beam and a second terahertz beam, called the reference beam. For homodyne detection, the reference beam has the same frequency as the object beam, in contrast to heterodyne detection, where the reference frequency differs from the object frequency. Heterodyne detection is often employed, when the frequency of the object beam is unknown, as, for instance, in the observation of astronomical objects. However, for the imaging of objects that do not actively radiate at terahertz frequencies, heterodyne detection is less suitable, since it requires two continuous-wave terahertz beams with different frequencies that must be phase-stable with respect to each other. Homodyne detection, however, requires only one source, because the object beam and the reference beam can be derived from the same source. Heterodyne detection will, therefore, not be discussed in more detail.

Figure 1.3 shows a schematic picture of homodyne detection. This detection scheme can be used for imaging and spectroscopy purposes by placing the object under study in the object beam. The object will affect both the am-

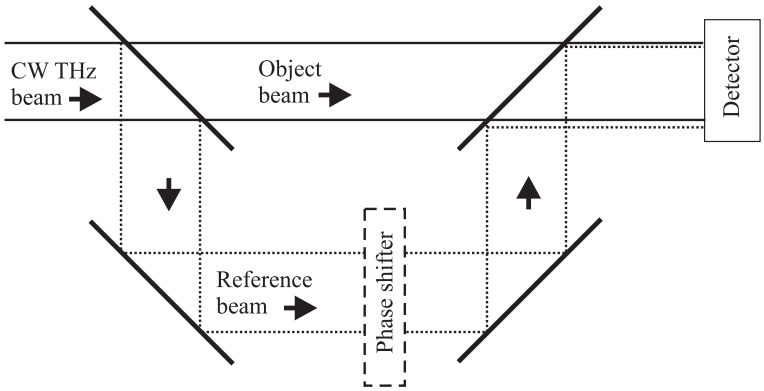

Figure 1.3: Schematic picture of terahertz homodyne detection. A continuous-wave terahertz beam is split into an object beam and a reference beam. The reference beam travels through a phase shifter, which shifts the phase of the reference beam with respect to the object beam. The object beam and the reference beam are superimposed on the detector.

plitude and the phase of the object beam. Both quantities can be measured by superimposing the object beam with a reference beam on the detector. The detector gives a signal proportional to $(C + E_{o0}E_{r0}\cos(\psi_{or}))$, where E_{r0} and E_{o0} are the electric-field amplitudes of the reference beam and the object beam, and ψ_{or} is the phase difference between the object and the reference beam. The value of the constant C is different for different types of homodyne detection. By changing the phase of the reference beam, both the amplitude and the phase of the object beam can be measured. Typically, a series of measurements is taken, each measurement with a slightly different value of ψ_{or}. The result of this series is, apart from the noise, a signal proportional to the cosine of ψ_{or}. The amplitude and phase of the cosine function is then determined from the data, usually by a Fourier transform. The amount of data that is required is determined by the noise level and the desired accuracy. To obtain a full spectrum, the frequency of the two beams is scanned, while both the amplitude and the phase are measured at each frequency. Note that the measurement of a spectrum requires two values to be scanned: the frequency of the terahertz beam and at each frequency the phase difference ψ_{or}.

For terahertz homodyne spectroscopy one needs a source that provides coherent narrow-band terahertz radiation. The frequency resolution of the setup is directly determined by the line width of the source and its stability. There are many sources available that enable a high frequency resolution, such as photomixers, backward-wave oscillators, and molecular gas lasers. Resolutions of less than 1 MHz are obtained with these sources. So far, however, no sources are available that combine a strong emission with a good tunability. This seriously limits the capability of the technique to measure a significant part of the terahertz spectrum in a reasonable time.

An overview of the many continuous-wave terahertz sources is available in several review articles.[1,17] Here, we would like to make some general re-

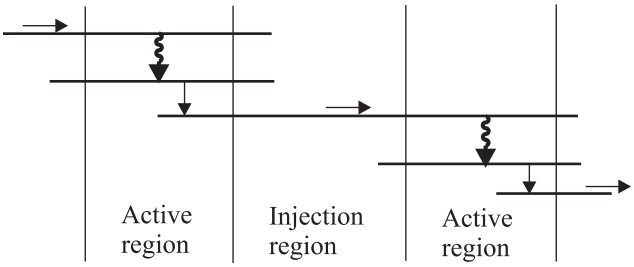

Figure 1.4: Schematic picture of the energy levels in the different regions of a quantum cascade laser. The arrows indicate the flow of electrons through the heterostructure. The radiative transitions are indicated by the wave-shaped arrows.

marks on the new development of the terahertz quantum cascade laser. The concept of the quantum cascade laser has only very recently been extended to terahertz frequencies.[3,4] In quantum cascade lasers, the laser transition occurs between the subbands formed from the conduction band in a heterostructure. Such heterostructures consist of a building block that is repeated many times. These building blocks contain an injector region and an active region as indicated in figure 1.4. In the active region, an electron drops from an excited level to a lower level under emission of a photon. In the injector region, this electron is then injected from the lower level to the excited level of the next active region. This way, an electron cascades down the potential staircase of the heterostructure, while emitting a photon at each building block. It may seem odd that the energy levels in the active layer on the right of figure 1.4 are lower than the levels in the left active layer, while the two layers are built identically. However, a strong electric field of several kV/cm is applied across the structure, which shifts the energy levels.

The terahertz quantum cascade laser has the advantage that it can produce powers in the milliwatt range in a device of small dimensions that can potentially be produced cheaply. These properties make the quantum cascade laser a good candidate for commercial applications. However, so far these lasers need to be cooled to at least liquid nitrogen temperatures, and the ability to tune the frequency of these lasers is very limited.

As for the sources, there are many types of detectors available to detect continuous wave radiation. Elaborate reviews are given in references 17–19.

1.2.2 Time-domain spectroscopy

The previous section discusses the techniques to measure the amplitude and phase at discrete terahertz frequencies. However, it is also possible to measure the electric field as a function of time, and obtain the spectrum by a Fourier transform of the time domain data. This is called time-domain spectroscopy. Historically, the problem in measuring the electric field of terahertz radiation as a function of time, is that no electronics is fast enough to follow the fast oscillations of the electric field. This problem was solved by using ultrafast

laser pulses for the generation and detection of terahertz radiation.[20] With ultrafast pulses, it is possible to directly measure an electric field oscillating at terahertz frequencies by a stroboscopic technique called time-gated detection. There are generally two methods to obtain time-gated detection: electro-optic detection and photoconductive antenna's. To explain time-gated detection, we consider the example of photoconductive antennas. Electro-optic detection plays an important role in this work and will be discussed in detail in chapter 2.

Photoconductive antenna's are fabricated on a piece of semiconductor material that is usually not conductive. However, an ultrafast laser pulse can be used to excite carriers to the conduction band, which instantaneously makes the material conductive. Note that this ultrafast laser pulse is so short that the variation of a terahertz electric field during the laser pulse is negligible. Shortly after the carriers are excited, they are trapped again; a process which rapidly shuts down the conductivity. During the short period that the antenna conducts, a terahertz electric field can induce a current through the antenna, which is measured with a sensitive current detector. However, the detector is insensitive to the terahertz electric field before and after the laser pulse, when the antenna is not conductive. In this way, the laser pulse functions as a time gate that we can use to selectively measure the terahertz electric field at a particular time. The electric field at other positions in time is obtained by scanning the time delay and repeating the experiment with a new laser pulse and a new terahertz pulse.

Time-gated detection requires that the ultrafast laser pulses are synchronized to the terahertz electric field. This is done by generating terahertz pulses with ultrafast optical pulses derived from the same laser that is used for the detection. One can use nonlinear optical effects and photoconductive antenna's for the generation of terahertz pulses. The power levels generated with these methods are difficult to compare with the power levels generated by continuous sources. The average power levels of 10 to 100 μW are low compared to the average powers of continuous sources, but the peak power can reach 1 W. More relevant to time-domain spectroscopy is the peak height of the electric field of the terahertz pulse, which can reach values up to 100 V/cm. This is a most relevant quantity, since it is directly proportional to the spectral amplitude. The frequency dependence of the spectral amplitude is determined by the shape of the terahertz pulse in the time domain, which often can be approximated by a single-cycle, Gaussian-shaped pulse.

Figure 1.5 shows an example of a terahertz pulse measured using ultrafast laser pulses. The electric field has one large oscillation followed by a long fluctuating tail. Note that the fluctuations in the tail are not random, but reproducible. The tail is caused by absorption and subsequent re-emission of terahertz radiation by water vapor molecules in the atmosphere. Contrary to the microwave region,[21] absorption by oxygen molecules is negligible in the terahertz region. The time scale of the features in figure 1.5 is on the order of 1 ps. Although this is a very small time scale from an electronics view point, it is much longer than the 15 fs duration of the laser pulse used to measure the electric field.

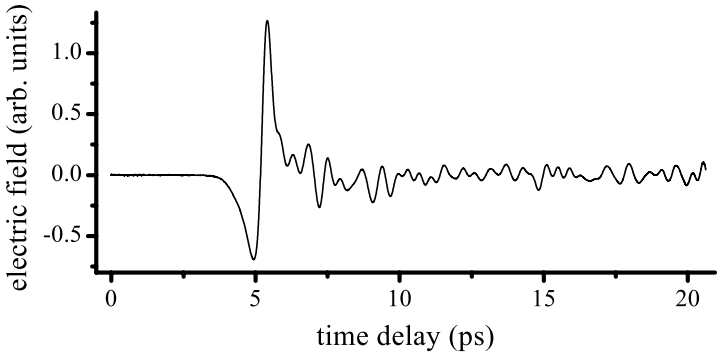

Figure 1.5: Measured electric field as a function of time of a typical terahertz pulse.

1.2.3 Homodyne versus time-domain spectroscopy

To compare homodyne spectroscopy and time-domain spectroscopy, we consider three system parameters: spectral resolution, signal-to-noise ratio and dynamic range. In terms of spectral resolution, which is the resolution that can be obtained in the spectral domain, homodyne spectroscopy is better than time-domain spectroscopy. The spectral resolution of homodyne spectroscopy is fundamentally limited by the line width of the source, which can be extremely narrow. Using homodyne spectroscopy, spectral resolutions below 1 MHz have been reported.[22] In a time-domain spectroscopy setup, however, the spectral resolution is usually on the order of 50 GHz.[23] Fundamentally, this spectral resolution is limited by the repetition rate of the ultrafast laser, which is typically 80 MHz for an oscillator and 1 kHz for an amplified system. However, a more practical limitation is the maximum travel range of the optical delay stage that controls the relative delay between the terahertz pulse and the ultrafast measurement pulse. If we assume that the practical limit on the travel range of such a delay stage is on the order of two meters, then the maximum spectral resolution in time-domain spectroscopy is on the order of 150 MHz.

The signal-to-noise ratio and the dynamic range are both related to the amplitude of the reference spectrum, which is the spectrum measured without object in the terahertz beam. The signal-to-noise ratio is defined as the spectral amplitude at a certain frequency divided by the standard deviation of that amplitude. The dynamic range is the spectral amplitude at a certain frequency divided by the standard deviation of the noise at the frequency *with the terahertz beam blocked*. The dynamic range is a measure of the sensitivity of the detector and determines the maximum amount of absorption one can tolerate before the measured signal is dominated by the noise. The signal-to-noise ratio, however, is a measure of the sensitivity of the complete system, and also includes noise due to fluctuations of the source. Note that a large difference between the signal-to-noise ratio and the dynamic range means that the noise due to random fluctuations of the source dominates the total noise

of the system.

A comparison of the signal-to-noise ratio and the dynamic range obtained with homodyne spectroscopy and with time-domain spectroscopy is difficult, as the published literature contains insufficient information for such a comparison. Based on the data that is available, we conclude that, at this moment, time-domain spectroscopy has better signal-to-noise ratios for comparable measurement times per spectral amplitude data point. However, the difference may be due to the fact that, so far, more effort has been put in time-domain spectroscopy than in homodyne spectroscopy. Homodyne spectroscopy and time-domain spectroscopy have been used to image objects with signal-to-noise ratios on the order of 100:1. However, achieving such a ratio with time-domain spectroscopy takes about 20 ms per pixel, while homodyne detection, until now, requires 200 ms. Also, the images obtained with homodyne spectroscopy were on a single-frequency basis, while time-domain spectroscopy measures the response at typically 60 frequencies simultaneously.[24]

A disadvantage of homodyne spectroscopy is that standing waves can occur in the optical system due to reflections. These standing waves are difficult to avoid and can induce systematic errors. In time-domain spectroscopy, reflections are much less of a problem. The reflections can be easily separated in the time domain, provided that the relative delay between the reflections is larger than the duration of the pulses. It is then even possible to obtain the spectrum of each reflection independently. If, however, subsequent pulses overlap, then separation in time is no longer possible, and similar problems as in homodyne detection arise. An advantage of homodyne spectroscopy is its potential to be used in cheap, compact systems, which is important for future commercial applications.

Concluding, homodyne spectroscopy and time-domain spectroscopy are both sensitive techniques applicable for imaging and spectroscopy. If the requirements on the spectral resolution are not too tight, then time-domain spectroscopy is an excellent method, since standing waves do not occur. Homodyne spectroscopy has the advantage of a better spectral resolution and has a higher potential to be used in cheap and compact systems. So far, however, the limited tunability of the sources and the longer data acquisition times limit the applicability of this technique.

1.3 Applications for terahertz radiation

This section discusses various potential applications of terahertz radiation. We do not give a complete overview of all applications, as we merely try to give the reader a sense of the potential of terahertz techniques.

In general, the advantages of using terahertz radiation compared to radiation from other regions of the electromagnetic spectrum are related to material properties. For instance, some materials are transparent at terahertz frequencies, while they are opaque at optical wavelengths. This opens the possibility to look through (parts of) objects. Also, some materials, such as gasses, show characteristic absorption features in the terahertz region. As we discuss

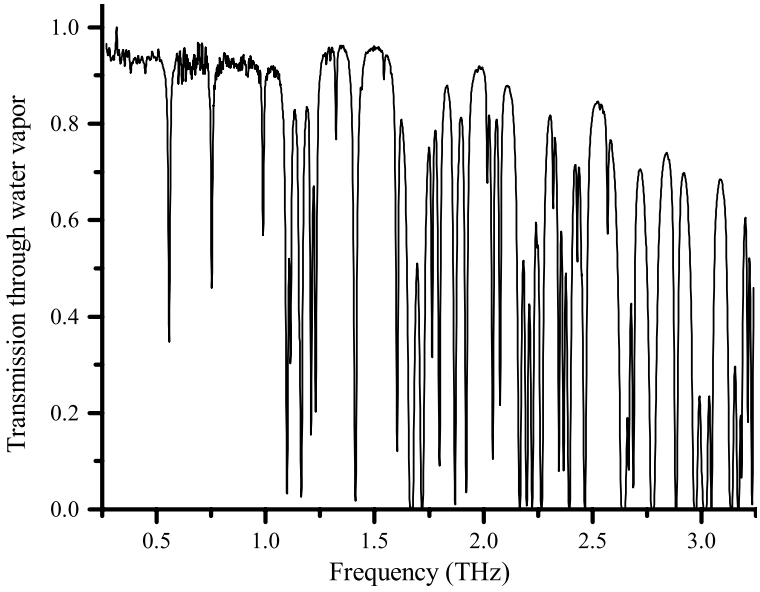

Figure 1.6: Measured transmission spectrum through a 1 m long air column with a 40% relative humidity.

potential applications, we will indicate which material properties makes the application interesting.

1.3.1 Astronomical and atmospherical spectroscopy

We discuss astronomical and atmospherical spectroscopy in the same section, because they rely on the same material property: rotational transitions in molecular gasses. The rotation of a molecule is quantized, and absorption and emission of terahertz radiation is associated with transitions between rotational energy levels. A molecules that is, for instance, thermally excited from the ground state to a higher rotational energy level, can emit a terahertz photon as it makes a transition to a lower energy level. The frequency of this photon is determined by the energy difference between the two levels. This results in a sharply peaked *emission* spectrum. On the other hand, the molecule can also absorb radiation at the transition frequency, which results in peaks in the *absorption* spectrum. The line width of the peaks in the absorption and emission spectra are very narrow, especially at low pressures, where the line width can be smaller than 1 MHz. As an example, figure 1.6 shows a measurement of the transmission spectrum of air. The water vapor in the air causes a large number of discrete absorption lines. The exact frequencies and relative strengths of these lines can serve as an unique "fingerprint" for identifying and quantitatively measuring water vapor.

Due to the narrow line width of rotational transitions of molecular gasses, an enormous number of different molecules can be identified simultaneously.

By measuring the spectrum of a gas mixture, it is possible to determine which molecules are present and how much of each molecule is present. This method is used to determine the content of our atmosphere and of gas clouds in outer space.

In the void between stars there are large clouds of gasses. These clouds are very important in astronomy, because they serve as a birth place of new stars. These clouds can not be detected in the visible part of the electromagnetic spectrum, but they do radiate at terahertz frequencies. By measuring the spectrum of this emission, the chemical composition of the clouds can be determined. This will be the mission of the Herschel telescope, which is a space observatory scheduled to be launched in 2007. It is important to do these observations in space, as the atmosphere absorbs almost all of the terahertz radiation from outer space.

Terahertz absorption in the atmosphere, a disadvantage for astronomical observations, can be used to study the earth's atmosphere. The chemical composition of our atmosphere is highly relevant from an environmental point of view, due to problems with the ozone layer and the greenhouse effect. These problems are associated with the relative and absolute abundance of different molecules, which can be measured very accurately with terahertz radiation. These measurement have been performed by balloon- and aircraft-borne detectors and by space-borne observatories (NASA's AURA mission[25]).

1.3.2 Inspection and security

Most package materials, such as paper and plastics, are transparent at terahertz frequencies. Therefore, terahertz radiation can be used for the inspection of the content of packages without having to open them. For example, Teraview,[26] a company that specializes in technologies related to terahertz radiation, currently investigates the detection of dangerous substances in envelopes. There is also an interest in imaging through clothing, as this can be used for the detection of concealed weapons. One could also think of applications related to quality control: checking whether the milk has gone sour without opening the milk carton.

Of course, it is even more useful to see though a container, if its contents can be identified with its spectral signature. Fortunately, a lot of substances have distinct features in their terahertz absorption spectra. Current research studies the features of, for instance, explosives. For this type of applications, detection methods that also measure the phase of terahertz radiation have an advantage over intensity-only methods. With phase information, it is possible to calculate the time needed by a terahertz wave to penetrate a (part of) an object, which provides information on the 3D structure of the object.

1.3.3 Biological and medical applications

There is an interest in biological and medical applications of terahertz radiation. Many complex biological molecules show characteristic absorption features in the terahertz region.[27] Other studies have shown that it is possible

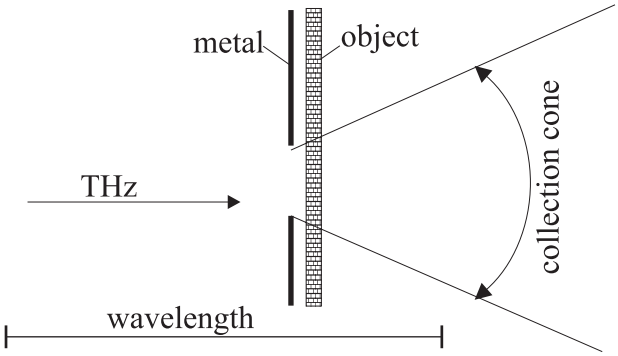

Figure 1.7: Schematic picture of the use of apertures in near-field imaging. A terahertz wave is incident on a metal sheet with an aperture which is smaller than the wavelength. The light transmitted within the collection cone is detected, which leads to a signal that is only affected by the part of the object close to the aperture.

to distinguish between healthy skin tissue and skin tissue with basal skin cell carcinoma, a form of cancer. Also, the label free probing of DNA in the terahertz region was demonstrated.[28]

One of the problems which hamper the development of medical and biological terahertz applications is the limited spatial resolution in terahertz imaging. In conventional imaging the spatial resolution is limited to about half a wavelength, which is typically 0.15 mm for terahertz radiation. However, many interesting biological and medical processes occur at a cellular level. Biological cells have dimensions on the order of 1 μm, which is much smaller than the spatial resolution of conventional terahertz imaging. Terahertz near-field imaging, however, can overcome this limitation.

1.3.4 Terahertz microscopy

Individual microscopic objects can only be investigated with terahertz radiation, if near-field techniques are used. With near-field techniques, the spatial resolution limit in conventional (meaning *not* near-field) imaging, which originates from diffraction effects, is avoided. This is achieved by locally enhancing or confining the terahertz electric field to areas much smaller than the wavelength of the light.

The most straightforward way to confine the electric field to sub-wavelength dimensions is with an aperture.[14] The object is scanned behind a metal sheet containing an aperture of sub-wavelength dimensions (figure 1.7). Some of the terahertz radiation is transmitted through the aperture and will then diffract to all directions in the forward half-space. Because the object is very close to the plate with the aperture, the transmitted wave is affected primarily by the part of the object close to the aperture, which results in a sub-wavelength resolution. This approach, however, does require that the object is very thin.

One of the disadvantages of the aperture technique, is the low transmission of the aperture. Bethe[29] already discussed that the energy transmitted by a sub-wavelength-sized aperture in a thin metal sheet goes down with the aperture radius to the sixth power. This transmission loss significantly deteriorates the signal-to-noise ratio and thus limits the size of the smallest usable aperture.

The problem of low signal-to-noise ratios is common to most near-field techniques. It is in the nature of electromagnetic waves that they resist being confined to dimensions smaller than the wavelength. Improvements, however, can be made with resonant structures such as antenna's, which can enhance a local electric field. Plasmon-assisted enhanced transmission through apertures[30] can also be seen as originating from resonant enhancement of surface waves.

1.4 This thesis

The goal of this thesis is to investigate various aspects of terahertz time-domain spectroscopy with the aim to develop a new terahertz microscopy technique. The near-field techniques needed to do microscopy at terahertz frequencies generally give small signals. It is therefore essential that the detection process is as sensitive as possible. Chapter 2 gives an elaborate discussion on electro-optic detection, which is the time-domain spectroscopy detection method used throughout this thesis. In this chapter a theory for electro-optic detection is described, which includes its dependence on the orientation of the different components of the setup. This chapter also shows how electro-optic detection can be used to measure the polarization of the terahertz pulse.

The signal-to-noise ratio can be improved, not only by optimizing the detection sensitivity, but also by minimizing the noise level. Chapter 3 investigates the influence of noise in terahertz time-domain spectroscopy experiments. For shot-noise limited detection, the signal-to-noise ratio can be improved by increasing the power in the optical probe beam. We investigate to which extent high probe powers result in adverse effects due to saturation of the photodiodes in the detector.

Chapter 4 presents calculations and measurements on various ways of generating synchronized terahertz pulses. We theoretically and experimentally investigate optical rectification, which is nonlinear optical process using the second-order nonlinear susceptibility ($\chi^{(2)}$). Terahertz generation by nonlinear processes is relevant for terahertz microscopy, since it can be used to make sources with sub-wavelength dimensions by tight focussing of the generating optical beams. Chapter 4 also discusses a different terahertz generation method, which uses photoconductive emitters. The dimensions of a conductive emitter are usually not sub-wavelength, but they are still important for near-field applications, because of their high output power.

For the terahertz near field close to conducting surfaces, surface waves in the form of surface plasmon polaritons can be very important. They are, for instance, relevant for terahertz near-field microscopy, which uses a metal tip.

It is even conceivable that metal wires could be used to effectively guide the terahertz wave to the sample in microscopy setups. Chapter 5 discusses the features of surface plasmon polaritons at terahertz frequencies. In particular, we investigate theoretically and experimentally, how terahertz surface plasmon polaritons propagate over metal wires.

Finally, we discuss a technique for near-field terahertz imaging that uses the local electric-field distortions around metal needles in chapter 6. The detection setup is discussed and measurements are presented. The frequency dependence of the terahertz spectrum measured in the near field is explained by a simple antenna model. The chapter is concluded with a speculation upon the resolution that is obtainable with the proposed terahertz microscopy setup.

Chapter 2

Electro-optic detection

Since the development of terahertz time-domain spectroscopy, electro-optic detection has become an increasingly popular way of measuring both the amplitude and phase of terahertz radiation.[31,32] Electro-optic detection is used in various applications, such as spectroscopy,[33,34] imaging,[35] tomography,[36] and microscopy.[37,38] Electro-optic detection is based on the nonlinear response of the polarization in a medium to an electric field. As an introduction, we first give a simplified scalar description of the nonlinear polarization response. Later, we will give a complete tensor description of the phenomenon. The polarization in a non-dispersive* medium can be written as[40]

$$P(t) = \varepsilon_0 \left(\chi^{(1)} E(t) + \chi^{(2)} E^2(t) + \chi^{(3)} E^3(t) + \dots \right), \tag{2.1}$$

where P is the polarization, E is the electric field, and ε_0 is the permittivity of vacuum. $\chi^{(1)}$, $\chi^{(2)}$ and $\chi^{(3)}$ are the electric susceptibilities of the first, second and third order respectively. Note that each term in the expansion is, in general, much smaller than the preceding term. In most cases, only the first-order susceptibility is important and all other terms can be neglected. However, there are cases where the higher-order terms are important. Suppose that a constant electric field E_1 and an electric field oscillating at an optical frequency E_2(t) are simultaneously present in a non-dispersive medium. Up to the second order in the electric field, the polarization is then given by

$$\begin{aligned} P(t) =& \varepsilon_0 \left(\chi^{(1)} E_1 + \chi^{(1)} E_2(t) + \chi^{(2)} E_1^2 + \chi^{(2)} E_2^2(t) + 2\chi^{(2)} E_1 E_2(t) \right) \\ =& \varepsilon_0 \left(\chi' E_2(t) + \chi^{(1)} E_1 + \chi^{(2)} E_1^2 + \chi^{(2)} E_2^2(t) \right), \end{aligned} \tag{2.2}$$

where $\chi' \equiv \chi^{(1)} + 2\chi^{(2)} E_1$ can be viewed as an effective susceptibility for the optical electric field, which is a function of E_1. This field-dependent susceptibility leads to a field-dependent refractive index as follows. The dielectric

*Gallot and Grischkowsky gave an excellent description of the effect of dispersion on electro-optic detection.[39]

constant ε_r, which equals the square of the refractive index n, is related to the polarization through

$$\varepsilon_r \varepsilon_0 E = P + \varepsilon_0 E. \tag{2.3}$$

With equation 2.2 and 2.3, we find that

$$n = \sqrt{\varepsilon_0(1+\chi')} = \sqrt{\varepsilon_0\left(1+\chi^{(1)}+2\chi^{(2)}E_1\right)}, \tag{2.4}$$

where all terms of equation 2.3 that do not oscillate with the same frequency as E_2(t) are disregarded. The effect that the refractive index depends on a DC electric field is called the electro-optic effect or the Pockels effect.

For simplicity, all quantities in equation 2.2 and 2.3 are written as scalars. In reality, the polarization and the electric field are vectors, while the susceptibilities are tensors. Due to the tensor character of the susceptibility, the refractive index of equation 2.4 can depend on the direction of the electric field. The medium can thus become birefringent and this birefringence can be controlled with the DC electric field E_1. Due to the birefringence, an optical beam that travels through the medium can experience a polarization change, which is proportional to the electric field.

The discussion above is also valid if the field E_1 varies slowly compared to the frequency of the optical wave. E_1 is then considered to be quasi-constant. In terahertz electro-optic detection, we measure the change in the birefringence caused by electric fields with terahertz frequencies. Terahertz electric fields have a much lower frequency than optical fields and can thus be considered quasi-constant. Figure 2.1 schematically show an electro-optic detection setup. The polarization of an optical probe pulse that travels through an electro-optic detection crystal changes due to the change in birefringence.[†] After the probe beam has travelled through the detection crystal, it is split into two beams with a polarizing beamsplitter. A signal proportional to the terahertz electric field is then obtained by measuring the difference in the powers of both beams with two photodiodes.

It is obviously important to have detailed knowledge of a technique that is so widely used as electro-optic detection. A detailed and complete description of this process can help experimenters optimize the detection sensitivity, can increase physical insight, and can make it possible to model complex processes, as in electro-optic near-field measurements.[38] The most-widely used detection crystals are optically isotropic. In previous papers the electro-optic signal in such crystals is calculated for a few distinct propagation directions of the probe beam, but no expressions are given for a general propagation direction.[37,42] The paper by Duvillaret et al. can be used for arbitrary probe propagation direction, but presents a figure of merit instead of the electro-optic signal.[43] Therefore the description of electro-optic detection in this paper is not complete and provides little quantitative information.

[†]It is also possible to perform electro-optic detection by measuring the change in the phase of the probe beam instead of the change in the polarization.[41] However, polarization modulation is by far the most widely-used technique, since phase-modulation techniques greatly suffer from noise induces by vibrations.

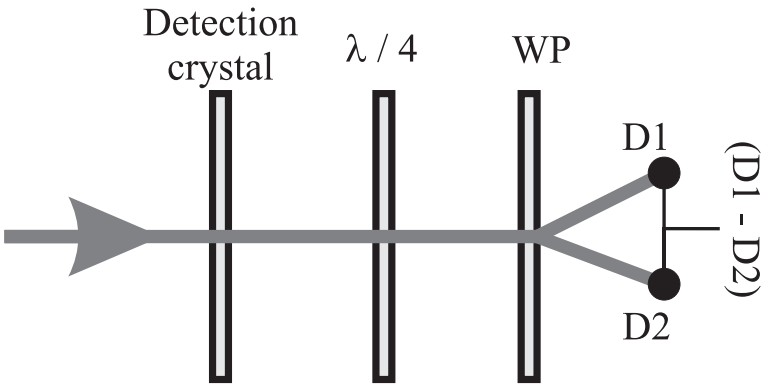

Figure 2.1: The general setup used in electro-optic detection. A probe pulse, which is originally polarized linearly, travels through a detection crystal and a $\lambda/4$ plate, and is then split by a Wollaston prism (WP). The difference in the intensity of the two beams is measured with a differential detector, which, apart from the electronics, consists of two photodiodes (D1 and D2).

The goal of section 2.1 is to derive an analytic expression of electro-optic detection in optically isotropic crystals, which shows the dependence of the detection process on the direction of the probe propagation, the probe polarization, and the terahertz electric field vector.

The electro-optic detection method described in section 2.1 measures one component of the terahertz electric field vector. Additional information is obtained in a measurement of the terahertz polarization. In the past, electro-optic polarization measurements were performed by sequential measurements between which either the input polarization[44,45] or the detection crystal orientation[46] had to be adjusted. An alternative approach uses multiple probe beams that follow different paths through the detection crystal,[47] which means that the different electric field components are not measured at exactly the same location.

The goal of section 2.2 is to present an electro-optic detection method that can measure the terahertz polarization using a single probe beam. The method has the potential to measure two components of the terahertz polarization simultaneously, and does not require changes to the initial probe beam polarization or to the crystal orientation. We demonstrate the potential of this technique in terahertz imaging and spectroscopy with two examples.

2.1 General theory for electro-optic detection

In this section, we give a full description of electro-optic detection in optically isotropic crystals, and show the dependence of the detection process on the direction of the probe propagation, of the probe polarization, and of the terahertz electric field.[48] Our approach is independent of the terahertz propagation direction, which makes the theory applicable to both collinear and

non-collinear situations. We assume that the optical probe pulse experiences a constant terahertz electric field, but the scope of the equations can be extended to varying electric fields by simple integration. The end result of the calculation is a small set of simple formulas, which are easy to use, which can help an experimenter find the optimum configuration for his particular application, and which provide valuable physical insight. All the relevant vectors in our final formulas will be expressed in the coordinate system formed by the crystallographic axes of the electro-optic detection crystal. All values can, therefore, directly be substituted into the equations without the need for time-consuming coordinate transformations. Our calculation is valid for all optically isotropic materials, so it is applicable to a large number of electro-optic detection crystals, such as ZnTe and GaP.

2.1.1 Calculation of the detector signal

In this section we will derive a simple formula describing electro-optic detection for arbitrary propagation and polarization directions of the probe, and for arbitrary size and polarization direction of the terahertz electric-field. The calculation is split into three parts. First, we will calculate the effect of an arbitrary terahertz electric field on the optical properties of the detection crystal. The calculation of the corresponding refractive indices and orientation of the refractive-index axes, both induced by an arbitrary terahertz electric field, is given. Second, we determine the electro-optic signal, where the refractive indices and the direction of the principal refractive-index axes are assumed known. Third, the results of the first and second part are combined into a general solution for the electro-optic signal.

Calculation of the terahertz-induced birefringence

In a birefringent crystal, there are generally two polarization directions for which a linearly polarized, plane wave is a solution to Maxwell's equations. Following Yariv, we call these two linearly polarized plane waves the propagation modes of the crystal.[49] A beam that is polarized in any other direction will experience a polarization change while travelling through the crystal. Each mode is characterized by a refractive index and a polarization direction. The polarization change occurring in a crystal of a certain thickness can be calculated by decomposing the incident wave along the polarization directions of the modes, propagating both modes through the crystal using the appropriate refractive index, and then adding the two modes up to get the polarization at the end of the crystal. Such a description is also valid in electro-optic detection, where the birefringence of the crystal is caused by the terahertz electric field. We will calculate the modes for the electro-optic detection crystal for arbitrary terahertz electric field and for arbitrary propagation direction of the probe beam.

Yariv provides an equation for the refractive indices and polarization directions of the two propagation modes.[49] This equation is derived directly from Maxwell's equations, and it is valid for all media in which there are no

free charges and currents, and which are nonmagnetic ($\mu = \mu_0$). The equation that defines the polarization modes is given by

$$\mathbf{D}_{0i} = n_i^2 \varepsilon_0 \left[\mathbf{E}_{0i} - (\hat{\mathbf{s}} \cdot \mathbf{E}_{0i})\, \hat{\mathbf{s}}\right], \tag{2.5}$$

where $\mathbf{D}_{0i}$ is the electric displacement vector, $\mathbf{E}_{0i}$ is the electric field vector, n_i is the refractive index, all corresponding to the i'th polarization mode of the probe, where $i \in \{1, 2\}$. The propagation direction of the probe is given by the unit vector $\hat{\mathbf{s}} = (s_x, s_y, s_z)$. In this thesis, we will use a hat (ˆ) to indicate a unit vector.

Equation (2.5) gives us the propagation modes of a crystal. However, the birefringence that is produced by the terahertz electric field still has to be quantified. For this purpose, we need to relate the electric displacement vector $\mathbf{D}_{0i}$ to the electric field vector $\mathbf{E}_{0i}$ with the permittivity tensor. The values of the permittivity tensor of a nonlinear crystal in the presence of a terahertz electric field are given by:

$$\varepsilon_{ij} = \varepsilon_0 \left(\delta_{ij} + \chi_{ij}^{(1)} + \sum_k \chi_{ijk}^{(2)} E_{Tk} \right), \tag{2.6}$$

where ε_{ij} is the element of the permittivity tensor on column i and row j, and δ_{ij} is a Kronecker delta. The permittivity of free space is ε_0. $\chi^{(n)}$ is the susceptibility of order n and $\mathbf{E}_T = \left(E_{Tx}, E_{Ty}, E_{Tz}\right)$ is the terahertz electric field in the detection crystal. Note that the electric field in the crystal differs from that in air or vacuum.

We will now use the fact that we are investigating optically isotropic materials. The only optically isotropic materials that exhibit an electro-optic effect and thus can be used as electro-optic detector are crystals with a cubic symmetry of the classes 23 or $\bar{4}3m$. The first-order susceptibility of these crystals is not directionally dependent, so it can be written as

$$\chi_{ij}^{(1)} = (\varepsilon_r - 1)\, \delta_{ij}, \tag{2.7}$$

where ε_r is the relative permittivity of the crystal. Using the symmetry of our crystal, we can also simplify the second-order susceptibility tensor. For this purpose, we use a coordinate system which corresponds to the crystal's main crystallographic axes. The x-axis of the coordinate system is the (100) axis of the crystal, the y-axis is the (010) axis, etc. In this coordinate system the second-order susceptibility of a cubic crystal is given by:

$$i \neq j \neq k \quad \Rightarrow \quad \chi_{ijk}^{(2)} = \chi^{(2)} \tag{2.8}$$

$$\text{otherwise} \quad \Rightarrow \quad \chi_{ijk}^{(2)} = 0. \tag{2.9}$$

When we use these symmetry arguments on equation 2.6, and write the result in matrix format, we get:

$$\bar{\bar{\varepsilon}} = \varepsilon_0 \begin{pmatrix} \varepsilon_r & \chi^{(2)} E_{Tz} & \chi^{(2)} E_{Ty} \\ \chi^{(2)} E_{Tz} & \varepsilon_r & \chi^{(2)} E_{Tx} \\ \chi^{(2)} E_{Ty} & \chi^{(2)} E_{Tx} & \varepsilon_r \end{pmatrix}, \tag{2.10}$$

where (E_{Tx}, E_{Ty}, E_{Tz}) are the components of the terahertz electric field with respect to the crystal axes.

Using equation (2.5), together with equation (2.10) and $\mathbf{D}_{0i} = \bar{\bar{\varepsilon}}\mathbf{E}_{0i}$, we get a matrix equation that determines the refractive indices and the electric-field vectors of the polarization modes

$$\begin{pmatrix} \varepsilon_r & \chi^{(2)}E_{Tz} & \chi^{(2)}E_{Ty} \\ \chi^{(2)}E_{Tz} & \varepsilon_r & \chi^{(2)}E_{Tx} \\ \chi^{(2)}E_{Ty} & \chi^{(2)}E_{Tx} & \varepsilon_r \end{pmatrix} \mathbf{E}_{0i} = n_i^2 \begin{pmatrix} 1-s_x^2 & -s_x s_y & -s_x s_z \\ -s_x s_y & 1-s_y^2 & -s_y s_z \\ -s_x s_z & -s_y s_z & 1-s_z^2 \end{pmatrix} \mathbf{E}_{0i}, \tag{2.11}$$

where i is 1 or 2, and n_1 and n_2 are the refractive indices when the polarization of the probe is along respectively the $\mathbf{E}_{01}$ and $\mathbf{E}_{02}$ vector. The components of the unit vector in the probe's propagation direction $\hat{\mathbf{s}}$ are indicated by s_x, s_y, and s_z in the coordinate system formed by the crystal axes. The unit vectors along polarization directions of the two propagation modes are given by

$$\hat{\mathbf{r}}_{ci} \equiv \frac{\mathbf{E}_{0i}}{\|\mathbf{E}_{0i}\|} \quad \text{with } i \in \{1,2\}. \tag{2.12}$$

We now define the difference between the refractive index with and the refractive index without terahertz field as $\Delta n_i \equiv n_i - \sqrt{\varepsilon_r}$. For sufficiently small Δn_i, we can make the approximation

$$n_i^2 = \left(\sqrt{\varepsilon_r} + \Delta n_i\right)^2 \simeq \varepsilon_r + 2\Delta n_i \sqrt{\varepsilon_r}. \tag{2.13}$$

We can use this to rewrite equation 2.11 as

$$\begin{pmatrix} A & E_{Tz} & E_{Ty} \\ E_{Tz} & A & E_{Tx} \\ E_{Ty} & E_{Tx} & A \end{pmatrix} \mathbf{E}_{0i} \simeq \left(A + 2\frac{\Delta n_i \sqrt{\varepsilon_r}}{\chi^{(2)}}\right) \begin{pmatrix} 1-s_x^2 & -s_x s_y & -s_x s_z \\ -s_x s_y & 1-s_y^2 & -s_y s_z \\ -s_x s_z & -s_y s_z & 1-s_z^2 \end{pmatrix} \mathbf{E}_{0i}, \tag{2.14}$$

where $A \equiv \varepsilon_r / \chi^{(2)}$.

The electric field vector of the probe beam has to be almost perpendicular to its propagation direction, if the birefringence of the crystal is very small.‡ In electro-optic detection the induced birefringence is usually very small, so it is reasonable to expect that the probe electric field is indeed approximately perpendicular to the probe's propagation direction. We therefore expect that the previous equation will look simpler in a coordinate system that has one of its axes along the propagation direction of the probe. We chose the following coordinate system

$$\hat{\mathbf{x}}' = s_x\hat{\mathbf{x}} + s_y\hat{\mathbf{y}} + s_z\hat{\mathbf{z}} \tag{2.15}$$

$$\hat{\mathbf{y}}' = \left(-s_z\hat{\mathbf{y}} + s_y\hat{\mathbf{z}}\right) / \sqrt{s_y^2 + s_z^2} \tag{2.16}$$

$$\hat{\mathbf{z}}' = \left[\left(s_y^2 + s_z^2\right)\hat{\mathbf{x}} - s_x s_y \hat{\mathbf{y}} - s_x s_z \hat{\mathbf{z}}\right] / \sqrt{s_y^2 + s_z^2}, \tag{2.17}$$

‡This can be verified by substitution of $\mathbf{D}_{0i} \simeq \varepsilon_r \mathbf{E}_{0i}$ in equation 2.5

where $\hat{\mathbf{x}}, \hat{\mathbf{y}}, \hat{\mathbf{z}}$ are the unit vectors of the *old* coordinate system, which were along the crystal axes. $\hat{\mathbf{x}}', \hat{\mathbf{y}}', \hat{\mathbf{z}}'$ are the unit vectors of the *new* coordinate system, and s_x, s_y, s_z are, as before, the components of the unit vector in the propagation direction of the probe with respect to the *old* coordinate system. The new coordinate system is defined such that $\hat{\mathbf{x}}'$ points in the propagation direction of the probe ($\hat{\mathbf{s}}$), and that $\hat{\mathbf{y}}'$ points in the direction of the cross product of $\hat{\mathbf{s}}$ and $\hat{\mathbf{x}}$. From here on, we will distinguish between the two coordinate systems by labelling all matrices and vectors in the new coordinate system with a prime. An arbitrary vector or matrix expressed in the old coordinate system can be transformed into the new system (and back) with the following transformation matrix P

$$\bar{\bar{P}} = \begin{pmatrix} s_x & 0 & \sqrt{s_y^2 + s_z^2} \\ s_y & -s_z / \sqrt{s_y^2 + s_z^2} & -s_x s_y / \sqrt{s_y^2 + s_z^2} \\ s_z & s_y / \sqrt{s_y^2 + s_z^2} & -s_x s_z / \sqrt{s_y^2 + s_z^2} \end{pmatrix}. \tag{2.18}$$

Vectors can be transformed with the equation $\mathbf{V}' = \bar{\bar{P}}^{-1}\,\mathbf{V}$, and matrices with $\bar{\bar{M}}' = \bar{\bar{P}}^{-1}\,\bar{\bar{M}}\,\bar{\bar{P}}$.

The above coordinate transformation is a valid rotation of the coordinate axes except for the special case of $\hat{\mathbf{s}} = \{1,0,0\}$. For this case, the transformation is not defined. However, the case that $\hat{\mathbf{s}} = \{1,0,0\}$ is, because of the symmetry of the crystal, completely equivalent to the cases that $\hat{\mathbf{s}} = \{0,1,0\}$ or $\hat{\mathbf{s}} = \{0,0,1\}$. For these directions the transformation *is* valid, so the coordinate transformation does not limit the generality of the theory. In the new coordinate system, equation 2.14 transforms into

$$\begin{pmatrix} A + 2E_{Tx}s_y s_z + 2E_{Ty}s_x s_z + 2E_{Tz}s_y s_x & \frac{E_{Tx}\left(s_y^2 - s_z^2\right) + E_{Ty}s_y s_x - E_{Tz}s_z s_x}{\sqrt{s_y^2 + s_z^2}} & \frac{-2E_{Tx}s_x s_y s_z + E_{Ty}s_z\left(-1 + 2s_y^2 + 2s_z^2\right) + 2E_{Tz}s_y\left(s_z^2 + s_y^2\right)}{\sqrt{s_y^2 + s_z^2}} \\ \frac{E_{Tx}\left(s_y^2 - s_z^2\right) + E_{Ty}s_y s_x - E_{Tz}s_z s_x}{\sqrt{s_y^2 + s_z^2}} & -2E_{Tx}\frac{s_y s_z}{s_y^2 + s_z^2} - 2\frac{\Delta n_i \sqrt{\varepsilon_r}}{\chi^{(2)}} & E_{Tx}s_x\frac{-s_y^2 + s_z^2}{s_y^2 + s_z^2} + E_{Ty}s_y - E_{Tz}s_z \\ \frac{-2E_{Tx}s_x s_y s_z + E_{Ty}s_z\left(-1 + 2s_y^2 + 2s_z^2\right) + 2E_{Tz}s_y\left(s_z^2 + s_y^2\right)}{\sqrt{s_y^2 + s_z^2}} & E_{Tx}s_x\frac{-s_y^2 + s_z^2}{s_y^2 + s_z^2} + E_{Ty}s_y - E_{Tz}s_z & -2E_{Tx}\frac{s_x^2 s_y s_z}{s_y^2 + s_z^2} - 2E_{Ty}s_x s_z - 2E_{Tz}s_x s_y - 2\frac{\Delta n_i \sqrt{\varepsilon_r}}{\chi^{(2)}} \end{pmatrix} \mathbf{E}'_{0i} = \mathbf{0}. \tag{2.19}$$

Where $\mathbf{E}'_{0i}$ is a vector in the new coordinate system that points along the polarization direction of the i'th propagation mode with a refractive index n_i. Note, that the above vector equation comprises a system of 3 equations.

Equation 2.19 seems very complicated, but it can be simplified. We can make the following approximation

$$A \equiv \varepsilon_r / \chi^{(2)} \gg \|\mathbf{E}_T\|, \tag{2.20}$$

which is generally valid for sufficiently small terahertz electric fields. This restriction is not stringent, since $\chi^{(2)}$ is usually very small. For instance, A equals 0.3 GV/cm for ZnTe, a much-used electro-optic detection crystal. For Ti:Sapphire oscillator systems, a peak terahertz electric field of 100 V/cm is considered high.[23] E_T/A is thus on the order of 10^{-6} or smaller.

We will now consider only the equation formed by the top row of the matrix of equation (2.19). Note, that only this row contains A. If we neglect all terms in the top row that do not contain A, we get the following equation for this row

$$\begin{pmatrix} A & 0 & 0 \end{pmatrix} \begin{pmatrix} E'_{ix} \\ E'_{iy} \\ E'_{iz} \end{pmatrix} = 0, \tag{2.21}$$

where E'_{ix}, E'_{iy}, and E'_{iz} are the components of the electric field of the probe. From this equation we get that

$$E'_{ix} = 0. \tag{2.22}$$

So the component of the probe's electric field in its propagation direction, is zero. This corresponds to a probe electric field which is perpendicular to the propagation direction, as was expected.

The top row of equation (2.19) has been used, but the information of the bottom two rows is still available. This information can be written as

$$\begin{pmatrix} -2E_{Tx}\frac{s_y s_z}{s_y^2+s_z^2} - 2\frac{\Delta n_i\sqrt{\varepsilon_r}}{\chi^{(2)}} & E_{Tx}\frac{s_y^2+s_z^2}{s_y^2+s_z^2} \\ E_{Tx}s_x\frac{-s_y^2+s_z^2}{s_y^2+s_z^2} + E_{Ty}s_y - E_{Tz}s_z & E_{Tx}s_x\frac{-s_y^2+s_z^2}{s_y^2+s_z^2} + E_{Ty}s_y - E_{Tz}s_z \\ -2E_{Tx}\frac{s_x^2 s_y s_z}{s_y^2+s_z^2} - 2E_{Ty}s_x s_z - 2E_{Tz}s_x s_y - 2\frac{\Delta n_i\sqrt{\varepsilon_r}}{\chi^{(2)}} & E_{Tx}\frac{s_y^2+s_z^2}{s_y^2+s_z^2} \end{pmatrix} \begin{pmatrix} E'_{iy} \\ E'_{iz} \end{pmatrix} = \begin{pmatrix} 0 \\ 0 \end{pmatrix}. \tag{2.23}$$

Note, that the left elements of Equation (2.19) have been left out. The value of these elements are irrelevant, since they are multiplied with E'_{ix}, which is zero. In this way, the problem is reduced from a three-dimensional matrix equation to a two-dimensional equation. The solution of this equation can be calculated straightforwardly. For the changes in the refractive index we get

$$\Delta n_1 = -\frac{\chi^{(2)}}{2\sqrt{\varepsilon_r}}\left(b - \sqrt{b^2+c}\right) \tag{2.24}$$

$$\Delta n_2 = -\frac{\chi^{(2)}}{2\sqrt{\varepsilon_r}}\left(b + \sqrt{b^2+c}\right), \tag{2.25}$$

with

$$b = E_{Tx}s_y s_z + E_{Ty}s_x s_z + E_{Tz}s_y s_x \tag{2.26}$$

$$c = E_{Tx}^2 s_x^2 + E_{Ty}^2 s_y^2 + E_{Tz}^2 s_z^2 - 2\left(E_{Tx}E_{Ty}s_x s_y + E_{Tz}E_{Ty}s_z s_y + E_{Tx}E_{Tz}s_x s_z\right). \tag{2.27}$$

We also find the following eigenvectors, which corresponds to the polarization directions of the propagation modes

$$\mathbf{E}'_{01} = \begin{pmatrix} 0 \\ -E_{Tx}s_x\frac{s_z^2-s_y^2}{s_z^2+s_y^2} - E_{Ty}s_y + E_{Tz}s_z \\ -\sqrt{b^2+c}+b-2E_{Tx}\frac{s_ys_z}{s_y^2+s_z^2} \end{pmatrix} \tag{2.28}$$

$$\mathbf{E}'_{02} = \begin{pmatrix} 0 \\ \sqrt{b^2+c}-b+2E_{Tx}\frac{s_ys_z}{s_y^2+s_z^2} \\ -E_{Tx}s_x\frac{s_z^2-s_y^2}{s_z^2+s_y^2} - E_{Ty}s_y + E_{Tz}s_z \end{pmatrix}. \tag{2.29}$$

It is interesting to note the square roots in equation (2.24) to (2.29). Due to these square roots, the refractive index change induced by the sum of two electric-field vectors does not equal the sum of the refractive index changes induced by each of the electric fields separately ($\Delta n(\mathbf{E}_{T1}+\mathbf{E}_{T2}) \neq \Delta n(\mathbf{E}_{T1}) + \Delta n(\mathbf{E}_{T2})$). The equations are thus not linear with vector summation of two terahertz electric fields. However, as will be shown, these nonlinearities cancel each other in the final equation for the signal obtained in electro-optic detection.

Relationship between the electro-optic signal and the terahertz-induced birefringence

In this section, we will calculate the signal obtained in electro-optic detection as a function of the difference between the refractive indices of the two propagation modes and as a function of the polarization direction of the probe beam. For now, the refractive indices and the polarization directions of the propagation modes, which are induced by a terahertz electric field, are assumed to be known. We consider an electro-optic detection setup, as displayed in figure 2.1, consisting of a quarter-wave ($\lambda/4$) plate, a Wollaston prism, a differential detector, and an electro-optic detection crystal. A linearly polarized, optical probe pulse experiences a polarization change in the electro-optic detection crystal due to the refractive-index difference, and becomes slightly elliptical. After the detection crystal, the probe beam travels through a $\lambda/4$ plate. The $\lambda/4$ plate is followed by a Wollaston prism, which splits the probe beam into two beams, which are polarized linearly and orthogonally to each other. An electronic signal is then obtained by measuring the difference in the intensity of the two beams with two photodiodes.

We use a geometry as defined in figure 2.2. In this picture $\hat{\mathbf{E}}_p$ is the initial polarization direction of the probe, and $\hat{\mathbf{r}}_{w1}$ and $\hat{\mathbf{r}}_{w2}$ are the polarization directions of the two beams after the Wollaston prism. The polarization directions of the two propagation modes of the detection crystal are labelled $\hat{\mathbf{r}}_{c1}$ and $\hat{\mathbf{r}}_{c2}$, and the polarization direction of the modes of the $\lambda/4$ plate are labelled $\hat{\mathbf{r}}_{l1}$ and $\hat{\mathbf{r}}_{l2}$. In this section, we do not define in which coordinate system the vectors are expressed. There is no need to do so, because, as we will see, the results of this section depend only on the relative angles between the different

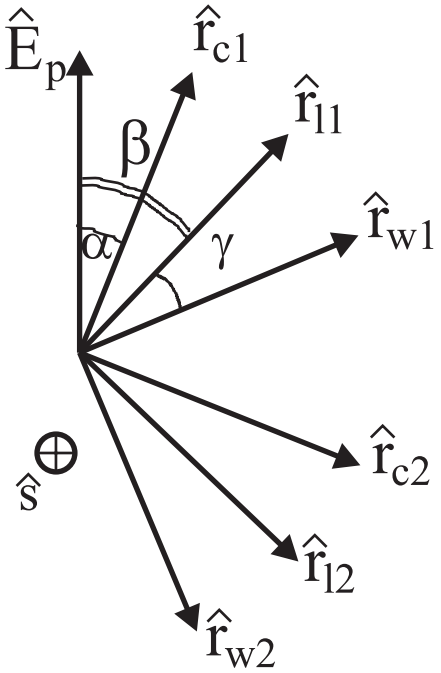

Figure 2.2: The relative orientation of the initial probe polarization $\hat{\mathbf{E}}_p$, the polarization direction of the two propagation modes of the detection crystal $\hat{\mathbf{r}}_{c1}$ and $\hat{\mathbf{r}}_{c2}$, the polarization direction of the two propagation modes of the $\lambda/4$ plate $\hat{\mathbf{r}}_{l1}$ and $\hat{\mathbf{r}}_{l2}$, and the polarization directions of the two beams after the Wollaston prism $\hat{\mathbf{r}}_{w1}$ and $\hat{\mathbf{r}}_{w2}$. The angle between $\hat{\mathbf{E}}_p$ and $\hat{\mathbf{r}}_{c1}$ is defined as α, the angle between $\hat{\mathbf{E}}_p$ and $\hat{\mathbf{r}}_{l1}$ as β, and the angle between $\hat{\mathbf{r}}_{l1}$ and $\hat{\mathbf{r}}_{w1}$ as γ. All vectors, except $\hat{\mathbf{s}}$, are in plane of the paper. The propagation direction of the probe $\hat{\mathbf{s}}$ is perpendicular to the plane of the paper, and points into the paper.

vectors, and these angles do not change by rotations of the coordinate system. The variables α, β, and γ are defined as respectively the angles between $\hat{\mathbf{E}}_p$ and $\hat{\mathbf{r}}_{c1}$, between $\hat{\mathbf{E}}_p$ and $\hat{\mathbf{r}}_{l1}$, and between $\hat{\mathbf{r}}_{l1}$ and $\hat{\mathbf{r}}_{w1}$.

The unit vector that corresponds to the initial polarization of the probe can be decomposed into the two propagation modes of the electro-optic crystal as

$$\hat{\mathbf{E}}_p = (\hat{\mathbf{r}}_{c1} \cdot \hat{\mathbf{E}}_p)\hat{\mathbf{r}}_{c1} + (\hat{\mathbf{r}}_{c2} \cdot \hat{\mathbf{E}}_p)\hat{\mathbf{r}}_{c2}. \tag{2.30}$$

In the crystal, each propagation mode experiences a phase change proportional to the refractive index of the mode. After propagation through the electro-optic crystal, the unit vector that points in the polarization direction of the probe is, in complex notation, given by

$$\begin{aligned} \hat{\mathbf{E}}_{pc} &= \exp(j\omega n_1 l/c)\hat{\mathbf{r}}_{c1}(\hat{\mathbf{r}}_{c1} \cdot \hat{\mathbf{E}}_p) + \exp(j\omega n_2 l/c)\hat{\mathbf{r}}_{c2}(\hat{\mathbf{r}}_{c2} \cdot \hat{\mathbf{E}}_p) \\ &= \exp(j\omega n_1 l/c)\cos(\alpha)\hat{\mathbf{r}}_{c1} - \exp(j\omega n_2 l/c)\sin(\alpha)\hat{\mathbf{r}}_{c2} \\ &= \exp(j\omega n_1 l/c)[\cos(\alpha)\hat{\mathbf{r}}_{c1} - \exp(j\omega \Delta n l/c)\sin(\alpha)\hat{\mathbf{r}}_{c2}]. \end{aligned} \tag{2.31}$$

Where ω is the radial frequency of the probe beam, l is the length of the crystal, n_1 and n_2 are the refractive indices of the two propagation modes of the electro-optic crystal, and c is the velocity of light in vacuum. The refractive index difference Δn is defined as $n_2 - n_1$. In the above equation, the complex exponential factors correspond to the phase changes of the electric fields of the modes accumulated at the end of the crystal.

We now use the approximation $\zeta \equiv |\omega \Delta n l/c| \ll 1$

$$\hat{\mathbf{E}}_{pc} \simeq \exp(j\omega n_1 l/c)[\cos(\alpha)\hat{\mathbf{r}}_{c1} - (1+j\zeta)\sin(\alpha)\hat{\mathbf{r}}_{c2}]. \tag{2.32}$$

We can use the same method to account for the propagation through the $\lambda/4$ plate as we used for the detection crystal. We can again decompose the probe into the two propagation modes and then propagate both modes through the $\lambda/4$ plate by applying the correct complex phase factor. A $\lambda/4$ plate is constructed such that the effective optical length for the two modes differ by a quarter of a wavelength. This corresponds to a difference in phase of 90°. The unit vector which points in the polarization direction of the probe beam after propagation through the $\lambda/4$ plate is thus given by

$$\begin{aligned}
\hat{\mathbf{E}}_{pl} &= \hat{\mathbf{r}}_{l1}(\hat{\mathbf{r}}_{l1}\cdot\hat{\mathbf{E}}_{pc}) + j\hat{\mathbf{r}}_{l2}(\hat{\mathbf{r}}_{l2}\cdot\hat{\mathbf{E}}_{pc}) \\
&\simeq \exp(j\omega n_1 l/c)\,\{\hat{\mathbf{r}}_{l1}\left[\cos(\beta-\alpha)\cos(\alpha) - \sin(\beta-\alpha)(1+j\zeta)\sin(\alpha)\right] \\
&\quad + j\hat{\mathbf{r}}_{l2}\left[-\sin(\beta-\alpha)\cos(\alpha) - \cos(\beta-\alpha)(1+j\zeta)\sin(\alpha)\right]\} \\
&= \exp(j\omega n_1 l/c)\,\{[\cos(\beta)\hat{\mathbf{r}}_{l1} + \zeta\cos(\beta-\alpha)\sin(\alpha)\hat{\mathbf{r}}_{l2}] \\
&\quad - j\left[\sin(\beta)\hat{\mathbf{r}}_{l2} + \zeta\sin(\beta-\alpha)\sin(\alpha)\hat{\mathbf{r}}_{l1}\right]\},
\end{aligned} \tag{2.33}$$

where the imaginary unit j takes into account the 90° phase difference. The polarization can now be decomposed along the axes of the Wollaston prism to get the intensities incident on the two photodiodes

$$\begin{aligned}
I_1 &= \frac{1}{2}\varepsilon_0\sqrt{\varepsilon_r}c\left|\hat{\mathbf{E}}_{pl}\cdot\hat{\mathbf{r}}_{w1}\right|^2 \\
&\simeq I_{\text{tot}}\Big\{\cos^2(\beta)\cos^2(\gamma) + \sin^2(\beta)\sin^2(\gamma) \\
&\quad + 2\zeta\sin(\alpha)\sin(\gamma)\cos(\gamma)\left[\cos(\beta)\cos(\beta-\alpha) + \sin(\beta)\sin(\beta-\alpha)\right]\} \\
&= I_{\text{tot}}\Big[\cos^2(\beta)\cos^2(\gamma) + \sin^2(\beta)\sin^2(\gamma) \\
&\quad + \zeta\sin(2\alpha)\sin(2\gamma)/2\Big]
\end{aligned} \tag{2.34}$$

$$\begin{aligned}
I_2 &= \frac{1}{2}\varepsilon_0\sqrt{\varepsilon_r}c\left|\hat{\mathbf{E}}_{pl}\cdot\hat{\mathbf{r}}_{w2}\right|^2 \\
&\simeq I_{\text{tot}}\Big[\cos^2(\beta)\sin^2(\gamma) + \sin^2(\beta)\cos^2(\gamma) \\
&\quad - \zeta\sin(2\alpha)\sin(2\gamma)/2\Big],
\end{aligned} \tag{2.35}$$

where we have neglected all terms of order ζ^2, and where $I_{\text{tot}} = I_1 + I_2 = \frac{1}{2}\varepsilon_0\sqrt{\varepsilon_r}c\|\hat{\mathbf{E}}_{pl}\|^2$ is the total intensity of the probe beam. The difference in the two intensities is given by

$$\Delta I = I_1 - I_2 \simeq I_{\text{tot}}\left[\cos(2\beta)\cos(2\gamma) + \zeta\sin(2\alpha)\sin(2\gamma)\right]. \tag{2.36}$$

This equation dictates that to reach the maximum detection sensitivity the experimenter should orientate the Wollaston prism relative to the quarter-wave plate in such a way that $\cos(2\gamma) = 0$. For this orientation the signal is maximized, and the common mode signal, which is a source of noise in the detection, is zero. Note, that, when $\cos(2\gamma) = 0$, the angle β is irrelevant. This means that, as long as the Wollaston prism is oriented correctly relative to the quarter-wave plate, the orientation relative to the initial probe beam polarization of the Wollaston prism and of the quarter-wave plate doesn't influence the measurement.

There is an electro-optic detection scheme different from the one we are describing now, that doesn't use a quarter-wave plate and a differential detector, but instead uses a pair of crossed polarizers around the detection crystal and a single detector. This setup is equivalent to ours, if we set $\gamma = 0$ and $\beta = \pi/4$. If these values are substituted in the previous equation, the term proportional to ζ vanishes. This means that the previously-neglected term proportional to ζ^2 becomes dominant. The terahertz electric field is proportional to ζ, so with crossed polarizers a signal is obtained that is proportional to the E_T^2, leading to relatively small signals and loss of the knowledge of the sign of the terahertz electric field.

If we now consider the most efficient configuration by setting $\gamma = 45^o$ and fill in the definition of ζ we get the following expression for the signal obtained in electro-optic detection

$$\frac{\Delta I}{I_{\text{tot}}} \simeq \sin(2\alpha)\frac{\omega \Delta n l}{c}. \tag{2.37}$$

So in electro-optic detection, the signal is linear with the terahertz induced refractive-index difference. The signal is zero, if the polarization direction of the probe is parallel to the polarization of one of the propagation modes of the crystal ($\sin(2\alpha) = 0$). This is easy to understand. If the polarization direction of the probe is parallel to the polarization of one of the propagation modes, then the probe experiences only one refractive index. In this case the probe remains linearly polarized and the electro-optic signal is zero. It should be noted, that the polarization of the propagation modes depend on the direction of the applied terahertz electric field. This means, that in addition to Δn, α also depends on the terahertz electric field.

Calculation of the terahertz-induced electro-optic signal

The previous results will now be used to find an expression for the electro-optic signal ($\frac{\Delta I}{I_{\text{tot}}}$) as a function of the amplitude and direction of the terahertz electric field. To calculate the electro-optic signal with equation (2.37), we first write the initial polarization direction of the probe beam in the new coordinate system ($\hat{\mathbf{E}}'_p$) as

$$\hat{\mathbf{E}}'_p \equiv \begin{pmatrix} 0 \\ \cos(\delta) \\ \sin(\delta) \end{pmatrix}, \tag{2.38}$$

where we have used that the probe beam is initially polarized linearly, and that its polarization direction is perpendicular to its propagation direction. According to the above definition, δ is the angle between the initial polarization direction of the probe and the $\hat{\mathbf{y}}'$ vector. With the transformation matrix of equation (2.18), we get the initial, probe polarization vector in the coordinate system formed by the crystal axes

$$\hat{\mathbf{E}}_p = \frac{1}{\sqrt{s_y^2 + s_z^2}} \begin{pmatrix} \sin(\delta)\left(s_y^2 + s_z^2\right) \\ -s_z\cos(\delta) - s_x s_y \sin(\delta) \\ s_y\cos(\delta) - s_x s_z \sin(\delta) \end{pmatrix}. \tag{2.39}$$

As we shall see, the sine and cosine of 2δ determine for which direction of the terahertz electric field the setup is sensitive. For a given polarization of the probe, the sine and cosine of 2δ can be calculated with the following equations

$$\sin(2\delta) = \frac{2E_{px}\left(E_{py}s_z - E_{pz}s_y\right)}{s_y^2 + s_z^2} \tag{2.40}$$

$$\cos(2\delta) = \frac{\left(E_{py}s_z - E_{pz}s_y\right)^2 - E_{px}^2}{s_y^2 + s_z^2}, \tag{2.41}$$

where E_{px}, E_{py}, and E_{pz} are the components of the unit vector in the direction of the probe's electric field with respect to the crystal axes. When using the previous equations, one has to take into account that the components of $\hat{\mathbf{E}}_p$ and $\hat{\mathbf{s}}$ are not completely independent, since the two vectors have to be perpendicular to each other.

We now rewrite equation (2.37), using equations (2.24), (2.25), and (2.12) and putting $\Delta n \equiv \Delta n_2 - \Delta n_1$, as

$$\begin{aligned} \frac{\Delta I}{I_{\text{tot}}} &\simeq \sin(2\alpha)\frac{\omega \Delta n l}{c} \\ &= \frac{2\omega\chi^{(2)}l}{c\sqrt{\varepsilon_r}}\sqrt{b^2+c}\,\left(\hat{\mathbf{E}}'_p \cdot \hat{\mathbf{r}}'_{c1}\right)\left(\hat{\mathbf{s}}' \cdot \left(\hat{\mathbf{E}}'_p \times \hat{\mathbf{r}}'_{c1}\right)\right) \\ &= \frac{2\omega\chi^{(2)}l}{c\sqrt{\varepsilon_r}}\sqrt{b^2+c}\,\left(\hat{\mathbf{E}}'_p \cdot \mathbf{E}'_{01}\right)\left(\hat{\mathbf{s}}' \cdot \left(\hat{\mathbf{E}}'_p \times \mathbf{E}'_{01}\right)\right) / \left\|\mathbf{E}'_{01}\right\|^2. \end{aligned} \tag{2.42}$$

In the previous equation, we used the following goniometrical equations

$$\sin(\alpha) = \hat{\mathbf{s}}' \cdot \left(\hat{\mathbf{E}}'_p \times \hat{\mathbf{r}}'_{c1}\right) \tag{2.43}$$

$$\cos(\alpha) = \hat{\mathbf{E}}'_p \cdot \hat{\mathbf{r}}'_{c1}. \tag{2.44}$$

The only physical properties used in these equations is that α is the angle between the unit vectors $\hat{\mathbf{E}}'_p$ and $\hat{\mathbf{r}}'_{c1}$, and that both these vectors are perpendicular to probe propagation direction $\hat{\mathbf{s}}'$.

Equation (2.42) is valid in each coordinate system. However, the equation will be used in the new coordinate system, because we have obtained an expression for $\mathbf{E}'_{01}$ that is in this coordinate system.

After the insertion of equations (2.28) and (2.38) into equation (2.42) and after some rearrangement we get

$$\begin{aligned}\frac{\Delta I}{I_{\text{tot}}} = -\frac{\omega\chi^{(2)}l}{c\sqrt{\varepsilon_r}}\Bigg[&\sin(2\delta)\begin{pmatrix} E_{Tx}\\ E_{Ty}\\ E_{Tz}\end{pmatrix}\cdot\begin{pmatrix} s_y s_z \frac{s_z^2+s_y^2-2}{s_y^2+s_z^2}\\ s_x s_z\\ s_x s_y\end{pmatrix}\\ &+\cos(2\delta)\begin{pmatrix} E_{Tx}\\ E_{Ty}\\ E_{Tz}\end{pmatrix}\cdot\begin{pmatrix} s_x \frac{-s_z^2+s_y^2}{s_y^2+s_z^2}\\ -s_y\\ s_z\end{pmatrix}\Bigg],\end{aligned} \tag{2.45}$$

which we can rewrite as

$$\frac{\Delta I}{I_{\text{tot}}} = \frac{\omega n^3 r_{41} l}{c}\left[\sin(2\delta)\left(\mathbf{E}_T\cdot\mathbf{S}_1\right)+\cos(2\delta)\left(\mathbf{E}_T\cdot\mathbf{S}_2\right)\right] \tag{2.46}$$

with

$$\mathbf{S}_1 = \begin{pmatrix} s_y s_z \frac{s_z^2+s_y^2-2}{s_y^2+s_z^2} & , & s_x s_z & , & s_x s_y\end{pmatrix} \tag{2.47}$$

and

$$\mathbf{S}_2 = \begin{pmatrix} s_x \frac{-s_z^2+s_y^2}{s_y^2+s_z^2} & , & -s_y & , & s_z\end{pmatrix} \tag{2.48}$$

using $n=\sqrt{\varepsilon_r}$ and $r_{41}=-\chi^{(2)}/\varepsilon_r^2$.[40,49]

With these equations the electro-optic signal can be calculated for arbitrary propagation and polarization directions of the probe and for arbitrary terahertz electric field direction. All quantities in these equations are expressed in the coordinate system formed by the crystallographic axes of the crystal, which makes the usage of the equations very straightforward.

Further insight is gained, if equation (2.46) is rewritten as

$$\frac{\Delta I}{I_{\text{tot}}} = \frac{\omega n^3 r_{41} l}{c}\left(\mathbf{E}_T\cdot\mathbf{V}\right) \tag{2.49}$$

with

$$\mathbf{V} \equiv \sin(2\delta)\mathbf{S}_1+\cos(2\delta)\mathbf{S}_2, \tag{2.50}$$

where all the information about the orientation of the probe propagation and polarization is concentrated in a single vector $\mathbf{V}$, which we call the sensitivity vector. The size of the electro-optic signal is simply proportional to the size of the component of the terahertz electric field in the direction of $\mathbf{V}$ times the length of the vector $\mathbf{V}$. Once a propagation direction has been chosen for the probe beam, an experimenter still has the freedom to select the probe polarization direction, which determines δ. By the selection of δ, both size and direction of $\mathbf{V}$ can be manipulated. In a lot of experiments the propagation direction is kept constant, while the signal is maximized by rotating the crystal.

In this process, the crystal is rotated to change δ such that the component of $\mathbf{V}$ in the direction of $\mathbf{E}_T$ is maximized. During the rotation of the crystal $\mathbf{S}_1$ and $\mathbf{S}_2$ do not change, because the crystal is rotated around the propagation direction of the probe.

It is interesting to note, if δ is changed from 0 to π in equation (2.50), the vector $\mathbf{V}$ describes an ellipse in 3D-space. An ellipse is fully described if the two semi-axes are known. To find these semi-axes, we calculated the extremes of the length of $\mathbf{V}$ as a function of δ for an arbitrary propagation direction of the probe with equation (2.50). The values of δ for which the length of $\mathbf{V}$ has an extreme are given by

$$\tan(4\delta_{\mathrm{ex}}) = \frac{2\,(\mathbf{S}_1 \cdot \mathbf{S}_2)}{\|\mathbf{S}_2\|^2 - \|\mathbf{S}_1\|^2}. \tag{2.51}$$

Once the values for δ_{ex} are known, then these values can be substituted in equation (2.50) to obtain the semi-axes. This will be done in the following chapter for a variety of different probe propagation directions.

In equation (2.46) all square-root terms, which were present in the expressions for the refractive indices and for the polarization direction of the propagation modes (equation (2.24) to (2.28)), have vanished. This means, that the electro-optic signal is linear with the terahertz electric field for every direction of probe propagation. The signal is even linear in the strict mathematical sense that not only the signal increases linearly with the size of the terahertz electric field, but also that a signal caused by the sum of two arbitrary terahertz electric-field vectors equals the sum of the signals caused by the two vectors. This is not trivial, since the two terahertz electric-field vectors do not have to point in the same direction.

2.1.2 Different probe propagation directions

In this subsection, the results from the previous section are used to calculate the sensitivity of the electro-optic detection setup for different propagation directions of the probe beam. From equation (2.49), we can see that there are two aspects that are important for the sensitivity to a terahertz electric field. These aspects are the length of the vector $\mathbf{V}$ and the angle between $\mathbf{V}$ and the terahertz electric field vector. In order to gain insight in the detection sensitivity we will separate these aspects and first look at the orientation dependence of $\mathbf{V}$. $\mathbf{V}$ depends on both the probe polarization and the probe propagation direction. As was discussed in section 2.1.1, the possible values of $\mathbf{V}$ for a particular probe propagation direction form an ellipse. In this subsection, we will focus on calculating the semi-axes of the ellipse for different propagation directions, because the ellipse is fully described by its semi-axes. The semi-axes are, by definition, the values of $\mathbf{V}$ for which the length of $\mathbf{V}$ as a function of the probe polarization direction has an extreme.

We thus investigate the sensitivity for different probe propagation directions by calculating minimum and a maximum values of $\mathbf{V}$. We consider probe beam propagation along three common crystallographic axes ($\langle 110 \rangle$,

Table 2.1: Calculation results for different propagation directions of the probe beam.

variable	$\langle 110 \rangle$	$\langle 111 \rangle^a$	$\langle 010 \rangle$	$\langle 345 \rangle$
s_x	$1/\sqrt{2}$	$1/\sqrt{3}$	0	$\frac{3}{10}\sqrt{2}$
s_y	$1/\sqrt{2}$	$1/\sqrt{3}$	1	$\frac{2}{5}\sqrt{2}$
s_z	0	$1/\sqrt{3}$	0	$\frac{1}{2}\sqrt{2}$
$\delta_{\max}$ (degrees)	0	—	0	4.3
$\lvert\mathbf{V}_{\min}\rvert$	$\frac{1}{2}$	$\frac{1}{3}\sqrt{6}$	0	0.69
$\mathbf{V}_{\min}/\lvert\mathbf{V}_{\min}\rvert$	$\begin{pmatrix} 0 \\ 0 \\ 1 \end{pmatrix}$	$\begin{pmatrix} -\frac{1}{3}\sqrt{6} \\ \frac{1}{6}\sqrt{6} \\ \frac{1}{6}\sqrt{6} \end{pmatrix}$	—	$\begin{pmatrix} -0.81 \\ 0.55 \\ 0.19 \end{pmatrix}$
$\lvert\mathbf{V}_{\max}\rvert$	1	$\frac{1}{3}\sqrt{6}$	1	0.91
$\mathbf{V}_{\max}/\lvert\mathbf{V}_{\max}\rvert$	$\begin{pmatrix} \frac{1}{\sqrt{2}} \\ -\frac{1}{\sqrt{2}} \\ 0 \end{pmatrix}$	$\begin{pmatrix} 0 \\ -\frac{1}{\sqrt{2}} \\ \frac{1}{\sqrt{2}} \end{pmatrix}$	$\begin{pmatrix} 0 \\ 1 \\ 0 \end{pmatrix}$	$\begin{pmatrix} -0.19 \\ -0.56 \\ 0.80 \end{pmatrix}$
$\hat{\mathbf{E}}_{p,\max}$	$\begin{pmatrix} 0 \\ 0 \\ 1 \end{pmatrix}$	$\begin{pmatrix} 0 \\ -\frac{1}{\sqrt{2}} \\ \frac{1}{\sqrt{2}} \end{pmatrix}$	$\begin{pmatrix} 0 \\ 0 \\ 1 \end{pmatrix}$	$\begin{pmatrix} 0.07 \\ -0.80 \\ 0.60 \end{pmatrix}$

[a] For the $\langle 111 \rangle$ direction, the length of $\mathbf{V}$ is constant and thus has no minima and maxima. Therefore, for this direction we show the $\mathbf{S}_1$ instead of $\mathbf{V}_{\max}$, $\mathbf{S}_2$ instead of $\mathbf{V}_{\min}$, and the polarization for $\delta = 0$ in stead of $\hat{\mathbf{E}}_{p,\max}$.

$\langle 111 \rangle$, and $\langle 010 \rangle$), and one arbitrary chosen direction, namely $\langle 345 \rangle$. For each of these propagation directions, table 2.1 shows the components of the unit vector in the propagation direction (s_x, s_y, and s_z), along with information about a maximum and a minimum length of $\mathbf{V}$. For one maximum, table 2.1 shows the direction of the probe polarization, the corresponding value of δ, the length of the vector $\mathbf{V}$, and a unit vector in the direction of $\mathbf{V}$. For one minimum the table gives the length of the vector $\mathbf{V}$, and a unit vector in the direction of $\mathbf{V}$. The direction of the probe polarization and the value of δ are not given for the minimum, since these values are trivial once the values for the maximum are presented. As was discussed in the previous chapter, the polarization at the minimum is just the polarization at the maximum rotated 45° around the probe propagation direction. This rotation corresponds to an increase of δ with $\pi/4$.

The contents of table 2.1 were calculated as follows. First, the vector in the propagation direction is normalized to the unit vector $\hat{\mathbf{s}} = (s_x, s_y, s_z)$. Secondly, these value for s_x, s_y, and s_z are substituted into equations (2.47) and (2.48) to obtain $\mathbf{S}_1$ and $\mathbf{S}_2$. Third, the values of δ for which $\mathbf{V}$ reaches a minimum or a maximum are calculated by substitution of $\mathbf{S}_1$ and $\mathbf{S}_2$ into equation (2.51). Fourth, the values for δ_{ex} are used to calculated the extremes of $\mathbf{V}$ with equation (2.50), and, finally, the same values for δ_{ex} are substituted into equation (2.39) to obtain the probe polarization at the extremes. We note that the extremes of the signal ($\Delta I / I_{\text{tot}}$) can be calculated straightforwardly from the

extremes of **V** with equation (2.49).

For a ⟨110⟩ direction of the probe, one of the maxima of **V** is located at δ = 0, which is directed along the ($1/\sqrt{2}$, -$1/\sqrt{2}$, 0) direction of the crystal. This means that the electro-optic signal is linear with the component of the terahertz electric field in the $\langle 1\bar{1}0 \rangle$ direction, if δ is set at 0°. The situation that δ = 0 corresponds to a probe polarization that is oriented along the z-axis of the crystal. However, if δ is set at 45°, then the length of **V** has a minimum, and the signal is proportional to the component of the terahertz electric field in the ⟨001⟩ direction. The difference between the minimum length of **V** and its maximum length is a factor 2. This means that, if we compare the case that the probe polarization is oriented for the maximum with the case that it is oriented for the minimum, while in both cases the terahertz electric field is aligned with **V**, the signal obtained at the maximum is twice the signal at the minimum.

For most applications, it is favorable to make the sensitivity as large as possible. For a ⟨110⟩ probe propagation direction this is achieved when δ = 0°. This corresponds to a setup in which the probe polarization direction is ⟨001⟩ or an equivalent direction (= $\langle 00\bar{1} \rangle$, $\langle 1\bar{1}0 \rangle$, or $\langle \bar{1}10 \rangle$), and in which the terahertz electric field direction is $\langle 1\bar{1}0 \rangle$ (or the equivalent $\langle \bar{1}10 \rangle$). The results for the ⟨110⟩ probe propagation direction are in agreement with the results in previous work.[42,43,50]

The vectors $\mathbf{S}_1$ and $\mathbf{S}_2$ are equal in length and perpendicular to each other, when the probe beam propagates along the ⟨111⟩ direction. This means that the ellipse that describes the orientation dependence of **V** is in fact a circle, and that the extremes of **V** are not defined. For the ⟨111⟩ propagation direction, the length of **V** is independent of the orientation of the probe polarization. The polarization direction only determines the direction of **V**, and thus to which component of the terahertz electric field the setup is sensitive. This can be an advantage for some applications, but the sensitivity is a factor $\frac{1}{2}\sqrt{6} \simeq 1.22$ lower compared to case of the ⟨110⟩ probe propagation direction. The results for the ⟨111⟩ probe propagation direction are in agreement with the results of reference 43.

For a ⟨010⟩ propagation direction, the vector $\mathbf{S}_1$ equals zero, so the ellipse of **V** for this direction is a line. The length of $\mathbf{S}_2$ is 1 for the ⟨010⟩ propagation direction, so **V** can be just as large as for the ⟨110⟩ propagation direction. However, while for the ⟨110⟩ propagation direction **V** is directed perpendicular to the propagation direction, for the ⟨010⟩ direction **V** is parallel to the propagation direction. In the common case that the probe beam and the terahertz beam propagate in the same direction, this means that for the ⟨010⟩ direction the setup is only sensitive to longitudinal electric fields, while for the ⟨110⟩ propagation direction it is only sensitive to transverse terahertz electric fields. This makes the ⟨110⟩ propagation direction well suited for transversal-wave detection, while the ⟨010⟩ can be used for longitudinal-wave detection.[38]

To illustrate the general applicability of our theory, the last column of table 2.1 shows the parameters for the more unusual ⟨345⟩ propagation direction. Although this direction is arbitrarily chosen, the calculations stay just

as simple. Uncommon propagation directions, like $\langle 345 \rangle$, are certainly not irrelevant. The angle between the $\langle 111 \rangle$ and the $\langle 345 \rangle$ direction is only 11.5°. If we take into account that a focussed beam is a sum of plane waves that have different propagation directions, then it is not difficult to imagine that a focussed probe beam with its optical axis along the $\langle 111 \rangle$ direction can have spatial components in the $\langle 345 \rangle$ direction.

The top picture of figure 2.3 shows the values that the length of $\mathbf{V}$ can have, as a function of the propagation direction of the probe. The propagation direction on the horizontal axis follows a path that begins at the $\langle 010 \rangle$ direction, and ends at the $\langle 001 \rangle$ direction via the $\langle 110 \rangle$ direction. This path is indicated visually in the bottom picture of figure 2.3. As can be seen in the top graph, the lengths of de vectors strongly depend on the probe propagation direction, but do not exceed 1.

We have discussed the effect of the orientation of the probe on the electro-optic signal. Now, the second aspect that is important to the sensitivity, the orientation of the terahertz electric field, will be considered. In most applications the terahertz beam propagates in the same direction as the probe beam. This means that the terahertz electric field is perpendicular to the probe propagation direction $\hat{\mathbf{s}}$. The orientation of the terahertz electric field relative to the crystal axes can still be changed by rotating the crystal around the propagation direction, but this doesn't change the fact that the terahertz electric field is perpendicular to the propagation direction. For such cases the possible sensitivity is proportional to the part of $\mathbf{V}$ that is also perpendicular to the propagation direction. This part can be written as

$$\begin{aligned} \mathbf{V}_\perp &= \mathbf{V} - \hat{\mathbf{s}}\,(\hat{\mathbf{s}} \cdot \mathbf{V}) && (2.52) \\ &= \sin(2\delta)\,(\mathbf{S}_1 - \hat{\mathbf{s}}\,(\hat{\mathbf{s}} \cdot \mathbf{S}_1)) + \cos(2\delta)\,(\mathbf{S}_2 - \hat{\mathbf{s}}\,(\hat{\mathbf{s}} \cdot \mathbf{S}_2))\,. && (2.53) \end{aligned}$$

Note, that, if the 3D position of $\mathbf{V}_\perp$ is tracked for different values of δ, then these positions again lie on an ellipse, just like $\mathbf{V}$. The ellipse formed by $\mathbf{V}_\perp$ is actually the projection of the ellipse of $\mathbf{V}$ on the plane perpendicular to the propagation direction.

The values that the length of $\mathbf{V}_\perp$ can have, are also displayed in figure 2.3. We see that the largest value for the length of $\mathbf{V}_\perp$ is found for the $\langle 110 \rangle$ propagation direction. This means this is the propagation direction for which the detection is the most sensitive to transversal electric fields of all the directions of the path indicated in the top picture of figure 2.3. It should be noted that this direction is not very critical, since a reasonable detection sensitivity is possible for a whole range of propagation directions. For example, the $\langle 111 \rangle$ propagation direction has a sensitivity which is only 18% less sensitive than the $\langle 110 \rangle$ direction. In figure 2.3 it also can be seen that the regions of $\mathbf{V}$ and $\mathbf{V}_\perp$ are practically the same over a wide range of propagation directions. For those directions the ellipse of $\mathbf{V}$ lies approximately in the plane perpendicular to the propagation direction. Only for directions that approach one of the crystallographic axes does $\mathbf{V}$ rotate toward the propagation direction, which leads to a decrease of $\mathbf{V}_\perp$.

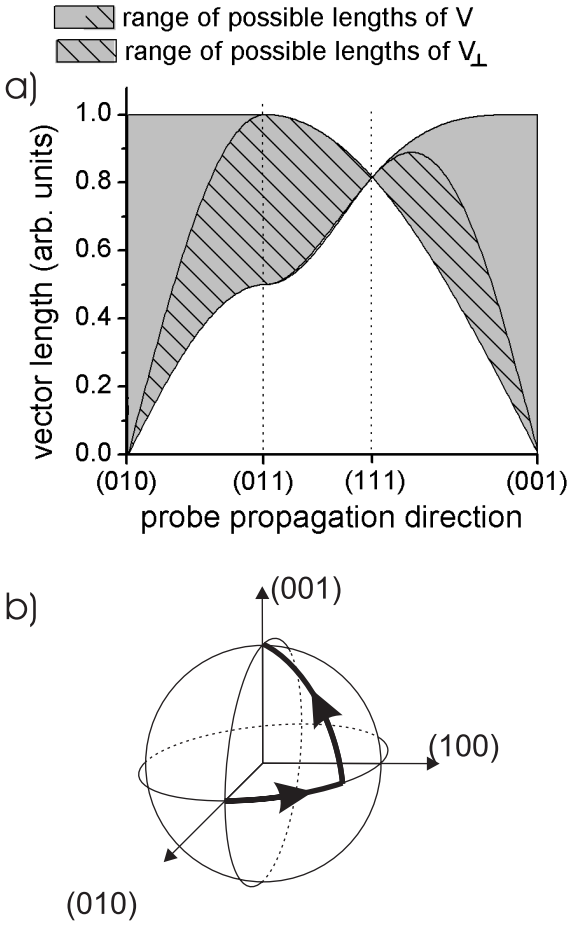

Figure 2.3: a) Values that can be obtained for the length of **V** and the length of the component of **V** perpendicular to $\hat{\mathbf{s}}$ ($\mathbf{V}_\perp$) as a function of the probe propagation direction. b) The path followed for the propagation direction displayed on the horizontal axis of graph a.

2.1.3 Conclusion

We have derived a simple, easy to use, and widely applicable set of equations that completely describes electro-optic detection of terahertz radiation in optically isotropic crystals. In the discussion of our results, they are applied to various propagation directions for the probe beam. These examples give results that agree perfectly with previously reported work.

2.2 Measuring the terahertz polarization

Most terahertz imaging techniques only measure one component of the electric-field vector. This makes the images obtained with these methods sometimes difficult to interpret. A decrease in the amplitude of the measured field, for instance, is commonly interpreted as being caused by absorption or scattering. However, such a decrease could also be caused by a rotation of the electric field vector induced by a birefringence present in the sample. Besides birefringence, there are various other effects that can change the direction of a terahertz electric field, such as not-normal-incidence reflection and multiple scattering.

In this section, we report on a method to measure both the direction and the length of the transversal terahertz electric-field vector using electro-optic sampling. We demonstrate the potential of this technique in terahertz imaging and spectroscopy with two examples. In the first example, we perform spectroscopic measurements on polystyrene foam. Surprisingly, this material shows an effective birefringence, which can be measured accurately with our new technique. In the second example, we show terahertz images of a plastic coin based on a measurement of the two transversal electric-field components at each pixel. The images clearly show that scattering or reflection at the edges of the coin results in a change in the polarization state of the terahertz beam.

2.2.1 Setup

Figure 2.4 shows a schematic drawing of the detection setup. The terahertz electric field is measured using the electro-optic effect, which causes a birefringence of the detection crystal proportional to the electric field. The birefringence causes a polarization change of the optical probe pulse, which is measured with a differential detection setup. A quarter-wave plate is placed before the ZnTe detection crystal, oriented such that the originally linear polarization of the probe beam becomes circular. Key element in our setup is the use of a ZnTe detection crystal with a (111) crystal orientation. This crystal orientation results in 18% smaller signals compared to the more commonly used (110) orientation (section 2.1.2). However, as we will discuss below, this orientation allows for the detection of both electric field components with equal sensitivities without any rotation of the detection crystal. A signal proportional to the terahertz electric field is obtained, by measuring the difference in the energy in the two orthogonal polarization directions of the probe beam

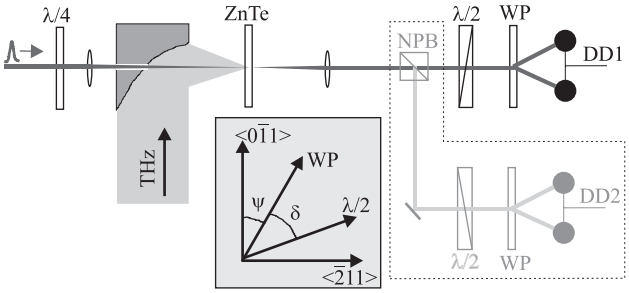

Figure 2.4: Schematic picture of the detection setup. The terahertz beam is focussed onto the ZnTe detection crystal with a parabolic mirror. The probe beam is sent through a quarter-wave plate ($\lambda/4$) and the parabolic mirror, and focussed onto the detection crystal. After collimation, the probe beam propagates through a half-wave plate ($\lambda/2$) and is split into two orthogonally polarized beams by a Wollaston prism (WP). The difference in the power of the two orthogonal polarizations is measured by a differential detector (DD1). Within the dotted frame it is shown how a nonpolarizing beamsplitter (NPB) can be used to create a second detection arm. The inset shows how the angles ψ and δ are defined by the relative orientation of the $\langle 0\bar{1}1\rangle$ and $\langle \bar{2}11\rangle$ axis of the ZnTe crystal, and the axes of the Wollaston prism and the half-wave plate.

with a Wollaston prism and a differential detector. A half-wave plate is placed before the Wollaston prism to set the direction of the terahertz electric field to which the measurement is sensitive. Without the half-wave plate, this would require an inconvenient rotation of both the Wollaston prism and the differential detector.

Using the same procedure as in section 2.1.1, the following expression is obtained for the power difference measured by the differential detector[51]

$$\Delta P = \frac{\sqrt{24}\pi n^3 r_{41} l P_{tot}}{3\lambda} \left[E_{\bar{2}11} \sin(2\psi - 4\delta) + E_{0\bar{1}1} \cos(2\psi - 4\delta)\right], \qquad (2.54)$$

where λ is the wavelength in vacuum of the probe beam, n is the refractive index of the ZnTe crystal for the probe beam, and l is the thickness of the crystal. The optical power incident on the differential detector is P_{tot}, and r_{41} is the only nonzero component of the electro-optic tensor of ZnTe. The angles ψ and δ are defined in the inset in figure 2.4. $E_{\bar{2}11}$ and $E_{0\bar{1}1}$ are the terahertz electric fields along respectively the $\langle \bar{2}11\rangle$ and $\langle 0\bar{1}1\rangle$ directions in the detection crystal. From equation 2.54, we can see that, either by a rotation of the half-wave plate or by a joined rotation of the Wollaston prism and the differential detector (changing ψ or δ), it is possible to decide which component of the terahertz electric field is measured by the detector.

2.2.2 Measurement results

In a measurement of two orthogonal electric-field components, it is important that, when measuring one field component, the influence of the other

field component is suppressed. The quality of this suppression in our setup is evaluated by measuring two orthogonal electric-field components for the case where the terahertz field is assumed to be polarized linearly. For this purpose, a wire grid polarizer proved necessary, because preliminary measurements indicated that our terahertz source, a photoconductive emitter,[23] produces a slightly elliptically polarized field. Figure 2.5A shows the measured electric field parallel and perpendicular to the transmission direction of the polarizer. The ratio between the peak-peak values of the electric fields is 0.014, and the ratio between the total power in the two pulses is 2552:1. Note that these numbers are probably an underestimation of the quality of the above mentioned suppression, as the residual field in the perpendicular direction can easily be attributed to a slight misalignment of the parabolic mirrors.

Figure 2.5B shows the two orthogonal electric fields measured when a 2 cm thick piece of polystyrene foam is placed just after the polarizer. Besides a shift in time, there is barely any change in the parallel component of the electric field when the foam is inserted. However, the amplitude of the perpendicular component, measured after a 22.5 degrees rotation of the half-wave plate, increases dramatically. To our surprise, the strength of this component proved to be a strong function of the azimuthal orientation of the polystyrene foam with the strongest signal plotted in Figure 2.5B. Furthermore, the energy ratio in the parallel and the perpendicular component proved to be a function of frequency, as can be seen in figure 2.5C. In this figure, we plot the difference between the spectral intensities of the parallel and the perpendicular component, normalized to the sum of these intensities. The figure clearly shows that for increasing frequency an increasing part of the terahertz energy is in the perpendicular component of the electric field.

The polystyrene foam measurement can partly be understood by assuming that anisotropies induced during fabrication of the foam cause the foam to be birefringent. We note that it is unlikely that surface effects play an important role, because the observed effects increased with a factor of two, when we doubled the thickness of the foam from 1 to 2 cm. To verify that the signals are caused by a birefringence in the foam, we measured the time delay of the parallel component, while rotating the foam around the azimuthal angle. The maximum changes in the time delay thus measured are 113.2 fs for the 2 cm thick piece and 66.7 fs for the 1 cm thick piece. When the refractive indices are assumed frequency-independent, these time delays correspond to a refractive-index difference of 1.7×10^{-3} for the 2 cm piece and 2.0×10^{-3} for the 1 cm piece. From these refractive-index differences, we calculate the relative intensity difference between the two polarization directions (solid lines, figure 2.5C). Below 1 THz, there is an excellent correspondence between the measurement and the calculation, which has no adjustable parameters. At higher frequencies, the agreement is somewhat worse. We note that at higher frequencies the birefringence model is no longer valid, because then the wavelength approaches the size of the bubbles in the foam, and we can no longer view the foam as an effective medium with frequency-independent refractive indices. However, the measurements are clear examples of the advantages of measuring both components of the terahertz electric field.

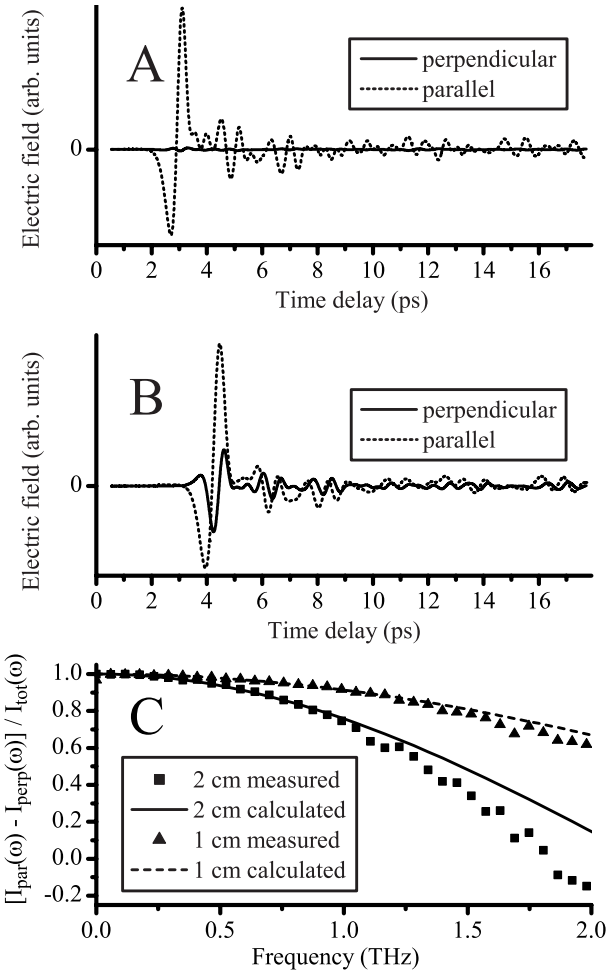

Figure 2.5: (A) Electric field as a function of time of the reference pulses, which travelled only through air, and (B) of the terahertz pulses after travelling through 2 cm polystyrene foam. The dotted and the solid lines in A and B are respectively the fields parallel and perpendicular to the transmission direction of the polarizer. Graph C shows the measured and the calculated relative intensity difference between the two polarization directions as a function of frequency for propagation through the 1 cm and the 2 cm thick piece of polystyrene foam.

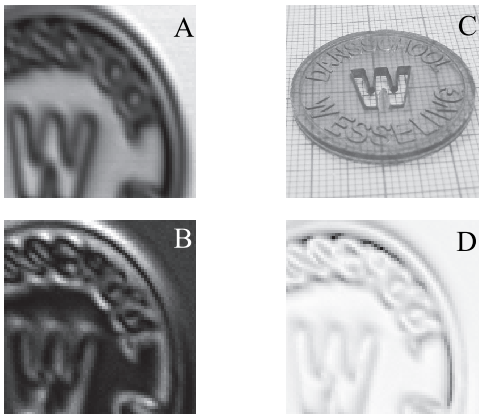

Figure 2.6: Terahertz images (A,B,D) and visible-light photograph (C) of a plastic coin. Left graphs: transmitted terahertz power measured parallel (A) and perpendicular (B) to the original polarization direction. (white = maximum transmission). (C) Visible-light photograph of the coin. (D) Plot of the angular rotation of the direction of the terahertz electric field (white = 0 degrees rotation, black = 45 degrees rotation).

Our measurement technique can also be applied to the field of terahertz imaging. Figure 2.6 shows terahertz images obtained by measuring the transmitted terahertz electric field, while scanning a plastic coin through the focus of the terahertz beam. Before this focus, a wire-grid polarizer is placed to polarize the terahertz beam. For comparison, a visible-light photograph of the coin is included (figure 2.6C). The two left images show the spectral power integrated between 0.8 THz and 1.0 THz for the parallel and the perpendicular component of the electric field. The images for the parallel component show distinct black lines at the edges of the coin. In contrast, the images for the perpendicular component show an enhanced power at the edges. This is consistent with a rotation of the electric-field vector due to scattering and reflection at the edges of the coin. This is even more clear in figure 2.6D, which shows the angular rotation of the terahertz electric field. This rotation is calculated by $\arctan(E_{\perp}/E_{//})$, where $E_{\perp}$ and $E_{//}$ are the spectral amplitudes between 0.8 THz and 1.0 THz of respectively the perpendicular and the parallel electric-field component. The image shows rotations of the electric field up to 45 degrees. Our results clearly indicate that the features at the edges are mostly due scattering/reflection and not due to absorption. It would not have been possible to make this distinction with a measurement of only one electric-field component.

Finally, we would like to point out that, although we here performed two *sequential* measurements of the two orthogonal polarization components, the setup can easily be extended to allow for the *simultaneous* measurement of the two transversal electric-field component. For this purpose, an extra detection arm can be created with a nonpolarizing beamsplitter and an additional half-wave plate, Wollaston prism and differential detector, as shown in the dotted

frame in figure 2.4. The two detection arms differ only in the orientation of their half-wave plates. These plates are orientated such that the two arms measure orthogonal components of the electric field. For instance, one arm measures $E_{0\bar{1}1}$, while the other simultaneously measures $E_{\bar{2}11}$.

2.2.3 Conclusion

We have presented a method to simultaneously measure the two orthogonal components of the electric field of a terahertz pulse. Key elements of this method are the use of a (111) orientated electro-optic detection crystal and the placement of a quarter-wave plate before the crystal. By using a half-wave plate to set the direction of the measured electric-field component, we avoid cumbersome rotations of the Wollaston prism and the differential detector. We have demonstrated the applicability of our method with two examples, one related to spectroscopy and one related to imaging.

Chapter 3

Noise

As in all measurements, noise is an important parameter in electro-optic detection. The noise level determines the measurement duration required to reach a desired signal-to-noise ratio. The terahertz noise level is even more important in near-field microscopy measurements. Imaging smaller objects, will, in general, lead to smaller signals. Therefore, the noise can limit the resolution, since objects smaller than this limit cannot be imaged within a reasonable amount of time.

From previous work, we know that the noise in terahertz electro-optic detection originates dominantly from fluctuations in the probe beam.[23] With the differential detection scheme described in chapter 2, noise due to random variations of the probe beam power can be suppressed. The photon shot noise measured by the two photodiodes is, however, not suppressed. The influence of photon noise can be reduced by increasing the power of the probe beam. However, high probe beam powers can lead to changes in the frequency response of the photodiodes due to saturation effects.[52–54]

The goal of this chapter is to investigate experimentally the influence of photodiode saturation in differential detection. More specifically, we discuss how saturation influences the ability of the differential detector to suppress noise due to variations of the probe beam power. Where possible, we present recommendations on how to suppress the adverse effect of saturation.

As an introduction to this topic, we first discuss the various noise sources in terahertz electro-optic detection in section 3.1. The discussion on photodiode saturation is given in section 3.2. Often, the measured noise can be reduced with the help of lock-in techniques. This practical side of terahertz measurements is discussed in appendix B.

3.1 Sources of noise

This section discusses the various noise sources in terahertz electro-optic detection. We define noise as the random variations of the measured signal. In electro-optic detection, this signal is the difference in the intensity on the two

photodiodes ΔI. Our definition of noise implies that random fluctuations of the terahertz source are also classified as noise. This may seem strange as it does not influence the sensitivity of the electric-field detection, but in most cases we are not interested in the electric field itself, but in changes in the electric field. To determine the refractive index of an object, for instance, we compare the measured electric field with and without the object in the terahertz beam. If the terahertz source fluctuates between the two measurements, then this leads to a variation in the value of the refractive index.

Noise due to fluctuation of the terahertz source determines the difference between signal-to-noise ratio and dynamic range, as defined in section 1.2.3. Signal-to-noise ratio is the ratio between the signal and the total noise. Dynamic range is the ratio between the signal, and the noise with the terahertz beam blocked, and thus does not contain noise due to fluctuations of the *source*.

We classify the noise sources in four categories. First, noise due to fluctuations of the source. Secondly, noise due to incoherent background radiation. Next, we consider noise due to fluctuations of the probe beam, and, finally, electronic noise in the detector.

3.1.1 Noise due to the terahertz source

The terahertz pulse is generated with a pump pulse, which is derived from the same laser as the probe pulse (section 1.2.2). Therefore, the electric field of the terahertz pulse is a function of the power in the pump pulse. This power fluctuates due to laser noise, which is present in all lasers. For lasers producing ultrafast pulses, a relative root-mean-square amplitude noise of 1% is considered reasonable. Therefore, fluctuations of the source in most cases dominate the total noise and thus the signal-to-noise ratio. Noise from the source is, however, not included in the dynamic range, for which we must consider other noise sources.

3.1.2 Noise from background radiation

The surroundings of a measurement setup emit thermal radiation. At room temperature, a significant portion of this radiation has a terahertz frequency. Due to this radiation, there is a constantly fluctuating electric field in each point in space, and thus also in/on our detector. Due to the principle of time-gated detection (section 1.2) time-domain spectroscopy is less sensitive to thermal radiation, because only fluctuations within the time window of the detection contribute to the detected noise. However, thermal noise can still play a significant role.

We estimate the contribution of thermal noise to the measured signal. For this we assume that the detector is only sensitive to one component of the terahertz electric field and is completely insensitive to the propagation direction of the thermal radiation. This second requirement is in many cases not completely valid. Electro-optic detection in thick crystals, for instance,

strongly depends on the propagation direction of the radiation, due to an effect called phase-matching.[55] However, since this is highly dependent on the exact measurement configuration and since we are only interested in the order of magnitude of the thermal noise contribution, we feel that the requirement is justified.

The average volume density of the energy in thermal fluctuations up to the frequency f_e is given by Planck's law

$$\begin{aligned}\langle u \rangle &= \int_0^{f_e} \mathrm{d}f \; \frac{8\pi h f^3}{c^3} \frac{1}{\exp(hf/k_B T) - 1} \\ &\simeq \frac{8\pi k_B T f_e^3}{3c^3} \qquad \text{for} \quad hf_e \ll k_B T,\end{aligned} \tag{3.1}$$

where k_B is Boltzmann's constant and T is the background temperature. The frequency f_e is determined by the cut-off frequency of the detection. The above energy density is the energy density of the total field.* This energy is equally distributed over the three components of the electric field, so one component of the electric field carries one third of the total energy. The average of the z-component of the electric field squared is given by[56]

$$\langle E_z^2 \rangle = \frac{\langle u \rangle}{3\varepsilon_0}. \tag{3.2}$$

The root mean square value (RMS) of the electric field component in the z-direction is thus

$$\sqrt{\langle E_z^2 \rangle} = \sqrt{\frac{8\pi k_B T f_e^3}{9c^3 \varepsilon_0}}, \tag{3.3}$$

$\sqrt{\langle E_z^2 \rangle}$ is the RMS value of the noise measured with a single probe pulse. In a typical measurement, the measured noise is an average over many pulses. This average can be expressed in terms of the noise equivalent field, which is the strength of a constant electric field that produces a signal equal to the rms value of the noise.[23] The noise equivalent field of the thermal background noise is given by

$$E_{NEF,ther} = \sqrt{\frac{8\pi k_B T f_e^3}{9c^3 \varepsilon_0} \frac{f_B}{f_{rep}}}, \tag{3.4}$$

where f_{rep} is the repetition rate of the laser and f_B is the bandwidth of the detection. The number of probe pulses in the average equals f_{rep}/f_B. Substituting T = 300 K, f_e = 3 THz, f_B = 10 kHz, and f_{ref} = 80 MHz, we find $E_{NEF,ther}$ = 4.0 mV/cm.

*The electric field and the magnetic field each contain half of the total energy in vacuum. This is taken into account in the relation between the electric field and the energy density (equation 3.2).

3.1.3 Noise from the probe beam

There are two noise contributions from the probe beam: laser amplitude noise and laser shot noise. We define laser amplitude noise as all fluctuations of the output power of the laser that are not related to the photon character of the laser light. Amplitude fluctuations of the probe beam cause fluctuations in the currents through photodiodes of the detector (figure 2.1). A large advantage of differential detection is that fluctuations common to the two photodiodes cancel. This cancellation is, however, never complete. The influence of remaining laser-amplitude noise can be reduced with lock-in techniques. The noise spectrum of a laser has an overall $1/f$ dependence. Modulation of the terahertz source at a high frequency makes it possible to filter-out the strong low-frequency noise, as is described in appendix B.

If laser amplitude noise is suppressed sufficiently, then laser shot noise can become the dominant noise source. The energy of the probe beam is quantified in photons. Statistical variations in the arrival times of these photons results in fluctuations in the power measured by the photodiodes. These fluctuations do not cancel out in differential detection, since the fluctuations in the two photodiodes are different. Lock-in techniques cannot reduce the influence of shot noise, since the noise spectrum of shot noise is flat, that is, the noise is independent of frequency. The influence of shot noise can only be reduced by increasing the power of the probe beam. Shot noise increases with the square root of the probe power, but the electro-optic signal increases proportional to the probe power. Therefore, the signal-to-noise ratio due to shot noise is proportional the square root of the power. If, for instance, the probe power increases with a factor of 4, then the signal-to-noise ratio will improve by a factor of 2. From reference,[23] we obtain that a noise equivalent field for shot noise from a 775 nm probe beam (9.3 mW power) with a 1 mm thick ZnTe detection crystal and a 10 kHz detection bandwidth is given by $E_{NEF,shot} = 13\ mV/cm$.

3.1.4 Electronic noise

The differential detector is also a noise source. The photodiodes produce a current proportional to the incident power level. As the current is quantified in electrons, it exhibits shot noise. Assuming a quantum efficiency of one, one electron in the current is generated by one photon of the probe beam, which makes current shot noise equivalent to the photon shot noise discussed in the previous section. There are also noise sources inherent to the structure of a photodiode, which are present even if the photodiodes are not illuminated. The noise level of a photodiode varies between different types of photodiodes, but usually is on the order of 10^{-15} W $\mathrm{Hz}^{-1/2}$. This noise level results in an equivalent terahertz electric-field of $E_{NEF,diode} = 0.3\ \mu$V/cm for electro-optic detection in a 1 mm thick ZnTe crystal with a 10 kHz bandwidth and a 10 mW probe beam.

The amplifier in the detector is also a noise source. However, if the constraints on the bandwidth of the detection are not too stringent, a good elec-

tronic design can ensure that this source can be neglected. One can therefore conclude that the total noise of the detector is dominated, not by noise from the electronics, but by laser amplitude noise, photon/electron shot noise and noise due to thermal background radiation. In our experiments, the dominant noise source is either laser amplitude noise or laser shot noise dependent on which laser system we use.

3.2 Photodiode saturation

In section 3.1 we argued that laser shot noise is the dominant noise source, if laser amplitude noise is suppressed by differential detection and if electronic noise is avoided by a good detector design.[23] The signal is proportional to the probe beam power and shot noise is proportional to the square root of the probe power. Therefore, the dynamic range in a shot-noise limited setup can only be increased by increasing the power in the probe beam. For this reason, high-power photodiode illumination is very common in the terahertz field, where powers are used of 10 mW or more per photodiode. The implicit assumption in this is, however, that the photodiodes employed in the differential detector continue to behave properly under high-power illumination.

We present experimental results that indicate two effects that deteriorate the sensitivity of the differential detector under high-levels of illumination.[57] First, we find that the high-power illumination causes a strong reduction in the detection bandwidth of our silicon photodiodes. Secondly, we find, associated with this bandwidth reduction, phase shifts in the electronic signal up to 100 degrees. When we increase the bias voltage across the photodiode, the adverse effects of the high-power illumination are reduced.

In differential detection, the phase shifts induced at high powers strongly reduce the ability of the detector to suppress amplitude noise, since no two photodiodes are identical, or are illuminated in exactly the same way. Based on this insight, we propose to increase the bias voltage over the photodiodes, when the optical power on the photodiodes is high. Additionally, the laser beam can be expanded to fill a large part of the active area of the photodiodes. These two measures improve the response of the differential detector under high levels of illumination, and insure a good amplitude-noise suppression.

3.2.1 Measurement setup

We employ two setups to investigate the effect of high-power illumination: one that measures the response of a single photodiode and one that measures the noise spectrum from a differential detector. To investigate the response of a single photodiode, a Si PIN photodiode (BPW34s) is illuminated by a Ti:Sapphire oscillator. This oscillator produces pulses with a pulse length of about 15 fs and a repetition rate of 80 MHz. The Ti:Sapphire oscillator can be considered as a continuous source, because its repetition rate is much higher than the bandwidth of the detector, which is about 1 MHz.

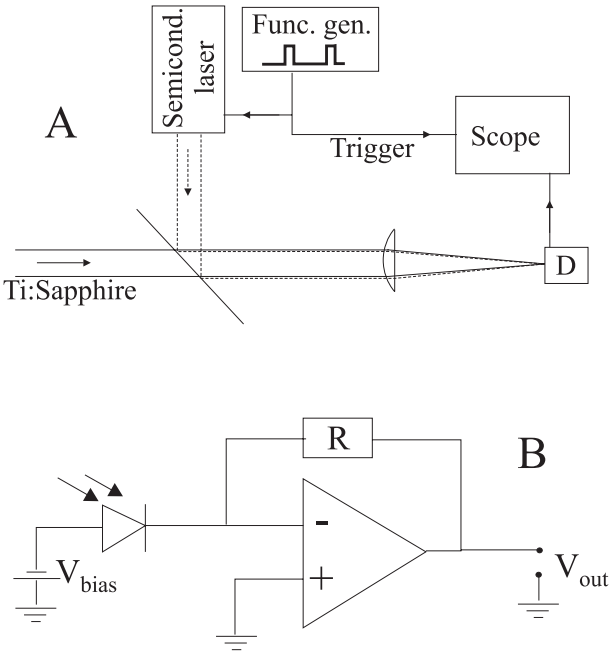

Figure 3.1: Schematics for the single-photodiode measurement. (Fig. A) A semiconductor laser is switched on/off by the pulses from the function generator, which are also used to trigger the oscilloscope. The beam from the semiconductor laser is combined with a beam from the Ti:Sapphire oscillator and focused onto the detector (D). The signal from the detector is recorded with the digital oscilloscope. (Fig. B) Schematics of the detector circuit with a single photodiode. R is the feedback resistance, V_{bias} is the bias voltage over the photodiode, and V_{out} is the output voltage of the detector.

As shown in Fig. 3.1A, the Ti:Sapphire beam propagates collinearly with a beam from a low-power semiconductor laser with a wavelength of 670 nm. This semiconductor laser generates square-wave pulses with a duration of 2 μs and a repetition rate of 1 kHz. We study the influence of the Ti:Sapphire illumination on the photodiode response to the pulses from the semiconductor laser. The Ti:Sapphire beam has an average power of several milliwatts and the peak power of the square-wave pulses is about 35 μW. Both beams are focused onto the same position on the BPW34s silicon PIN photodiode. This photodiode has an active area of 2.65 x 2.65 mm, of which only a small fraction is illuminated by the foci of the two beams.

Fig. 3.1B shows a schematic of the detector circuit in which the photodiode is embedded. The photodiode is reverse-biased by a voltage V_{bias}, which can be varied. In the detector circuit, the amplifier with the feedback resistor has the double function of amplifying the signal, while keeping the voltage over the photodiode fixed independent of the illumination level. For bias voltages larger than 1 V, the detector has a low-power bandwidth of 800 kHz. The signal from the detector is measured with the digital oscilloscope for different

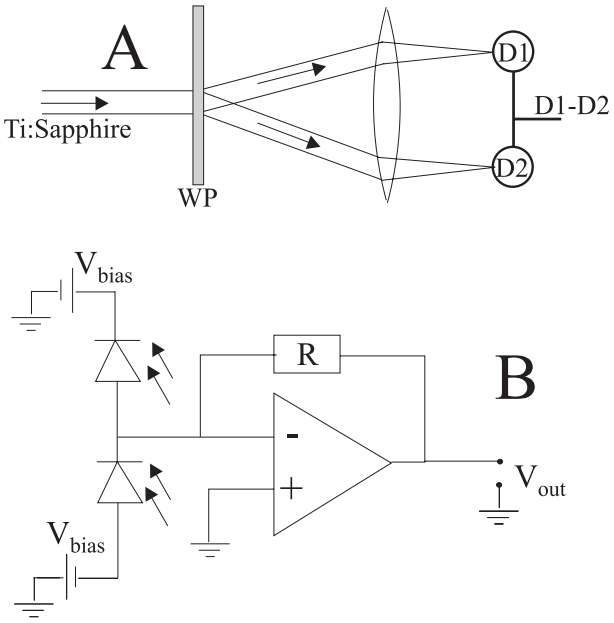

Figure 3.2: Schematics of the differential detector setup. Figure A shows the concept of the measurement. A Ti:Sapphire beam is split into to equal parts by a Wollaston prism (WP). The two beams are then focussed on the two photodiodes of the detector. Figure B shows a schematic of the electronics of the detector. The two photodiodes are each reverse-biased with a voltage V_{bias}. The difference in the currents through the photodiodes is amplified to the output voltage V_{out}.

values of the power of the Ti:Sapphire beam and for different values of the bias voltage across the photodiode.

The setup for measuring the noise from the differential-detection setup is shown in Fig. 3.2A. In this setup a beam from the Ti:Sapphire oscillator is split into two beams, having equal power, by a Wollaston prism. Each beam is focused onto one of the photodiodes of a differential detector. Fig. 3.2B shows a schematic of this detector. Both (BPW34s silicon PIN) photodiodes are reverse-biased with a 5 V voltage. The difference between the currents through the two photodiodes is amplified. The detector design insures a constant bias voltage over the photodiodes. The diameter of the foci are again small compared to the active area of the photodiode. When not illuminated, the detector has a noise level of only 0.06 μV Hz$^{-1/2}$.

3.2.2 Results

Figure 3.3 shows the response of the single photodiode to the 2 μs long pulses of the diode laser for different power levels of the Ti:Sapphire beam. The top figure shows a time trace of a 13 μs part of the measurement, which has a total duration of 1 ms. The measurements for Ti:Sapphire laser power levels at 6.7 mW and 3.7 mW should be compared with the reference measurement,

which is obtained with the Ti:Sapphire beam blocked. Figure 3.3A shows that the electrical signal from the photodiode is deformed and broadened in the presence of the Ti:Sapphire beam. It is also observed that the peak of the pulse shifts forward in time.

The effect of the Ti:Sapphire illumination on the photodiode response becomes more apparent in the spectra of the measurements. The fast fourier transforms (FFT) of the measurements for Ti:Sapphire laser powers of 6.7 mW and 3.7 mW are divided by the FFT of the reference measurement. This results in the amplitude spectra in Fig. 3.3B and in the phase spectra in Fig. 3.3C. From figure 3.3B it can be seen that the DC ($\omega = 0$) response from the detector shows no sign of photodiode saturation, even for a Ti:Sapphire power of 6.7 mW.

The amplitude and phase spectra show a remarkably strong influence of the Ti:Sapphire background power on the ability of the photodiode to detect the pulses from the semiconductor laser. The amplitudes of the spectra in Fig. 3.3B are unity at low frequencies, but decrease rapidly at higher frequencies. The -3 dB frequency is 196 kHz for 3.7 mW Ti:Sapphire power and 126 kHz for 6.7 mW Ti:Sapphire power. Remarkably, in Fig. 3.3C, we also see that the *phase* of the electrical signal rises from zero to a maximum of 55.7 degrees at 297 kHz for 3.7 mW and 96.8 degrees at 192 kHz for 6.7 mW.

Figure 3.4 shows the results of measurements with the single-photodiode detector, where the power of the Ti:Sapphire beam is kept constant at 6.7 mW and the bias voltage is varied. The corresponding amplitude and phase spectra in respectively Fig. 3.4A and Fig. 3.4B show that the effect of the Ti:Sapphire background power on the response of the photodiode is a strong function of the bias voltage. For the 20 V bias, there is only a moderate effect on the photodiode response. The amplitude decreases slightly at high frequencies and the phase changes moderately with a linear slope of 0.059 degrees/kHz. However, the photodiode response changes dramatically for smaller bias voltages. For a 2.5 V bias, the relative amplitude *increases* to 1.1, before it sharply decreases with a -3 dB point at 111 kHz. The phase shift at the 2.5 V bias has a peak of almost 180 degrees at 188 kHz. We note that the features in figure 3.4 are *not* caused by a change in the capacitance of the photodiode due to the change in the bias voltage. The capacitance of the photodiode changes with the bias voltage, but this has been corrected for by dividing the spectrum for the illuminated photodiode at each bias voltage with a reference measurement *at that bias voltage* with the Ti:Sapphire laser blocked. Measurements in which the diameter of the laser beam on the photodiode has been increased (not shown here), also result in a decrease in both the amplitude and phase distortions on the electrical signal.

It is clear from the previous results that the photodiode response changes drastically under high levels of illumination. To study the effect of this on differential detection, we show in Fig. 3.5 the noise spectra of the differential detector described in Fig. 3.2, measured for different values of the power of the Ti:Sapphire beam.

The spectra in Fig. 3.5 are approximately flat for low illumination levels as is appropriate for a shot-noise limited detector. However, at higher illumina-

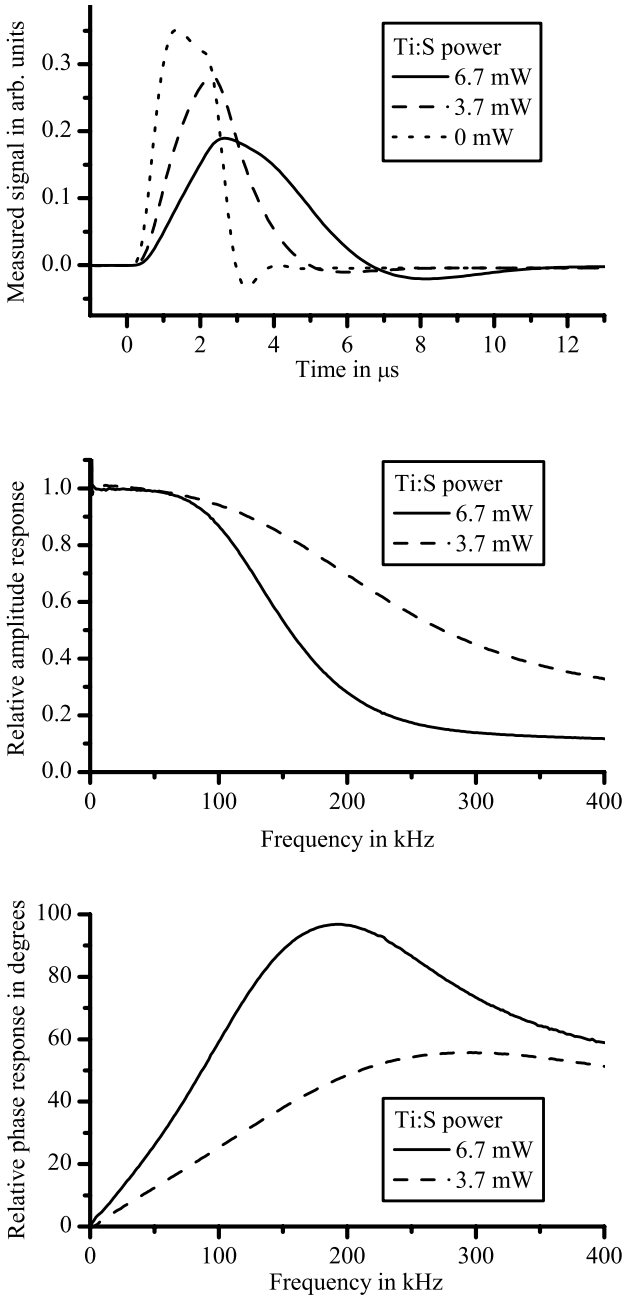

Figure 3.3: Measurement results for the illumination-dependent response of the single photodiode. Fig. A shows the measured signal as a function of time for Ti:Sapphire power levels of 6.7 mW and 3.7 mW, along with the reference measurement, which is recorded with the Ti:Sapphire beam blocked. Fig. B and C show the amplitude, respectively, the phase response calculated from the measurement.

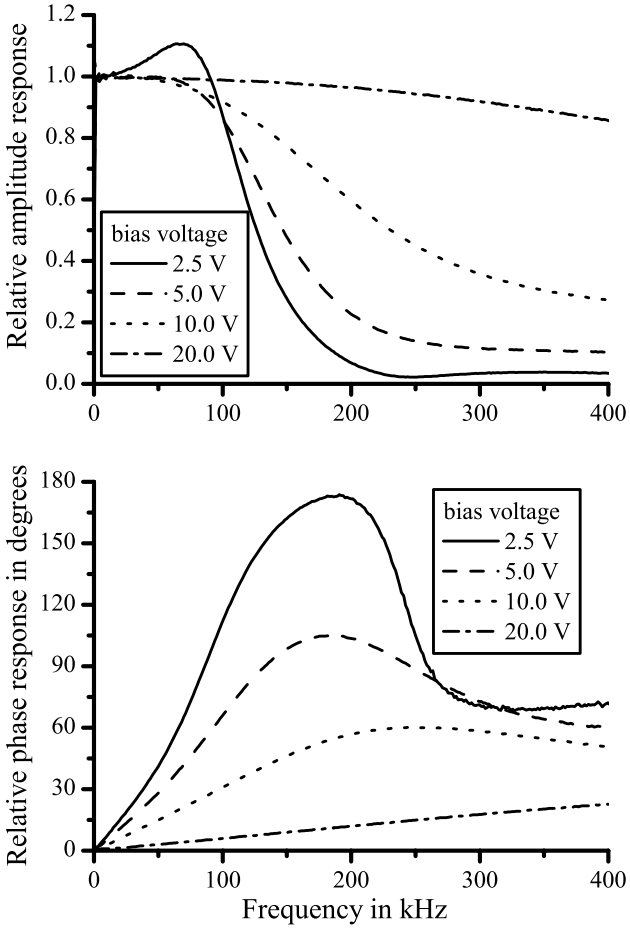

Figure 3.4: Single photodiode amplitude (Fig A.) and phase (Fig. B) response as a function of frequency for different bias voltages over the photodiode.

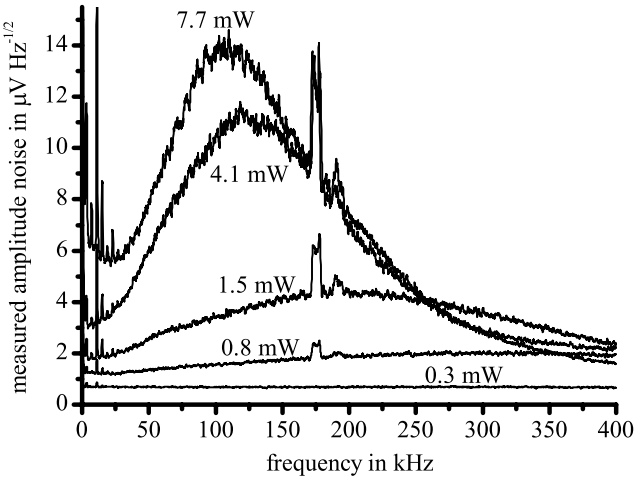

Figure 3.5: Measured noise spectra of the differential detector for different powers of the Ti:Sapphire beam. The powers indicated in the figure refer to the optical power per photodiode.

tion levels a bump emerges that narrows and increases in amplitude, until at 7.7 mW illumination the peak of the bump at 110 kHz is more than twice the noise amplitude at 20 kHz. For high power illumination (1.5 mW, 4.1 mW and 7.7 mW), the noise level is seen to decrease at high frequencies. The amplitude noise at 400 kHz for 7.7 mW illumination is even *lower* than for 0.8 mW illumination. We note that the sharp peak in figure 3.5 at 180 kHz is a characteristic line of the amplitude noise spectrum of our laser.

3.2.3 Discussion

The results in Fig. 3.3 and 3.4 clearly show that bandwidths of our photodiodes are strongly reduced, when the diodes are illuminated with a high average power. Coupled to this bandwidth reduction is a phase change that can reach values up to 100 degrees. In the literature, there are previous reports that high-power illumination on a photodiode can reduce the measurement bandwidth. However, we are surprised to find that an effect is already observed below 100 kHz, while previous reports, as far as we know, all deal with frequencies above 100 MHz.[52–54] Although this difference is probably caused by differences in carrier lifetimes and in the photodiode internal structure, this is not something that we completely understand.

We can explain the results obtained with the differential detector using the results for the single-photodiode detector. The single-photodiode measurement shows that at high levels of illumination the sensitivity of an individual photodiode decreases with frequency. This causes the noise decrease seen at high frequencies in Fig. 3.5. We note that this reduction of the noise will not cause an improvement of the signal to noise ratio, since the sensitivity of the

differential detector to any signal is also reduced.

As discussed in the previous section, we measure an increase of the noise from the differential detector under high levels of illumination. This can be explained, if the phase response of the two photodiodes in the differential detector is slightly different, since such a difference has a dramatic effect on the ability of the detector to suppress the amplitude noise from the laser. An ideal differential detector completely suppresses the amplitude noise, leaving shot noise as the dominant noise source. However, a differential detector with a phase difference in the response of the two photodiodes of 11.5 degrees has a theoretical amplitude noise suppression of only 20 dB. Such a small phase difference can easily be caused by a difference in the size or position of the foci on the photodiodes or by a difference within the fabrication tolerances of the photodiodes.

It is clear that high-illumination levels can cause problems in differential detection. However, our work provides useful insights that can be used to prevent these problems. A large improvement can be reached by increasing the bias voltage over the photodiodes. At higher bias voltages, the generated electron-hole pairs are more quickly removed from the depletion region, and thus the local carrier density is lower. As seen in Fig. 3.4, this substantially decreases the effect of the illumination on both the amplitude and the phase response of the detector.

Additionally, the problems can be reduced by increasing the diameter of illuminated region on the photodiodes, since our measurements show that this significantly reduces the saturation effects. Clipping at the edges of the photodiodes should, however, be avoided, since this can introduce an extra noise source due to vibrations of optical components and subsequent beampointing fluctuations.

3.2.4 Conclusion

We have measured significant changes in the response of our photodiodes at probe beam powers on the order of several milliwatts. These changes can reduce the ability of the differential detector to suppress noise caused by variations of the probe beam power. To suppress this adverse effect without increasing the influence of photon shot noise, we recommend to increase the bias-voltage over the photodiode and the diameter of the probe beam at the photodiodes.

Chapter 4

Terahertz generation

This chapter discusses two methods to generate ultra-short terahertz pulses. The first, generation by photoconductive emitters is briefly discussed in section 4.1. The second, optical rectification is described in more detail. Optical rectification is generally less efficient than generation by photoconductive emitters. However recently, optical rectification received increased attention, because it may play an important role in future terahertz microscopy techniques.[58,59] Optical rectification is terahertz generation by a focussed optical beam. The diameter of this focus can be much smaller than the terahertz wavelength, which effectively creates an emitter of sub-wavelength dimensions.

The literature on terahertz generation by optical rectification[60–65] is extensive. However, the theoretical description of this process proves to be complicated, because many approximations used in the description of other nonlinear optical processes are not valid in optical rectification. The terahertz wavelength can, for instance, not be neglected compared to the dimensions of the generation region. Also, the generated radiation does not propagate in one strictly defined direction, but covers a range of directions. This means that the terahertz electric field after collection and focussing of the emitted radiation is a function of the angular dependence of the emission.

The goal of section 4.2 is to derive an expression that describes the electric field of a terahertz pulse that is emitted by optical rectification and subsequently collected and focussed. Contrary to previous reports, we take into account the full angular dependence of the emitted terahertz radiation. The derived expression is used to gain insight in the influence of the width and length of the generation volume, the terahertz wavelength and the duration of the generating optical pulse.

The goal of section 4.3 is to experimentally verify the predicted dependence of optical rectification on the wavelength of the generating pulse and on the thickness of the generation crystal.

Optical rectification is a second-order ($\chi^{(2)}$) nonlinear process. Also possible, although uncommon, is the generation of terahertz radiation by third-order ($\chi^{(3)}$) processes. The optical rectification theory in section 4.2 can be

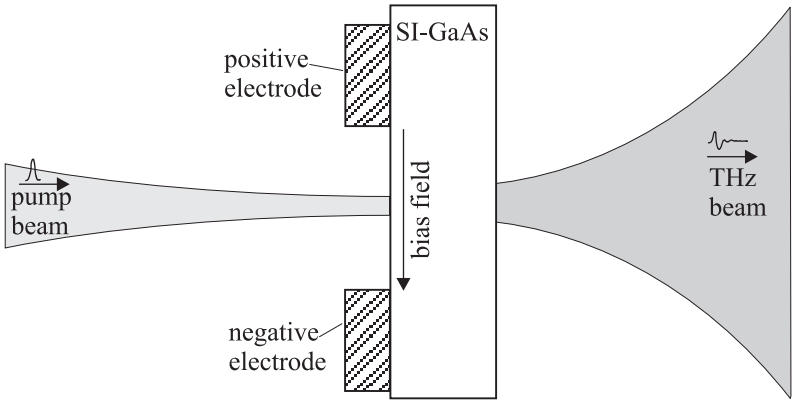

Figure 4.1: Schematic drawing of a photoconductive emitter. An optical pump beam is focussed on a piece of semi-insulating (SI) GaAs. Across the GaAs surface, two electrodes produce a bias electric field. Each pulse from the pump beam induces a current surge, which emits a terahertz pulse.

straightforwardly adapted to $\chi^{(3)}$ terahertz generation, as is shown in appendix A.

4.1 Photoconductive emitters

A much-used source of terahertz pulses is the photoconductive switch or photoconductive antenna.[66,67] We also use it often, because of the high terahertz electric fields that can be obtained with this device. Figure 4.1 shows a schematic drawing of such an emitter. Key element of this emitter is a piece of semiconductor, in this case GaAs, that under normal circumstances has a very high resistance. However, when an optical pulse hits the semiconductor, free carriers are created, which causes an instantaneous decrease of the resistance. Between pump pulses, the resistance of the semiconductor is high enough to prevent the bias field from producing any significant current in the semiconductor. However, the bias field immediately accelerates the carriers generated by the pump pulse, inducing a current across the semiconductor surface. The pump pulse functions as a switch that turns on the current, which is why this type of emitter is also called a photoconductive switch. We note that photoconductive switches can also be used for the *detection* of terahertz pulses, as briefly discussed in section 1.2.2.

The time derivative of the current is very high, due to the short duration of the ultrafast pump pulses. As will be shown in the next section (equation 4.9), a time-dependent current gives rise to radiation. The radiated electric field is proportional to the time derivative of the current, and a broadband terahertz pulse is radiated. In a slightly modified configuration, the generated terahertz pulse can contain frequency components up to 20 THz.

In practice, the bias field of a photoconductive emitter is modulated to

facilitate the use of lock-in techniques. These lock-in techniques can significantly reduce the measurement noise, as is discussed in detail in appendix B.

4.2 Theory of terahertz generation by optical nonlinearities

The nonlinear response of the polarization in a medium to an electric field was discussed in chapter 2 in the context of the *detection* of terahertz radiation. This nonlinear response can, however, also be used for the *generation* of terahertz radiation. Terahertz radiation can, for instance, be generated by the mixing of two optical beams, one with an electric field $E_0 \sin \omega_1 t$ and the other with an electric field $E_0 \sin \omega_2 t$. For non-dispersive media, the second-order nonlinear polarization is given by

$$\begin{aligned} P^{(2)}(t) &= \chi^{(2)} \{E_0 \sin(\omega_1 t) + E_0 \sin(\omega_2 t)\}^2 \\ &= \chi^{(2)} E_0^2 \Big\{1 - \tfrac{1}{2}\cos(2\omega_1 t) - \tfrac{1}{2}\cos(2\omega_2 t) \\ &\quad + \cos((\omega_1 - \omega_2)t) - \cos((\omega_1 + \omega_2)t)\Big\} \end{aligned} \tag{4.1}$$

Interestingly, each term of this polarization has a frequency different from the two frequencies of the original electric fields. There is a constant term, two terms at the double frequencies, a sum-frequency term and a difference-frequency term. According to Maxwell's equations, these polarization terms can radiate new fields, which thus have a different frequency compared to the generating beams. Here, we will uses the difference-frequency term, where the difference-frequency $\omega_1 - \omega_2$ is in the terahertz region. Note that the above equation is a simplification, which disregards the tensor character and the dispersion of the second-order nonlinear susceptibility $\chi^{(2)}$. These simplifications will be used throughout this section.

Practically, terahertz difference-frequency generation can be used as follows. Two optical beams overlap in a medium that is usually chosen to have a relatively large nonlinear response. The frequency of the optical beams can be on the order of 1000 THz, but the frequency difference between the two beam is much smaller, on the order of 1 THz. The nonlinear effects will induce a polarization in the medium, which oscillates at the difference frequency. That polarization radiates a terahertz beam at the difference frequency. In this way, a continuous wave, single-frequency terahertz beam is generated.

It is, however, also possible to use difference-frequency generation to generate terahertz *pulses* in a process called optical rectification. In this process, one optical beam is used that consists of a train of very short (10 - 100 fs) pulses. Due to the short duration of the pulses, the frequency bandwidth can be tens of terahertz wide. If the pulses travel through a nonlinear medium, then difference-frequency generation can take place between different frequency components within the pulse bandwidth. The net effect of the difference-

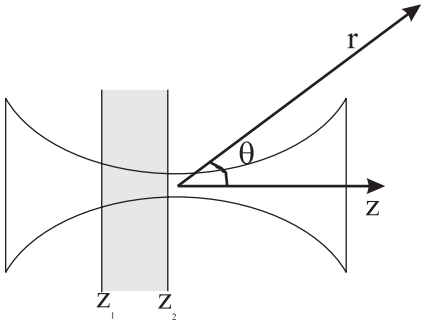

Figure 4.2: Schematic of the terahertz generation configuration. The picture shows the beam shape of the two monochromatic pump beams. The pump beams propagate in the z-direction. The generation region extends from the $z = z_1$ plane to the $z = z_2$ plane.

frequency generation process between all these frequency components is that each optical pulse can generate a terahertz pulse.

The subject of this section is the generation of terahertz pulses using the second-order nonlinear polarization. We calculate the spectrum of the radiated field, its angular dependence, and the electric field when the terahertz radiation is focused. To make the calculation easier, we will first look at the terahertz field generated by two monochromatic beams, and then make the next step to a pulsed source containing many frequency components.

The remainder of this chapter is organized as follows. In section 4.2.1, the nonlinear polarization induced by two monochromatic Gaussian beams will be calculated. Section 4.2.2 discusses the far field radiated by a general polarization distribution. The results of section 4.2.1 and 4.2.2 are combined in section 4.2.3 to find the far field radiated by the nonlinear polarization of the two Gaussian-shaped beams. This result is further analyzed by considering some special cases in section 4.2.4. In section 4.2.5 the angular dependence of the radiated field is used to calculate the electric field in the focus, when the radiation emitted in all forward directions is collected and focussed by a mirror. Section 4.2.6 completes the analysis by moving from two monochromatic pump beams to one pulsed pump beam (optical rectification).

4.2.1 Induced polarization

In this section, we calculate the low-frequency nonlinear polarization caused by two monochromatic pump beams of almost equal frequency. To avoid having to deal with reflections at crystal interfaces, we assume that our generation crystal is embedded in a medium with an identical refractive index for both pump beams and for the terahertz radiation, but with a zero $\chi^{(2)}$. In this section, the time dependent polarizations and electric fields are written in complex notation. One can obtain measurable quantities by taking the real part of each expression.

The coordinate system used has its origin in the center of the pump foci

with the z-axis in the pump-beam propagation direction. The generation crystal, which is the region with a nonzero $\chi^{(2)}$, extends from $z = z_1$ to $z = z_2$, as shown in figure 4.2. The beams are assumed to be collinear and to have a Gaussian spatial profile transverse to the propagation direction. Also, the length and position of both foci are assumed to be identical. The electric field of these beams can be written as (ref. 68, p. 664)

$$\begin{aligned} E_{g1}(t,x,y,z) &= \frac{jz_r E_{g10}}{(z+jz_r)} \exp\left\{ j(\omega-\omega_T/2)t \right. \\ &\quad \left. - jk(\omega-\omega_T/2)\left(z+\frac{1}{2}\frac{x^2+y^2}{z+jz_r}\right)\right\} \\ &\simeq \frac{jz_r E_{g10}}{(z+jz_r)} \exp\left\{ j(\omega-\omega_T/2)t \right. \\ &\quad \left. - j\left(k(\omega)-(\omega_T/2)\frac{\partial k}{\partial \omega}(\omega)\right)\left(z+\frac{1}{2}\frac{x^2+y^2}{z+jz_r}\right)\right\} \end{aligned} \tag{4.2}$$

$$\begin{aligned} E_{g2}(t,x,y,z) \simeq \frac{jz_r E_{g20}}{(z+jz_r)} &\exp\left\{ j(\omega+\omega_T/2)t \right. \\ &\left. -j\left(k(\omega)+(\omega_T/2)\frac{\partial k}{\partial \omega}(\omega)\right)\left(z+\frac{1}{2}\frac{x^2+y^2}{z+jz_r}\right)\right\}, \end{aligned} \tag{4.3}$$

where ω is the optical radial frequency, and ω_T is the radial frequency of the generated beam, which we assume to be in the terahertz region. The focus length of the two beams is identical and determined by z_r, which is equal to half the confocal parameter. The optical wavenumber in the medium is $k(\omega)$, and the waist spot size is $W_0 = \sqrt{2z_r/k(\omega)}$.[68] The electric-field strengths in the center of the focus are determined by E_{g10} and E_{g20}. In the above equation, the frequency dependence of the optical wavenumber has been approximated by a Taylor expansion ($k(\omega+\omega_T/2) \simeq k(\omega) + (\omega_T/2)\frac{\partial k}{\partial \omega}(\omega)$).

In equations 4.2 and 4.3, the two beams have an identical beam waist and an identical focus length. This is an approximation, since the focus length and the beam waist depend on the wavenumber, and the wavenumber of the two beams is not the same. However, the differences are very small, since their frequencies are almost equal.

The induced second-order polarization in non-dispersive media is given by[69]

$$\begin{aligned} P_g(t,x,y,z) &= \epsilon_0 \chi^{(2)} E^*_{g1}(t,x,y,z) E_{g2}(t,x,y,z) \\ &= \frac{\epsilon_0 \chi^{(2)} z_r^2 E^*_{g10} E_{g20}}{\left(z^2+z_r^2\right)} \exp\left\{ j\omega_T t - j\omega_T \frac{\partial k}{\partial \omega}(\omega) z \left(1+\frac{1}{2}\frac{x^2+y^2}{z^2+z_r^2}\right) \right. \\ &\quad \left. - z_r k(\omega)\frac{x^2+y^2}{z^2+z_r^2}\right\}, \end{aligned} \tag{4.4}$$

where we have again disregarded the tensor character of the susceptibility. To obtain the polarization at the difference frequency, the electric field of beam 2

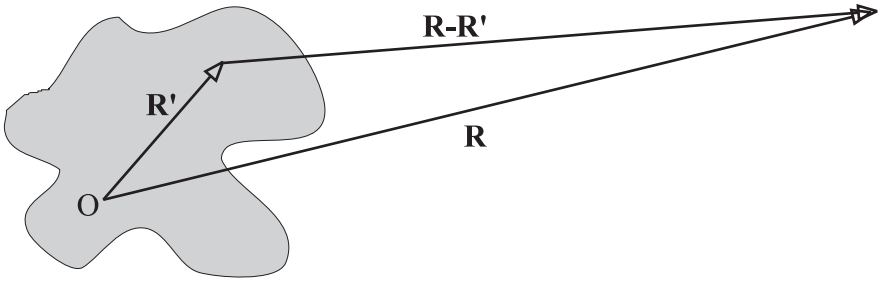

Figure 4.3: Geometry used to calculate the radiation produced by a limited area (grey) with an arbitrary distribution of currents and currents. O indicates the origin, **R'** the generation point and **R** the observation point.

was multiplied by the complex conjugate of the electric field of beam 1. The polarization at the sum frequency, which we do not use in this calculation, can be obtained by multiplying the field without the complex conjugation ($P_g = \epsilon_0 \chi^{(2)} E_{g1} E_{g2}$).

4.2.2 Radiation integral

We calculate the electric field radiated by an arbitrary distribution of charges and currents in the far-field approximation. The far-field approximation means that the distance between our observation point and the region with charges and currents is much larger than both the size of this region and the wavelength of the radiated field. The electric field generated by an arbitrary distribution of charges and currents (figure 4.3) is given by[70]

$$\begin{aligned}\mathbf{E}(t,\mathbf{R}) = \frac{1}{4\pi\epsilon_0\epsilon_r}\iiint \mathrm{d}\mathbf{R}' \Bigg\{ &\frac{\mathbf{R}-\mathbf{R}'}{\|\mathbf{R}-\mathbf{R}'\|^3}\left[\rho\right] + n_T \frac{\mathbf{R}-\mathbf{R}'}{c\|\mathbf{R}-\mathbf{R}'\|^2}\left[\frac{\partial\rho}{\partial t}\right] \\ &- \frac{n_T^2}{c^2\|\mathbf{R}-\mathbf{R}'\|}\left[\frac{\partial \mathbf{J}}{\partial t}\right]\Bigg\},\end{aligned} \tag{4.5}$$

where c is the velocity of light in vacuum, n_T is the terahertz refractive index in the medium. The terahertz relative permittivity of the medium is ϵ_r, and the permittivity of vacuum is ϵ_0. The charge density is ρ and the current density is $\mathbf{J}$. The above equation is generally valid, provided that the medium has a relative permeability of one ($\mu_r = 1$). The vector $\mathbf{R}$ indicates the position for which the electric field is calculated (observation point). After Lorrain,[70] quantities within square brackets are taken at the retarded time $t - n_T\|\mathbf{R} - \mathbf{R}'\|/c$. For instance, $\left[\frac{\partial\rho}{\partial t}\right]$ is equal to $\frac{\partial\rho}{\partial t}\left(t - n_T\|\mathbf{R}-\mathbf{R}'\|/c, \mathbf{R}'\right)$.

In the far-field approximation, the first term in the previous equation can be neglected, since it is proportional to the inverse of the second power of distance and thus decreases more rapidly with distance than the second and third terms, which go as one over the distance. With this approximation the

above equation becomes

$$\mathbf{E}(t,\mathbf{R}) = \frac{n_T}{4\pi\epsilon_0\epsilon_r c}\iiint \mathrm{d}\mathbf{R}'\left\{\left[\frac{\partial\rho}{\partial t}\right]\frac{\mathbf{R}-\mathbf{R}'}{\|\mathbf{R}-\mathbf{R}'\|} - \frac{n_T}{c}\left[\frac{\partial\mathbf{J}}{\partial t}\right]\right\}/\|\mathbf{R}-\mathbf{R}'\|, \quad (4.6)$$

There are two reasons not to be happy with this equation. First, the equation contains both the charge density and the current density. This is unnecessarily complicated, because these quantities are related to each other by charge conservation. Secondly, the direction of the electric field is unclear. In the far field, the electric field should be perpendicular to the propagation direction. However, the first term in equation 4.6 points parallel to the propagation direction, while the second term points in the direction of $\mathbf{J}$, which can be a complex function of the position $\mathbf{R}'$. It is not immediately apparent from equation 4.6, how the parallel component of the second term cancels the first term in the far field. Both issues can be dealt with, using charge conservation to express the time derivative of the charge density in the current density

$$\begin{aligned}\left[\frac{\partial\rho}{\partial t}\right] &= \left[-\nabla'\cdot\mathbf{J}\right]\\ &= -\left(\nabla'\cdot\mathbf{J}\right)\left(t-\frac{n_T}{c}\|\mathbf{R}-\mathbf{R}'\|,\mathbf{R}'\right)\\ &= -\nabla'\cdot\left(\mathbf{J}\left(t-\frac{n_T}{c}\|\mathbf{R}-\mathbf{R}'\|,\mathbf{R}'\right)\right)\\ &\quad+\left(\nabla'\left(t-\frac{n_T}{c}\|\mathbf{R}-\mathbf{R}'\|\right)\right)\cdot\left(\frac{\partial\mathbf{J}}{\partial t}\left(t-\frac{n_T}{c}\|\mathbf{R}-\mathbf{R}'\|,\mathbf{R}'\right)\right)\\ &= -\nabla'\cdot[\mathbf{J}] + \frac{n_T}{c}\frac{\mathbf{R}-\mathbf{R}'}{\|\mathbf{R}-\mathbf{R}'\|}\cdot\left[\frac{\partial\mathbf{J}}{\partial t}\right],\end{aligned} \quad (4.7)$$

where the prime in ∇' indicates that the derivative is with respect to $\mathbf{R}' = (x', y', z')$. It is important to understand the difference between $[\nabla'\cdot\mathbf{J}]$ and $\nabla'\cdot[\mathbf{J}]$. The difference is in the sequence of the substitution of the retarded time and the calculation of the divergence. In $[\nabla'\cdot\mathbf{J}]$, first the divergence is calculated and then the time is replaced with the retarded time. In $\nabla'\cdot[\mathbf{J}]$, first the retarded time is substituted, which means that the time has become dependent on the position $\mathbf{R}'$, the parameter to which the derivative is taken in the divergence.

Substituting the previous equation into equation 4.6 we get

$$\begin{aligned}\mathbf{E}(t,\mathbf{R}) \simeq \frac{n_T^2}{4\pi\epsilon_0\epsilon_r c^2}\iiint \mathrm{d}\mathbf{R}'\Bigg\{&-\frac{c}{n_T}\left(\nabla'\cdot[\mathbf{J}]\right)\frac{\mathbf{R}-\mathbf{R}'}{\|\mathbf{R}-\mathbf{R}'\|}\\ &-\left[\frac{\partial\mathbf{J}}{\partial t}\right]+\frac{\mathbf{R}-\mathbf{R}'}{\|\mathbf{R}-\mathbf{R}'\|}\left(\frac{\mathbf{R}-\mathbf{R}'}{\|\mathbf{R}-\mathbf{R}'\|}\cdot\left[\frac{\partial\mathbf{J}}{\partial t}\right]\right)\Bigg\}/\|\mathbf{R}-\mathbf{R}'\|.\end{aligned} \quad (4.8)$$

We use the approximation $\mathbf{R}-\mathbf{R}' \simeq \mathbf{R}$, except in the expression for the retarded time. This is valid, because the dimensions of the region with currents are much smaller then the distance $\mathbf{R}$ in the far-field approximation. The reason for the exception for the retarded time is that a small variation in the

propagation distance can already causes a phase-change of more that 2π. The following expression for the generated electric field is obtained.

$$\begin{aligned}\mathbf{E}(t,\mathbf{R}) \simeq & -\frac{n_T\hat{\mathbf{r}}}{4\pi\epsilon_0\epsilon_r cr}\iiint \nabla'\cdot[\mathbf{J}]\,\mathrm{d}\mathbf{R}' \\ & -\frac{n_T^2}{4\pi\epsilon_0\epsilon_r c^2 r}\iiint\left[\frac{\partial\mathbf{J}_\perp}{\partial t}\right]\mathrm{d}\mathbf{R}',\end{aligned} \tag{4.9}$$

where $r \equiv \|\mathbf{R}\|$ is the distance from the observation point to the generation region, and $\hat{\mathbf{r}} \equiv \mathbf{R}/\|\mathbf{R}\|$ is a unit vector in the direction from the generation region to the observation point. We have also used $\mathbf{J}_\perp \equiv \mathbf{J} - \hat{\mathbf{r}}\,(\hat{\mathbf{r}}\cdot\mathbf{J})$, which is the projection of $\mathbf{J}$ on the plane perpendicular to $\hat{\mathbf{r}}$. It is logical that $\mathbf{J}$ is projected in this way, since the electric field of radiation in an isotopic medium has to be perpendicular to the propagation direction.

The first term of equation 4.9 equals zero. The volume integral over the divergence of the current density can be rewritten to a surface integral over the current density using Gauss' theorem. This surface integral is zero, because, by definition, the currents vanish at the boundary of the generation region. Using $\mathbf{J} = \partial\mathbf{P}/\partial t$[70] the final equation for the electric field radiated by a polarization distribution is given by

$$\mathbf{E}_{rad}(t,\mathbf{R}) = -\frac{n_T^2}{4\pi\epsilon_0\epsilon_r c^2 r}\iiint\frac{\partial^2\mathbf{P}_\perp}{\partial t^2}\left(t - n_T\|\mathbf{R}-\mathbf{R}'\|/c,\mathbf{R}'\right)\mathrm{d}\mathbf{R}', \tag{4.10}$$

where $\mathbf{P}_\perp$ is, similar to $\mathbf{J}_\perp$, the projection of the polarization on the plane perpendicular to $\hat{\mathbf{r}}$. The equation is easily interpreted. The source of the radiated field is the second time derivative of the polarization. However, only the part of the polarization that is perpendicular to the propagation direction $\mathbf{R}$ contributes to the radiated field.

4.2.3 Generated field

In this section, the field radiated by the nonlinear polarization induced by two monochromatic beams is calculated. For this purpose, we use the expression for the induced nonlinear polarization of section 4.2.1, substitute it in the integral for the radiated field obtained in section 4.2.2, and solve the integral analytically.

If equation (4.4) is substituted into equation (4.10), then we obtain the radiated terahertz electric field

$$\begin{aligned}\mathbf{E}_{rad}(t,\mathbf{R}) = & \frac{\omega_T^2\chi^{(2)}E_{g10}^*E_{g20}z_r^2}{4\pi rc^2}\left(\hat{\mathbf{x}}-\hat{\mathbf{r}}\frac{x}{r}\right)\exp\left(j\omega_T t\right) \\ & \iiint\mathrm{d}\mathbf{R}'\,\frac{1}{z'^2+z_r^2}\exp\left\{-jk_T\|\mathbf{R}-\mathbf{R}'\|\right. \\ & \left.-j\omega_T\frac{\partial k}{\partial\omega}(\omega)z'\left(1+\frac{1}{2}\frac{x'^2+y'^2}{z'^2+z_r^2}\right)-z_r k(\omega)\frac{x'^2+y'^2}{z'^2+z_r^2}\right\}\end{aligned} \tag{4.11}$$

where k_T is the wavenumber at the terahertz frequency, and $\hat{\mathbf{x}}$ is the unit vector along the x-axis. The direction of the induced polarization is chosen to be the $\hat{\mathbf{x}}$ direction. We apply the following approximation

$$\begin{aligned} \|\mathbf{R}-\mathbf{R}'\| &= \sqrt{(x-x')^2+(y-y')^2+(z-z')^2} \\ &\simeq \sqrt{x^2+y^2+z^2} - \frac{xx'+yy'+zz'}{\sqrt{x^2+y^2+z^2}}. \end{aligned} \tag{4.12}$$

This approximation is called the Fraunhoffer approximation in diffraction theory. Note that this approximation for $\|\mathbf{R}-\mathbf{R}'\|$ is one order more accurate than the one used in section 4.2.2. It is necessary to be more accurate, since now $\|\mathbf{R}-\mathbf{R}'\|$ is in the complex exponential, and even small distance differences can cause significant phase differences. If approximation 4.12 is applied to the equation for the generated field (equation 4.11), the result is

$$\begin{aligned} \mathbf{E}_{rad}(x,y,z,t) = {} & \frac{\omega_T^2 \chi^{(2)} E_{g10}^* E_{g20} z_r^2}{4\pi c^2 \sqrt{x^2+y^2+z^2}} \exp\left(j\omega_T t - jk_T\sqrt{x^2+y^2+z^2}\right) \\ & \left(\hat{\mathbf{x}} - \hat{\mathbf{r}}\frac{x}{r}\right) \int_{x'=-\infty}^{\infty} \mathrm{d}x' \int_{y'=-\infty}^{\infty} \mathrm{d}y' \int_{z'=z_1}^{z_2} \mathrm{d}z' \frac{1}{z'^2+z_r^2} \\ & \exp\left\{ jk_T \frac{xx'+yy'+zz'}{\sqrt{x^2+y^2+z^2}} - j\omega_T \frac{\partial k}{\partial \omega}(\omega) z' \left(1+\frac{1}{2}\frac{x'^2+y'^2}{z'^2+z_r^2}\right) \right. \\ & \left. -z_r\left(k(\omega)+\frac{1}{2}\omega_T\frac{\partial k}{\partial\omega}(\omega)\right)\frac{x'^2+y'^2}{z'^2+z_r^2}\right\}, \end{aligned} \tag{4.13}$$

where we have assumed that there is only a nonlinear polarization in the region between the $z' = z_1$ and $z' = z_2$ planes. The integrals over x' and y' are solved with

$$\int_{x=-\infty}^{\infty} \exp\left(jAx - jBx^2 - Cx^2\right)\,\mathrm{d}x = \sqrt{\frac{\pi}{jB+C}} \exp\left(-\frac{1}{4}\frac{A^2}{jB+C}\right), \tag{4.14}$$

which results in

$$\begin{aligned}\mathbf{E}_{rad}(x,y,z,t) = \left(\hat{\mathbf{x}} - \hat{\mathbf{r}}\frac{x}{r}\right)\frac{\omega_T^2\chi^{(2)}E_{g10}^*E_{g20}z_r^2}{4\sqrt{x^2+y^2+z^2}c^2}\exp\left(j\omega_T t - jk_T\sqrt{x^2+y^2+z^2}\right)\\ \int_{z'=z_1}^{z_2}\mathrm{d}z'\frac{1}{k(\omega)z_r + \frac{1}{2}j\omega_T\frac{\partial k}{\partial\omega}(\omega)z'}\\ \exp\left\{jz'\left(k_T\frac{z}{\sqrt{x^2+y^2+z^2}} - \omega_T\frac{\partial k}{\partial\omega}(\omega)\right)\right.\\ \left. - \frac{1}{4}k_T^2\,\frac{x^2+y^2}{x^2+y^2+z^2}\,\frac{z'^2+z_r^2}{k(\omega)z_r + \frac{1}{2}j\omega_T\frac{\partial k}{\partial\omega}(\omega)z'}\right\},\end{aligned} \tag{4.15}$$

This equation can be simplified with a transformation from the (x, y, z) coordinate system to a spherical coordinate system (r, θ, ϕ)

$$\begin{aligned}\mathbf{E}_{rad}(r,\theta,\phi,t) = \mathbf{e}\frac{\omega_T^2\chi^{(2)}E_{g10}^*E_{g20}z_r^2}{4rc^2}\exp\left(j\omega_T t - jk_T r\right)\\ \int_{z'=z_1}^{z_2}\mathrm{d}z'\frac{1}{k(\omega)z_r + \frac{1}{2}j\omega_T\frac{\partial k}{\partial\omega}(\omega)z'}\\ \exp\left\{jz'\left(k_T\cos(\theta) - \omega_T\frac{\partial k}{\partial\omega}(\omega)\right)\right.\\ \left. - \frac{1}{4}k_T^2\sin^2(\theta)\frac{z'^2+z_r^2}{k(\omega)z_r + \frac{1}{2}j\omega_T\frac{\partial k}{\partial\omega}(\omega)z'}\right\}.\end{aligned} \tag{4.16}$$

The direction of the electric field is given by the vector $\mathbf{e}$, where

$$\mathbf{e} = \hat{\mathbf{x}} - \hat{\mathbf{r}}\frac{x}{r} = \begin{pmatrix} 1-\sin^2(\theta)\cos^2(\phi) \\ -\frac{1}{2}\sin^2(\theta)\sin(2\phi) \\ -\frac{1}{2}\sin(2\theta)\cos(\phi)\end{pmatrix}. \tag{4.17}$$

We define $k'_T \equiv \omega_T\frac{\partial k}{\partial\omega}(\omega)$, and make the approximation that $2z_r k(\omega) \gg z'k'_T$. This approximation is valid as long as the absolute value of z_1 and z_2 are much smaller than z_r times $k(\omega)/k'_T$. This is not a very stringent condition, because $k(\omega)/k'_T$ is a large number (≈ 100). Roughly speaking, the approximation is valid as long as the generation region does not extent far beyond the

pump focus. We get the following expression

$$\begin{aligned}\mathbf{E}_{rad}(r,\theta,\phi,t) \simeq \mathbf{e}&\frac{\omega_T^2\chi^{(2)}E_{g10}^*E_{g20}W_0^2}{8rc^2}\exp\left(j\omega_T t - jk_T r\right)\\ &\int_{z'=z_1}^{z_2} \mathrm{d}z' \exp\left\{jz'\left(k_T\cos(\theta) - k_T'\left(1-\frac{k_T^2}{8k^2(\omega)}\sin^2(\theta)\right)\right)\right.\\ &\left.-\frac{1}{4}k_T^2\sin^2(\theta)\frac{z_r}{k(\omega)}\left\{1+\frac{z'^2}{z_r^2}\left(1+\frac{k_T'^2}{k(\omega)^2}\right)\right\}\right\}\\ \simeq \mathbf{e}&\frac{\omega_T^2\chi^{(2)}E_{g10}^*E_{g20}W_0^2}{8rc^2}\exp\left(j\omega_T t - jk_T r\right)\\ &\exp\left(-\frac{1}{4}k_T^2\sin^2(\theta)\frac{z_r}{k(\omega)}\right)\\ &\int_{z'=z_1}^{z_2} \mathrm{d}z' \exp\left\{jz'\left(k_T\cos(\theta)-k_T'\right) - \frac{1}{4}k_T^2\sin^2(\theta)\frac{z'^2}{k(\omega)z_r}\right\},\end{aligned} \tag{4.18}$$

where in the second step we have used that $k_T \ll k(\omega)$ and $k_T' \ll k(\omega)$. The integral over z' can be solved analytically, which results in

$$\begin{aligned}\mathbf{E}_{rad}(r,\theta,\phi,t) \simeq \mathbf{e}&\frac{\omega_T^2\chi^{(2)}E_{g10}^*E_{g20}W_0^2}{8rc^2}\exp\left(j\omega_T t - jk_T r\right)\frac{\sqrt{\pi k(\omega)z_r}}{k_T\sin(\theta)}\\ &\exp\left(-\frac{1}{4}k_T^2\sin^2(\theta)\frac{z_r}{k(\omega)} - k(\omega)z_r\left(\frac{k_T\cos(\theta)-k_T'}{k_T\sin(\theta)}\right)^2\right)\\ &\left\{\mathrm{erf}\left(z_2\frac{k_T\sin(\theta)}{2\sqrt{k(\omega)z_r}} - j\sqrt{k(\omega)z_r}\frac{k_T\cos(\theta)-k_T'}{k_T\sin(\theta)}\right)\right.\\ &\left.-\mathrm{erf}\left(z_1\frac{k_T\sin(\theta)}{2\sqrt{k(\omega)z_r}} - j\sqrt{k(\omega)z_r}\frac{k_T\cos(\theta)-k_T'}{k_T\sin(\theta)}\right)\right\},\end{aligned} \tag{4.19}$$

where "erf" stands for the error function. We now have a full description of the radiated field. In the next section we will explore the physical meaning of the expression by looking at two limit cases.

4.2.4 Additional approximations

Case I: Negligible focus effects

We will look at two limits for the expression of the radiated electric field found in the previous section. First, we consider the case that $\max\{|z_1|, |z_2|\}\ k_T \ll$

$\sqrt{2}k(\omega)W_0$. Physically, this condition assures that the variation in the diameters of the pump beams can be neglected within the generation crystal. Under this condition equation 4.19 becomes

$$\begin{aligned}\mathbf{E}_{rad}(r,\theta,\phi,t) \simeq \omega_T^2\chi^{(2)}E_{g10}^*E_{g20}W_0^2\,\mathbf{e}\,\frac{\exp\left(j\omega_T t - jk_T r\right)}{8rc^2} \\ \exp\left(-\frac{1}{4}k_T^2\sin^2(\theta)\frac{z_r}{k(\omega)}\right)\exp\left(\frac{1}{2}j(z_2+z_1)\left(k_T\cos(\theta)-k_T'\right)\right) \\ (z_2-z_1)\,\mathrm{sinc}\left(\frac{1}{2}(z_2-z_1)\left(k_T\cos(\theta)-k_T'\right)\right),\end{aligned} \tag{4.20}$$

where the sinc function is defined as $\mathrm{sinc}(x) \equiv \sin(x)/x$. To obtain equation 4.20, an approximation of the error function is required. This approximation is derived starting from the integral notation of the error function[71]

$$\begin{aligned}\mathrm{erf}(x-jy) &\equiv \frac{2}{\sqrt{\pi}}\int_0^{x-jy}\exp\left(-t^2\right)\,\mathrm{d}t \\ &= \frac{2}{\sqrt{\pi}}\int_0^{-jy}\exp\left(-t^2\right)\,\mathrm{d}t + \frac{2}{\sqrt{\pi}}\int_{-jy}^{x-jy}\exp\left(-t^2\right)\,\mathrm{d}t \\ &= \mathrm{erf}(-jy) + \frac{2}{\sqrt{\pi}}\exp\left(y^2\right)\int_0^{x}\exp\left(-t'^2+2jyt'\right)\,\mathrm{d}t',\end{aligned} \tag{4.21}$$

which can be approximated by

$$\begin{aligned}\mathrm{erf}(x-jy) &\simeq \mathrm{erf}(-jy) + \frac{2}{\sqrt{\pi}}\exp\left(y^2\right)\int_0^{x}\exp\left(2jyt'\right)\,\mathrm{d}t' \\ &= \mathrm{erf}(-jy) - \frac{j}{\sqrt{\pi}y}\exp\left(y^2\right)\left(\exp(2jxy)-1\right),\end{aligned} \tag{4.22}$$

for arbitrary real y and $|x| \ll 1$.

Equation 4.20 can be further simplified by going to a new coordinate system (r', θ', ϕ'), which is translated a distance $(z_1+z_2)/2$ in the pump propagation direction. This new coordinate system has its origin in the center of the generation crystal, instead of in the center of the pump focus. In the new system, the radiated electric field can be written as

$$\begin{aligned}\mathbf{E}_{rad}(r',\theta',\phi',t) \simeq \mathbf{e}\,\omega_T^2\chi^{(2)}E_{g10}^*E_{g20}W_0^2\exp\left(-\frac{1}{2}j\left(z_1+z_2\right)k_T'\right) \\ \frac{\exp\left(j\omega_T t - jk_T r'\right)}{8r'c^2}\exp\left(-\frac{1}{4}k_T^2\sin^2(\theta')\frac{z_r}{k(\omega)}\right) \\ (z_2-z_1)\,\mathrm{sinc}\left(\frac{1}{2}(z_2-z_1)\left(k_T\cos(\theta')-k_T'\right)\right),\end{aligned} \tag{4.23}$$

where we used the far field approximation $(z_1 + z_2)/2 \ll r$. With this approximation, the coordinate transformation is given by

$$r' = r - \frac{1}{2}(z_1 + z_2)\cos(\theta) \tag{4.24}$$

$$\theta' = \theta \tag{4.25}$$

$$\phi' = \phi \tag{4.26}$$

In the nominator of the fraction of equation 4.20, but not in the complex exponential, r was further approximated to $r = r'$.

Equation 4.23 can be analyzed as follows. The equation contains a constant that includes the frequency of the terahertz electric field (squared), the nonlinearity of the medium ($\chi^{(2)}$), and $E^*_{g10}E_{g20}W_0^2$. The complex factor $\exp(-(z_1 + z_2)k'_T/2)$ is due to the propagation of the pump beams from the center of the pump focus to the center of the generation crystal.

The factor $\exp(j\omega_T t - jk_T r')/r'$ on the second line of the equation represents a spherical wave of which the amplitude depends on the vector **e**. The exponentially decaying factor represents the degree of focussing of the pump beams, and is discussed in more detail in the second half of this section.

The sinc function on the last line of equation 4.23 is related to a process called phase matching. If phase matching is achieved, then the electric fields originating from different z-coordinates in the generation crystal add up constructively in the far field. How well the generation process is phase matched is determined by the phase mismatch, which we define as $k_T\cos(\theta) - k'_T$. Phase matching effects can limit the angles in which generation is possible to a region around $\theta = \arccos(k'_T/k_T)$ for $k_T \geq k'_T$. The maximum and minimum angle that limit the generation cone, which we define as the cone in which the sinc function > 0.5, are given by

$$\theta_{min} = \arccos\left(\frac{k'_T}{k_T} + \frac{3.78}{k_T|z_2 - z_1|}\right) \quad \text{for} \quad \left|\frac{k'_T}{k_T} + \frac{3.78}{k_T|z_2 - z_1|}\right| \leq 1 \tag{4.27}$$

$$\theta_{max,k} = \arccos\left(\frac{k'_T}{k_T} - \frac{3.78}{k_T|z_2 - z_1|}\right) \quad \text{for} \quad \left|\frac{k'_T}{k_T} - \frac{3.78}{k_T|z_2 - z_1|}\right| \leq 1. \tag{4.28}$$

If $k_T/k'_T = 1$ (no phase-mismatch), $k_T = 2\,\pi$ / (100 μm), and $z_2 - z_1 = 0.5$ mm, then $\theta_{max,k} = 16.8°$. So even if the generation is perfectly phase-matched in the forward direction, phase matching effects limit the generation to reasonably small angles. Note that for a zero phase-mismatch equation 4.28 is not defined, which means that θ_{min} is simply zero.

If $k_T/k'_T = 1.05$, $k_T = 2\pi$ / (100 μm), and $z_2 - z_1 = 0.5$ mm, then $\theta_{max,k} = 24.5°$ and $\theta_{min} = 5.8°$. So, even a small phase mismatch can significantly change the angular dependence of the generated terahertz radiation. Also, the radiation in the strictly forward direction ($\theta = 0$) is already reduced by more than a factor of 2.

If $k_T \geq k'_T$, then the phase velocity of the radiated field is smaller than the group velocity of the optical beams. Under this condition, radiation is generated on the cone, which is defined by $k_T\cos(\theta) = k'_T$, and which is called

a Cherenkov cone.[72] This in analog to classical Cherenkov radiation from relativistic charged particles in dielectric media.

Case II: Negligible phase mismatch

We now go back to equation 4.19 and neglect phase matching effects ($k'_T = k_T \cos(\theta)$). Under that condition, the radiated field is given by

$$\mathbf{E}_{rad}(r,\theta,\phi,t) \simeq \mathbf{e}\frac{\omega_T^2 \chi^{(2)} E^*_{g10} E_{g20} W_0^2}{8rc^2} \exp\left(j\omega_T t - jk_T r\right) AB \tag{4.29}$$

with

$$A = \exp\left(-\frac{1}{4}k_T^2 \sin^2(\theta)\frac{z_r}{k(\omega)}\right), \tag{4.30}$$

$$B = \frac{\sqrt{\pi k(\omega) z_r}}{k_T \sin(\theta)}\left\{\mathrm{erf}\left(z_2\frac{k_T \sin(\theta)}{2\sqrt{k(\omega)z_r}}\right) - \mathrm{erf}\left(z_1\frac{k_T \sin(\theta)}{2\sqrt{k(\omega)z_r}}\right)\right\}. \tag{4.31}$$

The factor AB can be viewed as an effective generation length, which can be equal to or smaller than the length of the nonlinear region ($l = z_2 - z_1$), depending on the parameters of the pump foci. We analyze the influence of the focus diameter of the pump beams by considering two cases: a very tight focus, and a very weak focus. When the pump beams are weakly focussed, then the factor A limits the angles over which the induced polarization radiates to a maximum of

$$\theta_{max,a} = \arcsin\left(\frac{1.96}{k_T W_0}\right) \qquad \text{for} \qquad k_T W_0 \geq 1.96, \tag{4.32}$$

where $\theta_{max,a}$ is defined as the angle for which A equals $\frac{1}{2}$. If the pump beams are focussed weakly, then the factor B simply equals z_2 - z_1.

However, if the focus diameter W_0 is much smaller than the crystal length (second case), then the factor B limits the angles over which the induced polarization radiates. For $z_2 = l/2$ and $z_1 = -l/2$ the maximum angle is given by

$$\theta_{max,b} \simeq \arcsin\left(\frac{2.81\, k(\omega) W_0}{k_T l}\right) \qquad \text{for} \qquad k_T l \geq 2.81\, k(\omega) W_0, \tag{4.33}$$

where $\theta_{max,b}$ is defined as the angle for which B/l equals $\frac{1}{2}$.

So in the two limiting cases that the focus is tight or weak, the space angle in which radiation is emitted, can be reduced. Contrary to phase matching, there is no minimum generation angle associated to the degree of focussing. For the strictly forward direction ($\theta = 0$), AB is equal to l regardless of the diameter of the focus. The relation between the pump focus and the effective generation length is further illustrated in figure 4.4, where the factor AB is plotted as a function of the waist of the pump beams. The plot shows five

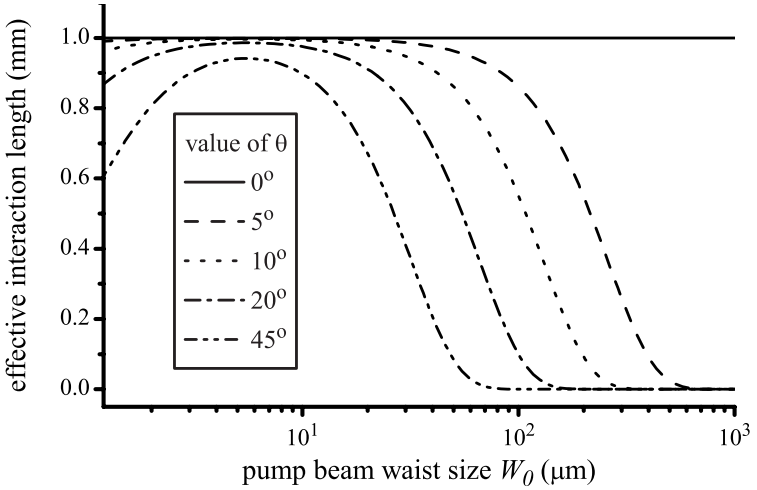

Figure 4.4: Calculated effective generation length (AB) as a function of the pump beam waist size W_0. The values that are used are z_2 = 0.5 mm, z_1 = -0.5 mm, k_T = 2π * 3 / (150 μm), and $k(\omega)$ = 2π * 3 / (1 μm).

lines that correspond to five different angles between the pump beam propagation direction and the propagation direction of the terahertz radiation. Note that, when the pump beams are focused to different beam waists, the factor $E^*_{g10}E_{g20}W_0^2$ in equation 4.29 remains constant. Any decrease of W_0^2 is compensated by an equal increase of $E^*_{g10}E_{g20}$, since the total power in the beams must remain constant.

Physically, the effective generation length AB is determined by the optical beam waist in the generation crystal. At positions in the crystal where this waist is larger than or on the order of the terahertz wavelength, the radiation is restricted to the forward propagation direction. This is more obvious in the limit of crystal lengths much smaller than the pump focus length. In this limit, the beam waist is constant over the length of the crystal, and the factor B can be approximated with

$$B = l \exp\left(-\frac{\left(\frac{1}{2}(z_1+z_2)\right)^2 k_T^2 \sin^2(\theta)}{4 z_r k(\omega)}\right), \tag{4.34}$$

where $l = z_2 - z_1 \ll 2\sqrt{2}z_r/(k_T W_0)$. The effective generation length then becomes

$$\begin{aligned} AB &= l \exp\left(-\frac{1}{4}k_T^2 \sin^2(\theta)\frac{z_r}{k(\omega)}\right) \exp\left(-\frac{\left(\frac{1}{2}(z_1+z_2)\right)^2 k_T^2 \sin^2(\theta)}{4 z_r k(\omega)}\right) \\ &= l \exp\left(-\frac{1}{8}k_T^2 \sin^2(\theta) W^2\right), \end{aligned} \tag{4.35}$$

where $W = W_0\sqrt{1+\left(\frac{1}{2}(z_1+z_2)\right)^2/z_r^2}$ is the diameter of the pump beam at the center of the generation crystal, which is displaced a distance $(z_1+z_2)/2$ from the center of the pump-beam foci. When phase mismatch is neglected, the radiated field strength is thus determined by the diameter of the pump beams at the generation crystal.

In conclusion, we learn from equation 4.29, 4.30 and 4.31, how the beam waist of the pump beams influences the terahertz generation process. This waist is not relevant for the on-axis generation. However, off-axis generation is suppressed, if the average diameter of the pump beam in the generation crystal is larger than the wavelength of the generated terahertz beam.

4.2.5 Effect of focussing in the detection

In common terahertz generation and detection setups, the terahertz radiation is focussed onto the detector, so that the detected electric field is as high as possible. To compare the measurements in such a setup with the theory developed here, the electric field in focus needs to be calculated. Starting point of this calculation is the electric field as a function of angle derived in the previous section. Of course, the electric field in the focus depends strongly on the exact configuration of the optics between the emission and the detection crystal. However, it is still valuable to calculate the electric field for a model system, because it creates some insight in how the electric fields radiated in different directions add up in the focus.

In our model system, the emission source is in the center of a spherical shell, where the half of the shell in the forward propagation direction is perfectly reflective and the other half is perfectly transparent, as is schematically shown in figure 4.5. In this configuration all terahertz energy radiated in the forward direction will be reflected and focussed back to the source. The shell is assumed to be in the far-field of the emitter. This configuration cannot be experimentally reached, because we cannot place both the emission and the detection crystal on the same position. The configuration is, however, a good model for cases where diffraction at the edges of lenses or mirrors and reflections at crystal interfaces is negligible.

The derivation is structured as follows. First, the results of the previous section will be used to obtain the field incident on the spherical shell. Then, the electric field of the reflected wave near the mirror is calculated. Finally, Kirchhoff's integral theorem is used to calculate the reflected electric field in the center of the shell. Kirchhoff's integral relates the electric field on an arbitrary point within a closed surface to the electric field on the closed surface, and is given by[73]

$$E(P_0) = \frac{1}{4\pi}\iint_S \frac{\exp(-jkr_{01})}{r_{01}}\left(\frac{\partial E}{\partial n}(P_1) + jkE(P_1)\right)\mathrm{d}S, \qquad (4.36)$$

where the integral is over all positions P_1 on the closed surface, $\frac{\partial}{\partial n}$ signifies a partial derivative in the outward normal direction at each point of S, and r_{01}

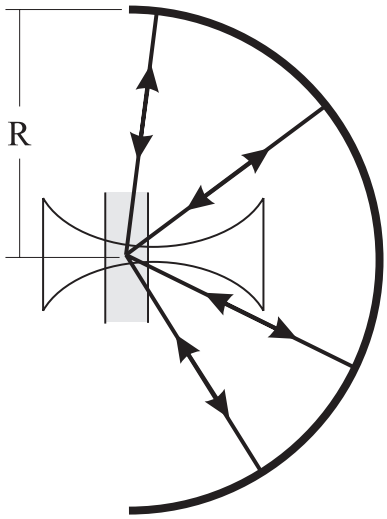

Figure 4.5: Schematic of the focusing of the terahertz radiation. The radiation originates from optical beams focussed into a nonlinear crystal, indicated by the shaded region, and is collected by the reflecting shell of a half sphere, the thick semicircle. The radiation reflects back, and is focussed. Both the thickness of the nonlinear crystal and the optical beam waist are much smaller than the radius of the spherical mirror R, but are drawn larger for clarity.

is the distance between the observation point P_0 and the point on the closed surface S.

The total terahertz electric field parallel to the reflective surface must be zero. The total electric field is equal to the sum of the incident field and the reflected field. The incident field is parallel to the reflective surface on each point of the mirror, since the size of the nonlinear crystal is much smaller than the radius of the spherical mirror. Therefore, the electric field of the reflected wave at the surface is simply the electric field of the incident wave multiplied by -1 ($E_{ref} = -E_{rad}$). For Kirchhoff's integral theorem, not only the electric field at the surface is needed, but also the derivative of the field in the direction of the surface normal. With equation 4.23 the derivative of the incident field is given by

$$\frac{\partial E_{rad}}{\partial n} = \frac{\partial E_{rad}}{\partial r'} = -\left(\frac{1}{R} + jk_T\right) E_{rad} \simeq -jk_T E_{rad} \tag{4.37}$$

where the mirror is assumed to be in the far field of the source, so that the radius of the mirror $R \ll 1/k_T$. If this is substituted into equation 4.36, it is seen that the term for the incident field multiplied by the factor jk_T is cancelled by the derivative of the incident field. This is a very useful property of the Kirchhoff's expression. Only radiation propagating inward (the reflected field) contributes to the integral, and outward propagating radiation (the incident field) can be neglected. For the reflected field at the mirror, we take that

$\partial E_{ref}/\partial n = -jk_T E_{rad}$. The sign is chosen such that reflected field is propagating inward.

Combining the above considerations and equation 4.23 for the radiated field, the electric field exactly in the center of the terahertz focus is found to be

$$\begin{aligned}\mathbf{E}_{foc}(t) \simeq & -jk_T\omega_T^2\chi^{(2)}lE_{g10}^*E_{g20}W_0^2\exp\left(-\frac{1}{2}j\left(z_1+z_2\right)k_T'\right)\\ & \frac{\exp\left(j\omega_T t-2jk_TR\right)}{16\pi c^2}\int_{\theta'=0}^{\pi/2}\mathrm{d}\theta'\,\exp\left(-\frac{1}{4}k_T^2\sin^2(\theta')\frac{z_r}{k(\omega)}\right)\sin(\theta')\\ & \mathrm{sinc}\left(\frac{1}{2}l\left(k_T\cos(\theta')-k_T'\right)\right)\int_{\phi'=0}^{2\pi}\mathrm{d}\phi'\,\mathbf{e}\left(\theta',\phi'\right),\end{aligned} \tag{4.38}$$

where l is the length of the generation crystal $(z_2 - z_1)$.

The integral over ϕ' is easily solved to get

$$\begin{aligned}\mathbf{E}_{foc}(t) \simeq & -j\,\hat{\mathbf{x}}\,k_T\omega_T^2\chi^{(2)}lE_{g10}^*E_{g20}W_0^2\exp\left(-\frac{1}{2}j\left(z_1+z_2\right)k_T'\right)\\ & \frac{\exp\left(j\omega_T t-2jk_TR\right)}{16c^2}\int_{\theta'=0}^{\pi/2}\mathrm{d}\theta'\,\exp\left(-\frac{1}{4}k_T^2\sin^2(\theta')\frac{z_r}{k(\omega)}\right)\sin(\theta')\\ & \mathrm{sinc}\left(\frac{1}{2}l\left(k_T\cos(\theta')-k_T'\right)\right)\left(1+\cos^2(\theta')\right).\end{aligned} \tag{4.39}$$

We rewrite this equation as

$$\begin{aligned}\mathbf{E}_{foc}(t) \simeq & -j\,\hat{\mathbf{x}}\,k_T l\,\omega_T^2\chi^{(2)}E_{g10}^*E_{g20}W_0^2\exp\left(-\frac{1}{2}j\left(z_1+z_2\right)k_T'\right)\\ & \frac{\exp\left(j\omega_T t-2jk_TR\right)}{12c^2}\,\mathrm{func}\left(k_TW_0,\,lk_T,\,\frac{k_T'-k_T}{k_T}\right)\end{aligned} \tag{4.40}$$

with

$$\begin{aligned}\mathrm{func}(C_1,\,C_2,\,C_3) \equiv & \frac{3}{4}\int_{x=0}^{1}\mathrm{d}x\,\exp\left(-\frac{1}{8}C_1^2\left(1-x^2\right)\right)\\ & \mathrm{sinc}\left(\frac{1}{2}C_2\left(x-1-C_3\right)\right)\left(1+x^2\right),\end{aligned} \tag{4.41}$$

where the integral over θ' has been replaced by an integral over x. A function has been introduced by the appropriate name "func". This function, which easily can be solved numerically, depends on three constants, C_1, C_2 and C_3.

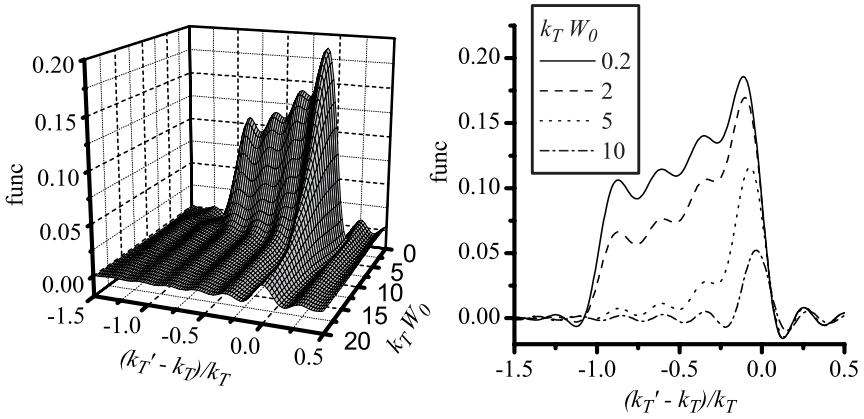

Figure 4.6: Graphs of func($k_T W_0$, 50, $(k'_T - k_T)/k_T$), which plays an important role in equation 4.40 for the focussed radiated field. The right graph shows cross-sections of the 3D graph on the left for different values of $k_T W_0$.

These constants are equal to respectively the pump focus diameter, the length of the generation crystal, and the phase mismatch in the pump propagation direction, each normalized to the terahertz wavenumber. Note that func is defined such that the input and output variables are dimensionless numbers. Furthermore, the function reduces to unity, if C_1 and C_2 go to zero, which corresponds to the limit of a tight focus in a very thin generation crystal. The value of func(C_1,C_2,C_3) can thus be seen as the extent to which the electric field in the center of the terahertz focus $\mathbf{E}_{foc}$ is reduced by focussing and phase matching effects.

We calculate the value of func($k_T W_0$, $k_T l$, $(k'_T - k_T)/k_T$) under different conditions to investigate the effect of focussing and phase-mismatching on the electric field in the terahertz focus. In these calculations, we assume a constant terahertz frequency and thus a constant k_T. Figure 4.6 shows the results of calculations, in which the pump focus diameter and the phase mismatch are varied, while the length of the generation crystal was kept constant. The length of the generation crystal l was fixed at $l = 50/k_T$, which means that l was about 8 terahertz wavelengths long. The calculations show a clear difference in the value of func($k_T W_0$, 50, $(k'_T - k_T)/k_T$) for positive and negative values of $k'_T - k_T$, especially for small values of $k_T W_0$. For small values of $k_T W_0$ figure 4.6 shows substantial values of func($k_T W_0$, 50, $(k'_T - k_T)/k_T$) for $(k'_T - k_T)/k_T$ between -1 and 0, while for positive values of $k'_T - k_T$ the value of func($k_T W_0$, 50, $(k'_T - k_T)/k_T$) rapidly diminishes.

The asymmetry of func($k_T W_0$, 50, $(k'_T - k_T)/k_T$) with respect of the sign of $(k'_T - k_T)/k_T$, can be explained with the off-axis generation (Cherenkov effect) described in section 4.2.4. $k'_T - k_T$ is the phase mismatch in the strictly forward direction ($\theta' = 0$). For negative $k'_T - k_T$, the terahertz generation can be phase matched at an angle, which is not possible for positive $k'_T - k_T$.

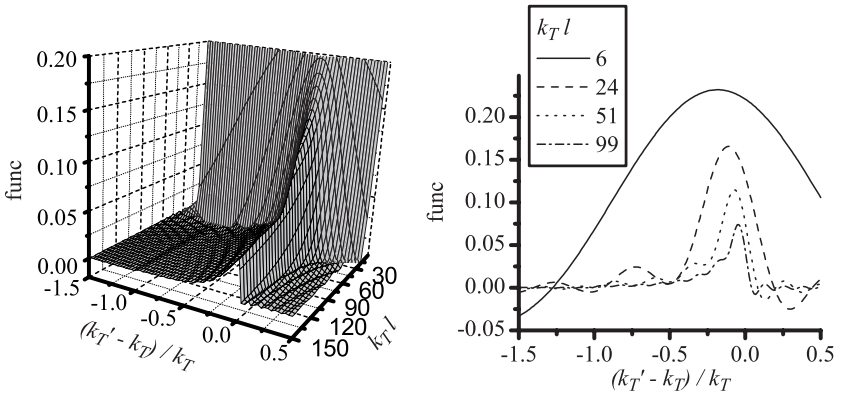

Figure 4.7: Graphs of func(5, $k_T l$, $(k'_T - k_T)/k_T$), which plays an important role in equation 4.40 for the focussed radiated field. The right graph shows cross-sections of the 3D graph on the left for different values of $k_T l$.

This off-axis phase matching is necessary for the terahertz generation to occur efficiently, which explains the calculated asymmetry. For large values of $k_T W_0$, however, off-axis generation is prohibited by focussing effects, which reduce the asymmetry with respect of the sign of $k'_T - k_T$.

Figure 4.7 shows calculations of the value of func(5, $k_T l$, $(k'_T - k_T)/k_T$), where both the crystal length and the phase mismatch in the forward direction are varied. The pump beam waist was kept constant at $W_0 = 5/k_T$. This corresponds to a pump beam waist approximately equal to 0.8 times the terahertz wavelength. Figure 4.7 shows a peak in the plot of func versus $(k'_T - k_T)/k_T$ that becomes narrower and smaller as the crystal length is increased. For longer crystal lengths, the terahertz electric field in focus is thus more sensitive to the phase-mismatch in the forward direction $(k'_T - k_T)$. Note that off-axis generation is strongly suppressed due to the relatively large value of $k_T W_0$. For $k_T W_0 = 5$, off-axis generation is limited to a maximum value of θ' of 23 degrees, as can be calculated with equation 4.32. The increased sensitivity to the phase-mismatch for increasing crystal lengths can be explained by considering the induced phase difference between the contributions to the radiated field from the front and from the back of the crystal. If this phase difference becomes in the order of π, then these contributions will destructively interfere. For small values of $k_T l$ (thin generation crystals), a large value of $(k'_T - k_T)/k_T$ is needed to cause a significant phase difference between the front and the back of the generation crystal. For thin crystals, phase matching thus limits the radiated field only for large values of $(k'_T - k_T)/k_T$. In thick crystals, however, a small value of $(k'_T - k_T)/k_T$ can be sufficient to reduce the electric field in the center of the terahertz focus.

Not only do the widths of the peaks in the right graph of figure 4.7 decrease for increasing $k_T l$; the height of the maxima also decreases. Note that this does *not* mean that the generated terahertz electric field decreases with increasing crystal length. Equation 4.40 for the electric field in the terahertz

focus ($\mathbf{E}_{foc}$) contains an extra factor $k_T l$, which is not included in func($k_T W_0$, $k_T l$, $(k'_T - k_T)/k_T$). The value of func($k_T W_0$, $k_T l$, $(k'_T - k_T)/k_T$) can thus be interpreted as a generation efficiency *per unit of crystal length*. This efficiency indeed decreases for increasing crystal length, because of the narrowing of the generation cone defined by equations 4.27 and 4.28.

Concluding, for efficient terahertz generation the pump beam waist should be smaller than the terahertz wavelength so that off-axis generation is possible. Using this off-axis generation efficiently requires a value of the phase mismatch $k'_T - k_T$ that is smaller than zero.

4.2.6 Optical rectification

Up to here, we have investigated terahertz generation by difference-frequency mixing of two monochromatic beams. In this way, terahertz radiation at one single frequency is generated. Another way to generate terahertz radiation is optical rectification, in which a very short optical pulse is focussed in a generation crystal. This optical pulse generates a nonlinear polarization pulse in the crystal by nonlinear effects. This polarization pulse radiates a broadband terahertz pulse.

In the calculation of terahertz generation by optical rectification, the results for monochromatic pump beams will be used. First, the nonlinear polarization caused by an optical pulse is calculated. As we will see, this polarization only differs with respect to the polarization created by the monochromatic pump beams by a position-independent constant. This means that we can use the results describing the monochromatic-pump case for the pulsed-pump case by simply making the appropriate change in the constants.

Equation 4.4, which gives the induced nonlinear polarization for monochromatic pump beams, changes in the case of broadband sources to[69]

$$\tilde{P}_g(\omega_T, x, y, z) = \epsilon_0 \sqrt{2\pi} \int_{-\infty}^{\infty} \mathrm{d}\omega \; \chi^{(2)}(\omega, \omega_T - \omega) \tilde{E}_g(\omega, x, y, z) \tilde{E}_g(\omega_T - \omega, x, y, z) \tag{4.42}$$

$$= \epsilon_0 \sqrt{8\pi} \int_{0}^{\infty} \mathrm{d}\omega \; \chi^{(2)}(\omega, \omega_T - \omega) \tilde{E}_g(\omega, x, y, z) \tilde{E}_g(\omega_T - \omega, x, y, z), \tag{4.43}$$

where $\tilde{E}_g$ is the Fourier transform of the generating electric field, and $\tilde{P}_g$ is the Fourier transform of the induced polarization. To make the step from equation 4.42 to 4.43, we used that $\chi^{(2)}(\omega_1, \omega_2) = \chi^{(2)}(\omega_2, \omega_1)$. We also used that the pump pulses do not contain terahertz frequency components and that thus $\tilde{E}_g(\omega_T) = 0$ for ω_T in the terahertz range, so that $\int_{-\infty}^{-\omega_T} \mathrm{d}\omega \ldots = \int_{-\infty}^{0} \mathrm{d}\omega \ldots$. Note that the tilde ˜ is used to indicate quantities in the frequency domain. We

define the Fourier transform as

$$\tilde{E}_g(\omega,x,y,z) \equiv \frac{1}{\sqrt{2\pi}} \int_{-\infty}^{\infty} \mathrm{d}t \; E_g(t,x,y,z) \exp\left(-j\omega t\right) \tag{4.44}$$

with the inverse transformation

$$E_g(t,x,y,z) \equiv \frac{1}{\sqrt{2\pi}} \int_{-\infty}^{\infty} \mathrm{d}\omega \; \tilde{E}_g(\omega,x,y,z) \exp\left(+j\omega t\right). \tag{4.45}$$

For the electric field of the broadband generation beam, we write

$$\tilde{E}_g(\omega,x,y,z) = \begin{cases} \tilde{E}_{g0}(\omega)\frac{jz_r}{z+jz_r} \exp\left\{-jk(\omega)\left(z+\frac{1}{2}\frac{x^2+y^2}{z+jz_r}\right)\right\} & \text{if } \omega \geq 0, \\ \tilde{E}_{g0}(\omega)\frac{-jz_r}{z-jz_r} \exp\left\{jk(\omega)\left(z+\frac{1}{2}\frac{x^2+y^2}{z-jz_r}\right)\right\} & \text{if } \omega < 0. \end{cases} \tag{4.46}$$

This is a Gaussian beam, just like equations 4.2 and 4.3, only here the two constant amplitudes E_{g10} and E_{g20} are replaced with the function $\tilde{E}_{g0}(\omega)$, which is the Fourier transform of the electric field right in the center of the pump focus. By definition $k(\omega) = k(-\omega)$. If the above equation is substituted in equation 4.43, and the wavenumber $k(\omega)$ is approximated with a Taylor expansion around the center frequency ω_0, we find that

$$P_g(\omega_T,x,y,z) \simeq \sqrt{8\pi}\epsilon_0 \frac{z_r^2}{z^2+z_r^2} \left(\int_0^{\infty} \mathrm{d}\omega \; \chi^{(2)}(\omega,\omega_T-\omega)\tilde{E}_{g0}(\omega)\tilde{E}_{g0}(\omega_T-\omega) \right) \exp\left\{ -j\omega_T \frac{\partial k}{\partial \omega}(\omega_0) z \left(1+\frac{1}{2}\frac{x^2+y^2}{z^2+z_r^2}\right) - z_r k(\omega_0) \frac{x^2+y^2}{z^2+z_r^2} \right\}. \tag{4.47}$$

This is exactly the same equation as equation 4.4, if we make the replacement

$$\chi^{(2)} E_{g10}^* E_{g20} \exp\left(j\omega_T t\right) \Rightarrow 2\sqrt{2\pi} \int_0^{\infty} \mathrm{d}\omega \; \chi^{(2)}(\omega,\omega_T-\omega)\tilde{E}_{g0}(\omega)\tilde{E}_{g0}(\omega_T-\omega). \tag{4.48}$$

This means that the complete derivation of the radiation terahertz field is the same for a pulsed pump beam as for the two monochromatic pump beams. From the equation for the monochromatic beams, it is possible to obtain the equation for a pulsed pump beam by the above parameter replacement. Equation 4.40 can therefore directly be used to get the terahertz electric field, radiated by a pulsed pump beam and then focussed

$$\tilde{E}_{foc}(\omega_T) \simeq -\frac{1}{6}\sqrt{2\pi} j \frac{\omega_T^2 k_T l W_0^2}{c^2} \left(\int_0^{\infty} \mathrm{d}\omega \; \chi^{(2)}(\omega,\omega_T-\omega)\tilde{E}_{g0}(\omega)\tilde{E}_{g0}(\omega_T-\omega) \right) \exp\left(-2jk_T R - \frac{1}{2} j \left(z_1+z_2\right) k_T' \right) \operatorname{func}\left(k_T W_0,\, l k_T,\, \frac{k_T'-k_T}{k_T} \right), \tag{4.49}$$

provided that $\omega_T \geq 0$. The values of $\tilde{E}_{foc}(\omega_T)$ for negative ω_T are determined by $\tilde{E}_{foc}(\omega_T) = \tilde{E}^*_{foc}(-\omega_T)$, because the terahertz electric field in the time domain has, of course, to be real.

The electric field of a Gaussian, bandwidth limited pump pulse in the center of the pump focus is defined as

$$E_{g0}(t) \equiv E_{g0} \exp\left(j\omega_0 t - 2\ln(2)\left(\frac{t}{\tau_0}\right)^2\right) \tag{4.50}$$

with the following Fourier transform

$$\tilde{E}_{g0}(\omega) = E_{g0}\frac{\tau_0}{2\sqrt{\ln(2)}} \exp\left(-\frac{\tau_0^2\left(\omega-\omega_0\right)^2}{8\ln(2)}\right), \tag{4.51}$$

where τ_0 is the full width at half maximum duration of the pump pulse intensity.

We express our final equation of this section in measurable quantities. Therefore, the electric field of the optical beam E_{g0} is related to power in the beam, which can be easily measured. This is done by integrating the square of the electric field, as defined in equation 4.46 and 4.49, over ω, x and y. The result of this integration is proportional to the energy in one pulse. In practice, ultrafast laser systems emit trains of pulses. The average power of such a train equals the energy in one pulse divided by the pulse repetition rate f_{rep}, and is given by

$$P_{avr} = \frac{\pi^{3/2} W_0^2 \tau_0 f_{rep} E_{g0}^2 c\varepsilon_0 n}{4\sqrt{2\ln 2}}, \tag{4.52}$$

where n is the refractive index for the optical pulse, which is taken to be a constant.

If we combine equation 4.49, 4.51 and 4.52, we finally reach an equation for the electric field strength of the focussed radiation from an optical rectification process

$$\begin{aligned}\tilde{E}_{foc}(\omega_T) \simeq -\frac{1}{3\sqrt{\pi}} j \frac{\omega_T^3 l}{c^4\varepsilon_0}\chi^{(2)}\frac{P_{avr}}{\tau_0 f_{rep}} \exp\left(-\frac{\tau_0^2\omega_T^2}{16\ln(2)}\right) \\ \exp\left(-2jk_T R - \frac{1}{2}j\left(z_1+z_2\right)k'_T\right) \operatorname{func}\left(k_T W_0,\, lk_T,\, \frac{k'_T-k_T}{k_T}\right),\end{aligned} \tag{4.53}$$

where the second order susceptibility $\chi^{(2)}$ has been assumed to be constant within the bandwidth of the pump pulse.

In experiments, one usually wishes to make the detected electric field as large as possible. In this context, we highlight a few properties of the above equation. For small values of ω_T, both $\exp(-\tau_0^2\omega_T^2/(16\ln(2)))$ and $\operatorname{func}(k_T W_0,\, lk_T,\, (k'_T - k_T)/k_T)$ reduce to one. Under that approximation, the generated

field is proportional to ω_T^3. This means that optical rectification is not a very efficient method to generate low-frequency (for instance < 100 GHz) radiation. Furthermore, the electric field is proportional to the average power of the optical beam P_{avr}, which is expected for a second-order nonlinear process. One would like the average power to be a high as possible, but practical issues, such as damage thresholds, limit the average power of almost all ultrafast laser sources to about 1 W. The repetition rate f_{rep}, however, varies orders of magnitude (1 kHz - 100 MHz) between different ultrafast laser systems. In low-repetition-rate systems the peak optical fields are stronger, which results in higher terahertz electric fields.

The duration of the optical pulses τ_0 is also an important parameter in equation 4.53, and influences the radiated field in two ways. First, a shorter pulse duration corresponds to a broader optical spectrum and thus also a broader terahertz spectrum. This is taken into account by the exponential factor in the first line of equation 4.53. Second, a shorter optical pulse has a higher peak electric field, which make the terahertz electric field inversely proportional to τ_0. It is clearly advantageous to have a very short pulse duration. Commercial Ti:Sapphire lasers can produce pulses with pulse durations down to 10 fs.

The terahertz electric field is proportional to the length of the generation crystal l, and therefore long generation crystals seem profitable. However, if $l \gg 1/k_T$, then the effect of any further increase in length will be countered by a decrease of func. Since k_T is a strong function of the terahertz frequency ω_T, this can result in an effective bandwidth limitation. Such a bandwidth limitation can also arise from the other two parameters of func, $k_T W_0$ and $(k'_T - k_T)/k_T$, which also depend on the terahertz frequency.

4.2.7 Conclusion

We have calculated the angular dependent field radiated by an optical beam with a cross-section with a Gaussian spatial profile. The beam consists of a train of ultra-fast pulses with a temporal intensity profile which is also Gaussian. We find an expression for the terahertz electric field in focus after focussing of this radiated field. From this expression, we draw the following conclusions.

The diameter of the optical beam determines to which extent the radiated field is limited to directions close to the propagation axis of the probe beam. No such limitation exists if the optical beam diameter is much smaller than the wavelength of the radiated field. If not, then the radiated field is limited to a solid angle around the pump propagation axis, which decreases in size for increasing optical beam diameter. Due to this limitation, the total field in focus will also decrease.

The length of the generation crystal determines the extent to which the terahertz radiation is limited by phase-matching. Provided that the phase velocity for the terahertz radiation is equal to or smaller than the group velocity for the optical beam, there is an angle for which the generation is perfectly phase-matched. If the length of the generation crystal becomes larger than the

wavelength of the radiation, then the radiation process will become increasingly limited around the perfectly phase-matched direction. As long as the generation crystal is much smaller than the terahertz wavelength, the terahertz electric field in focus is proportional to the crystal length. However, for longer generation crystals, the phase-matching effect can completely suppress any radiated field.

The duration of the optical pulse has two effects. For low terahertz frequencies, the terahertz field in focus is inversely proportional to the pulse duration. At high frequencies, the field strength is decreased, when the pulse duration times the terahertz frequency approaches unity.

4.3 Optical rectification measurements

Optical rectification, or $\chi^{(2)}$ pulse generation, is an important and frequently-used method to generate broadband terahertz radiation. As discussed in the previous section, phase matching plays an important role in the optical rectification process. Due to phase matching, terahertz radiation originating from different parts of the crystal will not necessarily add up constructively, which has a large influence on the size and shape of the generated terahertz pulse.

Many experimentalists tend to avoid phase-matching issues by the use of a very thin generation crystal.[74,75] In a thinner crystal, a difference between the optical group velocity and the terahertz phase velocity will cause a smaller phase difference, thus limiting the amount of destructive interference. However, a thin crystal is not the best choice for each application. First of all, decreasing the crystal thickness results in a decrease of the emitted terahertz power. Secondly, terahertz radiation emitted from thin crystals will suffer strongly from Fabry-Perot reflections at the crystal interfaces. Finally, thin crystals can be very fragile, which can be a drawback in commercial applications.

For a designer of a broadband terahertz system based on optical rectification it is important to understand how the generated terahertz spectrum is affected by phase matching. There have been previous reports on this issue focussing on both theory[60,62] and experiments.[33,64,76] However, none of the reported experiments show how the phase matching effects depend on the terahertz frequency, the wavelength of the generating pulse and the thickness of the generation crystal.

We investigated the role of phase mismatch on the generated terahertz pulse shape by using generation crystals of different thicknesses. In contrast to the previous section, which provides an extensive *theoretical* discussion, this section presents an *experimental* study of optical rectification. We find that changing the crystal thickness has a large effect on both the shape of the terahertz pulse and of the spectrum, which contains an oscillatory structure. Varying the pump-wavelength changes the oscillation period in the spectrum, in excellent agreement with a theoretical model that we use to describe our measurements. These results significantly increase our understanding of the generation of terahertz radiation by optical rectification, and can be used to

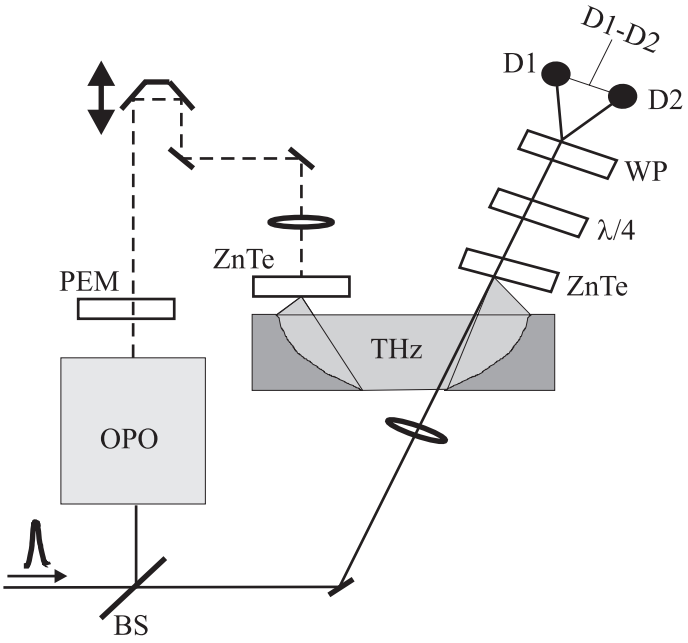

Figure 4.8: Schematic picture of the measurement setup. A beamsplitter (BS) splits the Ti:Sapphire beam (solid lines) into two parts. The larger part is used to pump the optical parametric oscillator (OPO), while the smaller part is used to detect the THz radiation. The beam from the OPO (dashed lines) goes through a photoelastic modulator (PEM) and an optical delay stage and is then focused onto a ZnTe generation crystal. The generated THz beam is first collimated and then focussed by two parabolic mirrors. In this focus the THz electric field is measured with a standard electro-optic detection setup, which consists of a ZnTe detection crystal, a quarter-wave plate ($\lambda/4$), a wollaston prism (WP) and a differential photodetector.

optimize the generation process.

4.3.1 Measurement setup

Figure 4.8 shows a schematic of the measurement setup. A Ti:Sapphire oscillator produces optical pulses with a duration of about 100 fs, a repetition rate of 80 MHz and a wavelength of 810 nm. The beam from this oscillator is split into two parts. The weaker part is used to detect the generated terahertz radiation, while the stronger part is used to pump an optical parametric oscillator (OPO). In the OPO, which is built around a $KTiOPO_4$ (KTP) nonlinear crystal, a parametric process converts the 810 nm, Ti:Sapphire pulses into pulses with a wavelength tunable between 1070 nm and 1240 nm and a pulse duration of about 150 fs. The OPO also produces a second beam, often referred to as the idler beam, but this beam is not used in the experiments reported here.

A photoelastic modulator (PEM) modulates the polarization of the beam

from the OPO. This polarization modulation results in a modulation of the terahertz electric field, which we need for lock-in signal processing. More information regarding photoelastic modulators and lock-in signal processing is given in appendix B. After the PEM, the beam from the OPO goes through an optical delay stage and is then focused onto a ZnTe crystal. The focused pulse generates a polarization in the crystal that follows the intensity envelope of the pulses (optical rectification). This induced polarization radiates a terahertz transient according to $E_{THz} \propto \frac{\partial^2 P}{\partial t^2}$ (see section 4.2.2). The terahertz radiation coming out of the crystal is collimated and then focussed onto a second ZnTe crystal together with the weaker split-off beam from the Ti:Sapphire oscillator. In this second ZnTe crystal, which is 1 mm thick, the terahertz electric field induces a change in the polarization of the Ti:Sapphire beam. This change is measured in a conventional electro-optic detection setup, leading to an electronic signal proportional to the terahertz electric field.[32]

With the above described setup, we have performed two sets of measurements. In the first set, the terahertz electric field was measured in three different generation crystals with thicknesses of 0.5 mm, 1 mm and 4 mm. The wavelength of the beam from the OPO is kept fixed at 1228 nm. In the second set of measurements, the thickness of the generation crystal was 1 mm, and terahertz pulses were generated with pump wavelengths of 1080 nm, 1148 nm and 1228 nm.

4.3.2 Measurement results

Figure 4.9(A-C) shows the power spectra for three different thicknesses of the ZnTe generation crystal, which were calculated from the measured THz electric fields displayed in Fig. 4.9(D-F). In the calculation of the spectra, zeros were added at the end of the time traces to smooth the spectra.

The spectra show that for all three thicknesses the power is very low at low frequencies ($<$ 0.5 THz) and is zero above approximately 2.5 THz. At intermediate frequencies, the effect of phase matching becomes clearly visible in Fig. 4.9(A-C). The spectra show oscillations with a period that decreases as the crystal thickness increases. The oscillations are far less pronounced in the measurement with the 4 mm thick generation crystal, than in the measurements with the other two crystals. In addition, for the 4 mm crystal the oscillations strongly decrease in amplitude above 1.5 THz.

Further insight in the origin of the oscillations shown in Fig. 4.9A-C is obtained by looking at Fig. 4.9F. Remarkably, this measurement shows that the terahertz signal consists of two pulses separated by about 4.5 ps. These pulses are not identically shaped; the second pulse is smaller and clearly contains fewer high-frequency components. Reflections in the generation crystal and the detection crystal have a delay of 78 ps and 21 ps respectively, and thus can not explain the pulses observed in Fig. 4.9F.

Figure 4.10 shows results from the second set of measurements in which we measured the terahertz radiation generated in a 1 mm thick ZnTe crystal for three different wavelengths of the generation beam, 1080 nm, 1148 nm and

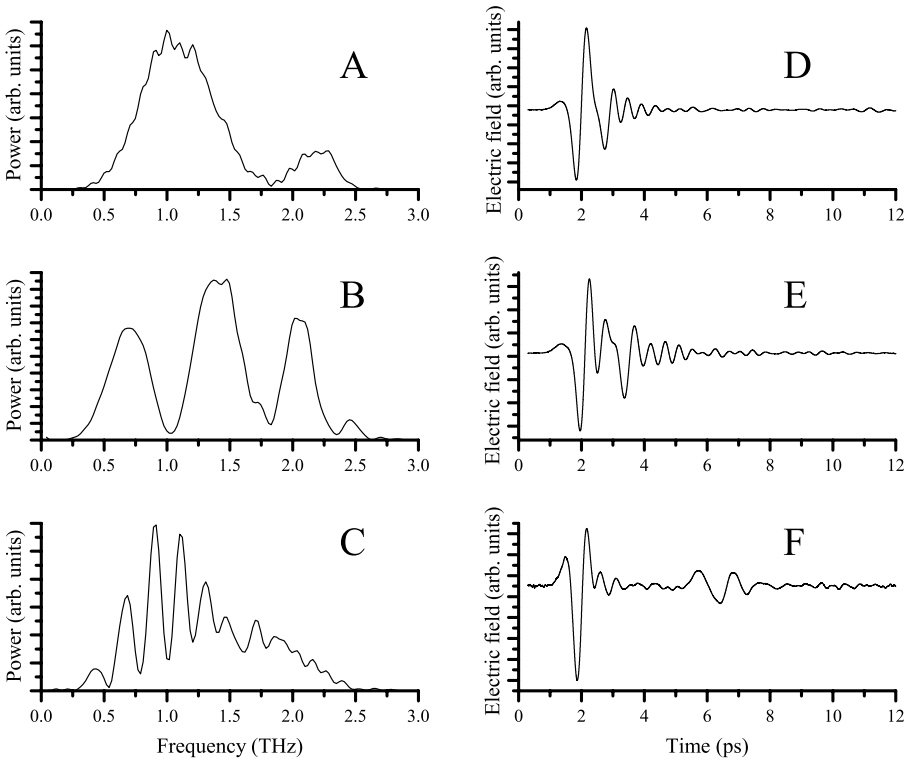

Figure 4.9: The measured terahertz power spectrum with the corresponding time traces. Fig. A and D show respectively the spectrum and the time trace for a 0.5 mm thick generation crystal, Fig. B and E for a 1.0 mm thick crystal, and Fig. C and F for a 4.0 mm thick crystal.

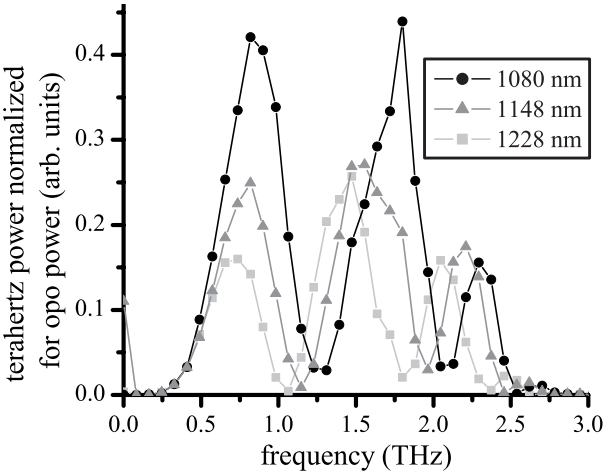

Figure 4.10: Measured power spectra of terahertz radiation generated and detected in two, 1 mm thick, ZnTe crystals. The three spectra are generated with an optical wavelength of 1080 nm, 1148 nm and 1228 nm respectively.

1228 nm. The measured electric fields have been divided by the power delivered by the OPO at each wavelength to enable a quantitative comparison of the terahertz powers generated at different pump wavelengths. For all three wavelengths, the spectra in Fig. 4.10 show strong oscillations. The period of the oscillations increases as the wavelength of the generating beam is decreased. We also observe that the amplitude of the oscillations increases with decreasing wavelength.

4.3.3 Model

The results of the previous section can be described with a simple model that includes phase matching effects in both the generation crystal and the detection crystal, and absorption of terahertz radiation in the generation crystal. We disregard various, less important effects, such as absorption of terahertz radiation in the detection crystal, phase matching in off-axis directions, reflections at the crystal surfaces, and dispersion acting on the generation beam, as it can be shown that these only produce small corrections.

We derive a simplified expression for the spectrum of the terahertz electric field radiated by optical rectification. For on-axis generation with a negligible pump-beam diameter, equation 4.23 gives

$$E_{Trad}(\omega_T) \propto \omega_T^2 l_g \exp\left(\frac{1}{2} j l_g \left(\omega_T \frac{\partial k_g}{\partial \omega} - k_T\right)\right) \operatorname{sinc}\left(\frac{1}{2} l_g \left(\omega_T \frac{\partial k_g}{\partial \omega} - k_T\right)\right) \tag{4.54}$$

where l_g is the thickness of the generation crystal, ω_T is the terahertz radial frequency, k_T is the complex wavenumber of the terahertz beam, and k_g is the wavenumber of the generating beam. Equation 4.54 does not contain a term

representing the limited range of ω_T that can be generated from the pump pulse. This is valid as long as the terahertz wavelength is much larger than the pump pulse length.

Using $k_T \equiv k_{Tr} - j\alpha$, where α is the terahertz absorption coefficient, equation 4.54 can be rewritten to

$$E_{Trad}(\omega_T) \propto \omega_T^2 \, \frac{1 - \exp\left(-\alpha l_g + j\Delta k_g l_g\right)}{\alpha - j\Delta k_g}, \tag{4.55}$$

where the phase mismatch in the generation crystal Δk_g is given by $\left(\omega_T \frac{\partial k_g}{\partial \omega} - k_{Tr}\right)$.

The fraction in Equation (4.55) can be viewed as the sum of two terms that correspond to the contributions from the front and the back of the crystal. The term $1/\left(\alpha - j\Delta k_g\right)$ can be regarded as the contribution from a part of the crystal near the back face with a length on the order of $|\alpha - j\Delta k_g|^{-1}$. The second term corresponds to a contribution from a part with similar length near the front of the crystal. This contribution is subject to absorption in the crystal ($\exp(-\alpha l_g)$) and gets an additional phase due to the phase mismatch ($\exp(j\Delta k_g l_g)$). The additional phase $\Delta k_g l_g$ is, neglecting dispersion in the terahertz regime, linear with the terahertz frequency. A linearly-increasing phase in the frequency domain corresponds to a delay in the time domain. The contribution to the electric field of the second term will thus give rise to a second pulse, delayed in time with respect to the contribution of the first term. However, for small delays the two contributions will (partly) overlap in time, will interfere, and will form one pulse. Note that in the limit of thin crystals ($|\alpha l_g - j\Delta k_g l_g| \ll 1$) Eq. (4.55) becomes $E_{Trad} \propto \omega_T^2 l_g$.

As can be found in literature,[39,55,77] phase matching in the *detection* crystal leads to multiplication of the incident field with $\sin\left(\frac{1}{2}\Delta k_d l_d\right) / \left(\frac{1}{2}\Delta k_d l_d\right)$, where l_d is the length of the detection crystal, and Δk_d is the phase mismatch in the detection crystal. Using this factor and Eq. (4.55), we find that the detected terahertz electric-field spectrum is proportional to

$$E_{Tdet}(\omega_T) \propto \omega_T^2 \, \frac{1 - \exp\left(-\alpha l_g + j\Delta k_g l_g\right)}{\alpha - j\Delta k_g} \, \frac{\sin\left(\frac{1}{2}\Delta k_d l_d\right)}{\frac{1}{2}\Delta k_d l_d}. \tag{4.56}$$

This equation is a strong function of the frequency of the emitted terahertz radiation, since α, Δk_g, and Δk_d depend on the terahertz frequency ω_T.

4.3.4 Discussion

An important aspect of the measurements is the oscillations visible in Fig. 4.9(A-C). These oscillations are due to phase matching in the generation crystal. The mismatch between the group velocity of the generating pulse and the terahertz phase velocity, determines the amount of destructive interference between the terahertz electric fields generated on different positions of the crystal. This phase mismatch is a strong function of the terahertz frequency,

which in non-dispersive media causes oscillations in the spectrum with a fixed period. However, the ZnTe crystal is dispersive, leading to variations in the period of the oscillation, which are most clear in Fig. 4.9B.

For thick crystals, contributions to the terahertz electric field from the center region of the crystal cancel. The 4 mm generation crystal is so thick that the remaining contributions from the crystal regions near the front and the back face are well separated in time, as seen in Fig. 4.9F. Hence, in this limit, the generated terahertz field consists of two well-separated pulses. This limiting shape of the generated terahertz field has been observed before in a study on optical rectification in $LiNbO_3$ and $LiTaO_3$ crystals.[64] The velocity of the terahertz pulse is lower than that of the generating pulse, so that the contribution from the back of the crystal arrives before the contribution from the front.

To explain the periodic feature in the measured spectra, we point out that two, equally shaped pulses in the time domain, give rise to an oscillation in the frequency domain. This remains true, if the separation between the two pulses is such that the pulses (partly) overlap. In figure (4.9) this leads to clear oscillations in the spectra, even for the 0.5 mm thick crystal, where the pulses are barely separated.

The two peaks in Fig. 4.9F are not equally shaped; the pulse from the front of the crystal is smaller and contains fewer high-frequency components. This decreases the modulation depth of the oscillations seen in Fig 4.9C. The main reason for the different shapes of the two pulses in Fig. 4.9F is that the pulse generated at the front of the crystal has to travel all the way through the ZnTe crystal and is thus strongly subject to absorption and dispersion. The power absorption coefficient of ZnTe rises from 2 cm^{-1} at 1 THz to 13 cm^{-1} at 1.6 THz,[78] which cannot be neglected for a 4 mm thick crystal. In addition, the focal length of the generating beam is smaller than the length of the crystal, which implies, in this case, that the diameter of the generating beam is larger at the front of the crystal than it is at the back. This leads to a reduced radiation efficiency at the front, and thus to less pronounced oscillations.

We now consider how the radiated terahertz spectrum depends on the wavelength of the generation pulse. As can be seen in figure 4.10, the period of the oscillations in the spectrum increases as the wavelength of the generation beam decreases. As this wavelength decreases, the phase mismatch in the terahertz generation process becomes smaller, and the minima of the oscillations shift toward higher terahertz frequencies.

Figure 4.11 shows the terahertz intensity spectrum for the generation-beam wavelengths of 1080 nm, 1148 nm and 1228 nm used in the experiments, calculated with Eq. (4.56). For the refractive indices of ZnTe at optical and terahertz frequencies, we have used, respectively, reference[79] and.[80] The terahertz absorption coefficient α is obtained from reference.[78] In the calculation l_d and l_g are both 1 mm and the wavelength of the detection beam is 810 nm.

Comparing Fig. 4.11 with Fig. 4.10, we find that the model accurately predicts the minima of the oscillations in the measured spectra. Closer examination shows that the largest distance between the measured and calculated minima is 62 GHz. This is an excellent agreement, considering the expected uncertainty in the values of the refractive indices.

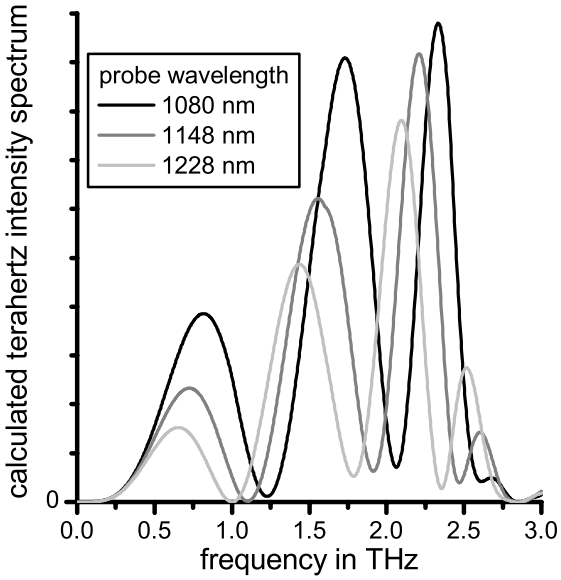

Figure 4.11: Terahertz intensity spectra calculated with Eq. (4.56). Three spectra are shown, corresponding to three different wavelengths for the optical beam used to generated the terahertz radiation.

The values of the oscillation minima in Fig. 4.10 do not reach zero intensity around 2 THz, which contrasts with the results around 1 THz. This feature of our measurement is also in good agreement with the calculated results of Fig. 4.11. Absorption weakens the contributions from the front of the crystal more than the contributions from the back, since the contribution from the front region has to travel longer through the crystal. This means that destructive interference between the front and the back region cannot be complete.

We conclude the discussion of the spectrum of the emitted terahertz radiation by considering the low- and high-frequency edges of the spectrum. From figures 4.9(A-C) it can be seen that at low frequencies, the power decreases to zero. This is due to the conversion from the nonlinearly induced polarization in the crystal to far-field radiation, since the radiated electric field of any polarization is proportional to the second time derivative of the polarization ($E_{THz} \propto \frac{\partial^2 P}{\partial t^2}$). A second time derivative corresponds to a factor $-\omega_T^2$ in the frequency domain, where ω_T is the terahertz radial frequency. The radiation efficiency at low frequencies, where phase matching effects are still negligible, is thus proportional to ω_T^2.

The lack of spectral content roughly above 2.5 THz in Fig. 4.9(A-C) is partly due to phase matching in the detection crystal as is confirmed in our calculations in Fig. 4.11. We emphasize that the detection process, which uses an 810 nm probe beam, is much better phase matched than the generation process. We have calculated that the detection efficiency should decrease with frequency due to phase matching in the detection crystal, until the detection

efficiency reaches zero at 2.8 THz. The detected signal suffers from additional frequency-dependent decreases due to absorption in the detection crystal, and due to the non-zero pulse-length of both the detection and the generation optical pulses. These effects are not included in our model, which explains the difference between measurement and calculation of the oscillation amplitudes at high frequencies.

4.3.5 Conclusion

We have presented measurements and calculations that show how the spectrum of a terahertz pulse generated by optical rectification depends on the thickness of the generation crystal and on the wavelength of the optical, generation pulse. The measured spectra have strong oscillations, which are caused by constructive and destructive interference between contributions to the radiated field from different parts of the crystal. This phase-matching effect is strongly dependent on the thickness of the crystal. In the measurement with a 4 mm thick crystal, all contributions to the radiated field from the central region of the crystal cancel out and only the contributions from regions near the two faces of the crystal survive, leading to the formation of two terahertz pulses, separated in time. The measured spectra depend on the wavelength of the generation beam, because this wavelength determines the phase mismatch.

Chapter 5

Surface plasmon polaritons

Recently, there has been an increased interest in the search for a good waveguide for the transportation of terahertz radiation.[81–86] The latest development in this field is the propagation of terahertz waves along bare metal wires with very little absorption and dispersion.[87,88] These waves are often denoted as surface plasmon polaritons. Indeed, measurements were shown in which two metal wires were combined to form, what could, eventually, become a medical probe.

In some terahertz near-field imaging techniques (chapter 6), bare metal wires, which function as antennas, are used to locally enhance the terahertz electric field. In such imaging techniques, the propagation of terahertz waves over metal wires might play an important role.

Many metal wires, however, are not bare. Thin dielectric layers can often be found on the surface of metal wires, applied intentionally or unintentionally through oxidation or contamination, and the effects of these layers on the propagation of terahertz pulses along the wire are not well-known.

In early literature, the propagation over metal wires is associated with the names of Goubau (Goubau wire) and Sommerfeld (Sommerfeld wave).[89–91] The Goubau wire has seldomly been applied in electronics, because the fields extended too far away from the wire. This caused scattering and dispersion due to coupling of the fields to the surroundings. At terahertz frequencies, however, the field extent is expected to be smaller, which reduces the problem of field coupling to the surroundings. It is therefore useful to evaluate the potential of metal wires as waveguides for terahertz radiation.

This chapter investigates the applicability of electromagnetic waves with frequencies in the terahertz range propagating over coated and uncoated metal wires. Although the theory of propagation of terahertz radiation over coated wires is known to a large extent, we re-derive this theory from first principles for instructive purposes in section 5.1 and 5.2. Section 5.1 describes surface plasmon polaritons on both uncoated and coated, planar metal surfaces, and section 5.2 provides a theoretical description of surface plasmon polaritons on coated metal wires. In section 5.3, we present the first measurements on the influence of propagation over a coated metal wire on the amplitude and

phase of ultrashort terahertz pulses. The measurements show the large dispersive impact of a polyurethane coating on the propagation along a copper wire, which we explain using the theory from section 5.2. The conclusions regarding the applicability of terahertz waves on metal wires, based on both theory and experiment, are given in section 5.4.

5.1 General Properties of plasmons

5.1.1 Surface waves

Electromagnetic wave propagation is described by Maxwell's equations. In optics, one commonly uses electromagnetic waves that propagate in three-dimensional space. However, Maxwell's equations also have solutions that propagate in two-dimensional space such as an interface between two media. These waves can move freely along this interface, but are bound to the surface by an exponential decay of the waves at both sides of the interface.

This subsection investigates under which circumstances electro-magnetic surface waves can exist at an interface between two media. Electromagnetic waves are described by Maxwell's equations in matter[56]

$$\nabla \cdot \mathbf{D} = \rho_f \tag{5.1}$$

$$\nabla \times \mathbf{E} = -\frac{\partial \mathbf{B}}{\partial t} \tag{5.2}$$

$$\nabla \cdot \mathbf{B} = 0 \tag{5.3}$$

$$\nabla \times \mathbf{H} = \mathbf{J}_f + \frac{\partial \mathbf{D}}{\partial t}, \tag{5.4}$$

where ρ_f is the density of free charges, and $\mathbf{J}_f$ is the volume current density due to free charges. The electric displacement vector is related to the electric field vector by $\mathbf{D} = \varepsilon\mathbf{E}$. The $\mathbf{H}$ vector is related to the magnetic field vector by $\mu\mathbf{H} = \mathbf{B}$. ε and μ are respectively the electric permittivity and the magnetic permeability.

We assume that there are no free charges and currents ($\rho_f = 0$, $\mathbf{J}_f = 0$). This does not mean that our theory is only applicable to insulators. Conductors can, under certain conditions, be considered as dielectrics as discussed in appendix C. In that case, the dielectric constant is modified to include the influence of the free carriers on the electric and magnetic fields. We investigate the propagation properties of the Fourier component of the fields with a radial frequency ω. In complex notation, the time dependence of this Fourier component is given by $\exp(j\omega t)$. Using this notation, Maxwell's equations are written as

$$\nabla \cdot \mathbf{D} = 0 \tag{5.5}$$

$$\nabla \times \mathbf{E} = -j\omega\mathbf{B} \tag{5.6}$$

$$\nabla \cdot \mathbf{B} = 0 \tag{5.7}$$

$$\nabla \times \mathbf{H} = j\omega\mathbf{D}. \tag{5.8}$$

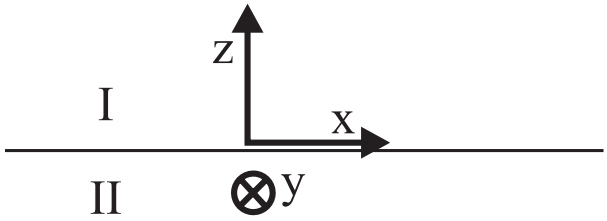

Figure 5.1: Surface wave geometry.

In homogeneous and isotropic media (ε and μ do not vary with position or with field direction), the following wave equations can be deduced from equation 5.5–5.8[56]

$$\nabla^2\mathbf{E} + \omega^2\varepsilon\mu\mathbf{E} = 0 \tag{5.9}$$

$$\nabla^2\mathbf{B} + \omega^2\varepsilon\mu\mathbf{B} = 0. \tag{5.10}$$

We consider surface waves propagating on the interface between two half-spaces (figure 5.1). Half-space I ($z > 0$) has an electric permittivity ε_I and a magnetic permeability equal to that of vacuum μ_0. Half-space II ($z < 0$) has an electric permittivity ε_{II} and a magnetic permeability μ_0. The two half-spaces thus have a different electric permittivity, but identical magnetic permeabilities. As ansatz for the electric and magnetic field of the surface wave in half-space I, we use

$$\mathbf{E}_I = E_I \begin{pmatrix} 1 \\ 0 \\ -jk_x/\kappa_I \end{pmatrix} \exp(-jk_x x - \kappa_I z) \tag{5.11}$$

$$\mathbf{B}_I = \frac{j\,E_I\,\omega\,\varepsilon_I\,\mu_0}{\kappa_I} \begin{pmatrix} 0 \\ 1 \\ 0 \end{pmatrix} \exp(-jk_x x - \kappa_I z), \tag{5.12}$$

which is a valid solution to Maxwell's equations for $z > 0$ if

$$\omega^2\varepsilon_I\mu_0 = k_x^2 - \kappa_I^2. \tag{5.13}$$

The complex wavenumber in the propagation direction k_x determines both the phase velocity and the absorption length of the surface wave. The real part of κ_I is also an important quantity, as it determines how well the wave is bound to the interface. The inverse of the real part of κ_I is equal to the penetration depth of the surface wave in region I, which we define as the distance from the interface for which the fields have decreased a factor $e = 2.718\ldots$. Note that the real part of κ_I should be positive, because the fields would otherwise increase exponentially for $z \to \infty$.

For the fields in half-space II, we use

$$\mathbf{E}_{II} = E_{II} \begin{pmatrix} 1 \\ 0 \\ jk_x/\kappa_{II} \end{pmatrix} \exp(-jk_x x + \kappa_{II} z) \tag{5.14}$$

$$\mathbf{B}_{II} = \frac{-j\, E_{II}\, \omega\, \varepsilon_{II}\, \mu_0}{\kappa_{II}} \begin{pmatrix} 0 \\ 1 \\ 0 \end{pmatrix} \exp(-jk_x x + \kappa_{II} z) \tag{5.15}$$

which is a valid solution to Maxwell's equations for $z < 0$ if

$$\omega^2 \varepsilon_{II} \mu_0 = k_x^2 - \kappa_{II}^2. \tag{5.16}$$

Similar to κ_I, the real part of κ_{II} determines the penetration depth in region II.

The fields need to match at the interface ($z = 0$). Hence, k_x is the same in both regions. Due to equation 5.6 and 5.8, the components of the electric and the magnetic field parallel to the interface must be continuous across the interface. The parallel component of the electric field is continuous if

$$E_I = E_{II}. \tag{5.17}$$

The parallel component of the magnetic field is continuous if

$$E_I\, \varepsilon_I\, \kappa_{II} = -E_{II}\, \varepsilon_{II}\, \kappa_I. \tag{5.18}$$

With equation 5.17 and 5.18, we obtain

$$\varepsilon_I\, \kappa_{II} = -\varepsilon_{II}\, \kappa_I. \tag{5.19}$$

The boundary conditions are fulfilled for a wavenumber in the propagation direction k_x given by (equation 5.13, 5.16 and 5.19)

$$k_x = \omega \sqrt{\frac{\mu_0 \varepsilon_I \varepsilon_{II}}{\varepsilon_I + \varepsilon_{II}}}, \tag{5.20}$$

where the propagation direction is arbitrarily set towards positive values of x. There are two possible set of values for κ_I and κ_{II}. The first set is

$$\kappa_I = j\omega\varepsilon_I \sqrt{\frac{\mu_0}{\varepsilon_I + \varepsilon_{II}}} \tag{5.21}$$

$$\kappa_{II} = -j\omega\varepsilon_{II} \sqrt{\frac{\mu_0}{\varepsilon_I + \varepsilon_{II}}}, \tag{5.22}$$

and the second set is

$$\kappa_I = -j\omega\varepsilon_I \sqrt{\frac{\mu_0}{\varepsilon_I + \varepsilon_{II}}} \tag{5.23}$$

$$\kappa_{II} = j\omega\varepsilon_{II} \sqrt{\frac{\mu_0}{\varepsilon_I + \varepsilon_{II}}}, \tag{5.24}$$

From the ansatz in equations 5.11–5.16 we thus find two valid solutions to Maxwell's equations.* However, only one of these two sets can describe a surface wave. Surface waves, by definition, must decay exponentially on both sides of the $z = 0$ interface. This means that the real parts of both κ_I and κ_{II} have to be positive. It is easy to see that if the real parts of both κ_I and κ_{II} are positive for one set, then they are both negative for the other set. This corresponds to a solution where the fields exponentially *increase* with the distance to the surface, which clearly is not proper behavior for a surface wave.

As an example, we consider a ZnTe-air interface at 1.5 terahertz. The permittivity of air $\varepsilon_I \simeq \varepsilon_0$, and the permittivity of ZnTe $\varepsilon_{II} \simeq \varepsilon_0(3.2 - 0.016j)$.[2,92] Substituting these values in equation 5.20 gives $k_x = 300 - 0.1j$ cm^{-1}. Equations 5.23 and 5.24 give $\kappa_I = 0.4 - 93.7j$ cm^{-1} and $\kappa_{II} = 5.2 + 960j$ cm^{-1}. These values for κ_I and κ_{II} have positive real parts and are thus consistent with a surface wave. In contrast, equations 5.21 and 5.22 give $\kappa_I = -0.4 + 93.7j$ cm^{-1} and $\kappa_{II} = -5.2 - 960j$ cm^{-1}, which is not consistent with a surface wave and can be disregarded.

The above values for the surface wave on a ZnTe-air interface can be interpreted as follows. The real part of κ_I is 0.4 cm^{-1}, which means that the fields extend $1/0.4 = 2.5$ cm in air. In the ZnTe medium, the real part of κ_{II} is such that the penetration depth is 1.9 mm. The field amplitudes of the surface wave thus decay faster in ZnTe than they do in air. The real part of k_x determines the phase velocity of the surface wave, which in this case is approximately equal to the phase velocity of a freely propagating plane wave in air. The imaginary part of k_x determines the absorption length of the surface wave. This absorption length is reasonably long; the surface wave can propagate approximately 10 cm before the field amplitudes are reduced a factor e.

Surface waves are not possible for all values of ε_I and ε_{II}. For some values,† the real part of either κ_I or κ_{II} is negative for both sets of values for κ_I and κ_{II} in equations 5.21–5.24. This means that the fields *increase* exponentially on one side of the interface. In that case, the wave is not bound to the surface.

5.1.2 Plasmon-polaritons on flat surfaces

Surface plasmon-polaritons are surface waves, where charge oscillations are coupled to oscillations of the electromagnetic field. On the one hand, the charges move under influence of an oscillating electric and magnetic field, according to Lorentz's force law. On the other hand, the moving charges change the electric and magnetic field, as described by Maxwell's equations (5.1–5.4). By definition, surface plasmon-polaritons require freely moving charge carriers, which means that they only arise at the surface of conductors.

To describe surface plasmon-polaritons, we use the results of the previous section, which are only valid in the absence of free carriers. However, as discussed in appendix C, it is possible to model metals as dielectrics with

*The total number of solutions is four, if one includes propagation in the negative x-direction.
†for instance, for $\varepsilon_I = \varepsilon_0(1 - 0.2j)$ and $\varepsilon_{II} = \varepsilon_0(1 - 0.1j)$.

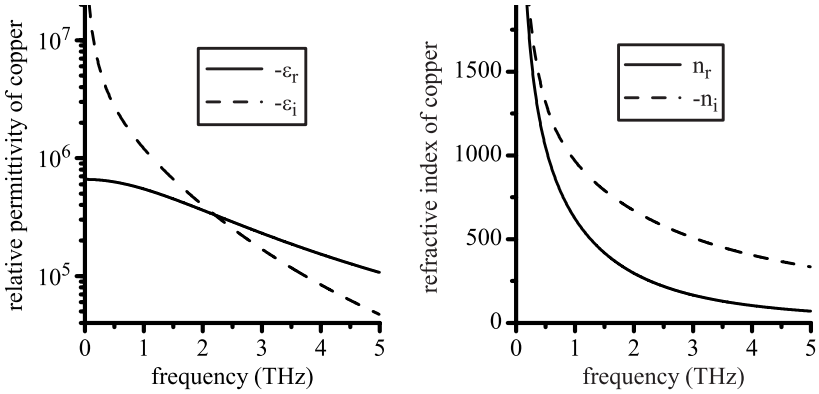

Figure 5.2: Calculated complex relative permittivity and complex refractive index of copper as a function of frequency.

a modified permittivity. This modified permittivity is approximated with a Drude model[93]

$$\varepsilon = \varepsilon_0 \left(\varepsilon_\infty - \frac{f_p^2}{f^2 - jff_\tau} \right), \tag{5.25}$$

where f is the terahertz frequency, f_p is the plasma frequency, which is determined by the free electron density, and f_τ is the damping frequency, which is determined by the electron scattering time. The high-frequency limit of the dielectric constant ε_∞ can be neglected for metals

$$\varepsilon = -\varepsilon_0 \frac{f_p^2}{f^2 - jff_\tau}. \tag{5.26}$$

Reference 93 provides the following Drude model parameters for copper: $f_p = 1787$ THz and $f_\tau = 2.20$ THz. Figure 5.2 shows the frequency dependence of the permittivity of copper calculated with these parameters and equation 5.26. Both the real and the imaginary part of the relative permittivity are negative and large (10^4–10^7) at terahertz frequencies. The real part has a low-frequency limit of -6.6×10^5. The imaginary part tends towards infinity for low frequencies. Below the damping frequency f_τ, the imaginary part is larger than the absolute value of the real part. For frequencies above the damping frequency, the imaginary part is smaller.

The refractive index of copper, equal to the square root of its relative permittivity, is also shown in figure 5.2. With decreasing frequency, both the real and imaginary part of the refractive index increase, while the difference between the two decreases. Note that the refractive-index values are much larger than the typical refractive index of dielectrics at terahertz frequencies, which have values on the order 1–10. The negative value of the imaginary part of the refractive index is a consequence of our choice for an $\exp(j\omega t)$ time dependence. For this time dependence, a negative imaginary part corresponds

to absorption, while a positive imaginary part would correspond to an amplification.

The properties of surface plasmon-polaritons on flat metal-air interfaces are determined by equations 5.20–5.24. We use the second solution, as this solution gives positive real parts for κ_{air} and κ_{metal} and thus describes a surface wave. The permittivity of air is approximated with the value for vacuum, which is assumed to be much smaller than the permittivity of the metal (ε_{metal}). This results in

$$k_x \simeq \frac{\omega}{c}\left(1 - \frac{\varepsilon_0}{2\varepsilon_{metal}}\right) \tag{5.27}$$

$$\kappa_{air} \simeq \frac{-j\omega}{c}\sqrt{\frac{\varepsilon_0}{\varepsilon_{metal}}} \tag{5.28}$$

$$\kappa_{metal} \simeq \frac{j\omega}{c}\sqrt{\frac{\varepsilon_{metal}}{\varepsilon_0}}. \tag{5.29}$$

These equations lead to the following properties of terahertz surface plasmon-polaritons.

- For $\varepsilon_0/\varepsilon_{metal} \ll 1$, the wavenumber of the surface plasmon-polariton k_x is approximately equal to the free-space wavenumber in vacuum ω/c . The plasmon-polariton thus propagates with almost no dispersion and absorption over the metal-air interface.

- κ_{metal} is proportional to the metal refractive index ($= \sqrt{\varepsilon_{metal}/\varepsilon_0}$). Due to the large value of this refractive index, the fields will extend only a short distance into the metal.

- κ_{air} is *inversely* proportional to the metal refractive index. The penetration depth in air will thus be much longer than the wavelength. For 1 THz and the previously mentioned values for copper, $\kappa_{air} = 0.153 - 0.099j$ cm^{-1}. This corresponds to a penetration depth of $1/0.153 = 6.5$ cm.

For a plasmon-polariton propagating on a planar copper-air interface, figure 5.3 shows the frequency dependence of a number of physical properties, which are calculated with equations 5.26–5.29. Both the penetration depth in air and in the metal increase for decreasing frequency. At zero frequency the fields extend infinitely far into both media. In the limit of high terahertz frequencies, the penetration depth in air decrease rapidly, while the penetration depth in copper has an asymptotic value of 27 nm, which is determined by the plasma frequency. Note the large difference between the two media in the value of the penetration depth, which is on the order of centimeters in air and on the order of 50 nm in copper.

The phase velocity of the copper-air surface plasmon-polariton (right graph of figure 5.3) is extremely close to the vacuum velocity of light. The relative difference between the two is on the order of 10^{-6}. This difference increases approximately quadratically with increasing frequency. The absorption length

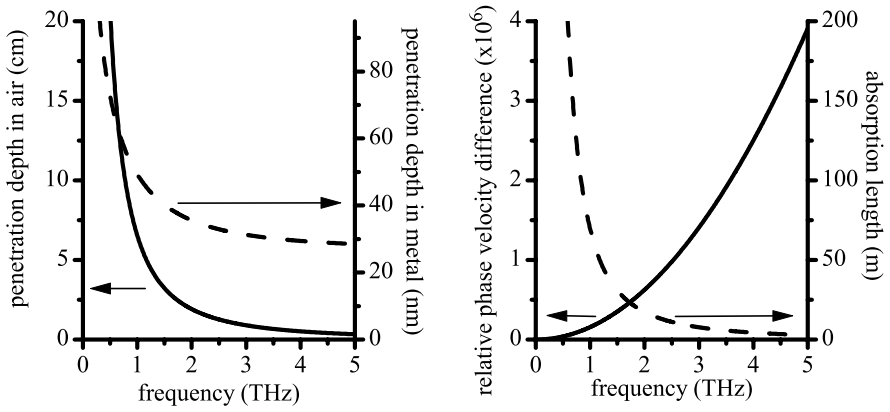

Figure 5.3: Calculated frequency dependence of the properties of a plasmon-polariton propagating on a planar copper-vacuum interface. The left graph shows the penetration depth both in air and in copper. The right graph displays on the left axis the difference between the plasmon-polariton phase velocity and the vacuum velocity of light divided by the vacuum velocity of light. The right graph also shows the absorption length of the plasmon-polariton (right axis).

of the plasmon-polariton, which is defined as the length after which the power in the surface wave is decreased by a factor e, is on the order of tens of meters. This absorption length decreases rapidly with increasing frequency and has a value of about 17 m at 2 THz.

5.1.3 Plasmon-polaritons on coated planar surfaces

Surface plasmon-polaritons are extremely sensitive to dielectric surface coatings, even if the coating thickness is much smaller than the free-space wavelength, which is the wavelength of a plane wave in vacuum with an identical frequency. Such dielectric layers could be applied intentionally, but could also arise from contaminations.

If a dielectric layer is applied to a metal in air, then electromagnetic waves can bounce back and forth between the metal-dielectric and the dielectric-air interface. Due to interference between the upward and the downward moving wave, the electric field component in the propagation direction can be much smaller near the dielectric-metal interface than it is near the the air-dielectric interface. As we will show, this has a large impact on the profile of the fields perpendicular to the interfaces.

For *thin* dielectric layers, the dielectric layer can be neglected, and the penetration depth perpendicular to the metal is determined by the conductance of the metal according to equation 5.28. For *thick* layers, however, the penetration depth of the wave above the dielectric is determined by the thickness and the refractive index of the dielectric layer. The purpose of this section is to estimate what, in this context, constitutes a thin or a thick layer. To be more precise, we calculate the penetration depth for a wave propagating along a di-

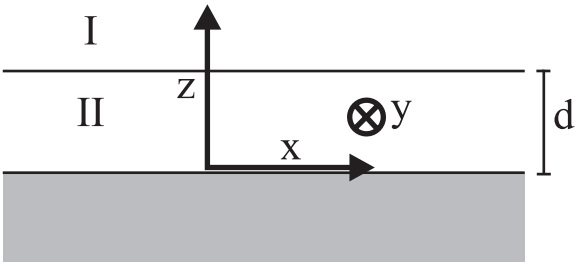

Figure 5.4: Geometry for calculating the properties of a wave propagating along a thin planar dielectric layer (II) between a perfect conductor (grey) and a dielectric half-space (I).

electric coating with a sub-wavelength thickness on a metal with a finite conductivity. From this calculation, we determine for which coating thicknesses the radial profile of the wave is determined by the parameters of the coating, and for which coating thicknesses the radial profile of the wave is determined by the resistivity of the metal.

As a steppingstone towards the case of a coating on a resistive metal, we first consider a dielectric layer with a thickness d on a planar, perfectly-conducting metal (figure 5.4). The dielectric layer extends from $z = 0$ to $z = d$ (region II), and has a permittivity ε_{II}. The permittivity in region I ($z > d$) is given by ε_I. The permeabilities in region I and II are equal to μ_0. Analogously to equation 5.11, the electric field in region I is defined as

$$\mathbf{E}_I = E_I \begin{pmatrix} 1 \\ 0 \\ -jk_x/\kappa_I \end{pmatrix} \exp(-jk_x x - \kappa_I(z-d)). \tag{5.30}$$

The electric field in region II can be viewed as the sum of a plane wave moving in the positive z direction ($\propto \exp(-j\kappa_{II}z)$) and one moving in the negative z direction ($\propto \exp(+j\kappa_{II}z)$). An ansatz for this sum is given by

$$\mathbf{E}_{II} = E_{II}^{+} \begin{pmatrix} 1 \\ 0 \\ -k_x/\kappa_{II} \end{pmatrix} \exp(-jk_x x - j\kappa_{II}z) + E_{II}^{-} \begin{pmatrix} 1 \\ 0 \\ k_x/\kappa_{II} \end{pmatrix} \exp(-jk_x x + j\kappa_{II}z), \tag{5.31}$$

where

$$k_x^2 = \omega^2\varepsilon_I\mu_0 + \kappa_I^2 = \omega^2\varepsilon_I\mu_0 - \kappa_{II}^2. \tag{5.32}$$

The four complex unknowns in these field equations (E_I, E_{II}^{+}, E_{II}^{-} and k_x) are related to each other by the boundary conditions.

The electric field parallel to the surface of a perfect conductor is zero. Therefore $E_{II}^{+} + E_{II}^{-} = 0$. With this relation, the electric field in the dielectric

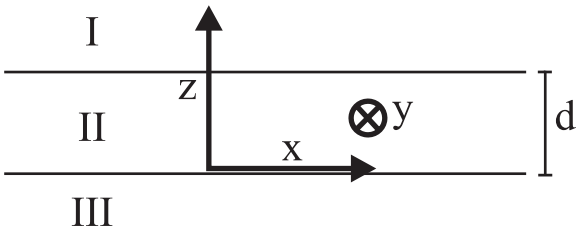

Figure 5.5: Geometry for calculating the properties of a wave propagating along a thin planar dielectric layer (II) between a metal (III) and a dielectric half-space (I).

layer can be written as

$$\mathbf{E}_{II} = E_{II}^{+} \begin{pmatrix} -2j\sin(\kappa_{II} z) \\ 0 \\ -2\cos(\kappa_{II} z) k_x / \kappa_{II} \end{pmatrix} \exp(-jk_x x). \tag{5.33}$$

The electric field in x-direction is continuous at $z = d$ if

$$E_I = -2jE_{II}^{+} \sin(\kappa_{II} d). \tag{5.34}$$

The electric displacement in the z-direction is continuous at $z = d$ if

$$\frac{-j\varepsilon_I k_x}{\kappa_I} E_I = \frac{-2\varepsilon_{II} k_x}{\kappa_{II}} E_{II}^{+} \cos(\kappa_{II} d). \tag{5.35}$$

Combining equation 5.34 and 5.35, we find the relation

$$\frac{\varepsilon_{II} \kappa_I}{\varepsilon_I \kappa_{II}} = \tan(\kappa_{II} d). \tag{5.36}$$

This relation can be solved together with equation 5.32 to get κ_I, which is the inverse of the penetration depth in region I. In the limit of a dielectric layer thickness much smaller than the free-space wavelength, this results in

$$\kappa_I = \omega^2 \mu_0 \frac{\varepsilon_I (\varepsilon_{II} - \varepsilon_I)}{\varepsilon_{II}} d. \tag{5.37}$$

For example if $\omega = 2\pi \times 1$ THz, $\varepsilon_I/\varepsilon_0 = 1$, $\varepsilon_{II}/\varepsilon_0 = 2$, and $d = 1$ μm then $\kappa_I = 2.2$ cm^{-1}. Note the large difference between the thickness of the dielectric layer (1 μm) and the extent of the field outside the layer ($1/2.2 = 0.46$ cm). Although this penetration depth seems large compared to the dielectric layer, it can be small compared to the penetration depth in air perpendicular to an uncoated, imperfectly conducting metal. For copper, for instance, the penetration depth is 6.5 cm, as was calculated in the previous section.

It is clear that a thin coating has a large impact on the propagation over a perfectly conducting metal. With such a coating, a bound surface wave

can exist with a penetration depth in air inversely proportional to the coating thickness. Section 5.1.2 showed that a similar surface wave can exist on an uncoated, resistive metal with a penetration depth in air proportional to metal refractive index. It is therefore logical to assume that the penetration depth in air for a coated, resistive metal is a function of the properties of both the coating and the metal.

We want to determine for which coating thicknesses the parameters for propagation over a coated metal are determined by the coating and for which coating thicknesses they are determined by the conductivity of the metal. Therefore, we calculate the propagation parameters for the geometry in figure 5.5. We assume that the resistivity is small so that the electric field parallel to the metal surface is much smaller than the electric field perpendicular to the metal surface. Note that for a perfect conductor the electric field parallel to the conductor is zero, while the electric field perpendicular to the conductor is, in general, nonzero. Also, we assume that the coating thickness is small so that the phase difference between the top and the bottom of the coating is much smaller than π. Under these conditions, the electric field in the coating ($0 < z < d$) can be approximated with[‡]

$$\mathbf{E}_{II} = \exp(-jk_x x) \begin{pmatrix} \delta E - j\kappa_{II} z E_0 \\ 0 \\ -E_0 k_x / \kappa_{II} \end{pmatrix}, \tag{5.38}$$

where $|\delta E| \ll |E_0|$ and $|\kappa_{II}|d \ll 1$, and

$$\omega^2 \varepsilon_{II} \mu_0 = k_x^2 + \kappa_{II}^2. \tag{5.39}$$

The electric field above the coating ($z > d$) is

$$\mathbf{E}_I = E_I \begin{pmatrix} 1 \\ 0 \\ -jk_x/\kappa_I \end{pmatrix} \exp(-jk_x x - \kappa_I (z-d)), \tag{5.40}$$

with

$$\omega^2 \varepsilon_I \mu_0 = k_x^2 - \kappa_I^2. \tag{5.41}$$

The electric field in the metal ($z < 0$) is

$$\mathbf{E}_{III} = E_{III} \begin{pmatrix} 1 \\ 0 \\ jk_x/\kappa_{III} \end{pmatrix} \exp(-jk_x x + \kappa_{III} z), \tag{5.42}$$

with

$$\omega^2 \varepsilon_{III} \mu_0 = k_x^2 - \kappa_{III}^2. \tag{5.43}$$

These field equations combined with the proper boundary conditions[§] lead to a dispersion relation given by

$$\frac{\kappa_{II}^2 d}{\varepsilon_{II}} - \frac{\kappa_I}{\varepsilon_I} = \frac{\kappa_{III}}{\varepsilon_{III}} \simeq j\omega \sqrt{\frac{\mu_0}{\varepsilon_{III}}}, \tag{5.44}$$

[‡]this equation is derived from equation 5.31 with $\delta E = E_{II}^+ + E_{II}^-$ and $E_0 = E_{II}^+ - E_{II}^-$

[§]The x-component of the electric field and the z-component of the electric displacement must be continuous across both interfaces.

where we used the result from section 5.1.2 that $\kappa_{III} \gg k_x$ so that $\kappa_{III}^2 \simeq -\omega^2 \varepsilon_{III} \mu_0$ (equation 5.43). With equations 5.39, 5.41 and 5.44, we get

$$\begin{aligned} \kappa_I &\simeq -\frac{\varepsilon_{II}}{2\varepsilon_I d} + \frac{\varepsilon_{II}}{2\varepsilon_I d}\sqrt{1 + 4\omega^2(\varepsilon_{II} - \varepsilon_I)\frac{\varepsilon_I^2}{\varepsilon_{II}^2}\mu_0 d^2 - 4j\omega\frac{\varepsilon_I^2}{\varepsilon_{II}\sqrt{\varepsilon_{III}}}\sqrt{\mu_0}d} \\ &\simeq \omega^2(\varepsilon_{II} - \varepsilon_I)\frac{\varepsilon_I}{\varepsilon_{II}}\mu_0 d - j\omega\frac{\varepsilon_I}{\sqrt{\varepsilon_{III}}}\sqrt{\mu_0}. \end{aligned} \tag{5.45}$$

This equation clearly indicates the transition between the limit that the coating can be neglected (equation 5.28) and the limit that the resistivity of the metal can be neglected (equation 5.37). From equation 5.45, it follows that a thin coating can be neglected for the propagation over a metal surface if

$$\frac{\omega d}{c} \ll \left| \frac{\varepsilon_{II}}{\varepsilon_{II} - \varepsilon_I}\sqrt{\frac{\varepsilon_0}{\varepsilon_{III}}} \right| \tag{5.46}$$

This is a very stringent condition. For instance, if the frequency is 1 THz, the medium in region I is air, the coating has a dielectric constant of 4, and the metal is copper, then the condition states that d must be much smaller than 65 nm to neglect the effect of the coating on the propagation of the surface wave. If there is sufficient contrast between the dielectric constant in and above the coating ($\varepsilon_{II}/(\varepsilon_{II} - \varepsilon_I)$ on the order of 1), then condition 5.46 is satisfied if the coating thickness d is much smaller than the penetration depth in the metal. Concluding, even coatings that are much thinner than the free-space wavelength of the radiation can have a large impact on the propagation of surface plasmon-polaritons.

5.2 Terahertz plasmon-polaritons on metal wires

Section 5.1 discussed the propagation of plasmon-polaritons on planar metal surfaces. Plasmon-polaritons can, however, also exist on curved surfaces. In this section, the propagation of plasmon-polaritons on metal wires is discussed. Wire plasmon-polaritons can propagate along the wire, which makes a metal wire a good candidate for a terahertz waveguide. Another possible application of a theory for wire plasmon-polaritons is the modelling for the propagation of electro-magnetic waves over antennas that are long compared to the wavelength of the radiation. Such antennas play an important role in some terahertz near-field imaging techniques (chapter 6), where they are used to locally enhance the terahertz electric field.

5.2.1 Dispersion relation for a cylindrical wire

The dispersion relation is derived for propagation over a coated wire in the cylindrically symmetric geometry shown in figure 5.6. We choose a cylindrical coordinate system, where r is the radial coordinate and ϕ is the azimuthal angle. The axis of a straight metal rod is the z-axis of our coordinate system. The model takes the possible presence of a coating into account with a

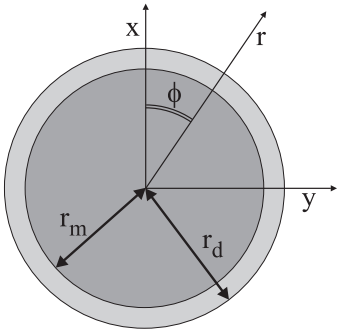

Figure 5.6: Geometry that is used in the calculations for the electromagnetic propagation over a coated metal wire. The metal wire has a radius r_m, and the coating has an outer radius r_d. The axis of the wire coincides with the z axis.

thickness $r_d - r_m$, because section 5.1.3 showed that such a coating can have a large impact on the propagation of a surface plasmon-polariton. The method used here to calculate the dispersion relation is similar to previously-reported methods.[91,94]

The propagation over the wire is determined by the electromagnetic wave equations (equation 5.9 and 5.10). In appendix D it is shown that the solutions of the wave equation in cylindrical coordinates consist of linear combinations of a Bessel function of the first kind and a Bessel function of the second kind. We consider only the so-called transversal magnetic (TM) solution, in which the magnetic field is strictly in the ϕ direction, since it can be shown that only this solution propagates with little absorption.[95]

The electric and magnetic fields of a coated metal wire in air are described by (see appendix D)

$$\text{air } (r > r_d) \begin{cases} B_\phi = [B_1 \mathrm{J}_1(\kappa_a r) + B_2 \mathrm{Y}_1(\kappa_a r)] \exp(-jk'z) \\ E_z = \dfrac{-j\omega\kappa_a}{k_a^2} [B_1 \mathrm{J}_0(\kappa_a r) + B_2 \mathrm{Y}_0(\kappa_a r)] \exp(-jk'z) \\ E_r = \dfrac{\omega k'}{k_a^2} [B_1 \mathrm{J}_1(\kappa_a r) + B_2 \mathrm{Y}_1(\kappa_a r)] \exp(-jk'z) \end{cases} \tag{5.47}$$

$$\text{dielectric } (r_m < r < r_d) \begin{cases} B_\phi = [B_3 \mathrm{J}_1(\kappa_d r) + B_4 \mathrm{Y}_1(\kappa_d r)] \exp(-jk'z) \\ E_z = \dfrac{-j\omega\kappa_d}{k_d^2} [B_3 \mathrm{J}_0(\kappa_d r) + B_4 \mathrm{Y}_0(\kappa_d r)] \exp(-jk'z) \\ E_r = \dfrac{\omega k'}{k_d^2} [B_3 \mathrm{J}_1(\kappa_d r) + B_4 \mathrm{Y}_1(\kappa_d r)] \exp(-jk'z) \end{cases} \tag{5.48}$$

$$\text{metal } (0 < r < r_m) \begin{cases} B_\phi = [B_5 \mathrm{J}_1(\kappa_m r) + B_6 \mathrm{Y}_1(\kappa_m r)] \exp(-jk'z) \\ E_z = \dfrac{-j\omega\kappa_m}{k_m^2} [B_5 \mathrm{J}_0(\kappa_m r) + B_6 \mathrm{Y}_0(\kappa_m r)] \exp(-jk'z) \\ E_r = \dfrac{\omega k'}{k_m^2} [B_5 \mathrm{J}_1(\kappa_m r) + B_6 \mathrm{Y}_1(\kappa_m r)] \exp(-jk'z) \end{cases}, \tag{5.49}$$

where k_a, k_d and k_m are the wavenumbers of respectively air, the dielectric and the metal. J_n is a n'th order Bessel function of the first kind, and Y_n is a n'th order Bessel function of the second kind. The complex constants B_1 to B_6 are to be determined by the boundary conditions. The parameters κ_a, κ_d and κ_m are defined as

$$\kappa_a^2 \equiv k_a^2 - k'^2 \tag{5.50}$$

$$\kappa_d^2 \equiv k_d^2 - k'^2 \tag{5.51}$$

$$\kappa_m^2 \equiv k_m^2 - k'^2 \tag{5.52}$$

Proper behavior for $r \to \infty$ is ensured by setting $B_2 = jB_1$.[95] Under that condition, the field strength at infinity tends to zero. $Y_n(\kappa_m r)$ goes to minus infinity for $r = 0$, so, to avoid a nonphysical singularity in equation 5.49, B_6 must be set to zero. Substituting these values of B_2 and B_6 into equations 5.47 and 5.49 gives

$$\underset{(r > r_d)}{\text{air}} \quad \begin{cases} B_\phi = B_1 H_1^{(1)}(\kappa_a r)\exp(-jk'z) \\ E_z = \dfrac{-j\omega\kappa_a}{k_a^2} B_1 H_0^{(1)}(\kappa_a r)\exp(-jk'z) \\ E_r = \dfrac{\omega k'}{k_a^2} B_1 H_1^{(1)}(\kappa_a r)\exp(-jk'z) \end{cases} \tag{5.53}$$

$$\underset{(0 < r < r_m)}{\text{metal}} \quad \begin{cases} B_\phi = B_5 J_1(\kappa_m r)\exp(-jk'z) \\ E_z = \dfrac{-j\omega\kappa_m}{k_m^2} B_5 J_0(\kappa_m r)\exp(-jk'z) \\ E_r = \dfrac{\omega k'}{k_m^2} B_5 J_1(\kappa_m r)\exp(-jk'z) \end{cases}, \tag{5.54}$$

where $H_n^{(1)} \equiv J_n + jY_n$ is a n'th order Hankel function of the first kind.

B_ϕ and E_z should be continuous across both the air/dielectric and the dielectric/metal interface. This leads to the following dispersion relation.

$$\frac{\kappa_a}{k_a^2}\frac{H_0^{(2)}(\kappa_a r_d)}{H_1^{(1)}(\kappa_a r_d)} = \frac{\kappa_d}{k_d^2}\frac{\frac{\kappa_d}{k_d^2}J_1(\kappa_m r_m)F_1 + \frac{\kappa_m}{k_m^2}J_0(\kappa_m r_m)F_2}{\frac{\kappa_d}{k_d^2}J_1(\kappa_m r_m)F_3 + \frac{\kappa_m}{k_m^2}J_0(\kappa_m r_m)F_4}, \tag{5.55}$$

where

$$F_1 = J_0(\kappa_d r_m)Y_0(\kappa_d r_d) - J_0(\kappa_d r_d)Y_0(\kappa_d r_m) \tag{5.56}$$

$$F_2 = J_0(\kappa_d r_d)Y_1(\kappa_d r_m) - J_1(\kappa_d r_m)Y_0(\kappa_d r_d) \tag{5.57}$$

$$F_3 = J_0(\kappa_d r_m)Y_1(\kappa_d r_d) - J_1(\kappa_d r_d)Y_0(\kappa_d r_m) \tag{5.58}$$

$$F_4 = J_1(\kappa_d r_d)Y_1(\kappa_d r_m) - J_1(\kappa_d r_m)Y_1(\kappa_d r_d). \tag{5.59}$$

This complex set of equations can be simplified, if the coating is sufficiently thin. For $(r_d - r_m) \ll r_m$, $k_d(r_d - r_m) \ll 1$ and $k_d(r_d - r_m) \ll |k_m^2 J_1(\kappa_m r_m)|/$

$|\kappa_m k_d \mathrm{J}_0(\kappa_m r_m)|$ the dispersion relation (equation 5.55) can be approximated with

$$\frac{\kappa_a \mathrm{H}_0^{(1)}(\kappa_a r_d)}{k_a^2 \mathrm{H}_1^{(1)}(\kappa_a r_d)} = \frac{\kappa_m \mathrm{J}_0(\kappa_m r_m)}{k_m^2 \mathrm{J}_1(\kappa_m r_m)} - \frac{\kappa_d^2}{k_d^2}(r_d - r_m). \tag{5.60}$$

From which we can obtain the dispersion relation for an uncoated wire by setting $r_d - r_m = 0$.

5.2.2 Terahertz plasmons on uncoated wires

In this section, the properties of a terahertz plasmon polariton propagating over an uncoated metal wire are calculated with equation 5.60. In particular, we consider the penetration depth both in air and in the metal, the phase velocity and the absorption length. The second part of this section discusses the frequency dependence of these properties, while the third part investigates the dependence of these properties on the radius of the wire. First, however, we discuss the penetration depth in air, which is difficult to define due to the complicated radial dependence of the field in this region.

Penetration depth in air

Equations 5.53 show that the radial dependence of B_ϕ and E_r is governed by $\mathrm{H}_1^{(1)}(\kappa_a r)$, and that the radial dependence of E_z is determined by $\mathrm{H}_0^{(1)}(\kappa_a r)$. Although E_z is, in general, much smaller than E_r, the radial dependence of both $\mathrm{H}_1^{(1)}(\kappa_a r)$ and $\mathrm{H}_0^{(1)}(\kappa_a r)$ have physical importance.

The total power transported in the propagation direction from r to $r + \mathrm{d}r$ is proportional to $B_\phi E_r r \mathrm{d}r$. In equation 5.53, it can be seen that this is proportional to $r|\mathrm{H}_1^{(1)}(\kappa_a r)|^2$. So by studying the radial dependence of $r|\mathrm{H}_1^{(1)}(\kappa_a r)|^2$, it can be found how close to the wire the plasmon polariton transports its energy.

The radial dependence of $r|\mathrm{H}_1^{(1)}(\kappa_a r)|^2$ is quite complicated. In fact one can distinguish two subregions within the air region, where the rate at which the function decays with radial distance is different. Close to the wire ($|\kappa_a r| \ll 1$ but $r \geq r_m$), the function can be approximated with[71]

$$r|\mathrm{H}_1^{(1)}(\kappa_a r)|^2 \simeq \frac{4}{\pi^2 \kappa_a^2 r}. \tag{5.61}$$

Using this approximation, $r|\mathrm{H}_1^{(1)}(\kappa_a r)|^2$ has decayed a factor e at a radial distance from the wire of $er_m \simeq 2.718 r_m$. For a wire with a diameter of 1 mm this corresponds to a distance of 1.36 mm. However, it cannot be concluded that most energy is transported within the er_m radius, since the integral over equation 5.61 from $r = r_m$ to $r = \infty$ diverges. To find the radius within which most energy is transported, the second subregion should be taken into account.

For $|\kappa_a r| \gg 1$, $r|\mathrm{H}_1^{(1)}(\kappa_a r)|^2$ can be approximated with[71]

$$r|\mathrm{H}_1^{(1)}(\kappa_a r)|^2 \simeq \frac{2}{\pi \kappa_a} \exp\left(-2\mathrm{Im}\{\kappa_a\} r\right). \tag{5.62}$$

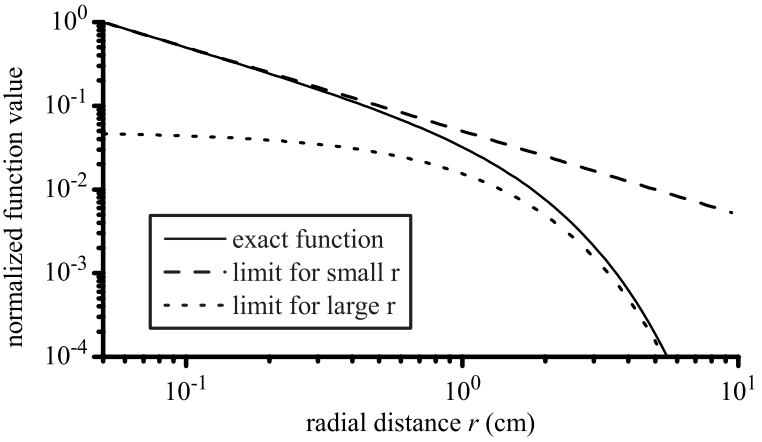

Figure 5.7: The radial dependence of the $r|\mathrm{H}_1^{(1)}(\kappa_a r)|^2$ function that describes the radial decay of the energy transported by a plasmon polariton propagating over a 1 mm thick copper wire at a frequency of 0.54 THz. The function is normalized to 1 at the surface of the wire. Also shown are the two approximations of the function as given by equations 5.61 and 5.62.

Under this approximation, $r|\mathrm{H}_1^{(1)}(\kappa_a r)|^2$ decays a factor e for an increase of the radial distance given by $1/2\mathrm{Im}\{\kappa_a\}$, where $\mathrm{Im}\{\kappa_a\}$ is the imaginary part of κ_a. The energy transported at a certain radial distance thus decreases proportionally to $1/r$, up until $|\kappa_a r| \gg 1$ where an exponential decay sets in.

The radial dependence of $r|\mathrm{H}_1^{(1)}(\kappa_a r)|^2$ is illustrated in figure 5.7. This graph shows $r|\mathrm{H}_1^{(1)}(\kappa_a r)|^2$ as a function of r for a 1 mm thick copper wire at 0.54 THz. The graph also shows the two approximations of this function given by equations 5.61 and 5.62. For low r ($\lesssim 3$ mm) the Hankel function's decay is well described by equation 5.61, which is inversely proportional to the radial distance. However, for high r ($\gtrsim 4$ cm) the Hankel function decays exponentially and is well described by equation 5.62.

We now turn from the radial dependence of B_ϕ and E_r ($\mathrm{H}_1^{(1)}(\kappa_a r)$) to the radial dependence of E_z ($\mathrm{H}_0^{(1)}(\kappa_a r)$). This radial dependence is important, as it determines how far any neighbouring objects should be removed from the wire to avoid a significant change in the propagation of the plasmon polariton. If an object is too close to the wire, then the electric field of the wave propagating on the wire can couple to the object, which can result in scattering, reflections, absorption, and dispersion. To estimate the minimum radial distance between the wire and neighbouring objects, assume that the neighbouring object is a metal cylindrical surface at a distance r_n from the center of the wire. The plasmon polariton will induce a current on this surface proportional to $E_z(r_n)$. The power dissipated per unit length by this current is proportional to $2\pi r_n|E_z(r_n)|^2$. The power absorbed in the neighbouring object should be negligible compared to the power absorbed in the wire, which is

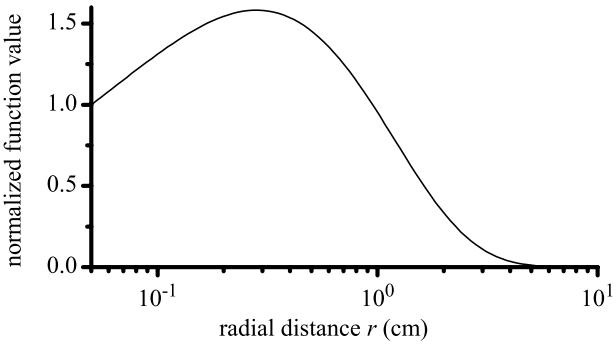

Figure 5.8: The radial dependence of the $r|\mathrm{H}_0^{(1)}(\kappa_a r)|^2$ function, which is relevant to estimate the influence of a neighbouring object, for a plasmon polariton propagating over a 1 mm thick copper wire at a frequency of 0.54 THz. The function is normalized to 1 at the surface of the wire.

proportional to $2\pi r_m|E_z(r_m)|^2$. This provides us with the following condition

$$r_n|\mathrm{H}_0^{(1)}(\kappa_a r_n)|^2 \ll r_m|\mathrm{H}_0^{(1)}(\kappa_a r_m)|^2. \tag{5.63}$$

We thus estimate that the value of $r_n|\mathrm{H}_0^{(1)}(\kappa_a r_n)|^2$, where r_n is the radial distance of the neighbouring object closest to the wire, should have decayed sufficiently to avoid a significant impact of the object on the propagation of a plasmon polariton over the metal wire. Figure 5.8 shows the radial dependence of $r|\mathrm{H}_0^{(1)}(\kappa_a r)|^2$ for a plasmon polariton propagating over a 1 mm thick copper wire at a frequency of 0.54 THz. Surprisingly, the function first increased with radial distance, until for $|\kappa_a r| > 1$ an exponential decay sets in similar to approximation 5.62. Note that the surroundings of the wire should be clear of objects up to distances that are fairly large compared to both the diameter of the wire and the free-space wavelength of the terahertz radiation.

Concluding, the radial dependence of the fields in air of a wire plasmon polariton is complicated, which makes it difficult to define a penetration depth in the region. However, the quantity $1/\mathrm{Im}\{\kappa_a\}$, which determines the exponential decay in both figure 5.7 and 5.8, provides us with a length scale that is relevant both for the radial dependence of the energy transport and for the influence of neighbouring objects. The dependence of this length scale on terahertz frequencies and diameter of the metal wire will be discussed in the next parts of this subsection.

Frequency dependence

Figure 5.9 shows results of calculations using equation 5.60 for a copper wire with a diameter of 1 mm. On the left axis of figure 5.9(a), the relative phase velocity difference, defined as the difference between the plasmon-polariton phase velocity and the vacuum velocity of light divided by the vacuum velocity of light, is plotted as a function of frequency. Although still very small

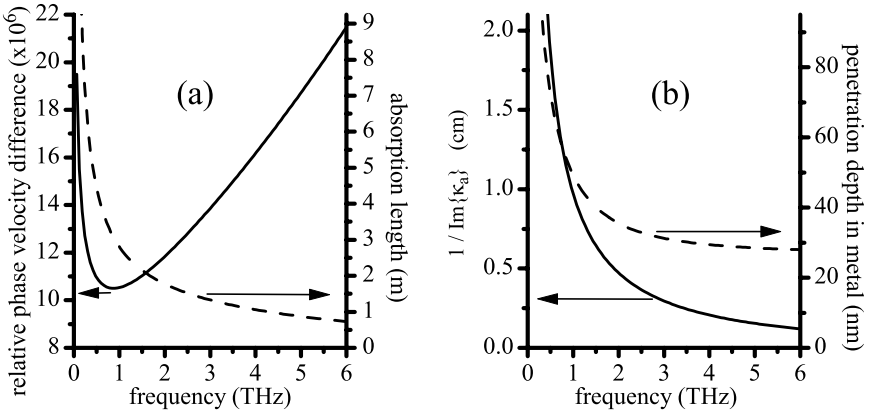

Figure 5.9: Calculated frequency dependence of the properties of a plasmon-polariton propagating on a copper wire with a 1 mm diameter in vacuum. Figure (a) displays on the left axis the difference between the plasmon-polariton phase velocity and the vacuum velocity of light, divided by the vacuum velocity of light. Figure (a) also shows the absorption length of the plasmon-polariton (right axis). Figure (b) shows the penetration depth in copper and $1/\mathrm{Im}\{\kappa_a\}$, which is the exponential decay length at large distances from the wire.

(about 10^{-5}), this difference is about an order of magnitude larger than the relative phase velocity difference for a planar copper surface, which has been plotted in figure 5.3. The relative phase velocity difference rapidly increases with decreasing frequency below 1 THz, which is also not the case for a plasmon-polariton on the flat metal surface.

The absorption length for the copper wire, which is plotted on the right axis of figure 5.9(a), decreases with increasing frequency and has a value of 2.8 m at 1 THz. This is about a factor 25 lower than for the flat copper surface. A plasmon polariton propagating over a wire has thus both more absorption and more dispersion than a plasmon polariton propagation over a planar surface. This is due to the cylindrical geometry of the wire. In the cylindrical geometric, the field lines are radially concentrated towards the wire, which leads to relatively higher fields at the metal interface. Therefore, a larger part of the energy in the wave is transported through the metal, which leads to an increased absorption and dispersion.

We also calculate the penetration depth of the electric field into the metal. The electric field in the metal is proportional to (equation 5.54)[71]

$$\mathrm{J}_0(\kappa_m r) \simeq \sqrt{\frac{1}{2\pi\kappa_m r}}\exp\left(-j\kappa_m r + j\frac{\pi}{4}\right), \tag{5.64}$$

which is valid if the imaginary part of $\kappa_m r$ is negative and has an absolute value much larger than one. This is quite generally true, as the condition implies a diameter of the wire that is much larger than the skin depth of the metal.

We define the penetration depth in the metal wire as the distance over which the absolute value of $\sqrt{r}E_z(r)$ has decreased by a factor e with respect to its value at the metal surface. The square root of r is included in this definition to take the cylindrical geometry into account. In the cylindrical geometry the energy transported at different radial distances is constant, if the field decay is proportional to $r^{-1/2}$. The field strength thus must decrease faster than $r^{-1/2}$ to make the transported energy decrease with increasing radial distance.

With equation 5.64, we find that the penetration depth in metal is equal to one over the imaginary part of κ_m. The penetration depth of copper as a function of frequency is plotted in figure 5.9(b) for a wire diameter of 1 mm. This penetration depth increases for decreasing frequency and is practically identical to the penetration depth for a plasmon polariton on a planar copper surface, which has been shown in figure 5.3.

In figure 5.9(b), $1/\mathrm{Im}\{\kappa_a\}$ is plotted as a function of frequency for a copper wire with a diameter of 1 mm. $1/\mathrm{Im}\{\kappa_a\}$ decreases for increasing frequencies similar to the penetration depth in air of a planar-surface plasmon in figure 5.3. However, the value of $1/\mathrm{Im}\{\kappa_a\}$ is about an order of magnitude smaller than the penetration depth for a planar surface. The energy in a wire plasmon polariton thus travels closer to the metal surface than the energy of a plasmon polariton on a planar surface. From the value for $1/\mathrm{Im}\{\kappa_a\}$ in figure 5.9(b), we estimate that there should be no objects within a radius of about a decimeter around the wire to ensure a free propagation of the surface plasmon polariton.

Dependence on the wire radius

The dispersion relation that governs the properties of a wire plasmon polariton (equation 5.60) depends on the diameter of the wire. Figure 5.10 shows calculations of this dependence for an uncoated copper wire in air with a frequency of 1 THz. The figure shows the relative difference between the phase velocity and the free-space velocity of light, the absorption length and $1/\mathrm{Im}\{\kappa_a\}$, which determines the exponential decay of the field at large radial distances. The penetration depth in the copper wire is not plotted, because its relative variation over the plotted range is negligible ($< 10^{-8}$).

None of the parameters in figure 5.10 reaches the values typical for a plasmon polariton on a flat surface, which have been calculated in section 5.1.2, even for a wire diameter of 1 cm. So even if the circumference of the wire is about a hundred times larger than the free-space wavelength, then the curvature of the wire still has a large impact on the properties of the surface plasmon polariton. In fact, a wire diameter on the order of meters is required to let the properties of the wire plasmon polariton approach that of a planar surface. The curvature of the wire is only negligible if the radius of curvature is much larger than the penetration depth in air of a planar-surface plasmon polariton, which we calculate to be on the order of a decimeter (figure 5.3).

The phase velocity of the wire plasmon polariton decreases with the diameter of the wire. However, this decrease is only significant for thin wires. For a 100 μm wire diameter, the relative difference in the velocity is only 7.6×10^{-5},

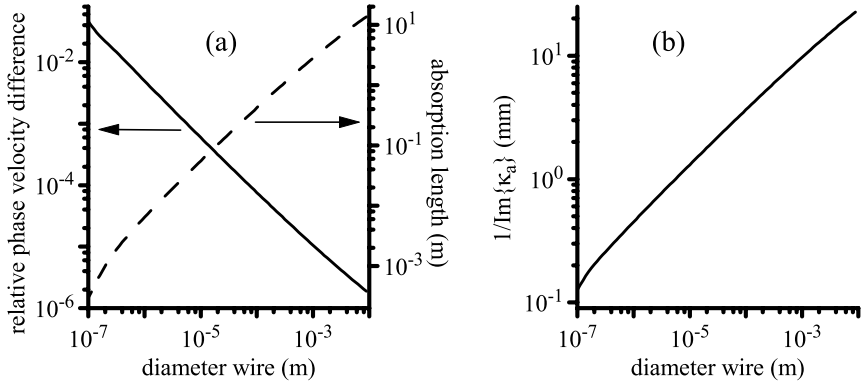

Figure 5.10: Calculated properties of a plasmon-polariton with a frequency of 1 THz propagating on a copper wire in vacuum as a function of the wire diameter. Figure (a) displays on the left axis the difference between the plasmon-polariton phase velocity and the vacuum velocity of light divided by the vacuum velocity of light. Figure (a) also shows the absorption length of the plasmon-polariton (right axis). Figure (b) plots $1/\mathrm{Im}\{\kappa_a\}$, which is the exponential decay length at large radial distances.

while at a wire diameter of 1 μm the phase velocity has decreased 0.5% compared to the vacuum velocity of light.

The absorption length decreases with the wire diameter. At a 1 μm wire diameter, the absorption length is only 6 mm. This means that the energy of the surface wave is absorbed after propagating over just millimeters of the wire. It is thus clear that for decreasing wire diameter, the wire becomes a less efficient waveguide for terahertz radiation.

In figure 5.10(b), $1/\mathrm{Im}\{\kappa_a\}$ is plotted as a function of the wire diameter. This property, which governs the exponential decay of the fields in equation 5.62, decreases slowly with the wire diameter. At a wire diameter of 1 μm, it still has a substantial value of 0.45 mm. For thin wire diameters, the exponential decay length is orders of magnitude larger than the diameter of the wire.

There proves to be little advantage in using micrometer-sized metal wires as a terahertz waveguide. The plasmon-polariton is bound closer to the wire surface for thinner wires, which can be helpful as it reduces the field coupling to the surroundings. However, very thin wires are required to significantly reduce the exponential decay length. Such thin wires have the considerable disadvantages that absorption and dispersion increase rapidly for decreasing wire diameter.

5.2.3 Terahertz plasmons on coated wires

As is shown in section 5.1.3, plasmon polaritons on planar surfaces are sensitive to thin coatings applied to the surface, even if the coating thickness is much smaller than the wavelength of the plasmon polariton. This section in-

vestigates to which extent this is also true for plasmon polaritons on wires.

From equation 5.55 the properties of a surface wave propagating on a coated copper wire in vacuum are calculated as a function of the thickness of the coating for the following parameters: the frequency is assumed to be 1 THz, the wire diameter is 1 mm and the refractive index of the coating is 2. The results of this calculation are shown in figure 5.11. The figures show two curves, which represent two independent solutions of the dispersion relation (equation 5.55). For thin coatings, there is only one solution to the dispersion relation, but as the coating becomes thicker other solutions become possible. Note that, although we have plotted only the first two solutions, these are not all solutions existing within the plotted range for the coating thickness. When the coating thickness reaches 171 μm, for instance, a third solution is possible, while the fourth solution is possible when the thickness becomes larger than 257 μm.

Figure 5.11(a) shows the effective refractive index, which is defined as the free-space velocity of light divided by the phase velocity of the surface wave. The refractive index is approximately 1.0 for thin coatings ($<$10 μm) and has a transition towards a value of 2.0, which is the refractive index of the coating, at larger coating thicknesses. For thin coatings most of the energy of the surface wave is transported through vacuum, while only a fraction of the energy is transported in the coating. Therefore, the effective refractive index for a thin coating is dominated by the refractive index of vacuum. However, if the coating thickness is on the order of or larger than the wavelength, then most of the energy is transported through the coating. In that case, the effective refractive index is dominated by the refractive index of the coating.

Figure 5.11(b) shows the absorption length as a function of the coating thickness. The absorption length decreases with increasing coating thickness approximately up to the thickness where the refractive index makes it transition from 1.0 to 2.0. Above this point, the absorption length increases again. Note that the absorption takes place in the metal, as the refractive index of the dielectric coating is assumed to be strictly real.

In figure 5.11(c), we have plotted $1/\mathrm{Im}\{\kappa_a\}$, which determines the exponential decay of the fields in air as discussed in section 5.2.2. This value decreases monotonically for increasing coating thickness until it reaches the asymptotic value of 28 μm. This asymptote is determined by the difference in the dielectric constant of air and the coating, as is easily verified with equations 5.32 and 5.36. Note that for large coating thickness ($>$ 100 μm) $1/\mathrm{Im}\{\kappa_a\}$ is smaller than the coating thickness. In that case, most of the energy is transported through the coating, instead of though air.

The dip in the absorption length in figure 5.11(b) is caused by an increase of the portion of the transported energy that flows through the metal. The portion of the total energy transported through either air, copper or the coating is logically a strong function of the penetration depth in air and in copper and of the coating thickness, since they determine the size of the area through which the energy in transported in the three regions. Due to the large value of the dielectric constant of copper, the penetration depth into the copper is practically independent of the coating thickness. However, figure 5.11(c) shows that the

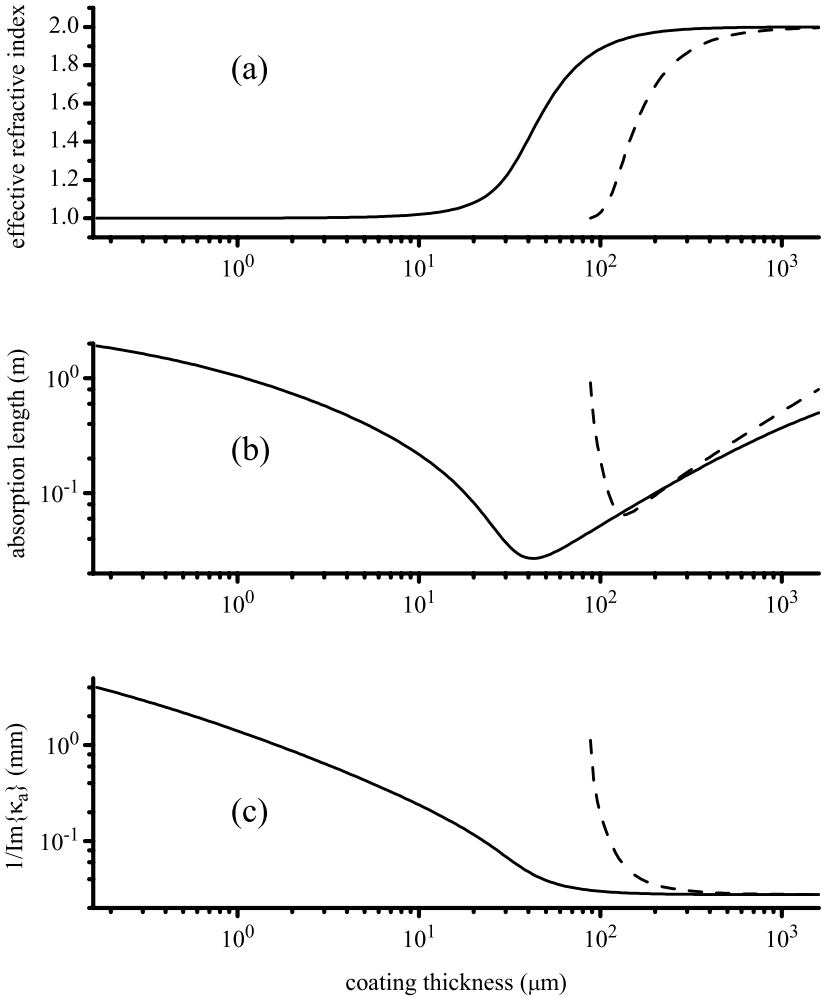

Figure 5.11: Calculated properties of a surface wave propagating on a coated copper wire in vacuum as a function of the thickness of the coating for the following parameters : 1 THz frequency, 1 mm wire diameter, and refractive index coating equal to 2.0. Figure (a) shows the effective refractive index, figure (b) shows the absorption length and figure (c) shows $1/\mathrm{Im}\{\kappa_a\}$. The two curves (solid and dashed) represent the first two independent solutions of the dispersion relation.

penetration depth in air *is* a strong function of the coating thickness. As the penetration depth in air decreases for increasing coating thickness, a smaller portion of the energy is transported through air. This means that a larger portion is transported through the metal, leading to more absorption. After the transition point, however, the portion of the energy that is transported inside the metal is decreased, due to the contribution of the energy transported within the increasingly thick coating, leading to a decrease in the absorption.

5.2.4 Model limitations

In section 5.2 a model has been developed describing the propagation of plasmon-polaritons on metal wires. As can be expected from a joint oscillation of electromagnetic waves and charge density waves, the properties of plasmon-polariton prove to be a strong function of the metal properties. Two comments are in order regarding the model used for the surface properties of the metal.

The first comment regards the surface roughness of the metal. In our model we have assumed that the surface is smooth. The reader should note that this means that the surface roughness is small compared to the penetration depth of the metal, which is on the order of 50 nm. On rough surfaces, the currents, which follow the surface, flow through more material, leading to an increased surface resistance.

The second comment regards the accuracy of the Drude model at terahertz frequency. This accuracy may be reduced due to the so-called anomalous skin effect. The anomalous skin effect arises if the penetration depth in the metal reaches the mean-free-path length of the electrons in the metal. The field can then no longer be assumed constant between two scattering events, as is assumed in the Drude model. The anomalous skin effect is discussed in more detail in appendix C.

With surface plasmons the terahertz surface properties of metals can be probed possibly with a very high sensitivity. This is especially interesting related to the anomalous skin effect, of which there is little to no experimental data at room temperature and terahertz frequencies. Concluding, the theory developed in the section has slight deficiencies, but a future study of these deficiencies might significantly increase our knowledge regarding the terahertz properties of metals.

5.3 Measurements of surface plasmon polaritons on coated wires

This section discusses measurements on the propagation of terahertz pulses over copper wires with and without a thin polyurethane coating. Our time-domain measurements of a terahertz pulse propagating along a 4 cm long wire, show that a coating of tens of micrometers thickness strongly distorts the terahertz pulse resulting in a chirped terahertz signal that lasts tens of picoseconds. A comparison with calculations based on the theory developed

in section 5.2, shows that the distortion of the terahertz pulse originates from the dispersive propagation of these waves along the coated wire. Remarkably, the propagation is dispersive although we assume that the coating material itself has a frequency-independent refractive index. Our work indicates that thin coatings can seriously distort terahertz pulses propagating along metal wires. At the same time, however, this offers the possibility to use metal wires as sensitive detectors of thin layers.

Figure 5.12 shows a schematic drawing of our setup. The terahertz pulses from our emitter are focussed onto one of two types of metal wires. The first wire is a bare copper wire with a diameter of 1 mm. The second wire is a copper wire with a diameter of 1 mm having a polyurethane coating, specified to be about 34 μm thick.[¶] A sharp copper needle is used to couple the terahertz radiation onto the wire.[88] The terahertz surface plasmon polariton propagates over the wire towards the detection crystal, which is a 1 mm thick $\langle 110 \rangle$ oriented ZnTe crystal and is held close to the end of the wire. For both the coated and the uncoated wire, the propagation distance from the detection crystal to the point where the terahertz pulse is coupled onto the wire is 4 cm. In the detection crystal, a birefringence is induced proportional to the instantaneous strength of the electric field of the terahertz wave. The induced birefringence is measured by a probe beam, which enters the detection crystal from the back and back-reflects at the front face. The terahertz-induced polarization change of the probe beam is then measured by a conventional electro-optic detection setup. More information regarding electro-optic detection is given in chapter 2. We note that large variations in the spectral content of the measured terahertz electric fields were observed for small changes in the exact position of the needle used to couple the terahertz pulses onto the system. This is not altogether unexpected, since moving the needle changes its position with respect to the frequency-dependent focus of the incident terahertz beam. In our measurements we optimized the position of this wire to maximize the measured spectral bandwidth.

In figure 5.13(a), we plot a time-domain measurement of the electric field of the terahertz pulse incident on the wire. The terahertz pulse is characterized by a sharp peak, followed by many oscillations, which are caused by absorption and re-emission of terahertz radiation by watervapor molecules in the atmosphere. Figure 5.13(b) shows the measured electric field versus time of the terahertz pulse after propagating over the 4 cm long bare copper wire. The striking differences between the pulse after propagation over the wire and the pulse incident on the wire, are the difference in the pulse shape and the increase of the pulse duration; The duration of the first positive peak changes from 0.7 ps for the incident pulse to 2.3 ps after coupling onto and propagation over the bare wire. This difference is probably caused by the frequency-dependent coupling of the terahertz pulse to the wire.[96] The dotted line in figure 5.13(c) shows the measured electric field as a function of time after propagation along the 4 cm long coated wire. The figure shows that the terahertz pulse has acquired a remarkably long tail having a time-dependent

[¶]The coated wire was obtained from Farnell (product #146531).

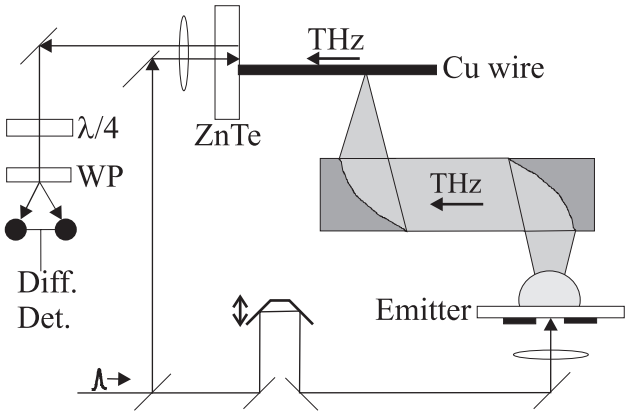

Figure 5.12: Schematic of the setup. A time-delayed pump pulse is focussed onto the biased GaAs emitter. The terahertz pulses generated by the emitter, are focussed and coupled onto the copper wire by a sharp copper needle, placed underneath the wire. The pulses then propagate over the wire to the ZnTe detection crystal. The electric field of the terahertz pulses in the detection crystal is then measured with a synchronized probe pulse, using a conventional electro-optic detection setup, consisting of a quarter-wave plate($\lambda/4$), a wollaston prism (WP) and a differential detector (Diff. Det.).

frequency, which clearly contrasts with the result for the uncoated wire.

In figure 5.13(c), we plot the electric field of a terahertz surface wave after propagation over 4 cm of coated wire, which is calculated with the dispersion relation derived in section 5.2.1 (equation 5.55). Results of the uncoated wire are not shown, as in the calculation the pulse shape is not changed significantly after propagation along this wire. In our calculations, we used a diameter of the copper wire of 1 mm and a coating thickness of 34 μm. We use 1.0 as the refractive index of air, and 2.5 as the refractive index of the coating, which is a reasonable value for polyurethane.[97] For the frequency-dependent refractive index of copper, we use the previously-mentioned model from Ordal et al.[93] For the initial, undistorted, surface wave, we assume a temporal shape that corresponds to the time-derivative of a Gaussian that has a duration of 2.1 ps. The results of the calculation are in remarkably good qualitative agreement with the measurement. The minor differences between calculation and measurement can easily be explained by the uncertainty in the exact shape of the input pulse or by the uncertainty in the refractive index of the polyurethane coating.

We can now understand the chirped terahertz signal as arising from the dispersion of the full system, consisting of the wire and the coating. To provide a physical picture for the origin of this dispersion, we calculated the electric and magnetic fields after 4 cm of propagation as a function of the radial distance ρ with equations 5.48 and 5.53. The results are plotted in figure 5.14 for four different frequencies: 50 GHz, 0.2 THz, 0.5 THz, and 1.5 THz. The fields were normalized to unity at the metal-coating interface. Figure 5.14

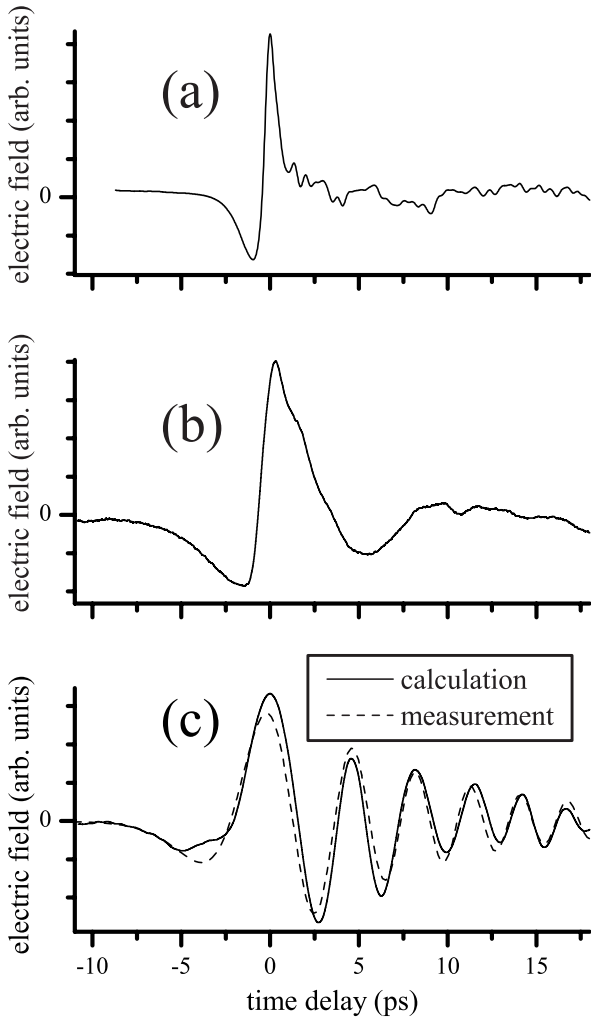

Figure 5.13: Measured electric fields as a function of time of the terahertz pulse incident on the wire (a) and of the pulse after propagating over 4 cm of the bare wire (b). Figure (c) shows the measured and the calculated pulse after propagation over the coated wire.

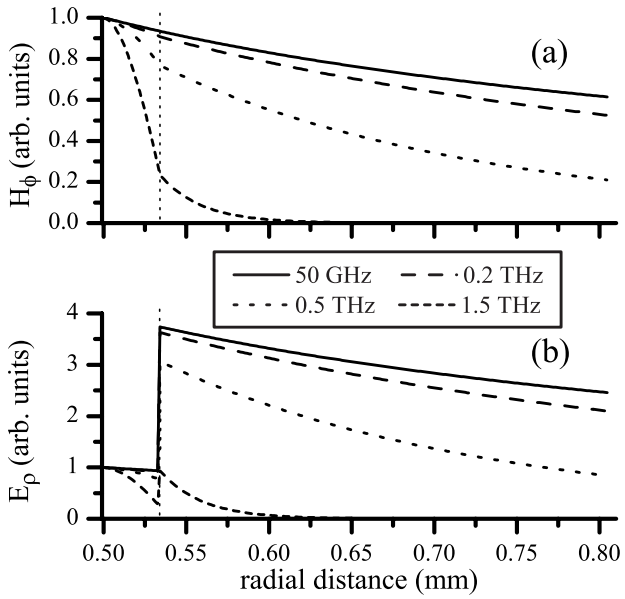

Figure 5.14: Magnetic field in the azimuthal direction (a) and electric field amplitude in the radial direction (b), both as a function of the radial distance from the center of the wire ρ. The metal surface is located at a radial distance of 0.5 mm. The position of the coating-air interface is indicated by the vertical thin dotted line.

clearly shows that for increasing frequency the decay of the fields with radial distance becomes faster. It is also shown that the strength of the electric and magnetic fields in the coating relative to the fields in air increases with frequency. Therefore, the fraction of the total terahertz energy that is transported within the coating increases with frequency. This means that the effective refractive index experienced by the surface wave increases with frequency, resulting in the dispersive pulse propagation seen in our measurements. The dispersion above is *not* an intrinsic property of the coating material itself, for which we have assumed a frequency-independent refractive index. In fact, the dispersion of the coating material plays only a small role in the dispersive wave propagation, and has been neglected here.

It is interesting to speculate on the sensitivity of the technique to detect the presence of extremely thin dielectric layers on wires. Surface plasmon polaritons on wires do not spread out, as surface plasmon polaritons on flat surfaces do,[98] thus enabling long interaction lengths. A calculation for a copper wire with a diameter of 1 mm and a 100 nm thick coating (refractive index 2.0) shows a measurable $\pi/20$ phase shift at 0.5 THz for a 59 cm long wire. We believe, therefore, that the detection of coatings with thicknesses in that range should be feasible.

In conclusion, we have presented time-domain measurements that show the effect of a thin coating on the propagation of terahertz surface plasmon

polaritons along metal wires. After propagation over 4 cm of coated wire, we found that the terahertz surface wave becomes fully dispersed, resulting in a terahertz signal that lasts tens of picoseconds, which is not the case in the measurements of an uncoated wire. A comparison with a theoretical model based on Maxwell's equations shows that the pulse distortion originates from the dispersive nature of wave propagation along the coated wire. This dispersion is due to the frequency dependence of the fraction of the wave's energy that travels through the coating. Our work shows that metal-wire waveguides could serve as sensitive probes of thin layers at terahertz frequencies.

5.4 Conclusion

We have studied the propagation of terahertz waves over coated and uncoated wires both experimentally and theoretically. The calculations for uncoated copper wires show that the electric fields extend millimeters to centimeters away from the wire surface. This means that a substantial region around the wire should be kept free of objects to avoid coupling of the electro-magnetic field to these objects. The distance that the fields extend from the wire can be decreased by decreasing the diameter of the wires, but only at the expense of an increase in the absorption and the dispersion.

An alternative method to confine the fields to a region closer to the wire is by applying a thin coating on the wire. However, both our calculations and our measurements show that even coatings that are much thinner than the wavelength of the terahertz radiation can strongly increase dispersion. Due to this large sensitivity, terahertz pulses on metal wires could be used to measure the properties of thin coatings.

In our calculations, we used a Drude model for the frequency-dependent dielectric constant of copper. However, the validity of this model at terahertz frequencies is under debate. The study of terahertz waves on metal wires may play an important role in this debate, because of the sensitivity of these waves to the metal properties.

Chapter 6

Near-field terahertz imaging

Diffraction, which limits the resolution in far-field imaging to about a wavelength, is an obstacle for a number of interesting new terahertz applications, as has been discussed in section 1.3.4. Breaking the diffraction limit would, for instance, make it possible to perform terahertz spectroscopy on extremely small volumes, and, ultimately on living cells. Work on the label free probing of DNA[28] and work by Walther et al.,[27] show that terahertz radiation can be used to distinguish between different biomolecules.

One way to overcome the diffraction limit is to limit the detection area with an aperture. For example, Mitrofanov et al.[99] have shown that, using a detector with an integrated aperture, near field images can be made with a spatial resolution determined by the aperture size, and not by the THz wavelength. Unfortunately, this method relies on extensive micro-fabrication and requires two parallel plates, namely one carrying the object and the other the detector, to be scanned along each other at close distance, which is difficult to do in practice. Also, since the aperture has a finite thickness, waveguide effects strongly attenuate long wavelength components,[100] which makes their detection difficult. Another approach to obtain sub-wavelength resolution[37] uses a laser to modulate the THz transmission of a small area on a semiconductor surface near the object. In this method, however, signals are small and the resolution is limited to the focus diameter of an optical beam, which is itself limited by diffraction.

An alternative for the use of apertures in near-field imaging is the use of sharp metal tips as local field enhancers.[101–103] The sharp metal tip is held in close contact to the sample under study, while light is scattered by the tip. The amount of scattered light is a function of the dielectric environment of the tip apex, which has sub-micrometer dimensions. By measuring the scattered light, while scanning the tip over the sample, an image can be obtained with a subwavelength resolution, determined by the size of the tip apex. A big advantage of this imaging technique is that it does not suffer from a waveguide cutoff, which limits the resolution in aperture techniques. Apertureless near-field imaging, which was originally developed at visible and mid-infrared wavelengths, has recently been demonstrated at terahertz

wavelengths.[38,104,105]

We developed an apertureless technique in which not the radiation scattered into the far field, but instead the near field close to the tip is measured. The advantage of near-field detection with respect to far-field detection is that one can directly measure the enhanced field around the tip, resulting in relatively strong signals. Our method to obtain a sub-wavelength resolution has four advantages. (i) The resolution is ultimately determined by the dimensions of the tip, not by the incident terahertz beam size. (ii) The measurements are background free. (iii) The detection setup measures in the near field, where the electric field can be strong. This provides sufficiently large signals and thus reduces the measurement time. (iv) The method has the more practical requirement of scanning a tip along a surface, instead of two surfaces parallel to each other.

We note that for none of the reported terahertz near-field apertureless techniques a sound direct measurement of the resolution has been reported. Resolution measurements for this kind of systems are tricky, due to so-called topographical artifacts. If the object under study is not flat, then the signal will be a function of the height of the tip with respect to the object's surface. This makes it difficult to separate signals from height variations from signals arising from changes in the frequency-dependent dielectric constant of the object. When the signal is caused by height variations one essentially measures the shape of an object which is not very exciting, because such measurements can be performed much better with, for instance, an atomic force microscope. The resolution should therefore be obtained from an image of a flat object, where the contrast mechanism is not caused by height variations but by refractive index or absorption variations.

This chapter describes a new terahertz near-field detection method, which shows a large potential for future terahertz microscopy measurements. Section 6.1 presents results from the near-field terahertz detection method. The frequency dependence of the signal obtained with this method is discussed in section 6.2. Section 6.3 concludes with an outlook on the resolution that might be obtained with our system.

6.1 Near-field terahertz detection

Figure 6.1 show a schematic of our near-field detection setup. As is displayed in this figure, the terahertz pulses, which have an average power of 40 μW, are focussed onto a copper tip, which has been sharpened in a FeCl etch bath. Our setup to generate terahertz pulses is described in section 4.1 and in reference 23. A 300 μm thick, (100) oriented GaP detection crystal is placed within a distance of several microns of the tip. The crystal surface closest to the tip is coated with a 300 nm thick Ge layer on top of a 133 nm thick SiO_2 layer. A synchronized, 800 nm probe pulse, derived from the same laser that generates the terahertz pulse, is focussed to about a 20 μm spot size on the coating, initially counter propagating with respect to the terahertz pulse. The thickness of the SiO_2 layer is chosen such that the amount of probe light reflected is

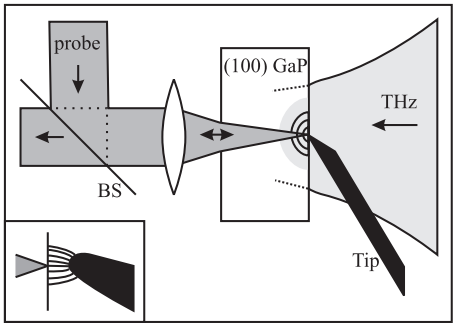

Figure 6.1: Schematic picture of the setup used. The terahertz radiation comes in from the right, and scatters at the tip. The probe beam comes in from the left, and is focussed on the crystal-air interface of an (100) GaP crystal. At this interface the probe beam polarization is changed by the terahertz electric field near the tip. The probe beam reflects back at the crystal interface, and is sent to the differential detection setup (not shown). The inset on the bottom left zooms in on the tip, and schematically shows the near-field electric field lines near the tip, which have a component perpendicular to the crystal surface.

maximized. The Ge layer is chosen sufficiently thick to absorb the transmitted probe beam. The coating, which has a negligible effect on the terahertz beam, thus prevents any probe light from reaching the tip. This eliminates any measurement errors that would have been caused by probe light scattered off the tip back towards the detector.

After the reflection at the coating the probe pulse is sent through a $\lambda/4$ plate and a Wollaston prism to a differential detector. When a terahertz electric field is present in the crystal, the electro-optic effect changes the probe polarization from linear to slightly elliptical. The amount of ellipticity is proportional to the instantaneous terahertz electric field, and is measured by the differential detector setup.

Section 2.1 describes that by selecting the orientation of the detection crystal, it is possible to select to which component of the terahertz electric-field vector an electro-optic detection setup is sensitive. We remind the reader that in an (110) oriented crystal, which is the conventionally used orientation in electro-optic detection, the probe polarization is only affected by electric fields parallel to the crystal surface. Here, however, using an (100) oriented crystal, the probe polarization is *only* changed by electric fields perpendicular to the crystal surface making the probe "blind" to the parallel polarized electric field of the incident terahertz pulse. Near the tip, however, as is illustrated in the inset of Fig. 6.1, the terahertz near field must have a component perpendicular to the crystal surface, since the electric field near a metal, in this case the tip, has to be perpendicular to the metal surface.

The inset of Fig. 6.2 shows the terahertz electric field as a function of the delay between probe and terahertz pulse, measured directly under the copper tip, which is pressed against the crystal. The power spectrum of this pulse is plotted in Fig 6.2. It contains frequencies from 0.1 THz to 2.5 THz and peaks

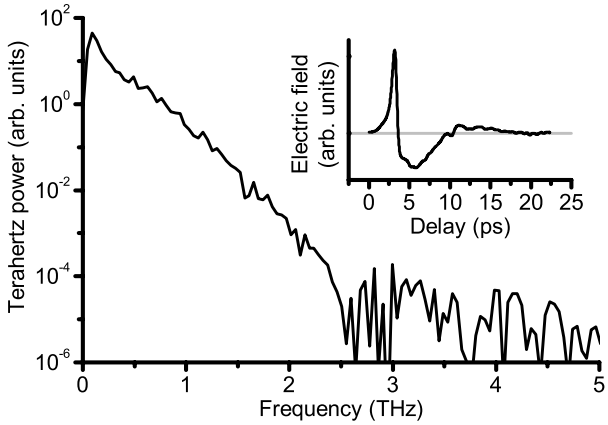

Figure 6.2: Terahertz power spectrum, calculated from the terahertz electric field as a function of delay shown in the inset. The measurement was performed with the tip pressed against the crystal, directly above the probe beam.

around 0.15 THz. The spectrum measured directly under the tip is substantially different from the spectrum of the pulse incident on the wire, as is discussed in section 6.2.

Although the measurement in figure 6.2 was obtained in less than a minute, we note that, in our setup, a measurement of a 25 ps long terahertz electric field pulse is obtained in 20 ms with a dynamic range of 50. This dynamic range was achieved with an optical probe beam power on the order of 200 μW. It has been shown in section 3.1 that the noise level in electro-optic detection is limited by probe laser shot-noise and that the dynamic range in a shot-noise limited system can be improved by increasing the power in the probe beam. The maximum power is determined by the saturation properties of the photodiodes in the differential detector, which are investigated in section 3.2. Using the recommendations in this section, probe beam powers on the order of 10 mW are feasible. It is thus clear that there is much room to improve our dynamic range, which is already superior to alternative methods.[104,105]

Fig. 6.3 shows the measured peak terahertz electric field as a function of the tip-crystal separation. The measurement covers a total distance of about 30 μm. The inset shows an additional measurement, which zooms in on the region close to the crystal. We have chosen the 0 μm position arbitrarily as the position where the signal reaches its maximum. The figure shows that the terahertz electric field decreases to 30% of its maximum value, when the tip-crystal distance increases to 6.5 μm, which clearly indicates near field behavior. When the tip is close to the crystal ($\sim$ 1 μm), it is abruptly attracted to the crystal, presumably by electrostatic forces, which gives rise to a sudden increase in the signal at 0 μm. The sharp, but smooth, decrease of the terahertz electric field when the distance to the crystal is increased only a few μm, is related to results obtained by Knoll et al.[106] at the much shorter wavelength of 10 μm. They found that the scattering cross-section of a tip close to a dielectric

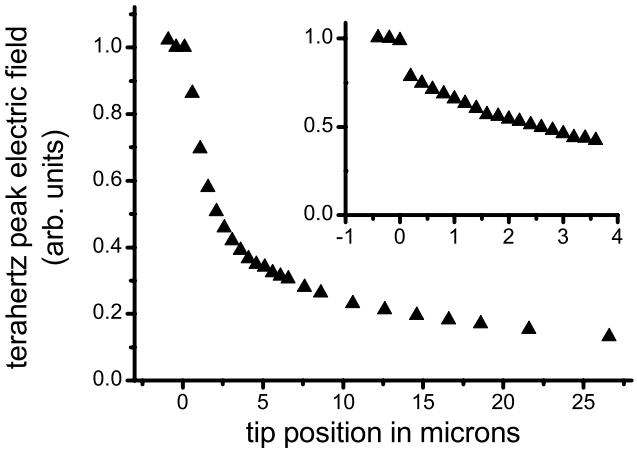

Figure 6.3: Measured peak terahertz electric field as a function of the tip-crystal distance. The inset shows a separate measurement of the region close to the crystal.

half-space is strongly increased due to an image charge induced in the dielectric medium. It is likely, that this effect also applies in our case, and that an increase of the scattering cross-section is related to the strong enhancement of the local terahertz electric field when the tip approaches the crystal.

In Fig. 6.4(a-d), we plot the integrated power of the terahertz pulses, measured while raster-scanning the tip across the crystal surface, for 4 different tip-crystal separations. The four measurements clearly show a rapid increase in the terahertz spot size for increasing tip-crystal distances. This is quantitatively expressed by the results in Fig. 6.4(e), where we plot the measured terahertz spot size, defined as the full width at half maximum (FWHM) of the intensity, as a function of the tip-crystal distance. The 0 μm point is chosen arbitrarily as the position where the spot size reaches its minimum. Fig. 6.4(e) clearly shows that the spot diameter increases more than a factor of 6 when the tip-crystal separation increases to 30 μm. This again strongly suggests that, close to the crystal, we are measuring in the near field of the tip. The figure also shows, that sub-wavelength resolution is easily obtained, even for relatively large tip-crystal distances. The smallest observed spot diameter in this measurement is 18 μm. A spectral analysis (not shown here) clearly proves that the spot diameters are independent of frequency, with a smallest spot corresponding to a maximum resolution of $\lambda/110$ at 0.15 THz.

Earlier measurements with a probe beam focal spot size of 50 μm gave a smallest terahertz spot size of 50 μm. The measured smallest spot size of 18 μm is again similar to the probe beam focal diameter of 20 μm, suggesting that the observed terahertz spot sizes are determined by the focal diameter of the probe. This indicates, that a spot size better than 18 μm is achievable in our setup, if we focus the probe beam tighter. Indeed, experiments in which the diameters of both the probe focus and the tip apex are further reduced show

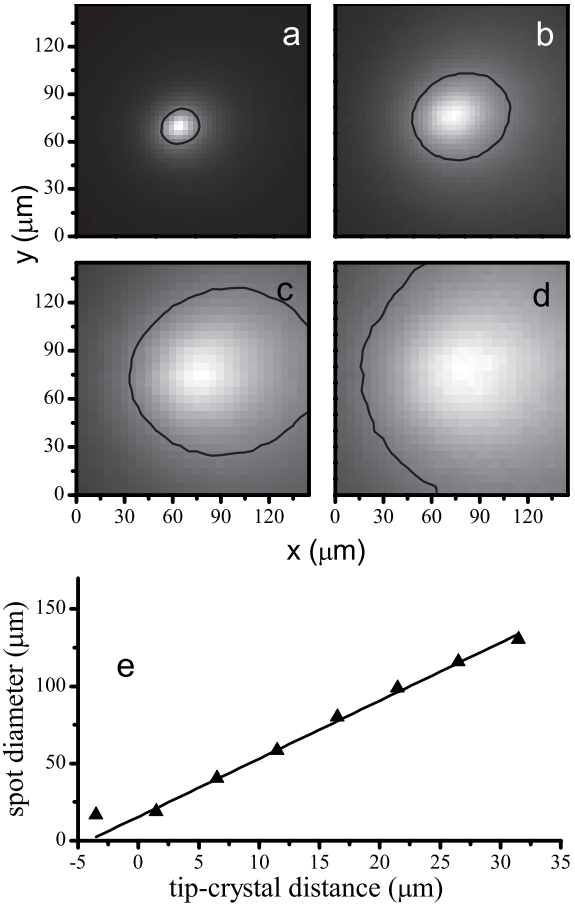

Figure 6.4: Terahertz intensity as a function of the xy position of the tip along the crystal. The scans (a) and (b) are 50 x 50 pixel images with a 3 x 3 μm^2 pixel size, and (c) and (d) are 30 x 30 pixel images with a 5 x 5 μm^2 pixel size. In the pictures (a), (b), (c), and (d), the tip is positioned at 0, 10, 20, and 30 μm distance from the crystal, respectively. The gray-levels run from zero (black) to maximum intensity (white), and are separately normalized for each scan. The black line is the FWHM of the spot. Graph (e) shows the measured FWHM spot diameter as a function of tip-crystal distance. The solid line is a linear fit through all points but the first.

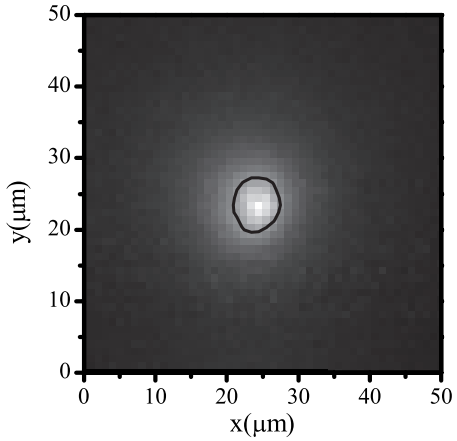

Figure 6.5: Terahertz intensity as a function of the xy position of the tip along the crystal. The scan is a 50 x 50 pixel image with a 1 x 1 μm^2 pixel size obtained with the tip in contact with the crystal. The gray-levels run from zero (black) to maximum intensity (white), and the black line indicates the FHWM of the spot.

spot sizes down to 7 μm (figure 6.5).

Ultimately, we envisage an experiment in which a thin sample is placed on the crystal underneath the tip. When the crystal is raster-scanned underneath the tip, a two-dimensional terahertz image of the sample is obtained. A high resolution, however, is only possible, if the physical size of the tip is smaller than the desired resolution. The obtainable resolution is further discussed in section 6.3.

The advantages of our method to use THz-TDS to produce near-field images are that it is coherent, intrinsically broadband, and uses only 40 μW of input power. Coherent detection offers the advantage of measuring both amplitude and phase, while broadband detection allows us to obtain information on a wide range of frequencies in one measurement. The possibility that a sample is heated significantly or even damaged is negligible in our setup, since we use low input powers. We note that the time-dependent nature of terahertz pulses makes it possible to use our setup for visible pump-terahertz probe measurements on microscopic systems.

In conclusion, we have presented a method to obtain a sub-wavelength resolution in terahertz imaging by electro-optically measuring the terahertz electric field close to a sharp copper tip in a (100) oriented GaP crystal. We demonstrate a smallest terahertz spot size of 7 μm, which is probably limited by the probe beam diameter.

6.2 Frequency dependence of the signal strength

In the measurements described in section 6.1, the terahertz electric field measured in the near field of a metal tip was different from the field incident on

this tip. This is further illustrated in figure 6.6, which shows measurements of both the incident field (a) and the near field (b). Compared to the incident field, the measured near field clearly decays faster with increasing frequency. The purpose of this section is to investigate the physical nature of this frequency dependence.

Focussing on the frequency dependence, we derive a proportionality between the incident field and the near field. In this derivation, two steps are distinguished. First, the incident field couples to the tip, which functions as an antenna, leading to currents and charges on the tip. Second, the electric charges on the tip induce a near field according to Coulomb's law.

The tip can be modelled as an antenna with a resistance, a capacitance and an inductance. In such a model, the current induced on the tip is related to the incident terahertz electric field by

$$I(\omega) \propto E_{inc}(\omega) / \left(R + j\omega L + \frac{1}{j\omega C} \right), \tag{6.1}$$

where E_{inc} is the strength of the incident electric field at the radial terahertz frequency ω. R is the total resistance, including the physical resistance, which accounts for losses due to the nonzero conductivity of the tip, and the radiation resistance, which accounts for losses due to re-emission by the tip. Capacitive coupling between different parts of the wire gives rise to the capacitance C. Inductive coupling between the current on different positions on the wire is incorporated by the inductance L.

The electric near field is not determined by currents, but by charges, as can be seen from equation 4.5. These charges arise on the tip, because the current must decrease towards the end of the tip. Assuming that the current abruptly goes to zero at the end of the tip, a point charge arises on the tip apex given by

$$Q(\omega) \propto \frac{j}{\omega} I(\omega). \tag{6.2}$$

The relation between the near field and the point charge is closely related to Coulomb's law and can be calculated from equation 4.5

$$E_{near}(\omega) \propto Q(\omega). \tag{6.3}$$

With equations 6.1, 6.2 and 6.3, the following proportionality is obtained

$$E_{near}(\omega) \propto E_{inc}(\omega) / \left(-j\omega R + \omega^2 L - \frac{1}{C} \right) \tag{6.4}$$

R, C and L are determined by the shape and size of the tip and also by the properties of the objects close to the tip, such as the detection crystal. An exact calculation of R, C and L would require a complicated 3D simulation of the system. However, physical insight is obtained using reasonable assumptions for the values of R, C and L. Here, we use R = 150 Ω, L = 20 pH and C = 0.1 pF. For these values, the coupling to the wire is dominantly capacitive for frequencies below 1.1 GHz, inductive for frequencies above 1.2 THz and resistive between these two frequencies.

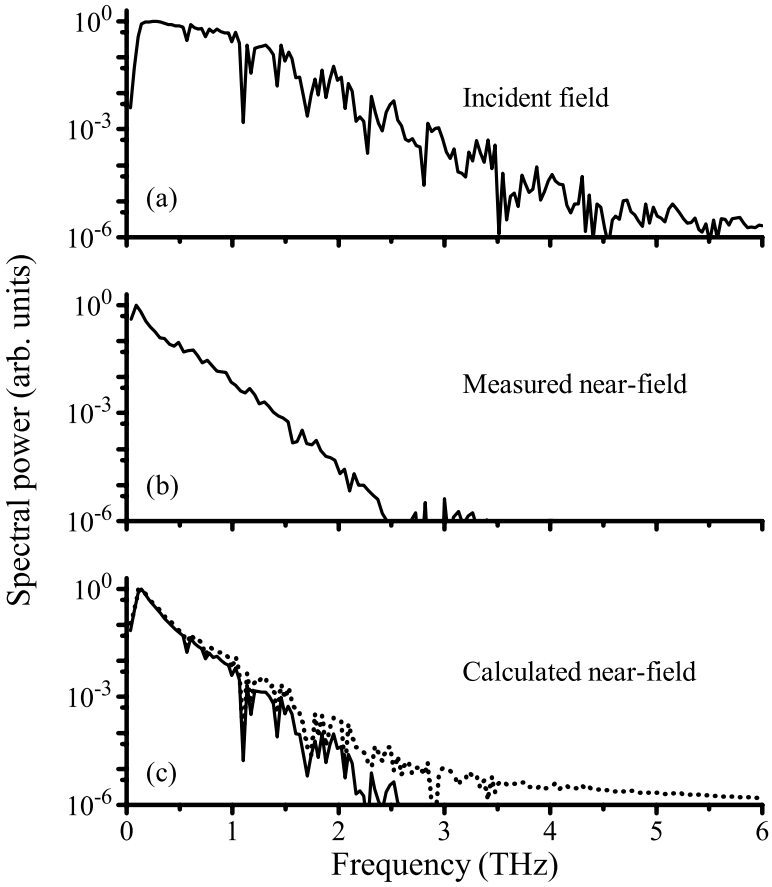

Figure 6.6: (a) Measured power spectrum of the terahertz pulse incident to the tip. (b) Power spectrum measured in the near field of the tip. (c) Calculated power spectrum of the terahertz near field, with R = 150, C = 0.1 pF, and L = 20 pH (solid line), and the power spectrum of the near-field calculated using resistive coupling only (dotted line).

Figure 6.6(c) shows the results of a calculation of the near field spectrum using equation 6.4 and the spectrum of the incident field in figure 6.6(a). The calculated near-field is in good agreement with the measured near-field in figure 6.6(b). The dotted line in figure 6.6(c) is the result of a calculation in with both capacitive and inductive coupling is neglected and the near field is assumed proportional to $E_{inc}(\omega)/\omega$. This approximation is already in reasonable agreement with the measurement, especially a low frequencies. We thus conclude that the frequency dependence of the near field can be approximated by that of a resistively coupled antenna up to a frequency of about 1 THz. Above 1 THz the inductance of the wire should be taken into account.

6.3 Obtainable resolution

In the near-field imaging experiment that we envisage, a thin sample is placed on top of the crystal, which is raster-scanned beneath the tip. As discussed previously, the resolution obtained in this system has not yet been directly measured. This section discusses the resolution that could be obtained with our system, the theoretical limits of the resolution and the relation between the resolution and the spot size measured in section 6.1.

The resolution is defined as the minimum distance between two point-like objects at which the objects can still be distinguished in the image. In the image formation of point-like objects, there are two important steps. First, the near-field around the tip polarizes the object. Due to its assumed small size, the polarized object can be regarded as a dipole. Second, the near-field of this dipole is measured by the probe beam in the detection crystal. This probe beam also measures the near-field coming directly from the tip. However, this contribution does not change as the crystal (with the objects on top) is scanned underneath the tip, because the probe beam maintains a fixed position with respect of the tip. Therefore, the contribution coming directly from the tip provides a background in the imaging process.

The probe beam diameter determines the resolution, if the diameter of the probe beam is much smaller than the dimensions of the tip. In that case (figure 6.7(a)), the near-field from the tip is approximately equal at two closely spaced, point-like objects (1 and 2). The strength of the dipoles induced in the two objects, which are proportional to the near field of the tip, is thus also approximately equal. Therefore, the objects can only be distinguished, if the probe beam is selectively sensitive for only one of the two dipoles. This is only possible if the diameter of the probe beam is smaller than the distance between the objects.

The tip, on the other hand, determines the resolution, if the diameter of the probe beam is much larger than the dimensions of the tip. In that case (figure 6.7(b)), the polarizations of two closely spaced, point-like objects (1 and 2) are measured with approximately equal sensitivity. Therefore, the objects can only be distinguished, if the near field of the tip decays sufficiently fast as a function of the distance from the tip to cause a sufficient difference in the polarization of object 1 and 2. The near-field decay length is approximately

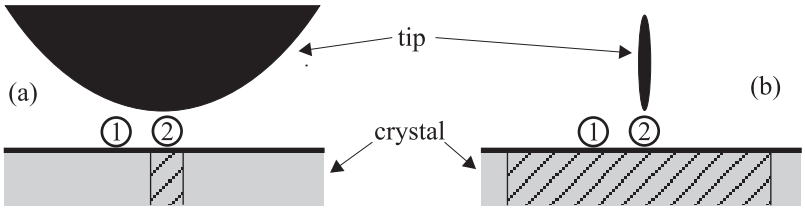

Figure 6.7: Schematic illustrating the resolution for the case that the tip dimensions are either much larger (a) or much smaller (b) than the diameter of the probe beam, which is indicated by the dashed regions. In both cases the point-like objects 1 and 2 can be distinguished separately.

proportional to the typical dimension of the tip. Smaller tips will thus result in improved resolutions.

Based on the considerations above, we conclude that the resolution is determined by the *smallest* value of the typical dimension of the probe beam in the detection crystal and the typical dimension of the tip. Note the difference with the spot size measured in section 6.1, which is determined by the *largest* value of these two typical values. The measured spot size thus give a upper limit for the obtainable resolution.

The minimal dimensions of the tip and of the probe focus determine the theoretical limit on the resolution in our method. Due to diffraction, the minimum diameter of the probe beam is on the order of the wavelength of the probe. For Ti:Sapphire-based laser systems, this wavelength is about 800 nm. It may seem that there is no theoretical limit on the dimensions of the tip. However, if the tip becomes much smaller than the diameter of the probe beam, then the volume of the detection crystal used to probe the near field decreases proportional to the third power of the tip dimension. The electro-optic signal is proportional to the detection volume and thus also decreases rapidly for decreasing dimension of the tip. A factor two decrease of the resolution, requires a factor two decrease of the tip dimension, which results in a factor eight decrease in the signal strength. The signal can, of course, not be measured if it drops below the noise level of the system. Thus, although there is no theoretical limit on the resolution, a practical limit arises from the demand for a reasonable signal-to-noise ratio.

It is clear that a high resolution requires small tips. Not only the apex diameter matters, but also the length of the tip, since the shaft of the tip also contributes to the signal.[107] It is, however, not necessary to use short tips, because the effective length of the tip can be strongly reduced by a modulation technique. In this technique, a piezoelectric modulator vibrates the tip perpendicular to the surface. Contributions to the signal from the tip apex are more sensitive to the modulation of the tip-sample distance than the contributions from the tip shaft. It is thus possible to suppress the contributions from the shaft by demodulation at an integer times the vibration frequency. This modulation technique was developed in the microwave region,[108] has been used in the infrared[106] and has also been introduced in the terahertz field.[104,107]

We note that, using this modulation technique, resolutions $<$20 nm have been obtained at mid-infrared frequencies.[109] We do not see any reasons why our method could not reach a similar resolution at terahertz frequencies.

6.4 Conclusion

A terahertz near-field detection scheme is presented that shows great potential for the near-field imaging of subwavelength-sized objects. Measured spot sizes down to 7 μm are strong indicators that a resolution at least on the order of microns is feasible. Based on results obtained at mid-infrared wavelengths, we estimate that resolutions on the order of tens of nanometer are feasible. In follow-up research, such a resolution should be measured directly with flat samples to avoid topographical artifacts.

Appendix A

$\chi^{(3)}$ terahertz generation

Section 4.2 discusses terahertz generation by the second-order ($\chi^{(2)}$) nonlinear polarization. It is, however, also possible to generate terahertz radiation using the third-order ($\chi^{(3)}$) nonlinear polarization, which is proportional to the third power of the electric field.[110] This appendix considers the radiated electric field in $\chi^{(3)}$ terahertz generation, and discusses some of the differences with $\chi^{(2)}$ terahertz generation.

We consider the mixing of three optical, monochromatic beams. The beams propagate collinear, and are focussed in a generation medium, which extends from $z = z_1$ to $z = z_2$. We assume that the generation medium is embedded in a medium with an identical refractive index to avoid reflections at the interfaces. Two of the three beams have nearly identical frequencies and are called fundamental beams. The third beam is called the harmonic beam, and has a frequency that is approximately twice the frequency of the fundamental beams. Analogous to the situation for $\chi^{(2)}$ terahertz generation (equation 4.2 and 4.3), we write for the electric fields of the generating beams

$$E_{f1}(t,x,y,z) = \frac{jz_{rf}E_{f10}}{\left(z+jz_{rf}\right)} \exp\left\{j\omega_0 t - jk(\omega_0)\left(z+\frac{1}{2}\frac{x^2+y^2}{z+jz_{rf}}\right)\right\} \tag{A.1}$$

$$E_{f2}(t,x,y,z) = \frac{jz_{rf}E_{f20}}{\left(z+jz_{rf}\right)} \exp\left\{j\omega_1 t - jk(\omega_0)\left(z+\frac{1}{2}\frac{x^2+y^2}{z+jz_{rf}}\right)\right\} \tag{A.2}$$

$$E_h(t,x,y,z) = \frac{jz_{rh}E_{h0}}{(z+jz_{rh})} \exp\left\{j\left(\omega_0+\omega_1-\omega_T\right)t - jk(2\omega_0)\left(z+\frac{1}{2}\frac{x^2+y^2}{z+jz_{rh}}\right)\right\} \tag{A.3}$$

where E_{f1} and E_{f2} are the electric fields of the fundamental beams, and E_h is the electric field of the harmonic beam. The strength and relative phase of the beams is determined by the complex constants E_{f10}, E_{f20} and E_{h0}. The radial frequencies of the two fundamental beams are ω_0 and ω_1, and the radial frequency of the harmonic beam is $\omega_0 + \omega_1 - \omega_T$. We have approximated

the wavevector of the second fundamental beam with $k(\omega_0)$. Likewise, the wavevector of the harmonic beam is approximated by $k(2\omega_0)$. The Rayleigh ranges of the fundamental beams are assumed equal and are denoted by z_{rf}. The Rayleigh range of the harmonic beam is denoted by $z_{\not\!h}$.

For a frequency independent $\chi^{(3)}$, the induced third-order polarization at the terahertz wavelength is given by[69]

$$\begin{aligned}
P_g(t,x,y,z) &= \epsilon_0\chi^{(3)}E_{f1}(t,x,y,z)E_{f2}(t,x,y,z)E_h^*(t,x,y,z) \\
&= \frac{-j\epsilon_0\chi^{(3)}z_{rf}^2 z_{\not\!h}E_{f10}E_{f20}E_{h0}^*}{\left(z+jz_{rf}\right)^2(z-jz_{\not\!h})}\exp\left\{j\omega_T t\right. \\
&\quad \left. -2jk(\omega_0)\left(z+\frac{1}{2}\frac{x^2+y^2}{z+jz_{rf}}\right)+jk(2\omega_0)\left(z+\frac{1}{2}\frac{x^2+y^2}{z-jz_{rf}}\right)\right\} \\
&= \frac{-j\epsilon_0\chi^{(3)}z_{rf}^2 z_{\not\!h}E_{f10}E_{f20}E_{h0}^*}{\left(z+jz_{rf}\right)^2(z-jz_{\not\!h})}\exp\left\{j\omega_T t - jz\left(2k(\omega_0)-k(2\omega_0)\right)\right. \\
&\quad \left. -\frac{1}{2}j\left(x^2+y^2\right)\left(\frac{2k(\omega_0)}{z+jz_{rf}}-\frac{k(2\omega_0)}{z-jz_{\not\!h}}\right)\right\}.
\end{aligned} \tag{A.4}$$

Just as for $\chi^{(2)}$ generation, we can use the radiation integral (equation 4.10) to calculate the terahertz electric field radiated by the third-order polarization. The details of this calculation can be found in section 4.2.3, which discusses the similar situation for $\chi^{(2)}$ generation. The calculated electric field is given by

$$\begin{aligned}
\mathbf{E}_{rad}(x,y,z,t) &= \frac{\omega_T^2\chi^{(3)}E_{f10}E_{f20}E_{h0}^*z_{rf}^2 z_{\not\!h}}{4\pi c^2\sqrt{x^2+y^2+z^2}}\exp\left(j\omega_T t - jk_T\sqrt{x^2+y^2+z^2}\right) \\
&\quad \mathbf{e}\int_{x'=-\infty}^{\infty}\mathrm{d}x'\int_{y'=-\infty}^{\infty}\mathrm{d}y'\int_{z'=z_1}^{z_2}\mathrm{d}z'\frac{1}{\left(z'+jz_{rf}\right)^2(z'-jz_{\not\!h})} \\
&\quad \exp\left\{jk_T\frac{xx'+yy'+zz'}{\sqrt{x^2+y^2+z^2}}-jz\left(2k(\omega_0)-k(2\omega_0)\right)\right. \\
&\quad \left.-\frac{1}{2}j\left(x'^2+y'^2\right)\left(\frac{2k(\omega_0)}{z'+jz_{rf}}-\frac{k(2\omega_0)}{z'-jz_{\not\!h}}\right)\right\}.
\end{aligned} \tag{A.5}$$

Solving the integrals over x′ and y′ we get

$$\begin{aligned}\mathbf{E}_{rad}(r,\theta,t) = &\frac{\omega_T^2 \chi^{(3)} E_{f10} E_{f20} E_{h0}^* z_{rf}^2 z_{\hbar}}{2c^2 r} \exp\left(j\omega_T t - jk_T r\right) \mathbf{e} \\ &\int_{z'=z_1}^{z_2} \mathrm{d}z' \frac{1}{\left(z' + jz_{rf}\right)\left(jz' k'_T + 2k(\omega_0) z_{\hbar} + k(2\omega_0) z_{rf}\right)} \\ &\exp\left\{ jz'\left(k_T \cos(\theta) - k'_T\right) \right. \\ &\left. - \frac{1}{2} k_T^2 \sin^2(\theta) \frac{\left(z' + jz_{rf}\right)\left(z' - jz_{\hbar}\right)}{2k(\omega_0) z_{\hbar} + k(2\omega_0) z_{rf} + jk'_T z'} \right\},\end{aligned} \tag{A.6}$$

with $k'_T = 2k(\omega_0) - k(2\omega_0)$, which is the value for k_T for which the generation is phase matched for $\theta = 0$. We again find the same expression for the phase mismatch $k_T \cos(\theta) - k'_T$ as in equation 4.23, only with a different definition of k'_T.

If we make the same approximations as for $\chi^{(2)}$ generation, namely that $z' k'_T \ll 2k(\omega_0)\left(z_{rf} + z_{\hbar}\right)$, $z_{rf} k'_T \ll 2k(\omega_0)\left(z_{rf} + z_{\hbar}\right)$ and $k_T \ll k(\omega_0)$, the above equation changes to

$$\begin{aligned}\mathbf{E}_{rad}(r,\theta,t) = &\frac{\omega_T^2 \chi^{(3)} E_{f10} E_{f20} E_{h0}^* z_{rf} z_{\hbar}}{4c^2 r k(\omega_0)\left(z_{rf} + z_{\hbar}\right)} \exp\left(j\omega_T t - jk_T r\right) \mathbf{e} \\ &\exp\left\{ -\frac{k_T^2}{4k(\omega_0)} \sin^2(\theta) \frac{z_{rf} z_{\hbar}}{z_{rf} + z_{\hbar}} \right\} \int_{z'=z_1}^{z_2} \mathrm{d}z' \frac{z_{rf}}{\left(z' + jz_{rf}\right)} \\ &\exp\left\{ jz'\left(k_T \cos(\theta) - k'_T\right) - \frac{k_T^2}{4k(\omega_0)} \sin^2(\theta) \frac{z'^2}{z_{rf} + z_{\hbar}} \right\}.\end{aligned} \tag{A.7}$$

This equation can be compared with equation 4.18 for the field radiated by the $\chi^{(2)}$ process. The form of the two equations is strikingly similar. The radiated electric field for $\chi^{(3)}$ terahertz generation follows from the field for $\chi^{(2)}$ generation after this substitution of variables:

original in eq. 4.18	$\rightarrow$	equivalent in eq. A.7
$\chi^{(2)} E_{g10}^* E_{g20}$	$\rightarrow$	$\chi^{(3)} E_{f10} E_{f20} E_{h0}^*$
z_r^2	$\rightarrow$	$z_{rf} z_{\hbar}$
$W_0^2 = \frac{2z_r}{k(\omega_0)}$	$\rightarrow$	$\frac{2z_{rf} z_{\hbar}}{(z_{rf} + z_{\hbar}) k(\omega_0)}$

Besides the proper change of variables, there is only an extra factor $z_{rf}/(z' + jz_{rf})$ in the integral over z'. This extra factor is due to the Gouy phase shift of the pump beams. The Gouy phase shift is an extra 180 degrees phase shift that

is acquired by an electromagnetic wave as it propagates through a focus.[68,111] $\chi^{(2)}$ terahertz generation is not sensitive to the Gouy phase shift of the pump beams, because its radiated field is proportional to $EE^* = |E|^2$ with E the electric field of the pump beam. The $\chi^{(2)}$ generation process is thus not affected by the phase of the pump beams. In contrast, the electric field radiated by a $\chi^{(3)}$ process is proportional to E^2E^*, and thus *is* sensitive to the Gouy phase shift.

To investigate the influence of the extra factor in equation A.7 due to the Gouy phase shift, we consider the value of the integral when the effect of the nonzero focus diameters is negligible ($k_T^2 z'^2 \ll k(\omega_0)(z_{rf} + z_{\hbar})$), and the integral over z' in equation A.7 can be written as

$$C_{ph.match} \equiv \frac{j}{l} \int_{-l/2}^{l/2} \mathrm{d}z' \, \frac{z_{rf}}{z' + jz_{rf}} \exp\left(jz'\Delta k z_{rf}\right), \tag{A.8}$$

where $\Delta k = k_T \cos(\theta) - k'_T$ is the phase mismatch. The generation crystal has a length $l = z_2 - z_1$, and is positioned in the center of the focus. Note that the above expression is always completely real. For very small values of l, $C_{ph.match}$ approaches unity. For larger values of l, the value of $C_{ph.match}$ changes due to phase matching. Unlike in the $\chi^{(2)}$ phase-matching process, the Gouy phase shift plays an important role in the $\chi^{(3)}$ phase matching process. To investigate the effect of the Gouy phase on the phase matching process, equation A.8 is calculated as a function of the length of the generation crystal for five different value of the phase mismatch (Figure A.1). We obtain results that are independent of the length (and diameter) of the pump beam focus by normalizing both l and Δk to the Rayleigh length z_{rf}.

Figure A.1 shows that the radiation is produced more efficient, if Δk is negative, when we compare it with a value of Δk that is equal in size but positive. Note that for $\chi^{(2)}$ generation, the strength of the radiated field is insensitive to the sign of Δk. In figure A.1, the line for $\Delta k z_{rf} = -1$ is even above the line for zero phase mismatch. The phase mismatch, in that case, partly compensates the effects of the Gouy-phase related factor. If the phase mismatch is zero, then the Gouy phase shifts on the generating beams will cause the terahertz radiation generated before the focus to be in opposite phase with the terahertz radiation generated beyond the focus point. Contributions from before the focus will (partly) cancel the contributions from after the focus. This results in an efficiency drop, when the crystal becomes larger then the focal lengths of the generating beams.

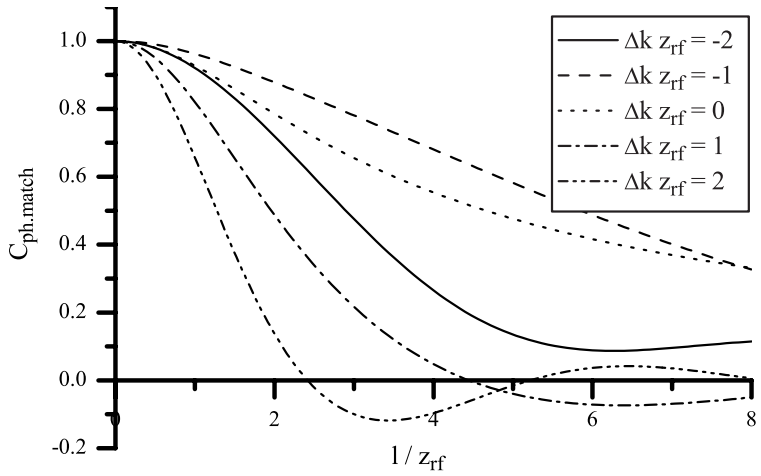

Figure A.1: The value of $C_{ph.match}$ as a function of the length of the generation crystal l for five different values of the phase mismatch Δk. Both l and Δk are normalized to the Rayleigh length of the fundamental beams z_{rf}

Appendix B

Modulation techniques

Figure B.1 show typical noise spectra of a Ti:Sapphire laser. The spectra show a strong increase in the noise below 200 Hz, a broad peak around 3 kHz and a series of sharp peaks with a 4 kHz spacing. Note that the power spectral density of the noise varies four orders of magnitude between 0 and 50 kHz. Because of this strong frequency dependence of the noise, it important to use modulation techniques in terahertz time-domain spectroscopy. This appendix explains and compares different modulation techniques within the context of terahertz time-domain spectroscopy.

The noise level within the frequency bandwidth that contains the measurement information should be as low as possible. Noise outside this information bandwidth is far less relevant, since this noise can be suppressed with electronic filters. Unfortunately, the information bandwidth usually starts at zero frequency, where the noise levels are high. Modulation can be used to shift the information to higher frequencies. In modulation techniques, the quantity that is measured, which in our case is the electric field of a terahertz pulse, is multiplied by a periodic function. We call this periodic function the modulation function and the inverse period of this function the modulation frequency. By modulation, the information is copied to higher frequencies, where the noise level is lower.

Figure B.2 illustrates modulation in the measurement of a terahertz pulse. The terahertz pulse is modelled by a Gaussian pulse, and is measured by slowly scanning the delay between terahertz pulse and probe pulse, where typically a 20 ps time delay is scanned in about 10 ms. The spectrum of the measured Gaussian pulse runs from DC to about 10 kHz, a region where the laser produces lot of noise. In this example, a chopper modulates the terahertz beam, and thus copies the information of the Gaussian pulse to higher frequencies, where these is less noise. A chopper is a device that alternatingly blocks and transmits either the optical beam that generates the terahertz beam or the terahertz beam itself. This results in the modulation function shown in figure B.2. As all periodic functions, the spectrum of the modulation function consists of delta peaks. As we will see, the amplitudes of these peaks are important parameters that can be used to compare different modulation tech-

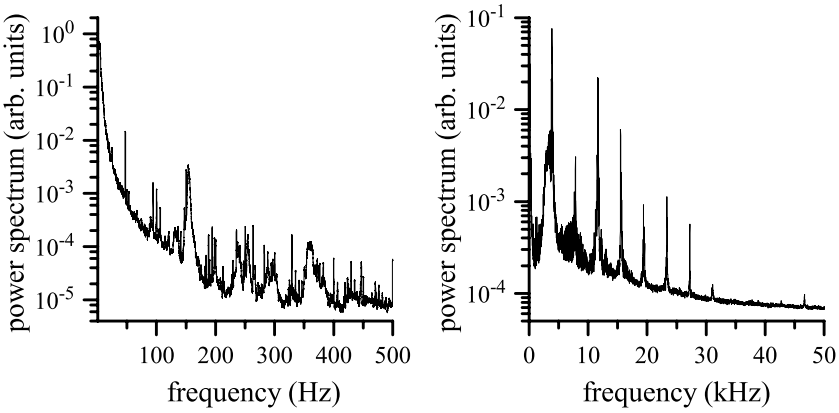

Figure B.1: Measured noise spectra of a Ti:Sapphire oscillator

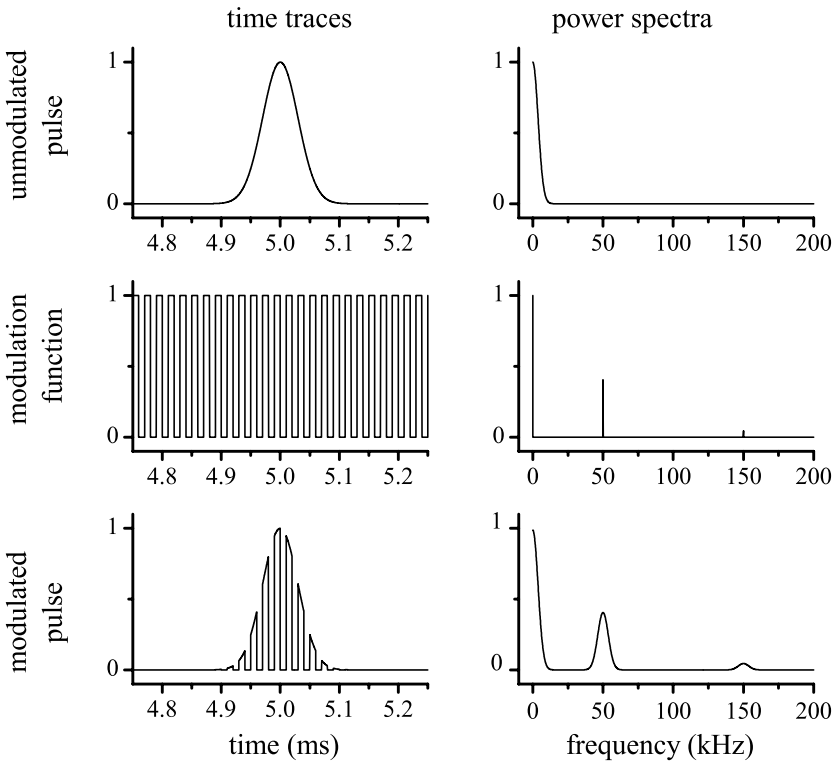

Figure B.2: Amplitude as a function of time (left graphs) and power spectra (right graphs) of an unmodulated Gaussian pulse, the modulation function and the modulated Gaussian pulse. The Gaussian pulse has a full width at half maximum of the intensity of 50 μs. The modulation function is a square wave with a frequency of 50 kHz.

niques. The bottom graphs display the amplitude as a function of time and the power spectrum of the modulated Gaussian pulse. The power spectrum graph shows three peaks, at DC, 50 kHz and 150 kHz. These peaks are all exact copies of the original spectrum of the Gaussian pulse, although the amplitudes of the peaks are different. With lock-in amplifiers, frequencies with a bandwidth around of one of the peaks can be selected, suppressing all noise and information outside this bandwidth with an electronic filter. For instance, the peak at 50 kHz can be selected with a lock-in amplifier synchronized to the 50 kHz component of the modulator signal. The signal-to-noise ratio of the measurement is then determined by the spectral amplitude of the 50-kHz pulse and the noise *around 50 kHz*.

It is clear that a good modulation technique should have a delta peak in the spectrum of the modulation function with two characteristics: a frequency at which the noise level is low, and an amplitude that is as high as possible. This provides us with a good quantitative measure to compare different modulation techniques. We will compare three different modulation techniques: modulation with a chopper, modulation by alternating the bias voltage of a photoconductive emitter and modulation with a photoelastic modulator (PEM). Modulation with a PEM has, until recently, never been used in the terahertz field, and is discussed in section B.1. Section B.2 continues with a comparison of different modulation techniques.

B.1 Photoelastic modulator

The photoelastic effect is the effect that stress in a solid causes a birefringence proportionally to the stress. A photoelastic modulator (PEM) uses the photoelastic effect to cause a polarization change of an optical beam that oscillates in time. We can use a PEM to modulate the output of optical rectification, since this terahertz generation method strongly depends on the polarization.

A PEM consists of a bar of an optically transparent material, in our case calcium fluoride, to which piezo-electric actuators are attached. These actuators vibrate at precisely the resonance frequency of the bar ($\approx$ 50 kHz), thus creating a standing acoustic wave. The period of this standing wave (the distance between two adjacent nodes) equals the length of the bar. The birefringence is proportional to the amplitude of the standing wave, and is thus a function of the position in the bar. However, due to the large period of the standing wave, the amplitude of the wave can be assumed constant over a relatively large aperture with a diameter on the order of 1 - 2 cm. A PEM, therefore, does not require any focussing of the optical beam, as is for instance the case with an acousto-optic modulator.

We consider the following configuration. A linearly polarized optical beam that consists of ultrafast pulses propagates through a PEM into a $\langle 110 \rangle$ oriented ZnTe crystal. In the ZnTe crystal, each optical pulse generates a terahertz pulse through the process of optical rectification (section 4.2). The efficiency of this generation process is a strong function of the polarization of the ultrafast pulse in the ZnTe crystal, and thus of the time-dependent birefrin-

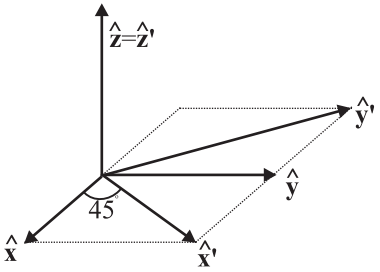

Figure B.3: Schematic display of the (x,y,z) and the (x',y',z') coordinate system.

gence of the PEM.

The original, linear polarization of the optical beam is aligned at 45 degrees with the birefringence axes of the PEM. After the PEM, we can write for the electric field of the optical beam

$$E_{y'} = \frac{1}{\sqrt{2}} E_0 \exp(i\phi/2) \tag{B.1}$$

$$E_{z'} = \frac{1}{\sqrt{2}} E_0 \exp(-i\phi/2), \tag{B.2}$$

where ϕ is the time-dependent phase difference induced by the time-dependent birefringence, and E_0 is the total electric field amplitude. Figure B.3 illustrates the coordinate systems used in this section. The axes of the coordinates y' and z' are along the birefringence axes of the PEM. The (x,y,z) coordinate system has its axes aligned with the crystalographic axes of the ZnTe crystal. The optical beam propagates parallel to the x' axis, which is $\langle 110 \rangle$ direction of the crystal. The $\langle 1\bar{1}0 \rangle$ direction is parallel to the y' axis, and $\langle 001 \rangle$ is parallel to the z' axis. Note that in this configuration the original pump beam polarization is in the $\langle 1\bar{1}\sqrt{2} \rangle$, and is thus *not* along the $\langle 1\bar{1}1 \rangle$ direction, which is the polarization direction for which the highest peak terahertz electric-field strength is obtained without modulation.[50] However, when modulating, the modulation depth should be optimized, which leads to the configuration presented here.

If we assume that the absorption in the ZnTe crystal is negligible, we can write for the nonlinear polarization in the ZnTe crystal[69]

$$P_x = \frac{1}{2} \varepsilon_0 \chi^{(2)} \left(E_y E_z^* + E_z E_y^* \right) \tag{B.3}$$

$$P_y = \frac{1}{2} \varepsilon_0 \chi^{(2)} \left(E_z E_x^* + E_x E_z^* \right) \tag{B.4}$$

$$P_z = \frac{1}{2} \varepsilon_0 \chi^{(2)} \left(E_x E_y^* + E_y E_x^* \right), \tag{B.5}$$

where the x, y and z axes are defined in figure B.3. These equations can be

rewritten to the lab (x', y', z') coordinate system using

$$\hat{\mathbf{x}}' = (\hat{\mathbf{x}} + \hat{\mathbf{y}}) / \sqrt{2} \tag{B.6}$$

$$\hat{\mathbf{y}}' = (\hat{\mathbf{x}} - \hat{\mathbf{y}}) / \sqrt{2} \tag{B.7}$$

$$\hat{\mathbf{z}}' = \hat{\mathbf{z}} \tag{B.8}$$

In the x', y', z' coordinate system, the nonlinear polarization is given by

$$P_{x'} = 0 \tag{B.9}$$

$$P_{y'} = -\frac{1}{2}\varepsilon_0 \chi^{(2)} \left(E_{y'} E^*_{z'} + E_{z'} E^*_{y'} \right) \tag{B.10}$$

$$P_{z'} = \frac{1}{2}\varepsilon_0 \chi^{(2)} E_{y'} E^*_{y'}, \tag{B.11}$$

where we have used that there is no electric field in the propagation direction ($E_{x'}$=0). Substituting equations B.1 and B.2 in the equation above yields

$$P_{y'} = -\frac{1}{2}\varepsilon_0 \chi^{(2)} |E_0|^2 \cos(\phi) \tag{B.12}$$

$$P_{z'} = \frac{1}{4}\varepsilon_0 \chi^{(2)} |E_0|^2. \tag{B.13}$$

We find that the nonlinear polarization in the $\langle 1\bar{1}0 \rangle$ direction ($P_{y'}$) is proportional to the cosine of ϕ. The polarization in the $\langle 001 \rangle$ direction ($P_{z'}$) is not modulated, and is thus not interesting for our purpose. The nonlinear polarization without PEM with a linear pump polarization in the $\langle 1\bar{1}1 \rangle$ direction is given by $P_{max} = -\frac{1}{3}\sqrt{3}\varepsilon_0 \chi^{(2)} |E_0|^2$.[50] This is the maximum nonlinear polarization than can be reached with an optical beam propagating along the $\langle 110 \rangle$ direction of a nonlinear cubic crystal. It is instructive to express the polarization for the modulated case in terms of this maximum polarization, as it provides an idea of the efficiency of the measurement technique. For the nonlinear polarization in the $\langle 1\bar{1}0 \rangle$ direction this expression is

$$P_{y'} = \frac{1}{2}\sqrt{3} P_{max} \cos\phi \tag{B.14}$$

The maximum of the modulated nonlinear polarization is thus a factor $\frac{1}{2}\sqrt{3} \simeq 0.866$ smaller than the optimal nonlinear polarization without PEM.

We set the amplitude of the acoustic wave in the PEM such that ϕ has a maximum value of π. ϕ is then equal to $\pi \cos(2\pi f_m t)$, where t is the time, and f_m is the frequency of the acoustic wave in the PEM. The electric field of the radiated terahertz pulse is proportional to the nonlinear polarization. The modulation function of a PEM is thus given by

$$M_{pem} = \frac{1}{2}\sqrt{3} \cos\left(\pi \cos(2\pi f_m t)\right). \tag{B.15}$$

where we consider only the radiated field in the y' direction, because the field in the z' direction is not modulated.

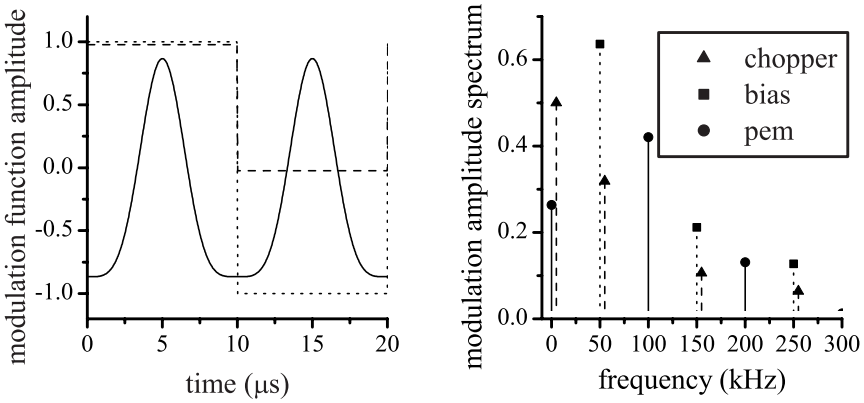

Figure B.4: Time domain and frequency domain calculation of the modulation function of three modulation techniques: modulation with a chopper (dashed line), with a square wave modulation of the emitter bias voltage (dotted line) and modulation with a PEM (solid line). In both graphs, the data for the chopper has been given an offset for clarity.

B.2 Comparison of modulation techniques

This section discusses and compares three modulation techniques. The first technique is modulation with a chopper, which alternatingly blocks and transmits the terahertz beam. The second method is to periodically switch the bias voltage of a photoconductive emitter between plus and minus its maximum value. The third technique is to use a PEM to modulate the terahertz beam generated by optical rectification, as described in the previous section.

Note that the purpose of this section is *not* to determine which is the best modulation technique. The choice for a modulation technique cannot be considered separately from the choice of a generation method. For instance, a photoconductive antenna is insensitive to the polarization of the generating pulse, and therefore cannot be modulated with a PEM.

Figure B.4 shows the modulation function of three different modulation techniques. The maximum phase difference in the PEM (ϕ) is set to π. The frequency of the chopper, of the bias-voltage square wave and of the acoustic wave in the PEM are all set at 50 kHz. Note that the modulation frequency of the PEM is 100 kHz, which is twice the frequency of the acoustic wave. This is a favourable property of modulation with a PEM, since the noise levels usually decrease with frequency. The spectra in figure B.4 show the multiple peaks in the frequency domain associated with each modulation function. The amplitude of these peaks is given by a Fourier series of the modulation function

$$m_k = \frac{1}{\tau} \int_0^\tau \mathrm{d}t M(t) \exp\left(-2\pi i k \frac{t}{\tau}\right), \tag{B.16}$$

where $M(t)$ is the modulation function, τ the modulation period and $k \in \mathbb{Z}$ is

the peak number.

The peaks in the spectra at zero frequency can be disregarded, since these peaks do not constitute any modulation. The following table gives the amplitudes of the first nonzero-frequency peaks.

	frequency	amplitude
chopper	50 kHz	0.318
bias voltage	50 kHz	0.637
PEM	100 kHz	0.420

Neither of these modulation methods has a peak with an amplitude of one. In fact, the value for the bias-voltage modulation ($= 2/\pi$) is the best possible value for *any* modulation scheme. In this modulation scheme, the amplitude of the terahertz electric field is constantly at its maximum value, while only the polarity of the electric field is modulated.

It is interesting to compare the signal-to-noise ratio (SNR) with and without modulation for the case that the noise amplitude is constant with frequency. As we will see, in that case the SNR is *reduced*, which makes it disadvantageous to modulate. However, by calculating how much the SNR is reduced, we can quantify how large the differences in spectral noise levels need to be to justify the use of a modulation scheme.

We step-by-step go through the modulation and demodulation process, and investigate how the SNR changes for a frequency-independent noise spectrum. The SNR is defined as the spectral amplitude of the signal divided by the spectral noise amplitude. In the modulation process, the signal amplitude spectrum is changed by a factor m_k, as defined in equation B.16. The noise spectrum is not affected by the modulation process. For a frequency-independent noise spectrum this means that modulation changes the SNR by a factor m_k. In the demodulation process, both signal and noise are copied from a bandwidth around the demodulation frequency to a bandwidth around frequency zero. It is important to note that the signal and the noise that end up at frequency f originate from *two* locations in the modulated spectrum. One part originates from frequency $f_d - f$ and the other from frequency $f_d + f$, where f_d is the demodulation frequency. Provided that the phase of the lock-in is set correctly, the signal contributions of the two locations add up constructively in the demodulation process. However, the noise values at the two frequencies are not equal, but are independent stochastic parameters. Stochastic parameters need to be summed quadratically, which means that of the sum of these two noise contribution equals $\sqrt{2}$ times the noise spectral density. Since the signal adds up constructively and the noise does not, demodulation increases the SNR by a factor $\sqrt{2}$. The combined effect of modulation and demodulation for a frequency-independent noise spectrum is thus a change of the SNR by a factor $\sqrt{2}m_k$. This factor is smaller than unity, which means that lock-in techniques reduce the SNR, if the noise spectrum is flat.

Lock-in techniques can only be beneficial, if the noise spectral density at frequencies around (harmonics of) the modulation frequency is smaller than the noise spectral density at low frequencies. Assuming that the noise spectral

density is constant on the scale of the information bandwidth, but is variable on the scale of the modulation frequency, the change in the SNR is given by

$$\frac{\text{SNR with lock-in}}{\text{SNR without lock-in}} = \sqrt{2} m_k \frac{N(k/\tau)}{N(0)}, \tag{B.17}$$

where $N(f)$ is the noise amplitude spectral density at frequency f. With equation B.17, we can give clear recommendations for the use of modulators in experiments: Use a chopper only, if the amplitude noise level at low frequencies is more than $1/(\sqrt{2}m_1) = 2.2$ times larger than the noise level at the modulation frequency $N(1/\tau)$. Use a bias-voltage modulation scheme only, if the N(0) is more than $1/(\sqrt{2}m_1) = 1.1$ times larger than $N(1/\tau)$. Use a PEM only, if the N(0) is more than $1/(\sqrt{2}m_1) = 1.7$ times larger than $N(1/\tau)$.

In the above, we assumed that the noise is approximately constant within the information bandwidth. This is no longer the case, if the noise spectrum contains sharp peaks. Such peaks can, for instance, be caused by interference from power lines. The noise spectrum of the Ti:Sapphire oscillator in figure B.1 has strong peaks with a 4 kHz spacing, which, we assume, are due to the feedback-system of the Millenia pump laser.

The influence of noise peaks on a measurement is completely different from the influence of a weakly frequency-dependent noise spectrum. In electronics, these peaks are not even referred to as noise, but as disturbances (for our definition of noise: section 3.1). An example of the different influence on a measurement is in averaging. Normally the noise level reduces proportionally to the square root of the number of averages, but the noise contribution of asynchronous peaks reduces proportionally to the number of averages. Noise peaks that are synchronous to the measurement are especially annoying, since averaging has no effect on these kinds of peaks. Synchronous peaks can, for instance, arise, if the loudspeaker used to vary the time delay couples vibrations to other mirrors. Concluding, noise peaks can be a big nuisance, and the modulation scheme should ensure that they do not occur within the information bandwidth.

When choosing between different types of modulators, the modulation frequency is also an important property. Experimenters need a modulation frequency around which the noise is minimal. Which modulation frequencies are possible, strongly depends on the modulation technique. A mechanical chopper is usually limited to lower frequencies (< 10 kHz), and can itself cause noise due to vibrations. An acousto-optic modulator can be used as a chopper at high frequencies, up to the tens of megahertz range. Unlike the modulation frequency of a chopper, the modulation frequency of a particular PEM is fixed. This frequency is determined by the physical size of the active medium, and is usually in the range of 50 kHz - 200 kHz. The modulation frequency of the bias voltage of a photoconductive emitter is easily controlled with a function generator, and has a maximum value in the order of 1 MHz, determined by the capacitance and resistance of the emitter.

In our optical rectification experiments, we have used a PEM from Hinds Instruments. This PEM has a modulation frequency of 113 kHz, and has an

active element of calcium fluoride with an useful aperture of 23 mm. This modulator has been chosen, because is allows a reasonably high modulation frequency, it is broadband and does not significantly lengthen our ultrafast pulses. In the experiments with a photoconductive emitter, we modulated the bias voltage at 50 kHz. We found that modulation with a PEM gave better experimental results than modulation with an optical chopper.

Appendix C

EM propagation through conducting media

The propagation of electromagnetic radiation through a conducting medium is often approximated by the wave equation with a dielectric constant that is modified to account for the conductivity. This is an approximation that requires two implicit assumptions; Ohm's law should be valid and the free charge carrier density should be negligible. This appendix discusses the validity of these assumptions at terahertz frequencies.

Anomalous skin effect

The validity of Ohm's law at terahertz frequencies is limited due to the so-called anomalous skin effect. In Ohm's law it is assumed that the current on a particular point is proportional to the local electric field. However, this is not valid if the electric field varies spatially on the scale of the mean free path of the carriers. It that case the current is not proportional to the electric field at a point, but is determined by the electric field averaged over the different points along the mean free path. This effect reduces the penetration depth into a conductor and is therefore called the anomalous skin effect.[112,113]

In a metal at room temperature, where electron-phonon scattering is dominant, the mean-free-path length is given by[112]

$$l_{mfp} = \frac{v_F \hbar}{k_B T}, \tag{C.1}$$

where v_F is the Fermi velocity of the electrons, which is 1.57×10^6 m/s for copper at room temperature.[114] This corresponds to a value for l_{mfp} of 40 nm.

Assuming that the Drude model (equation 5.26) is valid, the electric field penetration depth in a metal is

$$l_{pen} = \frac{c}{2\pi f} \operatorname{Re}\left\{ \frac{f_p}{\sqrt{f^2 + j f f_\tau}} \right\}^{-1}. \tag{C.2}$$

For copper (f_τ = 2.2 THz and f_p = 1787 THz)[93] at 2 THz, l_{pen} = 36 nm. The mean free path and the penetration depth are thus of the same order of magnitude. It seems therefore that an anomalous skin effect on the electromagnetic properties of metals is to be expected at terahertz frequencies.

Can the charge density be neglected?

We consider, assuming that Ohm's law is valid, under which condition the electromagnetic properties of a conducting medium can be described through a complex dielectric constant. Faraday's law for the rotation of the electromagnetic field is given by (equation 5.6)

$$\nabla \times \mathbf{E} = -j\omega\mathbf{B}, \tag{C.3}$$

where we have assumed a time dependence of $\exp(j\omega t)$. This equation can be rewritten by taking the rotation of both sides

$$\nabla(\nabla \cdot \mathbf{E}) - \nabla^2\mathbf{E} = -j\omega\nabla \times \mathbf{B}. \tag{C.4}$$

In this equation we substitute Ampère's law for the rotation of the magnetic field, which is given by (equation 5.8)

$$\nabla\times\frac{1}{\mu}\mathbf{B} = \mathbf{J}_f + j\omega\varepsilon\mathbf{E}, \tag{C.5}$$

where μ is the magnetic permeability and ε is the electric permittivity without free charge carriers. The current density of the free carriers is given by $\mathbf{J}_f$.

The result of the substitution of equation C.5 into equation C.4 is

$$\nabla(\nabla \cdot \mathbf{E}) - \nabla^2\mathbf{E} + j\omega\mu\mathbf{J}_f - \omega^2\varepsilon\mu\mathbf{E} = 0, \tag{C.6}$$

which is valid provided that μ does not depend on position.

We will use Ohm's law $\mathbf{J}_f = \sigma\mathbf{E}$, where σ is the complex conductivity of the medium, to get

$$\nabla(\nabla \cdot \mathbf{E}) - \nabla^2\mathbf{E} - \omega^2\varepsilon'\mu\mathbf{E} = 0, \tag{C.7}$$

where $\varepsilon' \equiv \varepsilon - j\frac{\sigma}{\omega}$ is the electric permittivity modified to account for the conductivity of the medium.

Assuming that $\nabla \cdot \mathbf{E} = 0$ results in the wave equation

$$\nabla^2\mathbf{E} + \omega^2\varepsilon'\mu\mathbf{E} = 0. \tag{C.8}$$

A conducting medium can thus be described as a dielectric with a permittivity ε', if divergence of the electric field can be neglected. To see under which condition this divergence is negligible, we consider Gauss' law (equation 5.5)

$$\nabla\cdot\varepsilon\mathbf{E} = \rho_f \tag{C.9}$$

with ρ_f the charge density of free charges. If the permittivity is isotropic and homogeneous, then this equation can be rewritten as

$$\nabla \cdot \mathbf{E} = \frac{\rho_f}{\varepsilon} \tag{C.10}$$

So if the divergence of the electric field is to be zero, then the charge density should be zero. The charge density is coupled with the current density by charge conservation

$$j\omega\rho_f = -\nabla \cdot \mathbf{J}_f. \tag{C.11}$$

Combining this equation with Ohm's law $\mathbf{J}_f = \sigma\mathbf{E}$ we get

$$\rho_f = \frac{j}{\omega}\nabla \cdot \mathbf{J} = \frac{j}{\omega}\left(\sigma\nabla \cdot \mathbf{E} + \mathbf{E} \cdot \nabla\sigma\right), \tag{C.12}$$

which with equation C.10 gives

$$\nabla \cdot \mathbf{E} = -\frac{\mathbf{E} \cdot \nabla\sigma}{j\omega\varepsilon'} \tag{C.13}$$

where ε' is, as before, defined as $\varepsilon - j\frac{\sigma}{\omega}$.

The conclusion is that the divergence of the electric field can be assumed zero, if the conductivity can be assumed to be homogeneous ($\nabla\sigma = 0$). This is generally true in metals. In metals, the free carrier density is sufficiently high to neglect any changes in the conductivity due to the electromagnetic field. However, there are a number of situations where the conductivity is not homogenous. The conductivity is, for instance, spatially dependent in the depletion layer of semiconductors. The conductivity is also not homogeneous in turbulent flows of plasmas, where local fluctuations in the density of the plasma will cause variations in the conductivity. A third example of a situation where the divergence of the electric is nonzero, is when the conductivity is changed by local excitation of carriers in semiconductors.

In general, it is valid to describe the electromagnetic properties of a conductor with a complex dielectric constant as long as Ohm's law is valid with a homogeneous complex conductivity.

Appendix D

Wave equation in cylindrical symmetric problems

The appendix derives cylindrical symmetric solutions to the wave equation. The calculation will be performed for the electric field, but is equally valid for the magnetic field. The wave equations are given by (equation 5.9)

$$\nabla^2 E_x + k^2 E_x = 0 \tag{D.1}$$

$$\nabla^2 E_y + k^2 E_y = 0 \tag{D.2}$$

$$\nabla^2 E_z + k^2 E_z = 0 \tag{D.3}$$

where $\vec{E} = (E_x, E_y, E_z)$ is the electric field vector and k is the wavenumber in the medium.

In a cylindrical coordinate system with coordinates (r, ϕ, z), ∇^2 is given by[115]

$$\nabla^2 = \frac{1}{r}\frac{\partial}{\partial r}\left(r\frac{\partial}{\partial r}\right) + \frac{1}{r^2}\frac{\partial^2}{\partial \phi^2} + \frac{\partial^2}{\partial z} \tag{D.4}$$

If this equation is substituted in the wave equations we get

$$\frac{1}{r}\frac{\partial}{\partial r}\left(r\frac{\partial E_x}{\partial r}\right) + \frac{1}{r^2}\frac{\partial^2 E_x}{\partial \phi^2} + \frac{\partial^2 E_x}{\partial z^2} + k^2 E_x = 0 \tag{D.5}$$

$$\frac{1}{r}\frac{\partial}{\partial r}\left(r\frac{\partial E_y}{\partial r}\right) + \frac{1}{r^2}\frac{\partial^2 E_y}{\partial \phi^2} + \frac{\partial^2 E_y}{\partial z^2} + k^2 E_y = 0 \tag{D.6}$$

$$\frac{1}{r}\frac{\partial}{\partial r}\left(r\frac{\partial E_z}{\partial r}\right) + \frac{1}{r^2}\frac{\partial^2 E_z}{\partial \phi^2} + \frac{\partial^2 E_z}{\partial z^2} + k^2 E_z = 0. \tag{D.7}$$

The field vectors are also transformed into the cylindrical system with

$$E_x = \cos(\phi)E_r - \sin(\phi)E_\phi \tag{D.8}$$

$$E_y = \sin(\phi)E_r + \cos(\phi)E_\phi. \tag{D.9}$$

We only look at solutions with cylinder symmetry, which means that E_r, E_ϕ and E_z are independent of ϕ. Using this symmetry and the above substitution, equations (D.5) to (D.7) can be rewritten as

$$\frac{1}{r}\frac{\partial}{\partial r}\left(r\frac{\partial E_r}{\partial r}\right) - \frac{1}{r^2}E_r + \frac{\partial^2 E_r}{\partial z} + k^2 E_r = 0 \tag{D.10}$$

$$\frac{1}{r}\frac{\partial}{\partial r}\left(r\frac{\partial E_\phi}{\partial r}\right) - \frac{1}{r^2}E_\phi + \frac{\partial^2 E_\phi}{\partial z} + k^2 E_\phi = 0 \tag{D.11}$$

$$\frac{1}{r}\frac{\partial}{\partial r}\left(r\frac{\partial E_z}{\partial r}\right) + \frac{\partial^2 E_z}{\partial z} + k^2 E_z = 0. \tag{D.12}$$

As an ansatz, the following solutions are used

$$E_r(r,z) = E'_r(r)\exp(-jk'z) \tag{D.13}$$

$$E_\phi(r,z) = E'_\phi(r)\exp(-jk'z) \tag{D.14}$$

$$E_z(r,z) = E'_z(r)\exp(-jk'z), \tag{D.15}$$

which leads to the following wave equations

$$r\frac{\partial}{\partial r}\left(r\frac{\partial E'_r}{\partial r}\right) + \left((k^2 - k'^2)r^2 - 1\right)E'_r = 0 \tag{D.16}$$

$$r\frac{\partial}{\partial r}\left(r\frac{\partial E'_\phi}{\partial r}\right) + \left((k^2 - k'^2)r^2 - 1\right)E'_\phi = 0 \tag{D.17}$$

$$r\frac{\partial}{\partial r}\left(r\frac{\partial E'_z}{\partial r}\right) + \left(k^2 - k'^2\right)r^2 E'_z = 0. \tag{D.18}$$

These differential equation are known as Bessel differential equations. The solutions to these equations are given by[71]

$$E'_r = C_{1r}\mathrm{J}_1\left(\sqrt{k^2 - k'^2}r\right) + C_{2r}\mathrm{Y}_1\left(\sqrt{k^2 - k'^2}r\right) \tag{D.19}$$

$$E'_\phi = C_{1\phi}\mathrm{J}_1(\sqrt{k^2 - k'^2}r) + C_{2\phi}\mathrm{Y}_1\left(\sqrt{k^2 - k'^2}r\right) \tag{D.20}$$

$$E'_z = C_{1z}\mathrm{J}_0\left(\sqrt{k^2 - k'^2}r\right) + C_{2z}\mathrm{Y}_0\left(\sqrt{k^2 - k'^2}r\right), \tag{D.21}$$

where $\mathrm{J}_n(x)$ is a Bessel function of the first kind and of the n'th order and $\mathrm{Y}_n(x)$ is a Bessel function of the second kind and of the n'th order. Various constants are indicated by subscripted Cs.

Bibliography

[1] D. H. Martin and K. Mizuno. The generation of coherent submillimetre waves. *Advances in Physics*, 25:211–246, 1976.

[2] P. D. Coleman. Far-infrared molecular lasers. *IEEE Journal of Quantum Electronics*, QE-9:130–138, 1973.

[3] R. Köhler, A. Tredicucci, F. Beltram, H. E. Beere, E. H. Linfield, A. G. Davies, B. A. Ritchie, R. C. Lotti, and R. Rossi. Terahertz semiconductor-heterostructure laser. *Nature*, 417:156–159, 2002.

[4] A. Tredicucci, R. Köhler, F. Beltram, H. E. Beere, E. H. Linfield, A. G. Davies, and D. A. Ritchie. Terahertz quantum cascade laser. *Physica E*, 21:846–851, 2004.

[5] M. van Exter, C. Fattinger, and D. Grischkowsky. Terahertz time-domain spectroscopy of water vapor. *Optics Letters*, 14:1128–1130, 1989.

[6] D. Grischkowsky, S. Keiding, M. van Exter, and C. Fattinger. Far-infrared time-domain spectroscopy with terahertz beams of dielectrics and semiconductors. *Journal of the Optical Society of America B*, 7:2006–2015, 1990.

[7] P. N. Saeta, J. F. Federici, B. I. Greene, and D. R. Dykaar. Intervalley scattering in GaAs and InP probed by pulsed far-infrared transmission spectroscopy. *Applied Physics Letters*, 60:1477, 1992.

[8] J. F. Frederici, B. I. Greene, P. N. Dykaar, F. Sharifi, and R. C. Dynes. Cooper pair breaking in lead measured by pulsed terahertz spectroscopy. *IEEE Transactions on Applied Superconductivity*, 3:1461–1464, 1993.

[9] R. R. Jones, D. You, and P. Bucksbaum. Ionisation of Rydberg atoms by subpicosecond half-cycle electromagnetic pulses. *Physical Review Letters*, 70:1236–1239, 1993.

[10] B. B. Hu and M. C. Nuss. Imaging with terahertz waves. *Optics Letters*, 20:807–809, 1995.

[11] Q. Wu, T. D. Hewitt, and X.-C. Zhang. Two-dimensional electro-optic imaging of THz beams. *Applied Physics Letters*, 69:1026–1028, 1996.

[12] D. M. Mittleman, S. Hunsche, L. Boivin, and M. C. Nuss. T-ray tomography. *Optics Letters*, 22:904–906, 1997.

[13] Z. Jiang and X.-C. Zhang. Single-shot spatiotemporal terahertz field imaging. *Optics Letters*, 23:1114–1116, 1998.

[14] S. Hunsche, M. Koch, I. Brener, and M. C. Nuss. Terahertz near-field imaging. *Optics Communications*, 150:22–26, 1998.

[15] W. F. Passchier, D. D. Honijk, M. Mandel, and M. N. Afsar. A new method for the determination of complex refractive index spectra of transparent solids in the far-infrared spectral region: Results of pure silicon and crystal quartz. *Journal of Physics D*, 10:509–517, 1977.

[16] O. Morikawa, M. Tonouchi, and M. Hangyo. A cross-correlation spectroscopy in subterahertz region using an incoherent light source. *Applied Physics Letters*, 76:1519–1521, 2000.

[17] P. H. Siegel. Terahertz technology. *IEEE Transactions on Microwave Theory and Techniques*, 50:910–927, 2002.

[18] T. G. Blaney. Radiation detection at submillimetre wavelengths. *Journal of physics E: Scientific instruments*, 11:856–881, 1978.

[19] P. L. Richards. Bolometers for infrared and millimeter waves. *Journal of Applied Physics*, 76:1–24, 1994.

[20] J. A. Valdmanis, G. A. Mourou, and C. W. Gabel. Subpicosecond electrical sampling. *IEEE Journal of Quantum Electronics*, QE-19:664–667, 1983.

[21] D. D. Duncan. Atmosphere transmission. In F. G. Smith, editor, *Atmosphere Propagation of Radiation*, volume 2, chapter 1.3. Infrared Information and Analysis Center and SPIE Optical Engineering Press, 1993.

[22] S. Verghese, K. A. McIntosh, S. Calawa, W. F. Dinatale, E.K. Duerr, and K. A. Molvar. Generation and detection of coherent terahertz waves using two photomixers. *Applied Physics Letters*, 73:3824–3826, 1998.

[23] G. Zhao, R. N. Schouten, N. van der Valk, W. Th. Wenckebach, and P. C. M. Planken. Design and performance of a THz emission and detection setup based on a semi-insulating GaAs emitter. *Review of Scientific Instruments*, 73:1715–1719, 2002.

[24] K. J. Siebert, H. Quast, R. Leonhardt, T. Löffler, M. Thomson, T. Bauer, and H. G. Roskos. Continuous-wave all-optoelectronic terahertz imaging. *Applied Physics Letters*, 80:3003–3005, 2002.

[25] http://aura.gsfc.nasa.gov/instruments/mls/introduction.html, February 2005.

[26] http://www.teraview.com/home_index.htm.

[27] M. Walther, P. Plochocka, B. Fischer, H. Helm, and P. U. Jepsen. Collective vibrational modes in biological molecules investigated by terahertz time-domain spectroscopy. *Biopolymers*, 67:310–313, 2002.

[28] M. Brucherseifer, M. Nagel, P. Haring Bolivar, H. Kurz, A. Bosserhoff, and R. Büttner. Label-free probing of the binding state of DNA by time-domain terahertz sensing. *Applied Physics Letters*, 77:4049–4051, 2000.

[29] H. A. Bethe. Theory of diffraction by small holes. *Physical Review*, 66:163–175, 1944.

[30] D. Qu, D. Grischkowsky, and W. Zhang. Terahertz transmission properties of thin, subwavelength metallic hole arrays. *Optics Letters*, 29:896–898, 2004.

[31] Q. Wu and X.-C. Zhang. Free-space electro-optic sampling of terahertz beams. *Applied Physics Letters*, 67:3523–3525, 1995.

[32] P. Uhd Jepsen, C. Winnewisser, M. Shall, V. Schya, S. R. Keiding, and H. Helm. Detection of THz pulses by phase retardation in lithium tantalate. *Physical Review E*, 53:3052–3054, 1997.

[33] A. Nahata, A. S. Weling, and T. F. Heinz. A wideband coherent terahertz spectroscopy system using optical rectification and electro-optic sampling. *Applied Physics Letters*, 69:2321–2322, 1996.

[34] M. Li, G. C. Cho, T.-M. Lu, X.-C. Zhang, S.-Q. Wang, and J. T. Kennedy. Time-domain dielectric constant measurement of thin film in GHz–THz frequency range near the Brewster angle. *Applied Physics Letters*, 74:2113–2115, 1999.

[35] K. Wynne and D. A. Jaroszynski. Superluminal terahertz pulses. *Optics Letters*, 24:25–27, 1999.

[36] B. Ferguson, S. H. Wang, D. Gray, D. Abbot, and X.-C. Zhang. T-ray computed tomography. *Optics Letters*, 27:1312–1314, 2002.

[37] Q. Chen and X.-C. Zhang. Semiconductor dynamic aperture for near-field terahertz wave imaging. *IEEE Journal of Selected Topics in Quantum Electronics*, 7:608–614, 2001.

[38] N. C. J. van der Valk and P. C. M. Planken. Electro-optic detection of subwavelength terahertz spot sizes in the near field of a metal tip. *Applied Physics Letters*, 81:1558–1560, 2002.

[39] G. Gallot and D. Grischkowsky. Electro-optic detection of terahertz radiation. *Journal of the Optical Society of America B*, 16:1204–1212, 1999.

[40] R. W. Boyd. *Nonlinear Optics*. Academic Press, Boston, 1992.

[41] Lionel Duvillaret, Stéphane Rialland, and Jean-Louis Coutaz. Electro-optic sensors for electric field measurements. I. theoretical comparison among different modulation techniques. *Journal of the Optical Society of America B*, 19:2692–2703, 2002.

[42] P. C. M. Planken, H.-K. Nienhuys, H. J. Bakker, and T. Wenckebach. Measurement and calculation of the orientation dependence of terahertz pulse detection in ZnTe. *Journal of the Optical Society of America B*, 18:313–317, 2001.

[43] Lionel Duvillaret, Stéphane Rialland, and Jean-Louis Coutaz. Electro-optic sensors for electric field measurements. II. choice of the crystals and complete optimization of their orientation. *Journal of the Optical Society of America B*, 19:2704–2715, 2002.

[44] W. H. Chen, W. K. Kue, S. L. Huang, and Y. T. Huang. On-wafer electrooptic probing using rotational deformation modulation. *IEEE Photonics Technology Letters*, 12:1228–1230, 2000.

[45] W.-K. Kuo, W.-H. Chen, Y.-T. Huang, and S.-L. Huang. Two-dimensional electric-field vector measurement by a $LiTaO_3$ electro-optic probe tip. *Applied Optics*, 39:4985–4993, 2000.

[46] K. Yang, L. P. B. Katehi, and J. F. Whitaker. Electro-optic field mapping system utilizing external gallium arsenide probes. *Applied Physics Letters*, 77:486–488, 2000.

[47] W. K. Kuo, S. L. Huang, T. S. Horng, and L. C. Chang. Two-dimensional mapping of electric-field vector by electro-optic prober. *Optics Communications*, 149:55–60, 1998.

[48] N. C. J. van der Valk and P. C. M. Planken. Full mathematical description of electro-optic detection in optically isotropic crystals. *Journal of the Optical Society of America B*, 21:622–631, 2004.

[49] A. Yariv. *Quantum Electronics*, chapter 5.2. John Wiley & sons, New York, second edition, 1975.

[50] Q. Chen, M. Tani, Zhiping Jiang, and X.-C. Zhang. Electro-optic transceivers for terahertz-wave applications. *Journal of the Optical Society of America B*, 18:823–831, 2001.

[51] W. A. M. van der Marel. Terahertz polarization imaging. Master's thesis, Delft University of Technology, Faculty of Applied Sciences, Optics Group, 2004.

[52] M. Young and R. A. Lawton. Saturation of silicon photodiodes at high modulation frequency. *Applied Optics*, 17:1103–1106, 1978.

[53] M. Dentan and B. de Cremoux. Numerical simulation of the nonlinear response of a P–I–N photodiode under high illumination. *Journal of Lightwave Technology*, 8:1137–1143, 1990.

[54] C.-K. Sun, I.-H. Tan, and J. E. Bowers. Ultrafast transport dynamics op P–I–N photodetectors under high-power illumination. *IEEE Photonics Technology Letters*, 10:135–137, 1998.

[55] H. J. Bakker, G. C. Cho, H. Kurz, Q. Wu, and X.-C. Zhang. Distortion of terahertz pulses in electro-optic sampling. *Journal of the Optical Society of America B*, 15:1795–1801, 1998.

[56] D.J. Griffiths. *Introduction in Electrodynamics*. Prentice Hall, New Jersey, third edition, 1999.

[57] N. C. J. van der Valk, R. N. Schouten, and P. C. M. Planken. Noise suppression of a differential detector under high-levels of illumination. *Review of Scientific Instruments*, 76:073104, 2005.

[58] J. Z. Xu and X.-C. Zhang. Optical rectification in an area with a diameter comparable to or smaller than the center wavelength of terahertz radiation. *Optics Letters*, 27:1067–1069, 2002.

[59] G. L. Dakovski, B. Kubera, and J. Shan. Localized terahertz generation via optical rectification in ZnTe. *Journal of the Optical Society of America B*, 22:1667–1670, 2005.

[60] J. R. Morris and Y. R. Shen. Far-infrared generation by picosecond pulses in electro-optical materials. *Optics Communications*, 3:81–84, 1971.

[61] Y. R. Shen. Far-infrared generation by optical mixing. *Progress in Quantum Electronics*, 4:207–232, 1976.

[62] David A. Kleinman and David H. Auston. Theory of electrooptic shock radiation in nonlinear optical media. *IEEE Journal Quantum Electronics*, QE–20:964–970, 1984.

[63] D. H. Auston and M. C. Nuss. Electrooptic generation and detection of femtosecond electrical transients. *IEEE Journal of Quantum Electronics*, 24:184–197, 1998.

[64] L. Xu, X.-C. Zhang, and D. H. Auston. Terahertz beam generation by femtosecond optical pulses in electro-optic materials. *Applied Physics Letters*, 61:1784–1786, 2000.

[65] Y. J. Ding. Quasi-single-cycle terahertz pulses based on broadband-phase-matched difference-frequency generation in second-order nonlinear medium: High output powers and conversion efficiencies. *IEEE Journal of Selected Topics in Quantum Electronics*, 10:1171–1179, 2004.

[66] J. T. Darrow, B. B. Hu, X.-C. Zhang, and D. H. Auston. Subpicosecond electromagnetic pulses from large-aperture photoconductive antennas. *Optics Letters*, 15:323–325, 1990.

[67] Y. C. Shen, P. C. Upadhya, E. H. Linfield, H. E. Beere, and A. G. Davies. Terahertz generation from coherent optical phonons in a biased GaAs photoconductive emitter. *Physical Review B*, 69:235325, 2004.

[68] Anthony E. Siegman. *Lasers*. University Science Books, Mill Valley, California, 1986.

[69] Max Schubert and Bernd Wilhelmi. *Nonlinear optics and quantum electronics*. John Wiley & Sons, New York, 1986.

[70] Paul Lorrain, Dale R. Corson, and François Lorrain. *Electromagnetic Fields and Waves*. W. H. Freeman and Company, New York, 1988.

[71] E. W. Weisstein. *The CRC Concise Encyclopedia of Mathematics*. CRC press LLC, Boca Raton, Florida, 1999. Available online through http://mathworld.wolfram.com/.

[72] D. H. Auston, K. P. Cheung, J. A. Valdmanis, and D. A. Kleinman. Cherenkov radiation from femtosecond optical pulses in electro-optic media. *Physical Review Letters*, 53:1555–1558, 1984.

[73] Joseph W. Goodman. *Introduction in Fourier Optics*. The McGraw-Hill companies, Inc, New York, second edition, 1996.

[74] R. Huber, A. Brodschelm, F. Tauser, and A. Leitenstorfer. Generation and field-resolved detection of femtosecond electromagnetic pulses up to 41 thz. *Applied Physics Letters*, 76:3191–3193, 2000.

[75] Kai Liu, Jingzhou Xu, and X.-C. Zhang. Gase crystals for broadband terahertz wave detection. *Applied Physics Letters*, 85:863–865, 2004.

[76] K. H. Yang, P. L. Richards, and Y. R. Shen. Generation of far-infrared radiation by picosecond light pulses in $LiNbO_3$. *Applied Physics Letters*, 19:320–323, 1971.

[77] M. Schall and P. Uhd Jepsen. Freeze-out of difference-phonon modes in ZnTe and its application in detection of THz pulses. *Applied Physics Letters*, 77:2801–2803, 2000.

[78] G. Gallot, Jiangquan Zhang, R. W. McGowan, Tae-In Jeon, and D. Grischkowsky. Measurements of the THz absorption and dispersion of ZnTe and their relevance to the electro-optic detection of THz radiation. *Applied Physics Letters*, 74:3450–3452, 1999.

[79] D. T. F. Marple. Refractive index of ZnSe, ZnTe, and CdTe. *Journal of Applied Physics*, 35:539–542, 1964.

[80] A. Manabe, A. Mitsuishi, and H. Yoshinaga. Infrared lattice reflection spectra of II-VI compounds. *Japanese Journal of Applied Physics*, 6:539, 1967.

[81] G. Gallot, S. P. Jamison, R. W. McGowan, and D. Grischkowsky. Terahertz waveguides. *Journal of the Optical Society of America B*, 17:851, 2000.

[82] R. Mendis and D. Grischkowsky. Plastic ribbon THz waveguides. *Journal of Applied Physics*, 88:4449, 2000.

[83] R. Mendis and D. Grischkowsky. Undistorted guided-wave propagation of subpicosecond terahertz pulses. *Optics Letters*, 26:846, 2001.

[84] H. Han, H. Park, M. Cho, and J. Kim. Terahertz pulse propagation in a plastic photonic crystal fiber. *Applied Physics Letters*, 80:2634, 2002.

[85] S. Hadjiloucas, R. K. H. Galvão, J. W. Bowen, R. Martini, M. Brucherseifer, H. P. M. Pellemans, P. Haring Bolivár, H. Kurz, J. Digby, G. M. Parkhurst, and J. M. Chamberlain. Measurement of propagation constant in waveguides with wideband coherent terahertz spectroscopy. *Journal of the Optical Society of America B*, 20:391, 2003.

[86] J. A. Harrington, R. George, and P. Pedersen. Hollow polycarbonate waveguides with inner Cy coating for delivery of terahertz radiation. *Optics Express*, 12:5263, 2004.

[87] K. Wang, A. Barkan, and D. M. Mittleman. Propagation effects in apertureless near-field optical antennas. *Applied Physics Letters*, 84:305, 2004.

[88] K. Wang and D. M. Mittleman. Metal wires for terahertz wave guiding. *Nature*, 432:376, 2004.

[89] A. Sommerfeld. Fortpflanzung elektrodynamischer wellen an einem zylindrischen leiter. *Annalen der Physik und Chemie*, 67:233, 1899.

[90] G. Goubau. Single-conductor surface-wave transmission lines. *Proceedings of the I.R.E.*, R117.1:619–623, 1951.

[91] L. W. Zelby. Propagation modes on a dielectric coated wire. *Journal of the Franklin Institute*, 274:85, 1962.

[92] M. Schall, M. Walther, and P. Uhd Jepsen. Fundamental and second-order phonon processes in CdTe and ZnTe. *Physical Review B*, 64:094301(8), 2001.

[93] M. A. Ordal, R. J. Bell, R. W. Alexander, L. L. Long, and M. R. Querry. Optical properties of fourteen metals in the infrared and far infrared: Al, Co, Cu, Au, Fe, Pb, Mo, Ni, Pd, Pt, Ag, Ti, V, and W. *Applied Optics*, 24:4493–4499, 1985.

[94] Y. Xu and R. G. Bosisio. Study of Goubau lines for submillimeter wave and terahertz frequency applications. *IEE Proceedings-Microwaves, Antennas and Propagation*, 151:460–464, 2004.

[95] J. A. Stratton. *Electromagnetic Theory*. McGraw-Hill Book Company, New York, 1941.

[96] K. Wang, D. M. Mittleman, N. C. J. van der Valk, and P. C. M. Planken. Antenna effects in terahertz apertureless near-field optical microscopy. *Applied Physics Letters*, 85:2715, 2004.

[97] O. L. Figovsky, L. S. Sklyarsky, and O. N. Sklyarsky. Polyurethane adhesives for electronic devices. *Journal of Adhesion Science and Technology*, 14:915, 2000.

[98] J. Saxler, J. Gómez Rivas, C. Janke, H. P. M. Pellemans, P. Haring Bolívar, and H. Kurz. Time-domain measurements of surface plasmon polaritons in the terahertz frequency range. *Physical Review B*, 69:155427, 2004.

[99] O. Mitrofanov, I. Brener, R. Harel, J. D. Wynn, L. N. Pfeiffer, K. W. West, and J. Federici. Terahertz near-field microscopy based on a collection mode detector. *Applied Physics Letters*, 77:3496–3498, 2000.

[100] K. Wynne, J. J. Carey, J. Zawadzka, and D. A. Jaroszynski. Tunneling of single-cycle terahertz pulses through waveguides. *Optics Communications*, 176:429–435, 2000.

[101] M. Specht, J. D. Pedarnig, W. M. Heckl, and T. W. Hänsch. Scanning plasmon near-field microscopy. *Physical Review Letters*, 68:476–479, 1992.

[102] F. Zenhausern, Y. Martin, and H. K. Wickramasinghe. Scanning interferometric apertureless microscopy: Optical imaging at 10 angstrom resolution. *Science*, 269:1083–1085, 1995.

[103] B. Knoll and F. Keilmann. Scanning microscopy by mid-infrared near-field scattering. *Applied Physics A, Materials Science & Processing*, 66:477–481, 1998.

[104] K. Wang, A. Barkan, and D. M. Mittleman. Sub-wavelength resolution using apertureless terahertz near-field microscopy. In *Conference on Lasers and Electro-Optics (CLEO)*. Optical Society of America, 2003.

[105] H.-T. Chen, R. Kersting, and G. C. Cho. Terahertz imaging with nanometer resolution. *Applied Physics Letters*, 83:3009–3011, 2003.

[106] B. Knoll and F. Keilmann. Enhanced dielectric contrast in scattering-type scanning near-field optical microscopy. *Optics Communications*, 182:321–328, 2000.

[107] P. C. M. Planken and N. C. J. van der Valk. Spot-size reduction in terahertz apertureless near-field imaging. *Optics Letters*, 29:2306–2308, 2004.

[108] E. A. Ash and G. Nicholls. Super-resolution aperture scanning microscope. *Nature*, 237:510–512, 1972.

[109] F. Keilmann. Scattering-type near-field optical microscopy. *Journal of Electron Microscopy*, 53:187–192, 2004.

[110] D. J. Cook and R. M. Hochstrasser. Intense terahertz pulses by four-wave rectification in air. *Optics Letters*, 25:1210–1212, 2000.

[111] L. G. Gouy. Sur une propiete nouvelle des ondes lumineuses. *Comptes Rendus de L'acadmie Des Sciences*, 110:1251–1253, 1890.

[112] E. M. Lifshitz and L. P. Pitaevskii. *Physical Kinetics*, volume 10 of *Course on Theoretical Physics*. Pergamon Press, Oxford, England, 1993. Translated from Russian.

[113] I. M. Lifshits, M. Ya. Azbel, and M. I. Kaganov. *Electron Theory of Metals*. Consultants Bureau, New York, USA, 1973. Translated from Russian.

[114] C. Kittel. *Introduction to Solid State Physics*. John Wiley & Sons, New York, USA, sixth edition, 1986.

[115] J. D. Jackson. *Classical Electrodynamics*. John Wiley & Sons, New York, second edition, 1975.

List of symbols

symbol	unit	description
B	T	magnetic field
c	ms^{-1}	speed of light in vacuum
C	F	capacitance
d	m	layer thickness
D	Cm^{-2}	electric displacement
E	Vm^{-1}	electric field
h	Js	Planck's constant
H	Am^{-1}	the "H" field
I	A	electric current
I	Wm^{-2}	intensity
j	–	imaginary unit
J	Am^{-2}	volume current density
k_B	JK^{-1}	Boltzmann's constant
k	m^{-1}	wavenumber
l	m	length
L	H	inductance
M	–	modulation function
n	–	refractive index
N	$\mathrm{V\,Hz}^{-1/2}$	Noise amplitude spectral density
P	Cm^{-2}	polarization
P	W	power
Q	C	electric charge
r_c	–	direction of the polarization modes of the detection crystal
r_l	–	direction of the polarization modes of a quarter-wave plate
r_w	–	polarization direction of the axis of a Wollaston prism
r_{41}	mV^{-1}	41 component of the electro-optic tensor
R	Ω	resistance
s	–	probe-beam propagation direction
t	s	time
T	K	temperature
u	Jm^{-3}	energy volume density
v	ms^{-1}	velocity
V	–	sensitivity vector of electro-optic detection
δ_{ij}	–	Kronecker delta

ε	Fm^{-1}	permittivity tensor
ε_0	Fm^{-1}	permittivity of vacuo
ε_r	–	relative permittivity or dielectric constant
ζ	rad	induced phase difference in electro-optic detection
λ	Cm^{-1}	line charge density
μ	Hm^{-1}	magnetic permeability
ρ	Cm^{-3}	charge density
$\chi^{(1)}$	–	first order electric susceptibility
$\chi^{(2)}$	mV^{-1}	second order electric susceptibility
$\chi^{(3)}$	m^2V^{-2}	third order electric susceptibility
ψ	rad	phase difference
ω	rad s^{-1}	radial frequency
τ	s	period (time)

Summary

In the daily life we encounter many devices that are able to make images, such as a camera, night-glasses, a radar-installation or an X-ray machine. These devices use different forms of radiation: visible light for a camera, infrared radiation for some types of night-glasses, microwave radiation for a radar-installation and Röntgen radiation for an X-ray machine. Whether a radiation type is suitable to image a particular object depends to a large extent on the interaction of the radiation with different materials. Röntgen radiation, for example, is very suitable to image the human skeleton, because it goes unhindered through skin, fat and muscles, but is absorbed by bones.

Terahertz (=10^{12} Hz) radiation is a form of electromagnetic radiation that is at this moment used rarely for imaging purposes. For a long time, there has been little attention for possible applications of terahertz radiation, because of a lack of good sources and detectors. However, there are indeed reasons to assume that imaging with terahertz radiation could be very useful. First, many materials, such as paper, plastics and clothing are transparent for terahertz radiation, while they block visible light. This opens the opportunity to look through objects. One can, for instance, consider checking the storage life of milk without opening the milk carton, or the security checks on concealed weapons at airports. Secondly, many materials have characteristic properties in the terahertz region that make a clear contrast between these materials possible. For instance, it is possible to specifically measure the concentration of gasses in a gas mixture. Also, different forms of DNA can be distinguished.

By the development of stronger sources and more sensitive detection methods, imaging with terahertz radiation becomes ever more attractive. However, for some applications, such as imaging biological cells, the resolutions of many terahertz imaging techniques are not good enough. This is caused by a fundamental physical limit, the diffraction limit, which dictates that the resolution of ordinary imaging techniques is limited to about half the wavelength of the radiation used. This effect also occurs in visible-light microscopes, where it limits the resolution to about 0.25 μm. However, since the wavelength of terahertz radiation is about a factor 1000 larger than that of visible light, the diffraction limit is a much bigger problem with terahertz radiation. For terahertz radiation, the diffraction limit on the resolution is about 0.1 mm. To use terahertz radiation for imaging microscopic objects, such as cells, the diffraction limit will thus have to be circumvented.

This thesis explores different aspects of terahertz imaging with the ultimate goal of the development of a terahertz microscopy technique. Two of these aspects are the generation and detection of terahertz pulses. By using terahertz sources that produce extremely short pulses, the reflection and absorption of objects can be measured rapidly at a large number of frequencies. We also describe the different noise sources in our measurements and discuss how the influence of these sources can be minimized. Terahertz waves that propagate over metal surfaces are studied, because of the possibly large influence of these waves in our microscopy setup. The last part of this thesis presents a new terahertz microscopy technique.

The four most important results of the research described in this thesis, are as follows: First, a detail description of our detection method has led to a extension of this method, which makes it possible to simultaneously measure not only the strength of a terahertz wave, but also its direction of vibration. Second, adverse effects prove to arise, if the power of the optical light beam used to measure the terahertz radiation is too high. Such high powers, however, are desirable, since the relative noise level is lower at high powers. We present different recommendations that suppress the adverse effects without increasing the average noise level. Third, the propagation of terahertz waves over metal surfaces proves to be very sensitive to extremely thin coatings applied on the metal surface. This result can potentially be applied to sensitive measurements on coatings. One can, for instance, consider the determination of the thickness and quality of the insulation on electricity cables. Finally, a new microscopy technique is presented, which circumvents the diffraction limit. With this technique, microscopy can be performed, potentially with resolutions on the order of tens of nanometers. However, more research is needed to scientifically demonstrate resolutions that are sufficient for microscopy.

Concluding, the different aspects of the use of terahertz pulses for microscopy purposes has been explored intensively. This has led to a new imaging technique that constitutes an important step towards terahertz microscopy.

Samenvatting

In het dagelijks leven komen we vele apparaten tegen die afbeeldingen kunnen maken, zoals een fotocamera, een nachtkijker, een radarinstallatie of een Röntgenscanner. Deze apparaten gebruiken verschillende vormen van straling: zichtbaar licht voor de fotocamera, infrarood straling voor sommige nachtkijkers, microgolfstraling voor de radarinstallatie en Röntgen straling voor de Röntgenscanner. Of een stralingsvorm geschikt is om een bepaald object af te beelden wordt in belangrijke mate bepaald door de interactie van de straling met verschillende materialen. Röntgenstraling, bijvoorbeeld, is erg geschikt om het menselijk skelet af te beelden, omdat het ongehinderd door huid, vet en spieren heen gaat, maar geabsorbeerd wordt door botten.

Terahertz (= 10^{12} Hz) straling is een vorm van elektromagnetische straling, die op dit moment nog weinig gebruikt wordt voor het maken van afbeeldingen. Lange tijd is er nauwelijks aandacht geweest voor de mogelijke toepassingen van terahertz straling, omdat er geen goede bronnen en detectoren voorhanden waren. Er zijn echter wel degelijk redenen om aan te nemen dat het afbeelden met terahertz straling erg nuttig zou kunnen zijn. Ten eerste zijn vele materialen, zoals papier, plastics en kleding, transparant voor terahertz straling, terwijl ze zichtbaar licht blokkeren. Dit opent de mogelijkheid om door objecten heen te kijken. Hierbij valt bijvoorbeeld te denken aan het controleren van de houdbaarheid van melk zonder het melkpak te openen, of het controleren van vliegtuigpassagiers op wapens die onder hun kleren verborgen zijn. Ten tweede hebben vele materialen karakteristieke eigenschappen in het terahertz gebied die een duidelijke contrast tussen deze materialen mogelijk maakt. Zo is het bijvoorbeeld mogelijk om specifiek de concentratie van gassen zoals waterdamp te meten in gasmengsels. Ook kunnen verschillende vormen van DNA van elkaar onderscheiden worden.

Door de ontwikkeling van sterkere bronnen en gevoeligere detectiemethoden wordt het afbeelden met terahertz straling steeds aantrekkelijker. Echter, voor sommige toepassingen, zoals het afbeelden van biologische cellen, is de resolutie van veel afbeeldingstechnieken met terahertz straling te beperkt. Dat komt door een fundamentele natuurkundige grens, de diffractielimiet, die bepaald dat de resolutie van gewone afbeeldingstechnieken wordt beperkt tot ongeveer de helft van de golflengte van de gebruikte straling. Dit effect treed ook op bij zichtbaar-licht microscopen, waar het de resolutie begrenst tot ongeveer 0.25 μm. Echter, doordat de golflengte van terahertz straling ongeveer

een factor 1000 groter is dan die van zichtbaar licht, is de diffractielimiet bij terahertz straling een veel groter probleem. Voor terahertz straling beperkt de diffractielimiet de resolutie tot ongeveer 0.1 mm. Om met terahertz straling microscopische objecten, zoals cellen, af te beelden, moet de diffractielimiet dus omzeild worden.

Dit proefschrift onderzoekt verschillende aspecten van het afbeelden met behulp van terahertz straling met als uiteindelijk doel de ontwikkeling van een terahertz microscopietechniek. Deze aspecten bevatten onder meer de generatie en detectie van terahertz pulsen. Door gebruik te maken van terahertz bronnen die korte pulsen uitzenden, kan in korte tijd de reflectie en absorptie worden gemeten voor een groot aantal terahertz frequenties. We beschrijven ook de verschillende ruisbronnen in onze metingen en bediscussiëren hoe de invloed van deze ruisbronnen kan worden geminimaliseerd. Terahertz golven die zich voortplanten over metalen oppervlakken, worden bestudeerd vanwege de mogelijk grote invloed van deze golven in onze terahertz microscopie-opstelling. Het laatste gedeelte van dit proefschrift presenteert een nieuwe terahertz microscopietechniek.

De vier belangrijkste resultaten van het onderzoek beschreven in dit proefschrift, zijn als volgt: Ten eerste heeft een gedetailleerde beschouwing van onze detectiemethode geleid tot een aanpassing van deze methode, waardoor het mogelijk is om tegelijk niet alleen de sterkte van een terahertz golf te meten, maar ook zijn trillingsrichting. Ten tweede blijken er nadelige effecten op te treden als het vermogen van de optische lichtbundel die gebruikt wordt om de terahertz straling te meten, te hoog wordt. Zulke hoge vermogen zijn echter wel gewenst, aangezien het relatieve ruisniveau bij hoge vermogens lager is. Er zijn verschillende aanbevelingen gedaan om de nadelige effecten te onderdrukken, zonder het relatieve ruisniveau te laten toenemen. Ten derde blijkt dat de propagatie van terahertz golven over metalen draden erg gevoelig is voor extreem dunne deklagen op het metaaloppervlak. Dit resultaat kan potentieel worden toegepast voor zeer gevoelige metingen aan deklagen. Hierbij kan bijvoorbeeld worden gedacht aan het bepalen van de dikte en de kwaliteit van de isolatielaag op elektriciteitsdraden. Tenslotte wordt een nieuwe microscopietechniek gepresenteerd, waarmee de diffractielimiet kan worden omzeild. Met deze techniek kan microscopie worden bedreven, potentieel met resoluties in de orde van tientallen nanometers. Er is echter nog meer onderzoek nodig om een resolutie die voldoende is voor microscopie, wetenschappelijk aan te tonen.

Concluderend is er intensief gekeken naar de verschillende aspecten van het gebruik van terahertz pulsen voor microscopiedoeleinden. Dit heeft geleid tot een nieuwe afbeeldingstechniek die een belangrijke stap is op weg naar terahertz microscopie.

Dankwoord

Uiteraard had dit boekje er niet kunnen zijn zonder de hulp van vele mensen. Ten eerste, natuurlijk, mijn begeleider en toegevoegd promotor: Paul Planken. Paul is degene die mij het vak van onderzoeker heeft bijgebracht en mij geleerd heeft de fysische betekenis te destilleren uit zowel metingen als formules. Op elk moment van de dag kon ik bij hem binnenlopen, wat ik erg op prijs heb gesteld. Paul, bedankt voor je geduld, je raad en het plezier dat ik heb gehad in onze wetenschappelijke discussies!

Mijn promotoren, Joseph Braat en Huib Bakker, wil ik bedanken voor de tijd die zij gestoken hebben in het zorgvuldig lezen en becommentariëren van mijn proefschrift. Door de vele krabbels in de kantlijn en de discussies die we hadden, is dit proefschrift een stuk duidelijker, leesbaarder en volledi ger geworden.

Mijn promotieonderzoek had nooit kunnen slagen zonder de hulp van de ondersteunde staf van Optica. In een wetenschappelijk onderzoek, waarin zich vaak onverwachte problemen voordoen, is het super fijn als het mogelijk wordt gemaakt om snel wat nieuws te proberen. Als ik wat nodig had, stonden jullie altijd direct voor me klaar. Rob, Marnix, Aad, Roland, Leen, Paul K., Yvonne en Lucia bedankt voor alle hulp! Raymond Schouten verdient hier een bijzondere vermelding. Raymond ontwierp en bouwde uitstekende electronische onderdelen voor mijn meetopstelling. Zijn bijdrage ging echter verder. Bij het bedenken en testen van nieuwe meetmethoden konden we altijd gebruik maken van zijn indrukwekkend technisch inzicht. Raymond, bedankt!

I would like to thank all members of the optics group for the enjoyable time I spend with them. Thanks for all the pleasant coffee breaks and lunches and the interesting discussions during the group meetings. The fun we had during our boat trip on the IJsselmeer is exemplary for the relaxed atmosphere within Optics.

Ik ben mijn promotie begonnen binnen de sectie Terahertz Imaging. Ik wil de mensen van Terahertz Imaging bedanken voor de leuke tijd die ik met ze heb gehad. Ook na de opheffing van Terahertz Imaging hebben deze mensen mij nog geholpen met hun ruime ervaring op terahertz gebied. Tom, Tjeerd, Niels, John en Rozemarie, bedankt voor alles.

Anton Buijserd van het AMOLF in Amsterdam bedank ik voor zijn hulp met de Ti:Saffier oscillator en de optisch parametrische oscillator (OPO). Anton heeft deze instrumenten, die de basis vormen van mijn meetopstelling, ontworpen en gebouwd.

Ik had niet kunnen komen waar in nu ben zonder de steun van mijn ouders, aan wie dit proefschrift is opgedragen. Zij hebben mij steeds gestimuleerd om mijn interesses uit te diepen. Pa en Ma, bedankt voor jullie toewijding en steun.

Tenslotte, bedank ik mijn lieve vrouw Corine. Corine was degene die mij weer met beide benen op de grond zette als mijn hoofd verdronk in wiskundige formules. Corine, bedankt voor je geduld, je spontaniteit en je liefde.

Biography

The author, Nick van der Valk, was born on May 15 1978 in Delft, the Netherlands. Between 1991 and 1996 he attended preparatory scientific education (in Dutch abbreviated by VWO) at the Westland College in Naaldwijk, where he developed an interest in technology in general and applied physics in particular. After his graduation from high school, he therefore enroled in the study for master of science in applied physics at the Delft University of Technology. This diploma was obtained "cum laude"in 2001. Since that time, Nick has been working on his Ph.D. project in the Delft University of Technology, first as a member of the Terahertz Imaging group and later as a member of the Optics group. The research conducted in the Ph.D. project is the basis of this thesis, which is to be defended November 28, 2005.

Publication list

Journal publications as first author

"Terahertz polarization imaging,"
N.C.J. van der Valk, W. A. M. van der Marel and P. C. M. Planken,
Optics Letters **30** (20), 2802-2804 (2005).

"Effect of a dielectric coating on terahertz surface plasmon polaritons on metal wires,"
N.C.J. van der Valk and P.C.M. Planken,
Applied Physics Letters **87**, 071106 (2005).

"Noise suppression of a differential detector under high-levels of illumination,"
N.C.J. van der Valk, R.N. Schouten and P.C.M. Planken,
Review of Scientific Instruments **76** (7), 073104 (2005).

"Influence of pump wavelength and crystal length on the phase matching of optical rectification,"
N.C.J. van der Valk, P.C.M. Planken, A.N. Buijserd and H. J. Bakker,
Journal of the Optical Society of America B **22** (8), 1714–1718 (2005).

"Full mathematical description of electro-optic detection in optically isotropic crystals,"
N.C.J. van der Valk, W. T. Wenckebach, and P.C.M. Planken,
Journal of the Optical Society of America B **21** (3), 622–631 (2004).

"Towards terahertz near-field microscopy,"
N. C. J. van der Valk and P. C. M. Planken,
Philosophical transaction of the Royal Society London A **362**, 315–321 (2004),

"Measurement of THz Spot Sizes with a $\lambda/200$ Diameter in the Near-Field of a Metal Tip,"
N.C.J. van der Valk and P.C.M. Planken,
Journal of Biological Physics **29** (2), 239-245 (2003).

"Electro-optic detection of sub-wavelength terahertz spot sizes in the near field of a metal tip,"
N.C.J. van der Valk , P.C.M. Planken,
Applied Physics Letters **81** (9), 1558-1560 (2002).

"Terahertz-microscopie,"
Nick van der Valk en Paul Planken Nederlands tijdschrift voor de Natuurkunde (NtvN),
68e jaargang (2002), nr 12.

Other journal publications

"Spot-size reduction in terahertz apertureless near-field imaging,"
P. C. M. Planken and N. C. J. van der Valk,
Optics Letters **29** (19), 2306-2308 (2004).

"Antenna effects in terahertz apertureless near-field optical microscopy,"
K Wang, D.M. Mittleman, N.C.J. van der Valk, and P.C.M. Planken,
Applied Physics Letters **85** (14), 2715-2717 (2004).

"Design and performance of a THz emission and detection setup based on a semi-insulating GaAs emitter,"
G. Zhao, R.N. Schouten, N. van der Valk, W. Th. Wenckebach, and P.C.M. Planken,
Review of scientific instruments **73** (4), 1715-1719 (2002).

"A terahertz system using semi-large emitters: noise and performance characteristics,"
G. Zhao, R. N. Schouten, N. van der Valk, W. Th. Wenckebach, and P. C. M. Planken,
Physics in Medicine and Biology **47**, 3699-3704 (2002).

Conference contributions

"Phase matching effects on THz generation by optical rectification,"
Nick van der Valk, Paul Planken, Anton Buijserd and Huib Bakker,
poster, 29th fall meeting of the section Atomic Molecular and Optical Physics (AMO), Nederlands Natuurkunde Vereniging (NNV), Lunteren, November 2004.

"Electro-optic detection of sub-wavelength THz spot sizes in the near field of a metal tip,"
N.C.J. van der Valk, and P.C.M. Planken,
oral presentation, The Rank Prize Funds mini-symposium on terahertz imaging and sensing, 31 maart tot 3 april 2003, awarded the "Best Contributed Paper"prize.

"Micrometer resolution with (sub)-millimeter waves,"
N. C. J. van der Valk and P. C. M. Planken,
oral presentation, Conference on Lasers and Electrooptics (CLEO/QELS 2003) Technical digest CD-ROM, CMP2, June 2003.

"Frequency filtering effects in a scattering near-field THz microscope,"
N.C.J. van der Valk and P. C. M. Planken,
poster, 28th fall meeting of the section Atomic Molecular and Optical Physics (AMO), Nederlands Natuurkunde Vereniging (NNV), Lunteren, November 2003.

"Electro-optic detection of sub-wavelength terahertz spot sizes in the near field of a metal tip,"
N.C.J. van der Valk, W. Th. Wenckebach, and P.C.M. Planken,
oral presentation (Post-deadline), Ultrafast Phenomena XIII Proceedings of the 13th International conference, Vancouver, BC, Canada, may 12-17, 2002 Editors: R. D. Miller, M. M. Murnane, N. F. Scherer, and A. M. Weiner Springer-Verlag, Berlin 2003.

"Electro-Optic detection of sub-wavelength terahertz spot sizes,"
N.C.J. van der Valk , P.C.M. Planken,
oral presentation, 27th fall meeting of the section Atomic Molecular and Optical Physics (AMO), Nederlands Natuurkunde Vereniging (NNV), Lunteren, November 2002.